Testing the Quantumness of Atom Trajectories

Dissertation
zur
Erlangung des Doktorgrades (Dr. rer. nat.)
der
Mathematisch-Naturwissenschaftlichen Fakultät
der
Rheinischen Friedrich-Wilhelms-Universität Bonn

von
Carsten Robens
aus
Erftstadt Gymnich

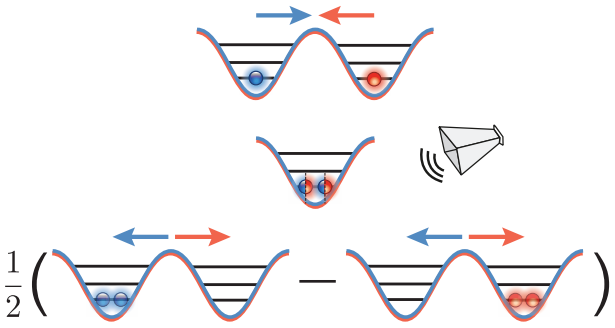

Bonn, 22.09.2016

Dieser Forschungsbericht wurde als Dissertation von der Mathematisch-Naturwissenschaftlichen Fakultät der Universität Bonn angenommen und ist auf dem Hochschulschriftenserver der ULB Bonn http://hss.ulb.uni-bonn.de/diss_online elektronisch publiziert.

1. Gutachter:	Prof. Dr. Dieter Meschede
2. Gutachter:	Prof. Dr. Jean-Michel Raimond
3. Gutachter:	Prof. Dr. Reinhard F. Werner
4. Gutachter:	Prof. Dr. Peter Koepke

Tag der Promotion:	07.02.2017
Erscheinungsjahr:	2017

Abstract

This thesis reports on a novel concept of state-dependent transport, which achieves an unprecedented control over the position of individual atoms in optical lattices. Utilizing this control I demonstrate an experimental violation of the Leggett Garg inequality, which rigorously excludes (*i.e.* falsifies) any explanation of quantum transport based on classical, well-defined trajectories. Furthermore, I demonstrate the generation of arbitrary low-entropy states of neutral atoms following a bottom-up approach by rearranging a dilute thermal ensemble into a predefined, ordered distribution in a one-dimensional optical lattice. Additionally, I probe two-particle quantum interference effects of two atom trajectories by realizing a microwave Hong-Ou-Mandel interferometer with massive particles, which are cooled into the vibrational ground state.

The first part of this thesis reports on several new experimental tools and techniques: three-dimensional ground state cooling of single atoms, which are trapped in the combined potential of a polarization-synthesized optical lattice and a blue-detuned hollow dipole potential; A high-NA (0.92) objective lens achieving a diffraction limited resolution of 460 nm; and an improved super-resolution algorithm, which resolves the position of individual atoms in small clusters at high filling factors, even when each lattice site is occupied.

The next part is devoted to the conceptually new optical-lattice technique that relies on a high-precision, high-bandwidth synthesis of light polarization. Polarization-synthesized optical lattices provide two fully controllable optical lattice potentials, each of them confining only atoms in either one of the two long-lived hyperfine states. By employing one lattice as the storage register and the other one as the shift register, I provide a proof of concept that selected regions of the periodic potential can be filled with one particle per site.

In the following part I report on a stringent test of the non-classicality of the motion of a massive quantum particle, which propagates on a discrete lattice. Measuring temporal correlations of the position of single atoms performing a quantum walk, we observe a $6\,\sigma$ (standard deviation) violation of the Leggett-Garg inequality. The experiment is carried out using so-called ideal negative measurements – an essential requisite for any genuine Leggett-Garg test – which acquire information about the atom's position while avoiding any direct interaction with it. This interaction-free measurement is based on our polarization-synthesized optical lattice, which allows us to directly probe the absence rather than the presence of atoms at a chosen lattice site. Beyond its fundamental aspect, I demonstrate the application of the Leggett-Garg correlation function as a witness of quantum superposition. The witness allows us to discriminate the quantumness of different types of walks spanning from merely classical to quantum dynamics and further to witness the decoherence of a quantum state.

In the last experimental part I will discuss recent results on collisional losses due to inelastic collisions occurring at high two-atom densities and demonstrate a Hong-Ou-Mandel interference with massive particles. Our precise control over individual indistinguishable particles embodies a direct analogue of the original Hong-Ou-Mandel experiment. By carrying out a Monte Carlo analysis of our experimental data, I demonstrate a signature of the two-particle interference of two-atom trajectories with a statistical significance of $4\,\sigma$.

In the final part I will introduce several new experiments which can be realized with the tools and techniques developed in this thesis, spanning from the detection of topologically protected edge states to the prospect of building a one-million-operation quantum cellular automaton.

Parts of this thesis have been published in the following articles:

[1] C. Robens, W. Alt, D. Meschede, C. Emary, A. Alberti, *Ideal Negative Measurements in Quantum Walks Disprove Theories Based on Classical Trajectories*, (2015), Phys. Rev. X 5, 011003

[2] A. Alberti, C. Robens, W. Alt, S. Brakhane, S. Brakhane, M. Karski, R. Reimann, A. Widera, D. Meschede, *Super-resolution microscopy of single atoms in optical lattices*, (2016), New Journal of Physics, 053010

[3] C. Robens, J. Zopes, W. Alt, S. Brakhane, D. Meschede, A. Alberti, *Low-entropy states of neutral atoms in polarization-synthesized optical lattices*, (2016), arXiv:1608.02410

[4] C. Robens, S. Brakhane, D. Meschede, A. Alberti, *Quantum Walks With Neutral Atoms: Quantum Interference Effects of One and Two Particles*, (2015), arXiv:1511.03569

[5] C. Robens, W. Alt, D. Meschede, C. Emary, A. Alberti, *Atomic "bomb testing": the Elitzur-Vaidman experiment violates the Leggett-Garg inequality*, (2016), in preparation

[6] A. Negretti, T. Calarco, C. Robens, W. Alt, D. Meschede, A. Alberti, *Optimal and fast transport control for coherent splittings of trapped atoms*, (2016), in preparation

The presented thesis is edited according to The Chicago Manual of Style, 16th ed. [7].

Contents

1 Introduction **1**

2 Experimental Techniques **3**

2.1 Cooling and Trapping Individual Neutral Atoms in an Optical Lattice 4

2.1.1 From the Background Gas Into the Optical Lattice 4

2.1.2 Storage Time of Atoms Trapped in a 1D Optical Lattice 10

2.1.3 A State Dependent Optical Lattice for Cesium 17

2.2 Super-Resolution Microscopy of Atoms in an Optical Lattice 19

2.2.1 Fluorescence Imaging of Neutral Atoms 20

2.2.2 Characterizing the Optical Response of the Imaging System 22

2.2.3 Localization of Atoms by Parametric Deconvolution 24

2.2.4 Outlook: Development of a High-NA (0.92) Objective Lens 25

2.3 Coherent Quantum State Manipulations 33

2.3.1 State Initialization and Detection 33

2.3.2 Coupling the Qubit States and its Representation on the Bloch Sphere 34

2.3.3 Microwave Driven Global Spin Rotations 36

2.3.4 Microwave Driven Local Spin Rotations 38

2.4 Population and Coherence Relaxation of Qubits in Polarization-Synthesized Optical Lattices 40

2.4.1 The Population Relaxation Time T_1 40

2.4.2 The Coherence Relaxation Time T_2 43

2.5 Three-Dimensional Ground State Cooling in a Blue-Detuned Hollow Beam Dipole Trap 45

2.5.1 The Blue-Detuned Hollow Beam Dipole Trap 46

2.5.2 Vibrational Ground State Cooling 53

3 Low-Entropy States of Neutral Atoms in Polarization-Synthesized Optical Lattices **67**

3.1 A Novel Approach to State-Dependent Transport 68

3.2 High Precision Polarization Synthesizer 69

3.2.1 Electro-Optical Setup of the Phase Lock 71

3.2.2 Intensity and Phase Noise 72

3.2.3 Spatial Polarization Inhomogeneities 74

3.2.4 Control Bandwidth of the Polarization-Synthesized Optical Lattice 75

3.3 Sorting Individual Atoms in Polarization-Synthesized Optical Lattices 75

3.3.1 Classical Atom Transport 76

3.3.2 A Novel Control Software and the Feedback Algorithm 78

3.3.3 Unity Filling in Polarization-Synthesized Optical Lattices 79

3.3.4 Pair Production and Parity Projection in Polarization-Synthesized Optical Lattices 81

3.4 Coherent Delocalization of the Atomic Wave Function . . . 83
3.4.1 Discrete-Time Quantum Walks . . . 83
3.4.2 Outlook: Speeding It up with Optimal Control . . . 84

4 Ideal Negative Measurements in Quantum Walks Test Single-Atom Trajectories 87
4.1 The Leggett-Garg Inequality . . . 88
4.2 Quantum Walks Falsify Classical Trajectories . . . 89
4.2.1 Quantum Mechanical Prediction . . . 90
4.3 Measuring the Quantumness of a Quantum Walk . . . 92
4.3.1 Quantum Witness . . . 92
4.4 Witnessing the Decoherence of a Quantum State . . . 92
4.5 Macroscopicity Measure and the Venalty . . . 94

5 Testing the Quantumness of Two-Atom Trajectories 97
5.1 Probing Two-Atom Collisions at High Densities . . . 97
5.1.1 State-Dependent Vibrational Excitations . . . 99
5.2 Microwave Hong-Ou-Mandel Interferometer with Massive Particles . . . 100
5.2.1 Monte Carlo Analysis of the Atomic Hong-Ou-Mandel Experiment . . . 103
5.2.2 Outlook: Further Enhancing the Hong-Ou-Mandel Signature . . . 105

6 Outlook 107

Bibliography 111

A Error Propagation Using Monte Carlo Samples 137
A.1 Example 1: Linear Function (Symmetric CI) . . . 137
A.2 Example 2: Non Linear Function (Asymmetric CI) . . . 138
A.3 Example 3: Combining Gaussian and Binomial Distributions . . . 139

B Useful Calculations in Quantum Optics 141
B.1 Electric Field, Intensity and Laser Power . . . 141
B.2 Different Mathematical Descriptions of Light Polarization . . . 143
B.2.1 Cartesian and Spherical Coordinates . . . 143
B.2.2 Jones Vector Representation . . . 143
B.2.3 The Poincaré Sphere and Stokes Parameter Representation . . . 143
B.3 Wigner-Eckart Theorem, Wigner Three and Six J Symbols, and Their Application . . . 144
B.4 Calculation of Scattering Rates Using the Kramers-Heisenberg Formula . . . 146

C The Nine Distinct Atomic Hong-Ou-Mandel Events 149

"The hallmark of this *second quantum revolution* is the realization that we humans are no longer passive observers of the quantum world that nature has given us."

— *Jonathan P. Dowling and Gerard J. Milburn [8]*

CHAPTER 1

Introduction

The development of quantum mechanics has inspired both theoretical and experimental physicists for more than a century. During the first period – today referred to as the *first revolution of quantum mechanics* [8] – significant scientific and technological breakthroughs were accomplished. Among these, two stand out noticeably: understanding absorption and emission of single photons stimulated the development of the laser [9, 10] and the concept of electrons and holes was a necessary prerequisite for semiconductor transistors [11, 12]. However, technological advances have not stopped and today, harnessing the quantum properties of single particles is no longer fiction [13]. Instead it has become a routine tool in modern quantum optics experiments. Furthermore, the quantum optics community is currently in an evolutionary state, where we transit from proof of principle experiments towards quantum technologies which utilize the control over the quantum world. While it is certainly a long and steep road before we reach the grand goal of building a universal quantum computer [14], it is beyond doubt that our journey has already started. [15].

Up until today several platforms suited to realize a universal quantum computer have been put forward and are currently being investigated by researchers around the world. Among these are ultracold atomic gases in optical lattices [16] or micro potentials [17–19], trapped ions [20], photons [21], artificial atom-like defects in solids [22, 23], and superconducting quantum circuits [24–27]. Furthermore, hybrid approaches that combine different advantages of the aforementioned systems are also considered [28]. At present, however, it is undetermined which of these technologies will succeed. For this reason it is becoming of increasing importance to develop stringent tests which allow for an objective comparison of different approaches.

This thesis aims to contribute to quantum computing using individual neutral atoms trapped in state-dependent optical lattices (see chap. 2 and chap. 3) and it further demonstrates rigorous tests of the superposition principle using the Leggett-Garg inequality [29] (see chap. 4) as well as entanglement by observing the Hong-Ou-Mandel interference of indistinguishable particles [30] (see chap. 5). Benchmarking different quantum systems is by no means the only purpose of rigorous tests of quantum mechanics. Despite the indisputable success of quantum mechanics so far, which has not failed to predict the behavior of the microscopic world, it is still an unresolved question how to reconcile the quantum mechanical worldview, where physical objects obey the unitary Schrödinger equation, with the macro-realistic one, where objects are in one definite state at all times [31]. This question is typically referred to as the measurement problem in quantum physics [32].

Several theories have been put forward to explain such a wave function reduction, which can be coarsely divided into two groups [33]: (a) interpretational solutions and (b) objective collapse theories. In 1985

Leggett and Garg (LG) derived an inequality relating correlation measurements performed at different times, thereby providing an objective criterion to distinguish between quantum (a) and macro-realistic (b) theories [29]. The experiments discussed in chapter 4 demonstrate that the trajectories of a single cesium atom are truly nonclassical and our findings constrain macro-realistic theories. In fact, our delocalized cesium atoms are the largest quantum objects which have been used to experimentally test the Leggett-Garg inequality employing noninvasive measurements [34]. Admittedly, our experimental violation of the Leggett-Garg inequality cannot be considered as a macroscopic test of quantum mechanics, since it tests the superposition of a single cesium atom which is at most delocalized over 2 µm. Nevertheless, 2 µm is already relatively large, considering that the diameter of human hair is just below 100 µm, while the average length of the bacterium *E. coli* is also 2 µm. Furthermore, our non invasive measurement technique may also be applied to test superposition states of even more macroscopic objects such as macromolecules and nanoparticles [35].

The Leggett-Garg inequality is considered to be the gold standard for testing the superposition principle of single particles [34]. Similarly, the Hong-Ou-Mandel effect is often regarded as a measure of the indistinguishability of photons [36–39]. Only recently, independent groups achieved the first demonstration of a Hong-Ou-Mandel interference with massive particles using tunneling between potential wells [17, 40] and in an atom interferometer-like experiment with metastable helium [41]. In chapter 5, I will demonstrate a complementary approach utilizing our novel polarization-synthesized optical lattice (see chap. 3) in combination with the experimental techniques introduced in chapter 2 to observe the Hong-Ou-Mandel type two-particle interference with cesium atoms. Furthermore, our polarization-synthesized optical lattice gives us an unprecedented control over the position of individual atoms in optical lattices. In chapter 3 we make use of this control – in a bottom-up approach – to generate arbitrary atom patterns, including unity filling of lattice sites, in a one-dimensional optical lattice. Our results show an alternative to the conventional top-down approach in optical lattices, which relies on a Mott insulator phase [42, 43].

Reaching the grand goal of building a universal quantum computer may be one of the greatest challenges experimental physics has faced so far [44]. This challenge arises partially from an inherent conflict: we aspire a well controllable quantum system, that is at the same time only weakly coupled to the environment, such that coherences are preserved for long times [45]. However, despite all experimental effort it is fundamentally impossible to realize a quantum system which is truly decoupled from the environment. For this purpose, theoretical physicists have developed several different techniques, such as quantum error correction [46] or topologically protected surface codes [47], to correct for inevitable errors of quantum devices. Nevertheless, the experimental level of precision required to utilize these techniques is rather demanding and so far only few experiments have passed the so-called error thresholds (e.g. [25, 48]). In order to reach the required error thresholds, we experimentalists need to meticulously investigate the physical mechanisms which lead to decoherence in our quantum systems. For this purpose, we aim to study the capability and potential limits of neutral atoms trapped in state-dependent optical lattices in chapter 2 and chapter 3. For example, we investigate the off-resonant scattering rates which limit the lifetime of our quantum information (see sec. 2.4.1), the fundamental limits of ground state cooling of atoms in optical potentials (see sec. 2.5.2), and the excitations caused by transport operations (see sec. 3.3.1).

The tools and techniques presented in this thesis open the path for several novel experiments, e.g. to study the robustness of topologically protected edge states in discrete-time quantum walks [49], explore few-body correlations arising from quantum statistics [50], realize quantum optical control of atom transport [6], simulate quantum electrodynamics [51], and investigate the Bose-Hubbard model with a controllable number of spin-1/2 particles [52].

CHAPTER 2

Experimental Techniques

Observing and manipulating individual atoms in a controlled fashion is an experimental challenge and requires several techniques. In the following chapter we will discuss the details of the experimental apparatus at hand, which resembles the one originally introduced in the PhD thesis of Michał Karski [53]. However, several essential features have been redeveloped from scratch (e.g. the capability to transport atoms depending on their internal state, see chap. 3), while others are novelties (e.g. three dimensional ground state cooling in a blue-detuned hollow beam see sec. 2.5.2). The present chapter gives an overview of the current state of the experimental apparatus including its capabilities used in the following chapters to realize: the bottom-up generation of low-entropy states (see chap. 3); an experimental violation of the Leggett Garg inequality, which disproves classical trajectory theories with quantum walks (see chap. 4); and first experiments with indistinguishable massive particles, such as the observation of the Hong-Ou-Mandel interference (see chap. 5).

The heart of the experimental apparatus is shown in figure 2.1, which consists of a one-dimensional

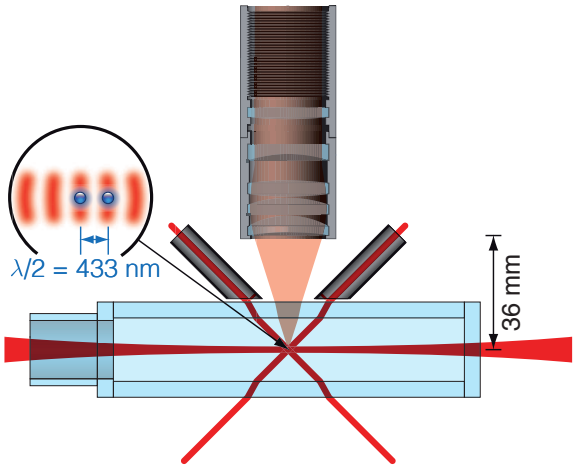

Figure 2.1: Illustration of the central part of the experimental apparatus: we form an optical lattice through the interference of two counter-propagating laser beams inside a vacuum glass cell. Cesium atoms are trapped in the bright regions of the optical standing wave pattern (see sec. 2.1.1). Illuminating trapped atoms with three pairs of counter-propagating molasses laser beams (see sec. 2.1.1) allows us to image individual atoms in the optical lattice by collecting their fluorescence with an objective lens (see sec. 2.2). This figure is adapted from Alberti et al. [2]

state-dependent optical lattice formed within a rectangular vacuum glass cell. Atoms trapped in this optical lattice can be imaged by recording the fluorescence light through a custom made microscope objective with a numerical aperture of NA = 0.23 [2, 54]. While – compared to state of the art objectives – the small numerical aperture prevents us from resolving atoms visually in single lattice sites, we developed a super-resolution algorithm, which allows us to determine their position numerically even for atoms in neighboring sites [2]. In general, our algorithm is closely related to those employed in super-resolution microscopy of biological structures [55–57]. The state-dependent optical lattice embodies the key feature that distinguishes our experimental apparatus from other experiments working with neutral atoms. While these experiments [17, 43, 58–61] rely on tunneling between different lattice sites, our optical lattice enables an active and coherent control of the atomic position. The conceptual idea of state-dependent transport is introduced in section 2.1.3, whereas the experimental details of our novel polarization-synthesized optical lattice are discussed in chapter 3.

2.1 Cooling and Trapping Individual Neutral Atoms in an Optical Lattice

2.1.1 From the Background Gas Into the Optical Lattice

Optical dipole potentials play an essential role in modern quantum optics experiments. The capability to create remarkably versatile conservative potentials – arising from laser beams and their interference – directly in free space has lead to a long list of successful experiments over the last two decades. Among these experiments is the all-optical realization of a Bose-Einstein condensate (BEC) [62]; the observation of the BCS-BEC crossover (named after Bardeen, Cooper, and Schrieffer) for ultracold fermionic lithium [58, 63]; and the realization of both bosonic and fermionic Mott insulators (named after Sir Nevill Mott) [43, 64, 65]. While these experiments are based on the dynamics of multiple atoms, more recently optical dipole potentials where shown to be exceptional tools to precisely control the quantum dynamics of individual atoms as well [17, 61, 66, 67].

One Dimensional Optical Lattice

Quantum mechanics describes the atom light interaction by a shift of the atomic energy levels ($E_i = \hbar\omega_i$), which is commonly referred to as AC-Stark shift. This atom light interaction can be understood more intuitively in a classical description, where the laser light is considered as an oscillating electrical field, which induces a dipole moment in the atom. The induced dipole moment then in turn interacts with the electric field giving rise to an optical dipole potential. A mathematical derivation of the optical potential using the Lorentz model can be found in nearly every textbook on quantum optics [68] or in Grimm et al. [69]. Therefore, let us come back to the quantum mechanical description. Using second order perturbation theory and the atom light interaction Hamiltonian $\mathcal{H}_{\text{int}}$ (see eq. (B.29) in appx. sec. B.4) we can calculate the light induced energy shift (ΔE_i):

$$\Delta E_i = \sum_{j \neq i} \frac{1}{\hbar} \frac{|\langle j| \mathcal{H}_{\text{int}} |i\rangle|^2}{\omega - \omega_{j \leftarrow i}} , \tag{2.1}$$

where $\hbar\omega$ is the energy of a single photon from the interacting light field and $\hbar\omega_{j \leftarrow i}$ the energy difference between the ith and jth energy level of the atom. Inserting the interaction Hamiltonian $\mathcal{H}_{\text{int}}$, which is proportional to the dipole operator $\vec{d}$, requires us to calculate transition matrix elements of the following type: $\langle j| \vec{d} |i\rangle$. These matrix elements can be obtained using the Wigner-Eckart theorem and by

subsequently applying the Wigner-3j and -6j symbols (see appx. sec. B.3). In general, it is important to calculate the contributions from all atomic energy levels E_j, as we will see in section 2.1.3. However, to gain more physical insight we will restrict ourself here to a two-level system – the atomic groundstate $|g\rangle$ and its first excited state $|e\rangle$ – interacting with a classical electric field as defined in appendix B.1 equation (B.2). Using the rotating wave approximation, equation (2.1) then simplifies to:

$$\Delta E = \pm\frac{1}{\hbar}\frac{|\langle e|\vec{d}|g\rangle|^2}{\Delta}|E_0|^2 = \pm\frac{6\pi c^2}{\omega_0^3}\frac{\Gamma}{\Delta}I\,, \tag{2.2}$$

where $\hbar\Delta$ is the energy difference between the ground and the excited state. In the last step we replaced the electric field amplitude by the corresponding light intensity I (see eq. (B.3) in appx. sec. B.1) and the matrix element $\langle e|\vec{d}|g\rangle$ by the decay rate:

$$\Gamma = \frac{\omega_0^3}{3\pi\epsilon_0\hbar c^3}|\langle e|\vec{d}|g\rangle|^2\,. \tag{2.3}$$

If the light intensity is spatially varying – either due to interference, or simply from a focussed laser beam – equation (2.2) gives us the desired optical potentials (see fig. 2.2(a)). These potentials can be either attractive or repulsive: If we choose a laser frequency ω_{red} smaller than the transition frequency ω_0 of the ground state $|g\rangle$, an atom in its ground state $|g\rangle$ is attracted towards regions of high laser intensity, whereas the excited state $|e\rangle$ gets repelled from these (red lines and curves in fig. 2.2(a)). In the opposite case ($\omega_{\text{blue}} > \omega_0$) we receive an additional sign change from Δ in the denominator of equation (2.2), hence, the light induced energy shift is in the opposite direction, resulting in inverted potentials (blue lines and curves in fig. 2.2(a)). In the first case the laser detuning is commonly referred to as red detuned, whereas the latter is referred to as blue detuned. These optical dipole potentials are conservative potentials, meaning that an attracted atom is not automatically trapped as well. Trapping depends on the kinetic energy of the atom, which is required to be smaller than U_0, the depth of the potential. It is noteworthy that the light shift of the excited state $|e\rangle$ cannot be explained by the classical Lorentz model. This opposite light shift, however, can be of importance especially for deep potentials and when the atom cycles between the two states (see Martinez-Dorantes [70]). Nevertheless, the heating arising from this effect can be neglected for the potential depths discussed within this thesis.

The optical dipole trap in our experimental apparatus is formed by two counter-propagating Gaussian laser beams ($\lambda_{\text{DT}} = 866\,\text{nm}$) which are focussed to a waist of $w_{\text{DT}} = 17\,\mu\text{m}$ inside the ultra high vacuum glass chamber (see fig. 2.1). The focussing lens system implemented in our experimental apparatus is documented in Förster [71]. Along the longitudinal direction, interference of the two counter-propagating beams forms a periodic cosinusoidal potential, which is commonly known as an optical lattice. Optical lattices can be seen as artificial crystals of light, which, unlike solid state lattices, are defect free and offer a wide range of experimentally controllable tuning parameters. The lattice constant a_{DT} of our one dimensional (1D) optical lattice is given by $\lambda_{\text{DT}}/2 = 433\,\text{nm}$. The transverse potential results directly from the focussed Gaussian beam. Consequently, the 1D optical lattice potential is given by:

$$U(z,\rho) = U_0\frac{w_{\text{DT}}^2}{w^2(z)}e^{-\frac{2\rho^2}{w^2(z)}}\cos^2\left(\frac{2\pi}{\lambda_{\text{DT}}}z\right), \tag{2.4}$$

where z and ρ are the longitudinal and transverse coordinates, $w(z)$ the Gaussian waist at position z, and U_0 the maximum potential depth. All experiments reported in this thesis – unless stated explicitly otherwise – span over a maximum distance of less than 200 lattice sites, which is one order of magnitude smaller than the Rayleigh length of the focussed laser beams. Hence, to a good approximation, we can

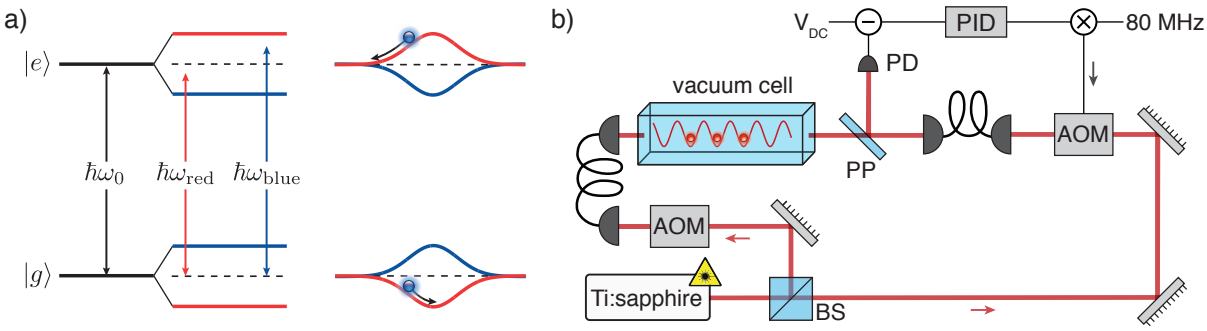

Figure 2.2: **(a)** Illustration of two-level atoms light shifts arising from the interaction with off-resonant electromagnetic radiation. Ground state atoms are attracted to bright regions, if the light frequency ω is red detuned to the two-level transition and *vice versa* if the light frequency is blue detuned. **(b)** Simplified opto-electrical setup to form a one dimensional optical lattice: The laser beam, generated by the Ti:sapphire laser source, is split into two equal parts using a beams splitter (BS). The intensity of each of the two emerging beams is controlled using a feedback loop, which steers the corresponding acousto-optic modulator (AOM). For illustration only one of two control loops is shown: before entering the vacuum glass a cell part of the laser beam is extracted using a pickup plate (PP) and the intensity recorded by a photodiode (PD). The photodiode voltage signal is subtracted by a computer controllable reference voltage V_{DC}, which then serves as an error signal for the analog proportional–integral–derivative (PID) controller, the output signal of which is mixed with a static 80 MHz RF signal to steer the corresponding AOM.

neglect the contributions from the curvature of the wavefront and the Gouy phase of the Gaussian beams to the optical lattice potential. While it is possible to derive the dynamics of a trapped atom directly from equation (2.4), it is more convenient to treat each lattice potential well individually in a harmonic approximation. Correspondingly, the wave function of a trapped atom is described by the well understood quantum harmonic oscillator model. Using the harmonic approximation we can directly compute the atomic oscillation frequencies ($\omega = 2\pi \times \nu$), often referred to as trapping frequencies, for the longitudinal (L) and transverse (T) directions:

$$\nu_{\mathrm{L}} = \sqrt{\frac{2U_0}{m_{\mathrm{Cs}}\,\lambda_{\mathrm{DT}}^2}} \tag{2.5}$$

$$\nu_{\mathrm{T}} = \frac{1}{2\pi}\sqrt{\frac{4U_0}{m_{\mathrm{Cs}}\,w_{\mathrm{DT}}^2}}\,, \tag{2.6}$$

where m_{Cs} is the mass of a single cesium atom. Figure 2.3(a) shows an illustration of the harmonic approximation along the longitudinal direction. The three depicted atoms occupy different energy levels, which are often referred to as vibrational levels. The occupied vibrational level, in fact, is determined by the kinetic energy – also referred to as temperature – of the atom itself.

So far, we have only considered the desired trapping effect of optical dipole potentials, neglecting the likelihood that a trapped atom can also scatter photons off these potentials. While in some cases we specifically use the photon scattering to our advantage (e.g. molasses cooling, see sec. 2.1.1, or Raman sideband cooling, see sec. 2.5.2), scattering photons with the optical lattice leads to undesired effects: Each scattering event increases the total energy of the atom by two photon recoil energies [72, 73], which thus results in heating and eventually the loss of atoms from the trapping potential (see sec. 2.1.2 for a detailed discussion and sec. 2.5.2 for the impact on the ground state cooling). Furthermore, as we

will discuss in section 2.4.1, scattering of photons also leads to decoherence, since they carry away information of the atoms quantum state. The scattering rate of a the two-level system can be calculated using the generalized Fermi's golden rule [74]:

$$\frac{1}{\tau} = \frac{2\pi}{\hbar^2}\left|\frac{1}{\hbar}\frac{\langle \mathrm{g}|\,\mathcal{H}_{\mathrm{int}}\,|\mathrm{e}\rangle\,\langle \mathrm{e}|\,\mathcal{H}_{\mathrm{int}}\,|\mathrm{g}\rangle}{\Delta}\right|^2 \tag{2.7}$$

$$= \frac{6\pi c^2}{\omega_0^3}\left(\frac{\Gamma}{\Delta}\right)^2 I\,. \tag{2.8}$$

The details of the calculation for cesium using the Kramers-Heisenberg formula [75] can be found in appendix B.4 and its application is discussed in section 2.4.1. If we compare the scattering rate (2.8) with the potential depth (2.2) we understand that it is desirable to use far off-resonant dipole traps, since the scattering rate scales as $1/\Delta^2$, while the potential scales only as $1/\Delta$. Furthermore, we also understand that the photon scattering rate is significantly higher for red-detuned optical dipole traps than for blue-detuned ones, since trapped atoms are located in regions with high photon densities. However, trapping atoms in purely blue-detuned dipole traps requires a three dimensional optical lattice [76] and more importantly would not allow us to transport atoms depending on their internal state (see sec. 2.1.3).

A simplified illustration of our 1D optical lattice and how it is formed is depicted in figure 2.2(b). In chapter 3 we will discuss the experimental setup in more detail, nevertheless, the simplified setup allows us to understand and discuss several relevant aspects. The laser source generating the desired wavelength $\lambda_{\mathrm{DT}} = 866\,\mathrm{nm}$ is a Ti-sapphire laser system[1] which delivers up to 2.5 W output power. The laser source beam is separated into the counter-propagating arms of the optical lattice using a beamsplitter. Both beams are intensity stabilized by a feedback loop which acts on the corresponding acousto-optic modulator (AOM). Only one of the two intensity feedback loops is exemplarily depicted in figure 2.2(b): Before entering the vacuum glass cell, a small fraction of the beam is extracted using a pickup plate. The pickup plate is a wedged glass plate, one side of which is anti reflection coated, whereas the other has a custom coating with 12 % reflectivity for both horizontally and vertically polarized beams under 45° angle of incidence (AOI). The extracted fraction is detected by a self built amplified photodiode (bandwidth 10 MHz). The recorded photodiode voltage is subtracted from a computer controlled reference voltage (V_{DC}) and fed to an analog PID controller (bandwidth 10 MHz), which generates a voltage signal that is mixed with a RF signal (80 MHz) to steer the corresponding AOM. The bandwidth of the entire control loop is approximately 1 MHz with a remaining relative intensity noise (RIN) of 0.04 % (details are discussed in section 3.2.2). The control loop bandwidth is primarily limited by the finite response time of the AOM [77], which arises directly from the speed of sound inside the AOM crystal.

The experimental sequences conducted with our experimental apparatus mainly involve two different modes of operation for the optical lattice: one for initial trapping and imaging, the other to precisely control the quantum state of the trapped atoms. In the former case we form a deep lattice potential using 30 mW of optical power in each of the two counter-propagating laser beams giving rise to a maximum potential depth of $U_0/k_{\mathrm{B}} = 370\,\mu\mathrm{K}$. In the latter the potential depth is reduced to 74 µK by using only 6 mW of optical power per lattice beam to reduce the previously discussed undesired scattering of lattice photons. To change from the illumination to the quantum control lattice setting, we use an 100 ms adiabatic cosinusoidal ramp of the control voltage V_{DC}, which is imprinted on the laser intensity by the intensity control loops. Using equation (2.5) and equation (2.6) allows us to calculate the expected longitudinal and transverse trapping frequencies of the quantum control lattice, $\nu_{\mathrm{L}} = 110\,\mathrm{kHz}$

[1] Coherent MBR 110 pumped by Coherent Verdi V18

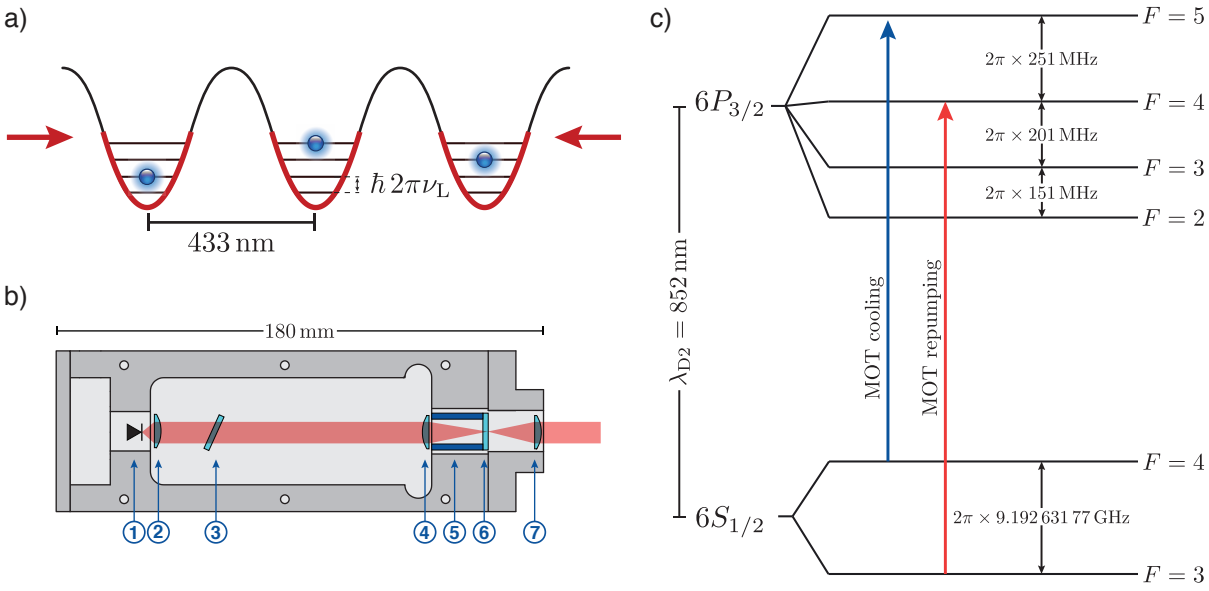

Figure 2.3: **(a)** Illustration of the harmonic approximation of individual potential wells from an optical lattice, which is formed by two counter-propagating laser beams. **(b)** Technical drawing of the interference-filter-stabilized (IF) external cavity diode lasers (ECDL): (1) laser diode, (2) laser diode collimation lens, (3) interference filter, (4) cats eye lens, (5) low voltage ring piezo stack, (6) partial reflective mirror, (7) final beam collimation lens. **(c)** Cesium D_2 transition hyperfine structure including the frequency splittings of the hyperfine energy levels. The blue arrow indicates the cooling transition, whereas the red one is used as repumping transition for the magneto-optical trap (MOT).

and $\nu_T = 1\,\text{kHz}$ respectively (see also fig. 2.3(a)).

A Magneto-Optical Trap for Cesium

To trap atoms in an optical lattice – which for the atom embodies a conservative potential – we require a mechanism to slow the atoms down, since their velocity follows a Boltzmann distribution with a mean velocity of circa $200\,\text{m}\,\text{s}^{-1}$ at room temperature. Therefore, even in the deep imaging lattice (370 µK), we would essentially never trap any atoms. Slowing down atoms can be achieved efficiently by scattering photons from a laser beam: for each absorbed photon the atom experiences a recoil – and hence receives a momentum transfer in the propagation direction of the laser beam – whereas the following photon emission is on average isotropic. Therefore, after scattering multiple photons, the atom is decelerated by the radiation pressure of the laser beam. This idea can be easily extended to three dimensions utilizing six laser beams forming three orthogonal pairs, where the lasers of each pair are counter-propagating. Such a laser configuration is also referred to as optical molasses. Making use of the Doppler effect we can ensure that an atom only absorbs a photon which travels in opposite direction by detuning the laser light slightly away from the atomic resonance (typically on the order of a few times the natural line width Γ) [78, 79]. For cesium, this cooling method reaches a minimal temperature of $T_{\text{Doppler}} = 125\,\mu\text{K}$ (corresponding to an average velocity of circa $0.1\,\text{m}\,\text{s}^{-1}$). However, while these optical molasses can efficiently cool atoms, it does not *per se* trap atoms, since the molasses cooling does not prevent the diffusion of atoms. This brings us to the magneto-optical trap (MOT). In its core, the MOT utilizes a magnetic field gradient, such that the absorption of photons also becomes position dependent. The magnetic field gradient – achieved by pair of coils in anti-Helmholz configuration, realizing a magnetic quadrupole field – lifts the

degeneracy of the Zeeman sublevels. This, in turn, means that a circular polarized laser beam induces either a σ^+ or σ^- transition depending on whether the atom is to the left or right of the magnetic zero crossing. The degeneracy of the Zeeman sublevels, furthermore, is similar to the Doppler effect: it shifts a detuned laser either in or out of resonance, leading to a position dependent force, which traps atoms in the center of the quadrupole field. A detailed description of the physical effects involved in a MOT can be found e.g. in Townsend et al. [80] and Staene et al. [81].

The experiments typically conducted with our experimental apparatus require only small ensembles of atoms ($n < 50$) to be loaded into the optical lattice. Hence, we can load atoms directly from the residual background vapor of the ultra high vacuum inside the glass cell (pressure $< 10 \times 10^{-10}$ mbar) sparing us the requirement of a multi chamber vacuum apparatus and long distance transport of cold atoms [82].

Following the outlined conceptual idea of a MOT that produces a trapped cloud of cold cesium atoms, we require only a single laser source (cooling laser), which is then split into six optical molasses beams. For a cesium ground state atom the D_2 $|F = 4\rangle \rightarrow |F' = 5\rangle$ transition is ideal (see fig. 2.3(c)), since it represents a closed transition[2]. However, off-resonant scattering ($|F = 4\rangle \rightarrow |F' = 4\rangle \rightarrow |F = 3\rangle$) eventually pumps atoms into the $|F = 3\rangle$ state. By employing a second laser source (repumping laser), which is resonant with the $|F = 3\rangle \rightarrow |F' = 4\rangle$ transition, we repump all atoms back into the $|F = 4\rangle$ ground state (see fig. 2.3(c)).

Employed Laser System: Both laser sources are interference-filter-stabilized (IF) external cavity diode lasers (ECDL). These lasers have been developed, built and characterized by ourselves based on the design introduced in Balliard et al. [83]. ECDL lasers use commercially available laser diodes within an external cavity to ensure stable single mode operation and a reduced linewidth, in comparison to the free running laser diode [84]. All types of ECDL lasers essentially make use of two components: (a) a wavelength selective element and (b) an optical feedback mechanism (see fig. 2.3(b) for a schematic overview of the IF-ECDL developed by our group). The separation of these two elements is the key difference of the IF-ECDL compared to the traditionally employed Littow configuration ECDL [85–87]. The Littrow configuration uses a diffraction grating for both wavelength selection and feedback, whereas the IF-ECDL uses a narrow bandwidth interference filter (FWHM 0.4 nm) for selection and a cat's eye retroreflector with a partially reflective mirror (30% reflectivity) for optical feedback (see fig. 2.3(b)). The cat's eye retroreflector makes the laser cavity less sensitive to mechanical noise, since it reduces the angular sensitivity by one order of magnitude for our specific application [88, 89]. The diffraction grating of the Littrow-configuration ECDL prevents such a cat's eye retroreflector, because the grating itself requires the laser beam to cover several grating lines. These improvements give rise to a spectrally narrow (Gaussian linewidth $\Delta\nu_{\mathrm{Ga}} < 10\,\mathrm{kHz}$, Lorentzian linewidth $\Delta\nu_{\mathrm{Lo}} < 2\,\mathrm{kHz}$) and long term stable laser source. In fact, once optimized, the laser remains mechanically maintenance free for years and can be stabilized to an atomic reference for up to several months without any readjustments. Such advances in the stability of laser sources are crucial to counter the increasing complexity of modern experimental setups.

The wavelength of each IF laser source is stabilized to a cesium vapor cell using polarization spectroscopy [90]. The MOT cooling laser is locked on the crossover transition [91] $|F = 4\rangle \rightarrow |F' = 3\rangle$ and $|F = 4\rangle \rightarrow |F' = 5\rangle$ of the D_2 line. This transition is red detuned by $2\pi \times 226\,\mathrm{MHz}$ from the cooling transition $|F = 4\rangle \rightarrow |F' = 5\rangle$. Using an acousto-optic modulator (AOM) in double pass configuration ($2 \times 110\,\mathrm{MHz}$) we shift the wavelength closer to the cooling transition to reach the desired detuning of a few times the natural line width Γ. The MOT repumping laser is directly locked on the $|F = 3\rangle \rightarrow |F' = 4\rangle$

[2] Dipole transition selection rules prevent an atom to decay from the excited state $|F' = 5\rangle$ into the $|F = 3\rangle$ ground state, see equation (B.28)

transition, to quickly repump atoms back into the cooling cycle.

2.1.2 Storage Time of Atoms Trapped in a 1D Optical Lattice

By now we understand how one can trap neutral atoms in an optical lattice, hence, the natural next question is: How long do atoms remain stored in such a lattice? In general, we need to distinguish between two situations: the storage time of atoms trapped in the lattice with continuous cooling and without. These situations are related to the previously mentioned two modes of operation. In the case where we want to image the atoms, or simply store them for longer times, we use the 370 µK deep lattice in combination with continuous molasses cooling. In fact, we image trapped atoms by recording scattered photons from the molasses cooling with our objective (see illustration in fig. 2.1 and the discussion in sec. 2.2). In the other case, when we want to precisely control the quantum state of the trapped atoms, we need to shield the atoms as much as possible from the environment. Therefore, we use the 74 µK deep lattice, which leads to less off-resonant scattering processes with photons of the optical lattice (see sec. 2.4.1).

We previously discussed the working principle and limit of free-space molasses cooling. However, once the atoms are cold enough to be trapped in the optical lattice, we enter a different regime where we can employ sub-Doppler cooling techniques using the optical molasses laser beams introduced in section 2.1.1. Each of the three molasses beam pairs produces a polarization gradient due to the counter-propagating circular polarized beams. These polarization gradients enable sub-Doppler cooling as explained in detail in Dalibard et al. [92]. In comparison to the Doppler limited molasses cooling, polarization gradient cooling requires a larger detuning from the $|F = 4\rangle \rightarrow |F' = 5\rangle$ transition and significantly reduced laser intensities. As we will see in the following, properly adjusted detunings and intensities of the molasses laser beams lead to temperatures below 10 µK in the 74 µK deep optical lattice, which is well beyond the Doppler limit of 125 µK. The polarization gradient cooling, in fact, provides a cooling rate which is much larger than the heating rates of the optical lattice. Therefore, an atom can only get lost from the lattice by elastic collisions with room temperature background vapor atoms [93]. Experimentally we measure a background limited storage time of circa 6 minutes which, in turn, can be used to estimate the pressure inside the vacuum chamber. Trapped atoms can collide with a variety of background vapor constituents (e.g. Cs, Ar, N_2, CO, H_2, CH_4), nevertheless, the background collision limited storage time is rather insensitive to the exact type of involved collision [93]. Following the calculation from Bjorkholm et al. [93] we infer that our background vapor pressure is on the order of $p \approx 5 \times 10^{-11}$ mbar.

The storage time of trapped atoms without continuous cooling, on the other hand, is limited by heating of the optical lattice. The experimental sequence used to measure this storage time is likewise also the fundamental building block of almost all experimental sequences presented in this thesis. Initially, atoms are loaded in the magneto-optical trap and subsequently transferred into the 370 µK deep optical lattice, where they are sub-Doppler cooled using the molasses beams. We can infer the initial number of loaded atoms by integrating the recorded scattered fluorescence photons (see Alberti et al. [2] and discussion in sec. 2.2). Subsequently the molasses beams are turned off and the lattice depth is adiabatically lowered to 74 µK, where the atoms remain in the dark for a given hold time. Finally the lattice depth is increased to its initial value and we infer the number of remaining atoms, again, by integrating the recorded fluorescence photons during molasses cooling. Each blue dot, shown in figure 2.4, indicates the fraction of surviving atoms obtained from such a storage time measurement for increasing holding times. Already after a few seconds a visible portion of the initially trapped atoms are lost, which is significantly shorter than the circa 6 minute storage time limited by background vapor collision (for comparison represented by the grey dashed line in figure 2.4). In the previous section, we identified one heating source, which is

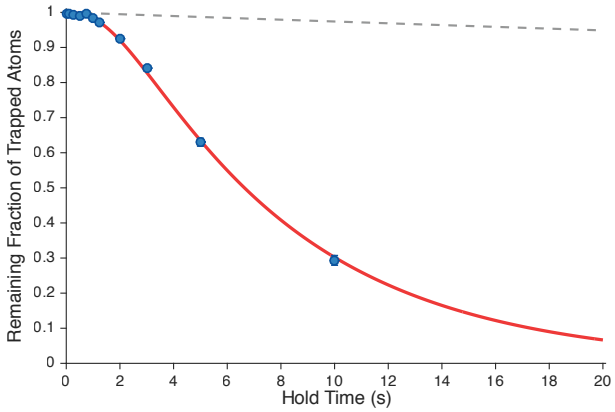

Figure 2.4: Storage time measurement of atoms which are trapped in our 1D optical lattice. Each blue dot represents an individual measurement. The red solid line shows the result of a numerical simulation using the Fokker-Planck equation, as discussed in sec. 2.1.2. For comparison, the grey dashed line shows the storage time, which is limited purely by background vapor collisions.

also present when trapped atoms remain in the dark: off-resonant scattering of lattice photons leading to recoil heating. The impact of these scattering events is not neglectable when cooling the atoms into their vibrational ground state (see sec. 2.5.2). However, the corresponding heating rate is smaller than those arising from technical fluctuations of the optical lattice, namely intensity and phase noise of the involved laser beams.

In the following sections we will discuss how these two technical noise sources can be mathematically modeled and quantitatively estimated using experimentally accessible observables [94]. These heating rates can then be used in combination with the Fokker-Planck equation [95, 96] to model precisely the experimentally obtained curve shown in figure 2.4. In fact, the red line shown in figure 2.4 is obtained by numerically solving the Fokker-Planck differential equation. This method allows us to gain valuable insight into the physical mechanism that primarily limits the storage time, which in turn, can be used to further improve the experimental apparatus (see sec. 2.1.2). Furthermore, employing a least square minimization of the numerically solved Fokker-Planck equation allows us to determine the temperature of the atomic ensemble [97, 98]. Inferring the exact temperature of a cold atomic ensemble itself is already a challenging task. Among various techniques the two most commonly used are the time-of-flight and the release-recapture method. The time-of-flight method is based on measuring the thermal expansion of an atomic ensemble after it is released into free space [99, 100]. On the contrary, the release-recapture method determines the temperature by lowering the optical lattice adiabatically until the potential depth is on the same or a lower order than the average temperature of the trapped atomic ensemble [101, 102]. For our experimental setup, the former method is experimentally not feasible, whereas the latter is complementary to the storage-time-measurement method.

Modeling and Characterizing the Intensity Noise Induced Heating Rate

While the employed intensity feedback loops (see figure 2.2(b)) greatly reduce the noise of the lasers, they cannot fully nullify them. Let us assume we have a cesium atom with mass m_{Cs}, which is trapped in a harmonic potential $V(x)$ at the position x_0. The intensity noise, hence, leads to fluctuations of the potential depth, which in turn can be modeled by a perturbation of the spring constant of the harmonic

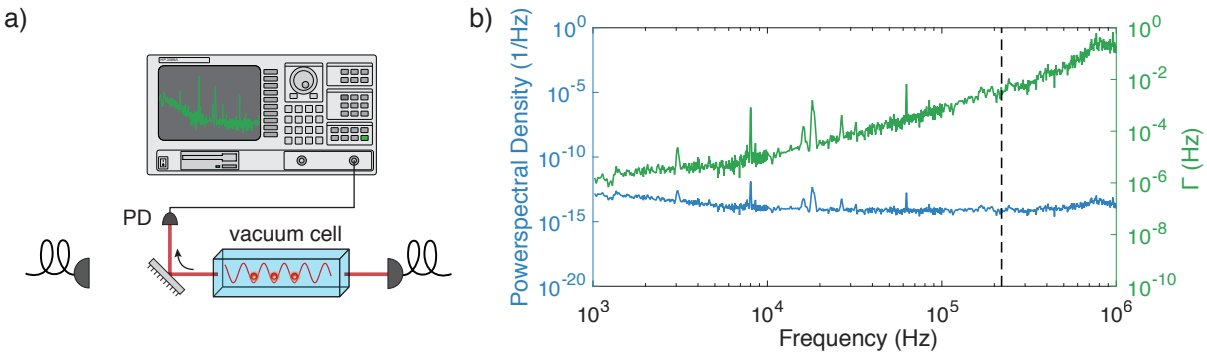

Figure 2.5: **(a)** Opto-electrical setup to measure the intensity noise of our optical lattice: each beams intensity noise is measured individually by reflecting the light onto a fast photodiode, the signal of which is analyzed with a spectrum analyzer. **(b)** Recorded relative intensity noise spectral density (blue) and corresponding heating rate Γ (green), according to equation (2.14). The dashed vertical line represents $2 \times \nu_L = 220\,\mathrm{kHz}$.

oscillator [94]:

$$V(x) = \frac{m_{Cs}}{2}(2\pi\nu)^2(1+\epsilon)(x-x_0)^2\,. \tag{2.9}$$

Using time-dependent perturbation theory we can then determine the transition rate $R_{n\pm2\leftarrow n}$ to excite or relax the vibrational level n of the trapped atom:

$$R_{n\pm2\leftarrow n} = \frac{\pi^2\nu^2}{8} S_I(2\nu)(n+1\pm1)(n\pm1)\,, \tag{2.10}$$

where S_I is the one-sided power spectral density of the intensity noise [103]. It is noteworthy that the transitions are parametric, hence, there are no transitions between the vibrational level n and $n \pm 1$. The heating rate for a single atom in the vibrational state n is given by the difference between the excitation $(n+2 \leftarrow n)$ and relaxation $(n-2 \leftarrow n)$ rate multiplied by the energy spacing of the harmonic oscillator. To calculate the average heating rate $\langle \dot{E}(t) \rangle$ for an atomic ensemble, we include the probability density $P(n,t)$ to find an atom in the vibrational state n:

$$\langle \dot{E}(t) \rangle = \sum_n P(n,t)\, 2\hbar\omega\, (R_{n+2\leftarrow n} - R_{n-2\leftarrow n}) \tag{2.11}$$

$$= \pi^2\nu^2 S_I(2\nu)\langle E(t)\rangle\,. \tag{2.12}$$

In the last step we made use of the fact, that the average energy of an harmonic oscillator is given by $\sum_n P(n,t)\,\hbar\omega\,(n+1/2)$. This result shows that parametric heating with a heating rate Γ leads to an exponential increase of the average energy:

$$\langle \dot{E}(t) \rangle = \Gamma \langle E(t)\rangle\,, \tag{2.13}$$

$$\Gamma = \pi^2\nu^2 S_I(2\nu)\,. \tag{2.14}$$

The heating rate Γ itself only depends on two experimental parameters: the trapping frequency ν and the power spectral density S_I. For our 1D optical lattice, we obtain the former using equation (2.5) and equation (2.6), which results in 110 kHz and 1 kHz, respectively. The latter can be measured as

outlined in figure 2.5(a): each beam's intensity noise is recorded separately using a fast photodiode[3], the signal of which is analyzed and saved by a spectrum analyzer[4]. The one-sided power spectral density thus obtained and the resulting heating rate are shown in figure 2.5(b). The quadratic dependency on trapping frequencies leads to a significant difference of the longitudinal and transverse heating rates, which amount to $\Gamma = 4.2\,\mathrm{mHz}$ for $\nu_\mathrm{L} = 110\,\mathrm{kHz}$ and $\Gamma = 0.002\,\mathrm{mHz}$ for $\nu_\mathrm{T} = 1\,\mathrm{kHz}$.

Modeling and Characterizing the Phase Noise Induced Heating Rate

Differential optical phase noise of the two laser beams forming the trap leads to a shaking of the harmonic oscillator's potential minima. Similar to the perturbation of the spring constant in the preceding section, this shaking can be modeled by a perturbation of the trap center x_0 [95, 96]:

$$V(x) = \frac{m_\mathrm{Cs}}{2}(2\pi\nu)^2(x - (x_0 + \epsilon))^2\,. \tag{2.15}$$

Using time-dependent perturbation theory again, we obtain the following transitions rate $R_{n\pm1\leftarrow n}$ for a trapped atom with vibrational level n:

$$R_{n\pm1\leftarrow n} = \frac{4\pi^4\nu^3}{h} m_\mathrm{Cs}\, S_\phi(\nu)\left(n + \frac{1}{2} \pm \frac{1}{2}\right), \tag{2.16}$$

where $S_\phi(\nu)$ is the one-sided power spectral density of the phase noise converted into units of m^2/Hz. Hence, the average heating rate of an atomic ensemble is given by:

$$\begin{aligned}\langle \dot{E}(t)\rangle &= \sum_n P(n,t)\, 2\hbar\omega\,(R_{n+1\leftarrow n} - R_{n-1\leftarrow n}) && (2.17)\\ &= 4\pi^4 m_\mathrm{Cs}\nu^4 S_\phi(\nu) && (2.18)\\ &= \dot{Q}\,, && (2.19)\end{aligned}$$

where we defined $\dot{Q}$ as the phase noise induced heating rate. In contrast to intensity noise, phase noise does not lead to exponential heating, instead it is independent of the atoms' energy. Nevertheless, since its magnitude grows with the fourth power of the trapping frequency it becomes significant for deep traps. In order to calculate $\dot{Q}$, we need to measure the optical phase noise, which is experimentally a bit more demanding than measuring the intensity noise. Differential phase noise, in general, can be obtained by creating a beat signal of the two constituents. As depicted in figure 2.6(a), we essentially create a Michelson interferometer by extracting a fraction of each beam – using a wedged pickup plate[5] – and retro reflecting one of the two extracted beams. The resulting beat signal is detected by the same fast photodiode, the signal of which is analyzed and recorded by the spectrum analyzer. Using a mirror mounted on a piezoelectric actuator (see fig. 2.6(a)) we employ a control loop (not depicted in fig. 2.6(a)) to stabilize the optical phase of one beam. This control loop is used to linearize the differential phase noise with a maximal signal to noise ratio (SNR). While a comprehensive description of the control loop is given in Boventer [104], two aspects are noteworthy: To accurately measure the differential phase noise, the control loop bandwidth needs to be chosen sufficiently smaller than the trapping frequencies – in this case we chose a bandwidth of 100 Hz. Furthermore, since the setup itself resembles a Michelson interferometer, it needs to be ensured that it is mechanically as stable as possible.

[3] Thorlabs: PDA10A-EC - Si Fixed Gain Detector, 200 – 1100 *nm*, 150 MHz BW
[4] HP: 3589A Spectrum/Network Analyzer, 10 Hz to 150 MHz
[5] Altechna: BK7 glass plate, 2° wedge, coating side 1: AR, coating side 2: PRs, PRp = 12 % for 45° AOI

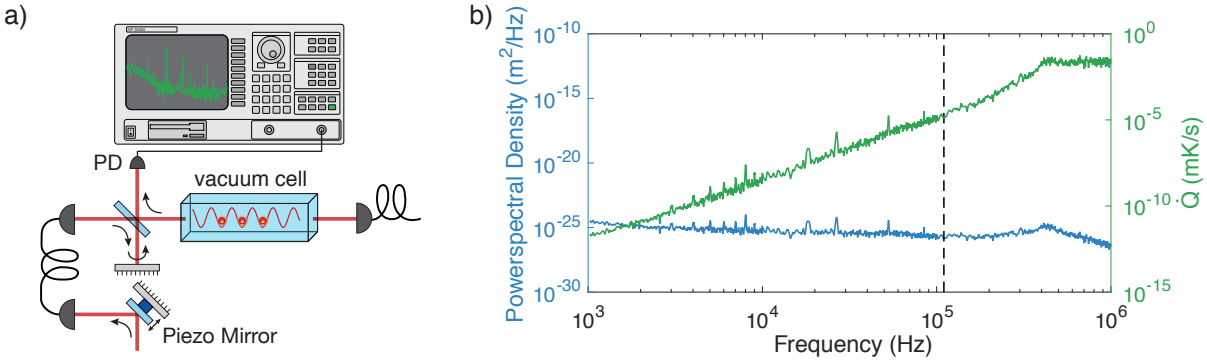

Figure 2.6: **(a)** Opto-electrical setup to measure the phase noise of our optical lattice: both counter-propagating laser beams are overlapped in a Michelson-like interferometer. A slow feedback loop stabilizes the difference between the two beams using a piezo mirror. The signal of the overlapped beams is recorded using a fast photodiode, the signal of which is analyzed with a spectrum analyzer. **(b)** Obtained phase noise spectral density (blue) and corresponding heating rate $\dot{Q}$ (green), according to equation (2.18). The dashed vertical line represents $\nu_L = 110\,\mathrm{kHz}$.

Otherwise the mechanical instabilities of the measurement setup will appear as optical phase noise. Therefore, both – the pickup plate and the retro reflection mirror – were mounted in a monolithic cube[6], the acoustic resonance frequencies of which are measured to be below the longitudinal trapping frequency. Once recorded we convert the one-sided power spectral density measured in units of $(^\circ)^2/\mathrm{Hz}$ into the desired units m^2/Hz by the following relation:

$$\Delta x = \frac{\lambda_{DT}}{2}\frac{\Delta\phi}{2\pi}\,. \tag{2.20}$$

The resulting phase noise heating rate for the longitudinal trapping frequency (110 kHz) amounts to $\dot{Q} = 13.5\,\mu\mathrm{K\,s^{-1}}$ and $\dot{Q} < 0.00001\,\mu\mathrm{K\,s^{-1}}$ for the transverse (1 kHz), respectively. The extracted values are comparable to those presented in Reimann [105], which are obtained from a different experimental apparatus, which utilizes similar hardware. So far we neglected the physical origin of this optical phase noise. Indeed, the phase noise arising from the laser source itself is substantially less, whereas mechanical vibrations should not play a significant role at 110 kHz. The majority of the optical phase noise arises from the electrical phase noise of the RF sources driving the AOMs (see figure 2.2 and discussion in the following), which are used to stabilize the beam intensities. These RF signals are generated using direct digital frequency synthesizers (DDS) based on the AD9954 chip from Analog Devices. While this DDS chip enables us to perform a variety of operations with the optical lattice – as we will see in the following chapter – it is outperformed by the latest generation of DDS chips (e.g. AD9915), which offer a two orders of magnitude reduced phase noise. In fact, we started a dedicated project to develop a versatile digital frequency synthesizer by interfacing a field programmable gate array (FPGA) with an AD9915 DDS chip. More information regarding this project can be found in Ramola [106].

Thermometry Using the Fokker-Planck Equation

Now that we obtained a mathematical description of intensity and phase noise heating for atoms trapped in an optical lattice, it is intriguing to see if we can use this insight to better understand the storage time measurement presented in figure 2.4. So far all calculations have been carried out using the quantum

[6] Owis: mounting cube W 40-4 with JT 40T-STPZ-O and JT40T-PHSZ-M insets

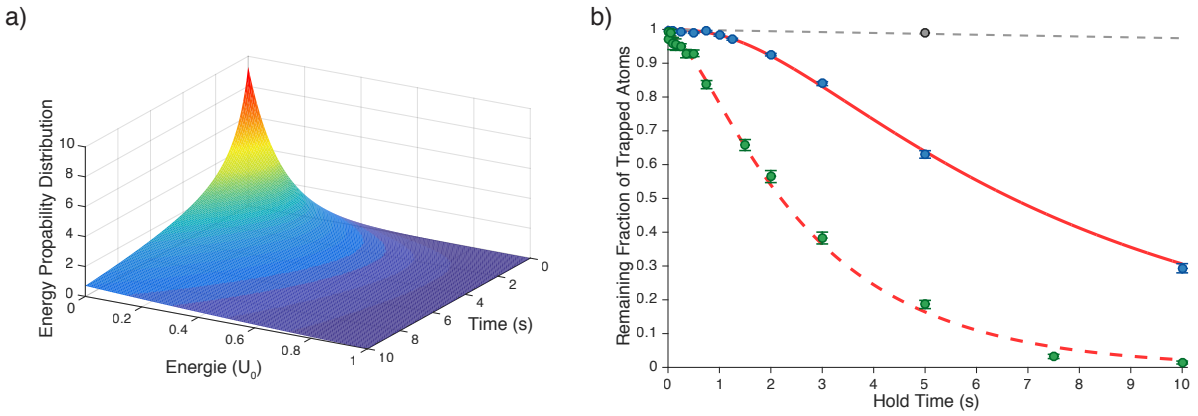

Figure 2.7: **(a)** Temporal evolution of ensemble of atoms trapped in an 1D optical lattice the energy of which is initially distributed according to the 1D Maxwell-Boltzman distribution given in equation (2.23). The dynamics are obtained by numerically solving the Fokker-Planck equation (2.22). **(b)** Different storage time measurements together with their numerical simulation using the Fokker-Planck equation. See section 2.1.2 for more details.

mechanical harmonic oscillator. While it is possible to describe the evolution of the energy distribution $n(E,t)$ quantum mechanically as well, we will restrict ourself here to a classical description, since coherences do not play a role. Following the idea presented in Gehm et al. [95, 96], we can use the Fokker-Planck equation to model the evolution of a trapped atomic ensemble [107]:

$$\frac{\partial n(E,t)}{\partial t} = \frac{\partial}{\partial E}\left[M_1(E)\, n(E,t)\right] + \frac{\partial^2}{\partial E^2}\left[D(E)\, n(E,t)\right] , \tag{2.21}$$

where M_1 is the first moment – the mean heating – and D the energy diffusion coefficient. In general we would need to solve this partial differential equation for all three spatial dimensions. However, we learned in the preceding sections that both the intensity and phase noise heating strongly depend on the trapping frequencies and that these differ by more than one order of magnitude for our one dimensional optical lattice. Hence, the longitudinal heating will lead to a loss of atoms long before they experience an effect of the transverse one, which allows us to restrict the analysis to one dimension. Using the derived transition rates given in equation (2.10) and equation (2.16), we obtain the following 1D Fokker-Planck equation:

$$\frac{\partial n(E_\mathrm{L},t)}{\partial t} = \left(\frac{\Gamma_\mathrm{L}}{2}E_\mathrm{L}^2 + \dot{Q}_\mathrm{L}E_\mathrm{L}\right)\frac{\partial^2 n(E_\mathrm{L},t)}{\partial E_\mathrm{L}^2} + \left(\Gamma_\mathrm{L}E_\mathrm{L} + \dot{Q}_\mathrm{L}\right)\frac{\partial n(E_\mathrm{L},t)}{\partial E_\mathrm{L}} , \tag{2.22}$$

where the index L denotes the longitudinal trap direction and we used $E_\mathrm{L} = (n + 1/2)\hbar\omega_\mathrm{L}$. To solve the partial differential equation numerically, we furthermore need an initial distribution for $n(E,t)$ as well as boundary conditions. For atoms trapped in an optical lattice and cooled by molasses cooling, the former is well described by a 1D Maxwell-Boltzman distribution:

$$n_0 = 2\sqrt{\frac{U_0}{k_\mathrm{B}T}}\, e^{-\frac{E_\mathrm{L}U_0}{k_\mathrm{B}T_0}} , \tag{2.23}$$

which depends on the trap depth U_0 and more interestingly on the temperature T_0. As we will see in the following, this dependency allows us to not only extract the heating rates from a storage

Table 2.1: Heating rates and atom ensemble temperatures obtained from non-linear least squares fits of the simulated storage time to the corresponding measurements shown in figure 2.7. The contribution of the intensity heating rate is too small to be fitted, hence, we assume the static value obtained from equation (2.14). The storage time represents the time at which 50 % of the initially trapped ensemble is lost.

Line in figure 2.7(a)	T_0	Γ	$\dot{Q}$	Storage time
Solid red	$(7.8 \pm 0.7)\,\mu\mathrm{K}$	4.2 mHz	$(7.5 \pm 0.3)\,\mu\mathrm{K\,s^{-1}}$	6.6 s
Dashed red	$(14.2 \pm 1.0)\,\mu\mathrm{K}$	4.2 mHz	$(20.0 \pm 0.7)\,\mu\mathrm{K\,s^{-1}}$	2.2 s

time measurement, but also the initial temperature of the atomic ensemble. Before we can determine the boundary conditions, we need to reconsider our model assumptions. So far we approximated the optical lattice potential wells by a harmonic oscillator, since we only considered deeply trapped atoms. However, once their vibrational level increases sufficiently, the atoms experience the anharmonicity of the cosinusodial potential [108], where this approximation breaks down. Nevertheless, we will disregard this anharmonicity in the following and consider an atom as lost once its energy exceeds the trap depth U_0. This can be partially justified by the exponential energy dependence of the intensity noise heating, which heats out atoms quickly once they have become hot. The time an atom spends in this anharmonic regime, hence, is rather neglectable. To model the loss of atoms we choose an absorptive boundary for $E_\mathrm{L} > U_0$, whereas we designate a reflective one for $E_\mathrm{L} < 0$ to avoid unphysical energies. Figure 2.7(a) shows the resulting energy probability distribution $n(E, t)$, which is obtained from numerically solving the Fokker-Planck partial differential equation using Matlab [109] for an initial ensemble temperature $T_0 = 10\,\mu\mathrm{K}$, $\Gamma = 4.2\,\mathrm{mHz}$, and $\dot{Q} = 13.5\,\mu\mathrm{K\,s^{-1}}$. The energy probability distribution $n(E, t)$, in turn, can be used to generate a theoretical prediction of the storage time measurement by integrating over the energy, which corresponds to the remaining fraction of atoms at time t. Hence, we engineered a model, depending only on the temperature, Γ, and $\dot{Q}$, which predicts the storage time of atoms trapped in an optical lattice.

The solid red line in figure 2.7(b) shows the result from a non-linear least squares fit of the simulated storage time to the measured one indicated by the blue data points (same ones as shown in fig. 2.4) and likewise the red dashed line for the green data points. The obtained values for T_0, Γ, and $\dot{Q}$ are summarized in table 2.1. The initial temperatures are well within the range one expects from sub-Doppler molasses cooling for a trap depth of 74 µK [101]. Their difference can be attributed to slightly different molasses cooling parameters in combination with an increased phase noise heating rate $\dot{Q}$. In fact, the storage time measurement represented by the green data points was obtained by deliberately increasing the electronic phase noise of the digital RF frequency synthesizers driving the AOMs. The storage time values given in table 2.1 correspond to the time, when half of the initial ensemble is lost. Furthermore, it turns out that the atom's storage time in the optical lattice of our experimental apparatus is primarily limited by phase noise heating. Figure 2.8(a) and figure 2.8(b) both show the numerically calculated storage time for different values of Γ and $\dot{Q}$ for an initial temperature $T_0 = 8\,\mu\mathrm{K}$. While the storage time remains essentially constant if one varies Γ over three orders of magnitude, it shows a strong dependence on the phase noise $\dot{Q}$. As previously discussed, we recently developed a versatile digital frequency synthesizer [106], which reduces the electronic phase noise by two orders of magnitude compared to the currently employed DDS. This improvement should boost the storage time of trapped atoms so far that it becomes only limited by background gas collisions, represented by the dashed horizontal line in figure 2.8. To confirm this hypothesis we conducted a storage time measurement, in which we reduced the phase noise of the optical lattice further by employing the same digital frequency synthesizer to drive the AOMs (see fig. 2.2). Employing a single, common frequency synthesizer removes the differential

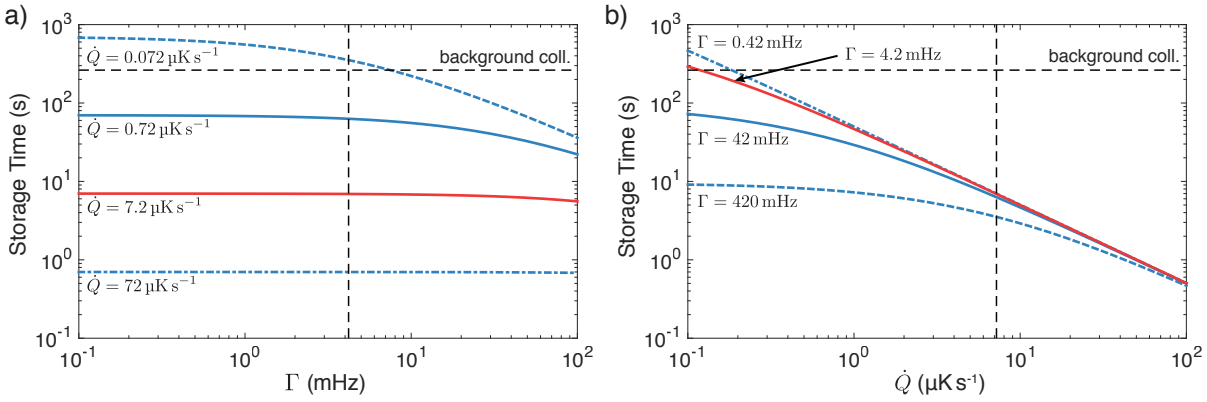

Figure 2.8: 50 % storage time **(a)** as a function of the intensity noise heating rate Γ and **(b)** of the phase noise heating rate $\dot{Q}$. The solid red and dashed vertical black lines correspond to the current situation in the experimental apparatus at hand. The additionally shown blue lines represent heating rates, which are increased or decreased by an order of magnitude. The dashed horizontal black lines represent the upper limit due to background vapor collisions.

phase noise, while – by additionally ensuring that the optical path lengths of the laser beams are equal – it also strongly suppresses common mode phase noise. The grey point depicted in figure 2.7(b) shows the resulting surviving fraction of atoms, which nicely agrees with the background collisions limited storage time, represented by the dashed grey line in fig. 2.7(b).

2.1.3 A State Dependent Optical Lattice for Cesium

The concept of state-dependent optical trapping was originally introduced by Jaksch et al. [110] and simultaneously by Deutsch et al. [111]. It has since been used in cold atom experiments to coherently transport neutral atoms [112], which enabled the realization of e.g. controlled collisions between neutral atoms [113], quantum walks of single neutral atoms [66], or a digital atom interferometer [114]. The core challenge of state-dependent trapping is to engineer two independently controllable, yet spatially overlapped, optical lattices which trap atoms conditioned on their internal atomic state. As illustrated in figure 2.9(a), in our laboratory we realize these potentials for cesium atoms by utilizing the different AC vector polarizability of the hyperfine levels, such that an atom in the cesium hyperfine level $|\uparrow\rangle := |F = 4, m_F = 4\rangle$ is attracted only by σ^+-polarized light, whereas one in $|\downarrow\rangle := |F = 3, m_F = 3\rangle$ is predominantly attracted by σ^--polarized light. The two hyperfine levels likewise embody a pseudo spin-1/2 system, which we will use as our qubit system throughout this thesis. These two qubit states can, furthermore, be coupled via microwave radiation at 9.2 GHz (see sec. 2.3).

By only considering the fine instead of the hyperfine structure of cesium, the AC vector polarizability can be understood more intuitively. The corresponding level scheme is shown in figure 2.9(b). Using the multilevel version of equation (2.2) it is clear, that we can find a wavelength which is red detuned to the D_2 transition ($^2P_{3/2}$) and simultaneously blue detuned to the D_1 transition ($^2P_{1/2}$), such that an atom in state $|\uparrow'\rangle := |J = 1/2, m_J = +1/2\rangle$ effectively feels no potential arising from σ^--polarized light since the attractive and repulsive potentials cancel out precisely. At the same time this atom still experiences an attractive potential from σ^+-polarized light. Likewise an atom in state $|\downarrow'\rangle := |J = 1/2, m_J = -1/2\rangle$ experiences only the attractive potential from σ^--polarized light, while the potential of σ^+-polarized light is effectively zero. This gives us exactly the desired state-dependent optical potentials. Coming

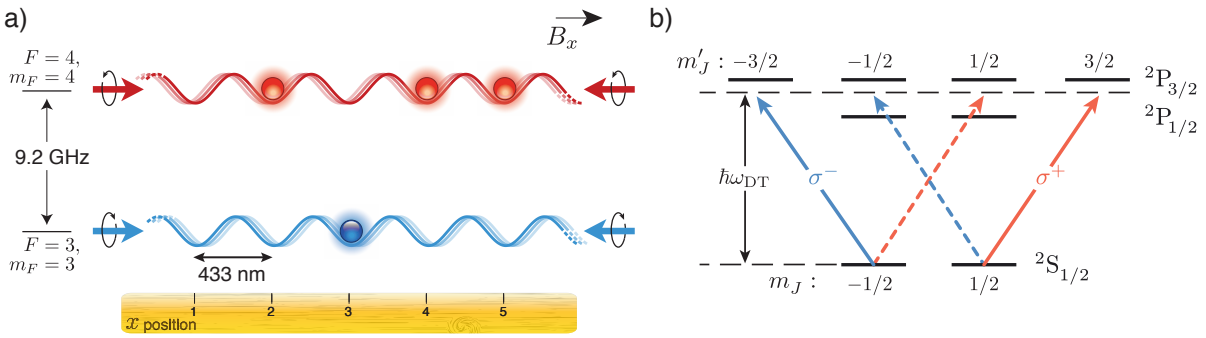

Figure 2.9: **(a)** State-dependent optical lattices acting selectively on either one of two long-lived hyperfine states of a cesium atom. Upper and lower lattices originate from σ^+ and σ^- circularly polarized standing wave light fields, respectively. This figure is adapted from Robens et al. [1]. **(b)** Cesium D_1 and D_2 transition fine structure energy levels. By choosing a so-called magic wavelength λ_{DT} of cesium, atoms with $m_J = -1/2$ are attracted only by σ^- polarized light, whereas atoms with $m_J = +1/2$ are attracted by σ^+ polarized light. This figure is adapted from Döring [115].

back to our qubit hyperfine states $|\uparrow\rangle$ and $|\downarrow\rangle$, it unfortunately turns out that we cannot directly map these onto the fine structure states $|\uparrow'\rangle$ and $|\downarrow'\rangle$. Instead performing a basis transformation from the hyperfine to the fine structure representation gives us:

$$|\uparrow\rangle = |I = 7/2, m_I = 7/2\rangle \otimes |\uparrow'\rangle \,, \tag{2.24}$$

$$|\downarrow\rangle = \sqrt{\frac{7}{8}}\,|I = 7/2, m_I = 7/2\rangle \otimes |\downarrow'\rangle - \sqrt{\frac{1}{8}}\,|I = 7/2, m_I = 5/2\rangle \otimes |\uparrow'\rangle \,. \tag{2.25}$$

Consequently, it is impossible to find a wavelength where each qubit state only couples to one of the two circular polarizations. A thorough calculation including transitions to higher excited levels [115] yields a magic wavelength $\lambda_{DT} = 865.9\,\text{nm}$, where the potentials of the qubit states are given by:

$$U_\uparrow = U_{\sigma^+} \,, \tag{2.26}$$

$$U_\downarrow = \sqrt{\frac{7}{8}}U_{\sigma^-} + \sqrt{\frac{1}{8}}U_{\sigma^+} \,. \tag{2.27}$$

Therefore, the $|\uparrow\rangle$ state is perfectly decoupled from σ^--polarized light, whereas the $|\downarrow\rangle$ state experiences some of the σ^+-polarized light.

Since we work in a deep optical lattice, such that tunneling between lattice sites is fully negligible, the trajectory of an atom in the $|\uparrow\rangle$ ($|\downarrow\rangle$) state is determined by the motion of its σ^+ (σ^-) lattice, giving rise to state-dependent transport. The state-dependent transport scheme of all experiments prior to those presented in this thesis – including those conducted in our group [66, 114, 116] – were based on the first experimental realization by Mandel et al. [112]. This experimental realization, however, is limited to simultaneously shifting both of the optical lattices in opposite directions by at most one lattice site. To hurdle down this shortcoming, we devised a novel scheme for spin-dependent transport based on a high precision, large bandwidth synthesizer of polarization states of light, the experimental details of which are discussed in chapter 3.

Lastly it is noteworthy that cesium is an ideal candidate for state-dependent optical transport. Being an alkali metal, cesium can be efficiently cooled and trapped, while its heavy mass – in comparison to other

alkali metals – leads to a large fine structure splitting of $\lambda_{D1} - \lambda_{D2} = 43\,\text{nm}$. A large splitting is desirable, since we want to avoid off-resonant scattering of lattice photons and the state-dependent optical trapping itself requires us choose a wavelength in between the D_1 and D_2 transition. In fact, as we will see in section 2.4.1, off-resonant scattering of lattice photons puts a hard boundary on the time where we can use our qubit states, before they loose their information to the environment. An interesting alternative is provided by group III atoms: these atoms possess the particularity of an inverse energy level structure, which allows the realization of state-dependent optical lattices, in principle, arbitrarily detuned from resonance. However, it needs to be considered that substantially more experimental effort to cool and trap those atoms is required [117–122].

2.2 Super-Resolution Microscopy of Atoms in an Optical Lattice

For most modern quantum optics experiments optical detection and manipulation of individual atoms in neighboring sites of an optical lattice has become a central tool, e.g. for quantum information processing [16, 67, 123–129], quantum simulations [66, 122, 130–132], and recently for studying strongly correlated Fermi systems at the single particle level [133–136]. Resolving the positions of individual atoms with single-site resolution represents a technological challenge, since in optical lattices the distance between two lattice sites is on the order of the optical lattice wavelength. Nevertheless, over the last few years significant advances have been accomplished on both ends of the detection problem: Sophisticated algorithms nowadays allow us to reconstruct the position of individual atoms even in small clusters at high filling factors, including unity filling (see sec. 2.2.3). Furthermore, the newest generation of atom imaging systems have almost reached the maximum attainable optical resolution, which is bound by the diffraction limit. In fact, the record is currently held by the microscope objective designed and constructed by our group, which is discussed in section 2.2.4.

The imaging system which is currently employed in the experimental apparatus (see Alberti et al. [2] for details) has an optical resolution of $r_A = 1.9\,\mu\text{m}$, according to Abbe's diffraction limit. However, to achieve single-site resolution we need to extract the position of single trapped atoms with an uncertainty smaller than the lattice constant a ($0.433\,\mu\text{m}$). In analogy to super-resolution imaging in biological systems, we can determine the position of our atoms beyond the optical resolution by precisely knowing its point spread function and the underlying noise. Following Bobroff [137], in one dimension the localization precision of the fluorescence peak produced by a single atom can be estimated by

$$(\Delta x)^2 = \frac{\text{RMS}_{\text{PSF}}^2 + \Delta_p^2/12}{N} + \frac{4\sqrt{\pi}\cdot \text{RMS}_{\text{PSF}}^3 \cdot \sigma_b^2}{\Delta_p N^2}\,, \tag{2.28}$$

where it is assumed that the fluorescence signal is integrated over $n_\perp$ pixels in the direction transverse to the lattice, and that RMS_{PSF} is the RMS width of a Gaussian point spread function, Δ_p is the size of a detector pixel in the object plane, N is the average number of recorded photons per atom, and σ_b is the RMS background noise [2]. In the literature, extensions of the result in equation (2.28) can be found for two dimensions [138] and, using the statistical theory based on the Fisher information matrix, for a generic disc point-spread function (e.g., Airy disc) [139]. Note also that the localization precision in equation (2.28) concerns only a single localized emitter, which is the case, for example, of an isolated fluorophore in photo-activated localization microscopy or of a very sparsely filled optical lattice. In addition, it is noteworthy that, when employing an electron multiplying CCD camera (as is the case of the present work), a factor 2 must to be added in front of $\text{RMS}_{\text{PSF}}^2$ in equation (2.28) to account for the effectively halved quantum efficiency due to the electron multiplying excess noise [140].

In the following, we intend to give an estimate of the localization precision of our imaging system based on equation (2.28): The $\mathrm{RMS}_{\mathrm{PSF}}$ of our imaging system is circa 1.5 µm (see sec. 2.2.2) and the parameter Δ_p can be calculated by dividing the detector pixel size (16 µm) by the magnification (55, see Alberti et al. [2]). The number of photoelectrons (ph. e^-) recorded on the EMCCD sensor per single atom can be estimated by knowing the photon scattering rate, the solid angle of the microscope objective into which photons are emitted, and the exposure time. Atoms illuminated with nearly resonant light at $\lambda_\mathrm{f} = 852\,\mathrm{nm}$ emit photons at the maximal rate of $\Gamma/2$ for strong saturation, with $\Gamma \approx 2\pi \times 5\,\mathrm{MHz}$ being the radiative decay rate for cesium. However, to prevent atoms from hopping along the lattice during imaging, the saturation parameter is typically chosen much smaller [141, 142] ($s \approx 0.01$), which reduces the scattering rate by a factor of 10 or more [143]. The solid angle directly depends on the NA of the imaging system according to the formula $\Omega/4\pi = (1 - \sqrt{1 - \mathrm{NA}^2})/2 \approx 1\,\%$. By additionally taking into account the finite quantum efficiency of the CCD camera $\mathrm{QE}(\lambda_\mathrm{f}) \approx 30\,\%$ as well as photon losses (circa 6 %) due to both reflections from optical surfaces (e.g. the vacuum glass cell) and the transmission of a narrow-band optical filter, we expect to detect about 1 000 ph. e^- per atom for a single fluorescence image with an exposure time of $T = 1\,\mathrm{s}$. For comparison, in our experiments we record about 1 300 ph. $\mathrm{e}^-\,\mathrm{s}^{-1}$ per atom. The measured background-noise distribution has a RMS width σ_b of about 0.6 ph. e^- per camera pixel (see Alberti et al. [2]). Since we integrate the fluorescence images along the direction transverse to the 1D optical lattice, the variance of the background noise σ_b^2 is multiplied by the number of transverse pixels $n_\perp$ (typically $n_\perp \approx 40$). Hence, based on equation (2.28) we expect a localization precision of $\Delta x \approx 60\,\mathrm{nm}$, which is sufficiently smaller than the separation between two lattice sites. By using longer exposure times it is possible to improve the resolution even further, however, at the cost of decreasing the duty cycle and increasing the probability for atoms to either hop to adjacent lattice site or to be lost because of heating and background gas collisions.

2.2.1 Fluorescence Imaging of Neutral Atoms

Fluorescence imaging embodies the core method of acquiring information about the atoms trapped in our optical lattice, which enables us to infer e.g. the number of trapped atoms, their qubit state (see sec. 2.3.1 and sec. 3.3.1), or the exact lattice site which they occupy (see sec. 2.2.3). In section 2.1.2 we already discussed how to capture cesium atoms from the residual background gas and transfer them into the deep optical lattice ($U_0/k_\mathrm{B} = 370\,\mu\mathrm{K}$), where they are illuminated using optical molasses beams. The fluorescence light emitted by the atoms at $\lambda_\mathrm{f} = 852\,\mathrm{nm}$ is then collimated by a diffraction-limited objective lens (effective focal length $f_1 = 36\,\mathrm{mm}$) [54] and imaged onto an electron multiplying CCD (EMCCD) camera[7] by a plano-convex tube lens (focal length $f_2 = 2\,\mathrm{m}$), see also figure 2.1. This imaging system corresponds to an infinity-corrected microscope. We employ an EMCCD camera as our detector since they offer a read-out noise which is more than one order of magnitude smaller, even compared to scientific-grade CCD sensors [144].

Figure 2.10(a) exemplarily shows a fluorescence image of eight trapped atoms, which are loaded into the 1D optical lattice in stochastic positions and subsequently imaged with an illumination time of 1 s. The intensity distribution for each atom exhibits a characteristic elliptical shape elongated along the radial direction of the optical lattice with an aspect ratio of about 6:1 (FWHM along the axial direction of 1 µm). The elongated shape originates from the thermal motion of trapped atoms (circa 40 µK for $U_0/k_\mathrm{B} = 370\,\mu\mathrm{K}$ by sub-Doppler cooling) in the radial direction, along which the confinement of the atoms is weaker due to the vaguely focussed Gaussian beam of the optical lattice. Along the lattice direction, instead, trapped atoms can be regarded as localized point sources with a Dirac-delta

[7] Andor: iXon DV897DCS-FI

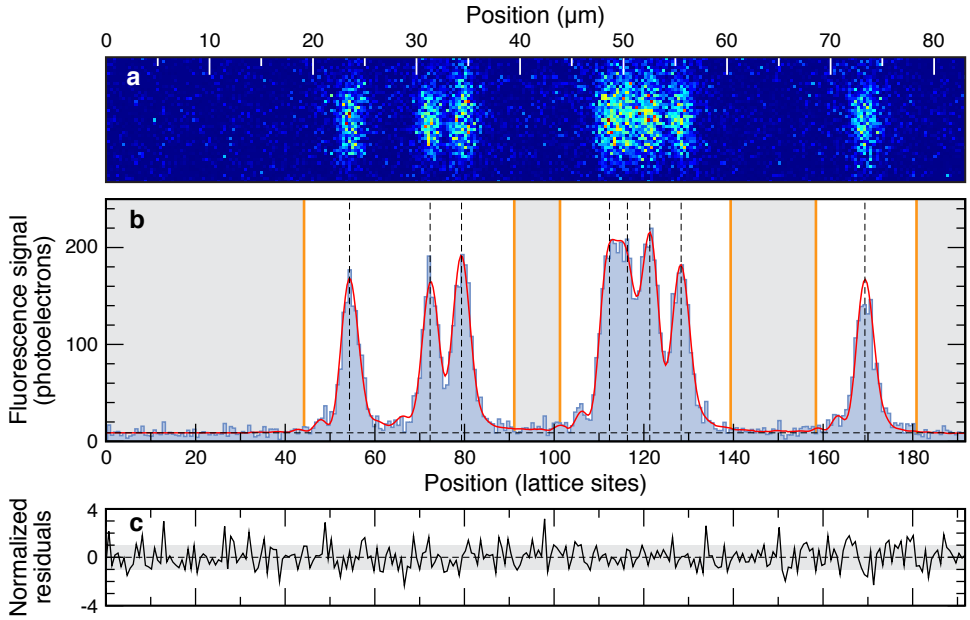

Figure 2.10: **(a)** Image of atoms in a 1D optical lattice acquired with a 1 s exposure time. (**b**) The corresponding integrated intensity distribution. The image is subdivided into regions of interest (white regions) and regions with no fluorescence signal (grey regions), which are used to determine the constant background baseline (dashed horizontal line). The solid red line shows the result of the parametric deconvolution, whereas the vertical dashed lines show the positions of the atoms constrained on a periodic lattice. The distance of the atoms from the leftmost one are 18, 25, 58, 62, 67, 74, 115 in units of lattice sites. **(c)** Normalized residuals between the integrated fluorescence signal and the fitted model, resulting in a reduced $\chi^2 = 0.835$. This figure is originally published in Alberti et al. [2].

longitudinal distribution

$$O(x, y) = O(y)\,\delta(x)\,, \tag{2.29}$$

where the radial motion is incorporated by a radial intensity distribution $O(y)$. This assumption is valid, because the extent of the axial thermal motion (FWHM $\approx 60\,\mathrm{nm}$) as well as the previously mentioned drift of the optical lattice ($\leq 20\,\mathrm{nm/s}$ [126]) is one order of magnitude smaller than the optical resolution. Because we are primarily interested in extracting the precise position of atoms along the optical lattice, we integrate the acquired images along the radial direction as depicted in figure 2.10(b), which reduces the complexity of the following parametric deconvolution to one-dimension. The continuous curve overlapped with the integrated fluorescence signal shows the end result of the parametric deconvolution problem presented in section 2.2.3, which yields atoms' positions with single lattice-site precision. In fact, we can determine the distance between pairs of atoms in discrete units of the lattice-site separation ($a = 433\,\mathrm{nm}$) with a statistical confidence much higher than 99 %. Figure 2.10(c) shows the residuals between the reconstructed distribution and the measured signal, normalized to the expected noise strength. The uniform distribution of residuals with RMS spread around one attests the goodness of the parametric deconvolution, which is ensured by an accurate knowledge of the line spread function of the imaging system as well as of the noise model. While we discuss how to reconstruct the line spread function of the imaging system in the following, the information of the noise model can be found in Alberti et al. [2].

2.2.2 Characterizing the Optical Response of the Imaging System

One key element to achieve a resolution beyond the diffraction limit is the accurate knowledge of the response of our imaging apparatus. More precisely, it is important for the parametric deconvolution problem to know exactly the imaged fluorescence intensity distribution of a single illuminated atom. Since we are working with a digital camera sensor, the optical response of the imaging system is given by the convolution of the microscope objectives point spread function $P(x, y)$ with the detector pixel function $\mathcal{R}_\mathrm{p}(x, y)$ [145]:

$$P_\mathrm{CCD}(x, y) = (\mathcal{R}_\mathrm{p} * P)(x, y)\,. \tag{2.30}$$

As argued in the previous section all our experiments are based on reconstructing the atoms' position in the 1D optical lattice with single site fidelity, which allows us to integrate the acquired images along the radial direction. Therefore, we need to reconstruct the convolution with the line spread function (LSF), which is mathematically defined by integrating the point spread function in one dimension ($L(x) = \int P(x, y)\mathrm{d}y$). Superimposing multiple integrated intensity distributions of sufficiently isolated atoms (such as the rightmost atom in figure 2.10(b)), allows us to increase the signal-to-noise ratio [145] and further reconstruct the LSF with sub-pixel resolution. This process is referred to as image registration in digital signal processing.

Reconstructing the Line Spread Function with Sub-Pixel Resolution: We make use of a recursive algorithm to process single-atom images, whose end result should ideally converge to L_CCD, the one-dimensional version of equation (2.30). The algorithm is composed of a preparatory procedure followed by an iterative one.

The first step of the preparatory procedure consists in identifying those regions of interest containing exactly one atom well separated from other atoms by several Abbe radii r_A (typically 10) in order to allow us not only to reconstruct the central peak of the LSF but also the tails containing the diffraction fringes. In the next step, we apply a Fourier filter to each single-atom image to remove high-spatial-frequency noise. The filter utilizes the fact that every optical system with a hard aperture has a cutoff in the optical transfer function (OTF), defined as the Fourier transform of L_CCD, exactly at the Abbe frequency $1/r_\mathrm{A} = 2\mathrm{NA}/\lambda_\mathrm{f}$. After discrete Fourier transformation (DFT) of the integrated intensity distributions, the filter sets the amplitude of all frequencies beyond the Abbe cut-off (typically $> 1.2/r_\mathrm{A}$ to reduce Fourier artifacts) to zero because these frequencies components do not carry physical information (OTF = 0 in this region). The effect of Fourier filtering is significant for our imaging system because the Abbe frequency is three times smaller than the Nyquist frequency of $0.5\,\mathrm{pixel}^{-1}$ – the frequency up to which noise appears if not filtered out. The last step of the preparatory procedure to reconstruct the LSF consists in interpolating the noise-filtered single-atom distributions with sub-pixel resolution, which allows us to reposition them in the subsequent iterative procedure with high precision. Because of the finite bandwidth of the OTF, the integrated fluorescence signal can be interpolated with an arbitrary spatial resolution using the Whittaker–Shannon interpolation formula: We extend the DFT fluorescence distribution in Fourier space beyond the Abbe cut-off with zero values (zero padding), so that the number of points in the Fourier space is increased by an integer factor s with respect to the original number. The inverse DFT of the zero-padded signal results in an upsampled distribution, where the width of a sub-pixel is equal $1/s$ of the original pixel's width. The size of the sub-pixel is chosen smaller than the estimated localization precision (typically $s = 8$ so that $1/8\,\mathrm{pixel} = 37\,\mathrm{nm} < \Delta x$ for a magnification of 55, see eq. (2.28)). An alternative yet equivalent application of the Whittaker–Shannon interpolation formula operates directly in position space by convolving the spatial distribution with a sinc function.

The iterative part of the reconstruction algorithm consists primarily of two steps. In the first one, we

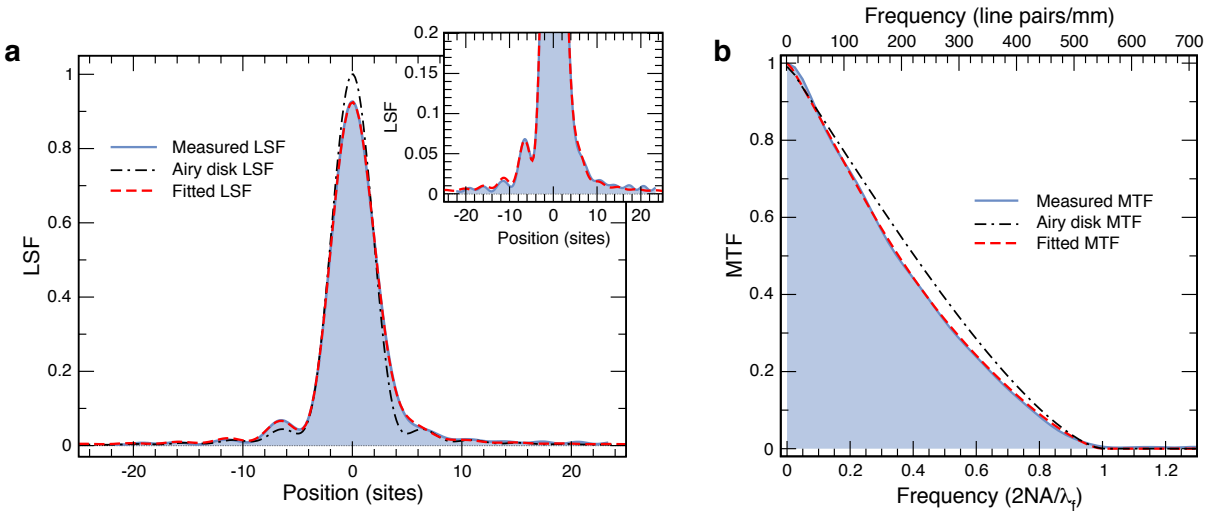

Figure 2.11: (**a**) The solid blue line shows the reconstructed LSF from more than 200 single-atom images, the dash-dotted black line shows the ideal, diffraction-limited LSF derived from an Airy disk with NA = 0.228, and the dashed red line represents the fitted model based on a wavefront expansion in Zernike polynomials. The dash-dotted curve is normalized to have a maximum value of 1, while the other two curves are normalized to the same area of the dash-dotted one. (**b**) Corresponding modulation transfer functions. All three curves show the hard cut-off at the Abbe frequency $1/r_A$. This figure is originally published in Alberti et al. [2]

obtain the position of each atom by a non-linear least squares fit of the model distribution L_{CCD} to the recorded fluorescence signal (see sec. 2.2.3 for more details). The precise (unrounded) value of the atom position is used to shift and align all noise-filtered sub-pixel-interpolated intensity distributions. Hence, superimposing all images gives a reconstruction of the fluorescence distribution of a single atom with a signal-to-noise ratio enhanced by a factor $\sqrt{N_{\mathrm{at}}}$, where N_{at} is the number of superimposed single atoms (typically a few hundreds). The reconstructed distribution L_{guess} provides us with a new estimate of L_{CCD}. The iterative algorithm stops when no change is observed (typically after 5 to 10 iterations). For the first iteration, we use a Gaussian function to determine the position of single atoms in the case where no LSF function is *a priori* known.

A mathematical derivation (see Alberti et al. [2]) shows that this algorithm converges to

$$L_{\mathrm{guess}}(x) = (\mathcal{R}_x * \mathcal{R}_{\mathrm{sp}} * \mathcal{R}_{\mathrm{p}} * L)(x)\,, \tag{2.31}$$

instead of the desired expression in equation (2.30), where $\mathcal{R}_x$ is the probability distribution of the non-linear least squares estimator of the single-atom position for an atom ideally positioned in the origin $x = 0$ (with a RMS width $\Delta x \approx 60\,\mathrm{nm}$, see eq. (2.28)), and $\mathcal{R}_{\mathrm{sp}}$ the sub-pixel function equivalent to the pixel function $\mathcal{R}_{\mathrm{p}}$ but s times narrower. However, since the "blurring" effect of both additional convolutions in equation (2.31) is on the order of a few tens of nanometers, we conclude that $L_{\mathrm{guess}}(x) \approx (\mathcal{R}_{\mathrm{p}} * L)(x)$ to a good approximation.

Analysis of the Reconstructed Line Spread Function: Beyond its importance to retrieve the atoms' positions with maximal localization precision, the line spread function contains valuable information on the performance of the optical system. Figure 2.11(a) shows the reconstructed LSF obtained with the algorithm outlined above. In the case of an aberration-free imaging system, the point spread function

Table 2.2: Result of the wavefront fitting to the measured LSF expressed in terms of low-order Zernike polynomials. The overall wavefront distortion is obtained by adding the different contributions in quadrature. 1D fitting of our model to the LSF cannot prevent a certain ambiguity on the identification of wavefront distortion angles (not displayed).

	Defocus	Astigmatism	Coma	Trefoil	Spherical
Orders (radial, azimuthal)	(2,0)	(2,2)	(3,1)	(3,3)	(4,0)
RMS wavefront distortion (λ units)	0.016(2)	0.048(2)	−0.007(1)	−0.025(1)	0.013(1)

is described by the well-known Airy disk, the corresponding LSF of which is displayed for comparison in the same figure. Besides an overall agreement, the reconstructed LSF exhibits a lower maximum and a distinct asymmetry such that the higher-order diffraction peaks are only visible on the left-hand side. These differences arise from optical aberration, where a naive guess suggests that comatic aberration could account for the observed asymmetry. Mathematically, the point spread function is defined by computing the modulus square of the Fourier transform of the electric field (wavefront) at the pupil (Fraunhofer diffraction). The wavefront contains all information about optical aberrations and can be expressed in the basis of Zernike polynomials [146]. To gain insight into the nature and amount of the optical aberrations affecting our optical system, we fitted to the reconstructed LSF the one obtained from a wavefront expansion in low-order Zernike polynomials up to spherical aberration. The fitted LSF is displayed in the same figure, demonstrating a remarkable agreement with the experimental curve. A detailed list of the Zernike coefficients is given in table 2.2, which shows that the leading aberration contribution arises from astigmatism and not coma. Combining all contributions in the table yields an overall RMS wavefront error of $\approx \lambda/17$ (whereas the peak-valley deviation is $\lambda/3$), which corresponds to a Strehl ratio of 0.87 defined as the ratio between the maxima of the measured point spread function (PSF) and the ideal one. In addition, the wavefront analysis gives a precise estimate of the actual numerical aperture of the optical system, NA = 0.228(3). The deviation between the estimated numerical aperture and the one of the objective lens design (NA = 0.29) is most likely caused by clipping at the knife-edge apertures along the imaging path.

Figure 2.11(b) shows the modulation transfer function (MTF = |OTF|) of the reconstructed LSF compared to that of an aberration-free optical system and of the fitted wavefront model. The MTF of an optical system with a hard aperture has a geometrical interpretation, which explains the shape as well as the hard cut-off. In general, it can be shown that the MTF is given by convoluting the pupil function with itself, where displacements of the electric field distribution in the convolution integral directly translate into spatial frequency units of the MTF [147]. Therefore a hard aperture, and the resulting discontinuous pupil function of an optical system, translate into a cut-off of the MTF at the Abbe frequency. This cut-off also provides a direct method to extract the actual NA of the optical system without resorting to fitting wavefront distortions.

2.2.3 Localization of Atoms by Parametric Deconvolution

The algorithm used to determine the exact positions of individual atoms, which is employed within this thesis, is described in detail in Alberti et al. [2] and embodies an improved version of the one originally published in Karski et al. [125]. While the original algorithm was sufficient to extract the number of lattice sites between well-isolated atoms in a one-dimensional optical lattice, it lead to unreliable results when dealing with small clusters of atoms. However, especially the generation of low-entropy states

presented in section 3.3.3, or the Hong-Ou-Mandel experiment presented in section 5.2, requires us to precisely determine the position of each atom even when every lattice site is occupied.

The revised parametric deconvolution process, which retrieves the position of atoms, comprises several stages: (1) The 1D integrated fluorescence images are divided into regions of interest (ROIs), each with a small number of atoms. (2) The number of atoms is determined for each ROI based on the total number of photoelectrons. (3) We create a model function of the fluorescence distribution for the given number of atoms and (4) use it to obtain a first estimate of the positions of atoms employing a spectral-density estimation algorithm. (5) The estimated positions provide the starting values for a non-linear least squares estimate, which yields the location of atoms with improved precision. (6) We further enhance the localization accuracy by an additional stage that constrains the atoms' positions to the discreteness of the optical lattice and merges all ROIs together.

To keep things short we will skip here the details of each stage, which can be found in Alberti et al. [2].

2.2.4 Outlook: Development of a High-NA (0.92) Objective Lens

In the preceding sections we discussed how we can use numerical tools to extract the position of individual atoms in the 1D optical lattice with a localization precision much smaller than the lattice spacing of 433 nm, despite the fact that our optical resolution is $r_A = 1.9\,\mu m$ according to the Abbe's diffraction limit. Nevertheless, this process is computationally demanding and, furthermore, even with our improved algorithm it becomes unreliable for large clusters of atoms ($n > 10$). Hence, it is highly desirable to further increase localization precision, which in principle can be achieved either by upgrading the objective lens, increasing the lattice spacing, or by imaging the fluorescence of a higher excited level. The latter, in the case of cesium, means that instead of the D_2 line ($6S_{1/2} \rightarrow 6P_{3/2}$), one could use the transition $6S_{1/2} \rightarrow 7P_{3/2}$ with $\lambda_f = 455\,nm$, or the transition $6S_{1/2} \rightarrow 7P_{1/2}$ with $\lambda_f = 459\,nm$. While the maximally attainable resolution of $r_{max} = 228\,nm$ is tempting, in reality one is unfortunately limited by the almost three orders of magnitude reduced fluorescence rate of these transitions in comparison to the D_2 line. As time is of essence when imaging atoms – background vapor collisions lead to atom losses – we want to image our atoms in the shortest possible time. Therefore, the lower fluorescence rate leads to a reduced SNR, which in turn leads to a worse localization precision in comparison to the one obtained from imaging D_2 fluorescence light.

Improving the localization precision by increasing the lattice spacing is a solution which has been widely used in the cold atom community. For example the optical lattice, described in Cennini et al. [148], is realized using a far off-resonant CO_2-laser, which has a wavelength of $\lambda_{DT} = 10.6\,\mu m$. Two counter-propagating laser beams, hence, give rise to an optical lattice with a spacing of 5.3 µm. However, this is also not an option for us, since the state-dependent transport requires us to employ a laser with $\lambda_{DT} = 866\,nm$. Nevertheless, there is another option to increase the lattice spacing: changing the angle of the interfering laser beams. For instance, the optical lattice presented in Wang et al. [128] is formed by blue-detuned laser beams which intersect each other at 10° AOI, giving rise to an optical lattice spacing of 4.9 µm. We recently put forward a proposal [49] in which we explain, how one can realize state-dependent transport of cesium in two dimensions. The optical lattice presented in this proposal makes use of the idea – to change the AOI of the interfering laser beams – which increases the lattice spacing from 433 nm to 612 nm.

The last option is to upgrade the objective lens. According to the Abbe criterium, the optical resolution is given by $r_A = \lambda_f/(2\,NA)$. Since we are imaging the D_2 transition fluorescence ($\lambda_f = 852\,nm$) of cesium which is trapped in vacuum (refraction index $n = 1$) the largest achievable numerical aperture is $NA = n\,\sin(\alpha) = 1$, for $\alpha = 90°$, and hence the maximally attainable resolution amounts to $r_{max} = 426\,nm$. This resolution, however, is practically unachievable because it would require us capture half of the entire

emitted fluorescence. Instead, the best cold atom microscope has a numerical aperture of NA= 0.80 [131], which in our case would give rise to a resolution of $r_{\mathrm{NA}=0.82} = 520\,\mathrm{nm}$. Inspired by this work, I have designed an improved objective lens which achieves a diffraction limited resolution of 460 nm with a numerical aperture of NA= 0.92. This objective lens will be the central part of the next generation experiment, which is described in detail in Brakhane [149]. In the following we will discuss the conceptual idea of this objective lens and how one can measure the optical performance of such a high numerical aperture objective lens.

Designing a High-NA Objective Lens: Before going into the details of the lens design process, one may ask the question why it is at all necessary at all to develop a custom high-NA objective lens, instead of obtaining one which is commercially available. In fact, essentially every major lens design company offers an air-objective lens with a numerical aperture of NA > 0.9. Looking closer at the specs of these objective lenses one quickly notices that the working distance – the distance between the last surface and the focus – is on the order or below 1 mm. Therefore, to use such an objective lens for single atom imaging, we need to employ it inside the ultra high vacuum chamber. However, while there exist a few vacuum compatible commercially available lens systems, to the best of my knowledge, none exist which can be employed in a vacuum on the order of 10^{-11}mbar. This arises largely from the fact that these objective lenses consist of a large number of optical lenses (typically $n > 10$), which are used to correct for chromatic aberration and reduce the tolerance requirement of each lens [150].

There exist a few commercially available objective lenses with a long working distances and moderate numerical apertures (NA < 0.7). However, these lens systems are *per se* also not useful for single atom imaging, since, if we want to employ the objective lens outside of the vacuum system, we need to compensate the aberrations arising from passing through the vacuum window. Therefore, instead of using off the shelf available objective lenses one also requires a custom lens design. This concept is for instance used in the group of Immanuel Bloch [132], who achieves single site resolution with a NA = 0.68 objective lens.

Another path has recently become the state of the art to image atoms trapped in an optical lattice. It combines a single lens inside the vacuum chamber with an objective lens outside and was pioneered – for the cold atom community – by the group of Markus Greiner [131]. The lens inside the vacuum chamber is hemispherical and based on a solid immersion lens (SIL). Solid immersion lens microscopy is a technique, which – similar to oil or water immersion – makes use of a refractive index larger than one to boost the numerical aperture and, hence, increases the optical resolution. If the object to be imaged is located directly on the surface of the SIL, a hemispherical lens will boost the numerical aperture of the following objective lens by the refractive index n, without introducing any optical aberration. Using gallium phosphide (GaP), which has a refractive index of $n_{\mathrm{GaP}} > 3$, Wu et al. [151] achieved a numerical aperture of NA = 2.0. Unfortunately it is not possible to trap cold atoms directly on the lens surface, since one would need to cool the entire lens down to a few μK. Instead a certain amount of space in between the objective lens and the optical trap is required, such that the Casimir-Polder force does not attract the atoms towards the lens surface. In the case of the SIL employed in the experimental apparatus described in Bakr et al. [131], this amounts to 15 μm. The optical lattice is then formed by reflecting laser beams of the front surface of the lens. This geometry, however, would not allow us to realize state-dependent transport. Instead, we require a working distance of at least 120 μm (> 4× the waist of the beams), to form the lattice directly in front of the objective lens by counter-propagating laser beams [49]. While the lens design of Markus Greiners group has been successfully implemented in a variety of other experimental setups [65, 121, 131, 134], it has one intrinsic design flaw: the SIL inside the vacuum and the objective lens outside need to be aligned carefully with respect to each other,

Table 2.3: Summary of the new NA = 0.92 objective lens design values in comparison with the design values of the NA = 0.29 objective lens system which is employed in the experimental apparatus at hand [54].

	NA = 0.92 objective lens	NA = 0.29 objective lens
Optical resolution	460 nm	1 470 nm
Strehl ratio	0.99	1.00
Collection angle	134°	33°
Collection solid angle	$2\pi \times 0.60$ sr	$2\pi \times 0.04$ sr
Working distance	0.15 mm	36.50 mm
Field of view	±35 µm	±500 µm
Effective focal length	11.96 mm	36.00 mm
Depth of focus	0.5 µm	8.2 µm
Design wavelength	852 nm	852 nm
Chromatic bandwidth	±17 nm	±400 nm
Collimated beam diameter	22 mm	16 mm

especially since the vacuum window in between the two induces aberrations depending on the alignment. Furthermore, this alignment will change over time as all objects are all separately mounted. Therefore, a compact ultra high vacuum compatible objective lens would be highly desirable.

Here, I present a novel lens design concept specifically tailored to the requirements of cold atom experiments, which overcomes all of the aforementioned difficulties. The objective lens reaches diffraction limited imaging with a numerical aperture of NA = 0.92 while employing exclusively two lenses. Its field of view spans over 70 µm corresponding to circa 100 lattice sites. The design is depicted in figure 2.12(a) and the details of the surfaces are given in figure 2.12(b)-(d). Instead of a hemispherical lens, we employ a Weierstrass sphere, which – when employed for solid immersion lens microscopy – boosts the numerical aperture of the following objective lens by a factor n^2 instead of n as in the case of the SIL. This greatly reduces the requirements on the numerical aperture of the following lens system, in fact in our case the following objective lens is simply a single aspheric lens with NA = 0.35. Both lenses are made out of N-SF10 [152] and manufactured by Asphericon GmbH, a company specialized on manufacturing custom lenses. We optimized the design for a working distance of 150 µm to meet the above mentioned requirement. Due to the long working distance, the Weierstrass sphere itself introduces a significant amount of aberration, which is compensated by carefully tailoring the surface profile of the aspheric lens up to 10th order. For this purpose we developed a MATLAB [109] ray tracing toolbox, which is used to perform a non-linear least squares optimization of the residual optical path difference. The mechanical stop of the Weierstrass sphere (see fig. 2.12(a)) allows to precisely set the distance between the two lenses and, furthermore, prevents clipping of the lasers that form the optical lattice. Both lenses are mounted with ultra high vacuum compatible glue inside a ceramic holder (Al_2O_3), which is manufactured by BeaTec GmbH. We went through a vigorous tolerance function analysis of all parameters that may deteriorate the image quality including deviations from the ideal lens surface, changes in lens thickness or the refractive index, as well as misalignments causing a change of the lens angle or displacements along the lateral/axial direction. This analysis revealed that despite the large numerical aperture the lens system is surprisingly insensitive to parameter deviations. Therefore it is possible to rely on the manufacturing tolerances (±1 µm) of both, the lenses and the holder, to assemble and glue the objective lens without monitoring the optical performance during the process. In its application the objective lens is directly mounted inside a ultra-low birefringence dodecagonal glass cell [153], therefore, it is important to match the thermal expansion coefficients of all involved materials (for more details see

a)

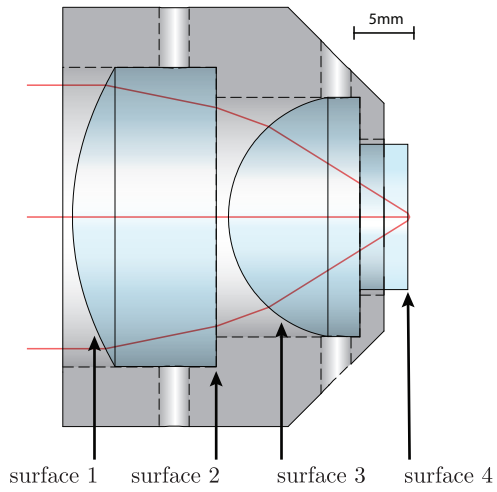

d)

Surface	Parameter	Value
surface 1	CA	22.5 mm
	3/	- (2) RMSi $<$ 0.1 µm
	4/	0.5' (0.005)
	5/	1 × 0.04; L1 × 0.063; E0.3
	MIL	S/D 10-5
surface 2	CA	22.5 mm
	3/	1 (0.2)
	4/	-
	5/	1 × 0.04; L1 × 0.063; E0.3
	MIL	S/D 10-5
surface 3	CA	18.0 mm
	3/	- (1) RMSi $<$ 0.04 µm
	4/	0,5'
	5/	1 × 0.04; L1 × 0.063; E0.3
	MIL	S/D 10-5
surface 4	CA	12.0 mm
	3/	RMSi $<$ 0.0005 µm "superpolished"
	4/	-
	5/	1 × 0.04; L1 × 0.063; E0.3

b)

Surface	Radius	Thickness	Aperture radius	Glass	Aspheric surface
surface 1	22.366 mm	12.00 mm	12.50 mm	N-SF10	yes
surface 2	inf.	1.00 mm	12.50 mm	AIR	no
surface 3	10.175 mm	14.97 mm	10.0 mm	N-SF10	no
surface 4	inf.	150.35 µm	10.0 mm	AIR	no

$$z = \frac{Y^2}{R(1+\sqrt{1-(1+k)Y^2/R^2})} + A_2Y^2 + A_4Y^4 + A_6Y^6 + A_8Y^8 + A_{10}Y^{10}$$

Surface	Conic constant (k)	A_2	A_4	A_6	A_8	A_{10}
surface 1	-0.651	-	1.33×10^{-6}	-2.90×10^{-8}	2.86×10^{-10}	-1.47×10^{-12}

c)

Surface	Type	Wavelength	AOI	Reflectivity	Polarisation
surface 1-3	Anti Reflection	845 nm - 898 nm	0 ° - 32 °	R $\leq$ 0.5%	p, s
surface 4	Anti Reflection	845 nm - 898 nm	0 ° - 67 °	R $\leq$ 0.5%	p, s
	Reflection	1025 nm - 1070 nm	0 ° - 5 °	R $\geq$ 98%	p, s

Figure 2.12: Summary of the high-NA (0.92) objective lens: **(a)** section drawing of the lens design consisting of an aspheric (left) and a Weierstrass-sphere solid immersion lens (right) placed in a ceramic holder (grey); **(b)** surface parameters of the four lens surfaces; the aspheric surface coefficients A_i of surface 1 are defined according to the surface equation z; **(c)** details of the surface coatings: all surfaces have an anti reflection coating for 845 nm - 898 nm, additionally surface 4 is reflective for 1 064 nm; **(d)** surface roughness parameters according to ISO 10110: 3/ surface form tolerances, 4/ Centering Tolerances, 5/ Surface Imperfection Tolerances.

Brakhane [149]). A summary of the microscope lens properties in comparison to the currently employed one is given in table 2.3. It is noteworthy that the objective lens is specifically designed to image cesium fluorescence light at 852 nm and experiences rather strong chromatic aberrations resulting in a diffraction limited bandwidth of 35 nm (837 nm - 872 nm). However, this chromatic bandwidth indeed exceeds the expectations one typically obtains when employing a Weierstrass sphere [151]. Furthermore, it is possible to adjust the lens design – by modifying the surface of the aspheric lens – allowing diffraction limited imaging at other wavelengths[8].

Our developed objective lens provides a compact and robust solution to acquire images of atoms trapped in an optical lattice with a resolution that is close to the maximally physically achievable one. Especially the robustness of the objective is not to be underestimated as experimental setups are becoming continuously more complex. Just recently a novel lens concept by Gissibl et al. [154] has been introduced, which may lead to extremely compact and robust objective lenses using 3D printing techniques. However, the currently obtainable numerical apertures and the imaging quality, in general, do not meet our standards.

Characterizing a High-NA Objective Lens: Characterizing the optical performance of a high-NA objective lens is a demanding task in itself, since it is not trivial to find an ideal point source which can be imaged. While there exist a variety of state of the art approaches [155], they require substantial experimental effort. Trapped atoms in optical lattices are ideal point like radiation sources, even though, it is desirable to characterize an objective optically before the entire experimental apparatus comes together. Consequently, Felix Kleißler tested the suitability of different point sources in his master thesis [156], including fast electron beam manufactured pinholes, light scattering nano particles (PMMA and TiO_2), and an aluminum coated tapered tip of an optical fiber. It turns out that the tapered fiber resembles best a point like radiation source, and hence we will only discuss the details of this measurement. The advantages and disadvantages of the other point sources can be found in [156].

Aluminum coated tapered optical fibers are typically used for scanning near-field optical microscopy [157–159](SNOM) and, therefore, can be obtained commercially from various companies. In our case we use a SNOM-fiber with a tip diameter of approximately 200 nm[9]. The experimental setup to image the radiation from a SNOM-fiber is depicted in figure 2.13(a): the light that is gathered by our high-NA objective lens passes through a motorized iris[10] and is then focussed onto a beam profile CCD-camera[11] using a tube lens with a focal length of 750 mm. The SNOM-fiber is mounted on a 3D translation stage[12], which allows to adjust the position precisely while simultaneously observing the image from the CCD-camera. Figure 2.13(b) shows the recorded image of the SNOM-fiber radiation. The corresponding azimuthally integrated fluorescence distribution is shown in 2.13(c) and the radial modulation transfer function in 2.13(d). The overall shape resembles an Airy disc which one would expect when imaging a perfect point source with a low numerical aperture objective. However, a closer inspection reveals that the rotational symmetry is slightly broken and that the radius of the recorded distribution is a bit larger then the one from an ideal Airy disc. The crucial question is whether these deviations arise from optical aberrations or whether they are related to the high numerical aperture and the SNOM-fiber. In the following we will discuss how one can extend the theoretical model presented in section 2.2.2 to incorporate additional effects. However, let us first recapitulate that mathematically, the

[8] Using the MATLAB toolbox we confirmed that the same design works for imaging fluorescence light of the cesium $6S_{1/2} \rightarrow 7P_{1/2}$ transition with $\lambda_f = 459$ nm.
[9] Lovalite: E50-MONO780-AL-200
[10] Owis: IBM 65
[11] Ophir: Spiricon LW230
[12] Thorlabs: MAX302/M

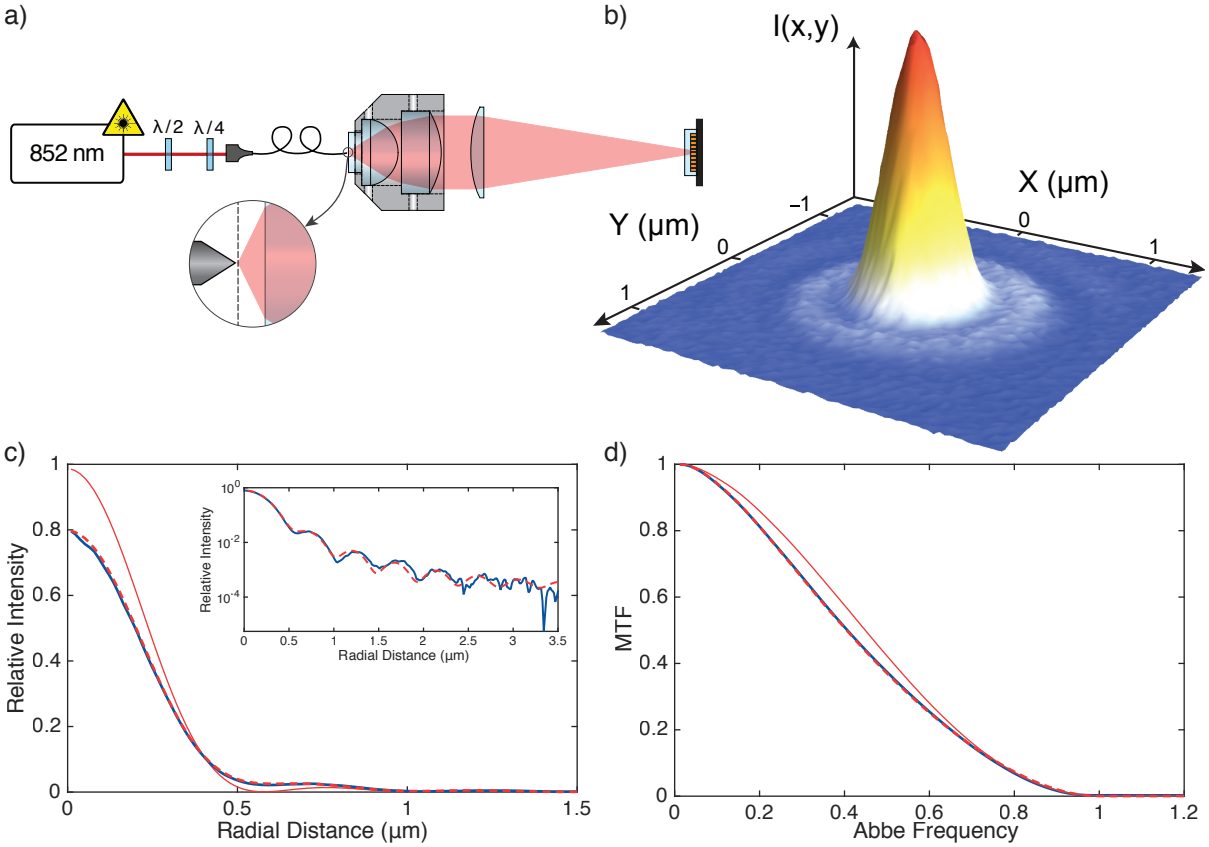

Figure 2.13: **(a)** Optical setup employed to image the tip of a SNOM-fiber. **(b)** Two-dimensional point spread function recorded with the beam profile CCD-camera. **(c)** The solid blue line represents the azimuthally integrated point spread function, the dashed red line the azimuthally integrated fitted model based on a wavefront expansion in Zernike polynomials, and the solid red line a azimuthally integrated simulated point spread function assuming the SNOM-fiber is perfectly in focus. The inset attests the quality of the fit. **(c)** Corresponding modulation transfer functions of the azimuthally integrated point spread functions.

point spread function is defined by:

$$\mathrm{PSF} = \left| \mathcal{F}\left[P(x,y)\, E_0(x,y)\, e^{i\,2\pi\, R(x,y)} \right] \right|^2 , \tag{2.32}$$

where $\mathcal{F}$ is the 2D Fourier transformation, P the pupil function given by the aperture, E_0 the electric field amplitude, and R the wavefront of the collimated beam. As before, the wavefront of the beam can be expressed by an expansion in low-order Zernike polynomials.

It is known that aberration free objective lenses with high numerical apertures, in general, do not produce a collimated beam with a homogeneous intensity distribution even when gathering light from a perfect point emitter [160, 161]. Instead the intensity distribution of the collimated beam depends on the so-called apodization. When designing an objective one can always adjust the lens surfaces such that the on-axis optical path difference amounts to zero, which leads an aberration free image. However, it is physically impossible to fulfill this criterium for the entire field of view. Instead, one can only make the objective lens insensitive to certain aberration. One example is the so-called Abbe's sine apodization condition, where we demand that the objective lens is in first order insensitive to comatic aberration over

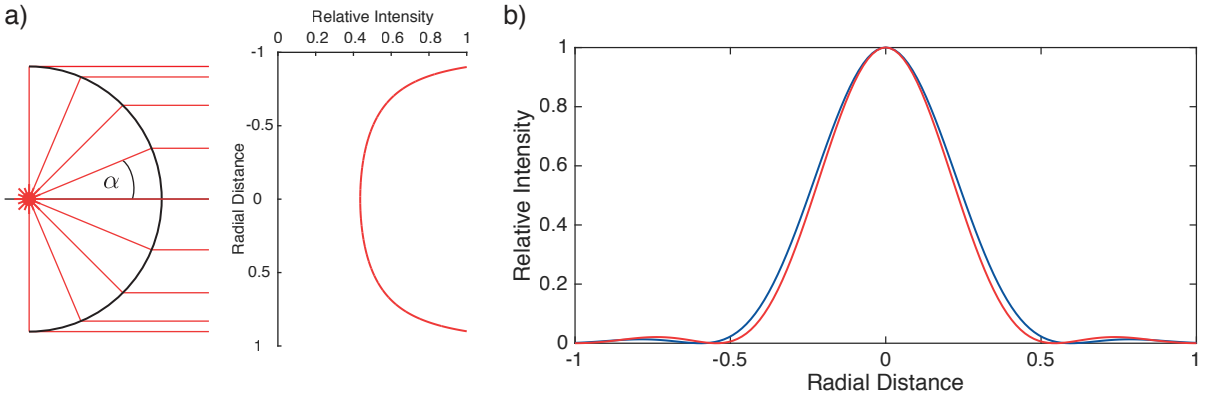

Figure 2.14: **(a)** Illustration of the apodization arising from our high-NA objective lens system. Apodization occurs when collimating an isotropic radiation source with a high-NA lens, which leads to a radially inhomogeneous beam. **(b)** The red line represents a point spread function for an NA = 0.92 objective lens with the apodization effect and the blue line without. Apodization according to the Abbe's sine condition leads to a narrower PSF.

the field of view [162]. Mathematically, therefore, an ideal lens that fulfills the Abbe's sine condition can be described by a spheric principle plane (see fig. 2.14(a)) and its resulting apodization function – the function that converts the ideal point source into a collimated beam with an inhomogeneous intensity distribution – is given by:

$$A_{\text{Abbe}}(\alpha) = \frac{1}{\cos(\alpha)}\,. \tag{2.33}$$

Besides the Abbe's sine condition there also exist other conditions, e.g. the Herschel condition (to cancel astigmatism), or the Helmholtz condition (to achieve a constant magnification over the field of view) [162, 163]. Using the Matlab ray tracing toolbox we analyzed the apodization of our objective lens, which agrees nicely with the Abbe's sine condition. This means that the collimated beam has more intensity towards the edge (see fig. 2.14(a)), and hence when focussed with a low numerical aperture tube lens leads to a point spread function which is no longer described by an Airy disc. To incorporate this effect in our mathematical model (see eq. (2.32)), we convert the apodization function into Cartesian coordinates and replace the constant electric field E_0 with:

$$E_0(x,y) = E_0\,\sqrt{A_{\text{Abbe}}(x,y)}\,. \tag{2.34}$$

Figure 2.14(b) shows how the apodization condition alters the PSF of our high-NA objective lens. Since the Abbe apodization criterium gives more relative weight to the outer part of a collimated beam, the PSF has a narrower central peak in comparison to the Airy disk.

An ideal point source is defined by its radially homogeneous emission of light. While the SNOM-fiber comes close to this for moderate emission angles, Obermüller et al. [164, 165] showed that this is not the case for emission angles of more than 10°. In general, transmission of light through a sub-wavelength aperture is a complicated process which requires solving Maxwell's equations analytically [166]. Nevertheless, the measurements presented in Obermüller et al. [164, 165] reveal that the radial intensity distributions can be well approximated by a Gaussian function for angles up to 90°. Furthermore, in the case of a linear polarization the Gaussian distribution parallel to the dipole axis is narrower than the one perpendicular to it. For our 200 nm SNOM-fiber tip this amounts to a RMS with $\sigma_{\parallel} \approx 50$ degree and $\sigma_{\perp} \approx 65$ degree. The Gaussian distributed emission leads to the exact opposite effect than the apodization

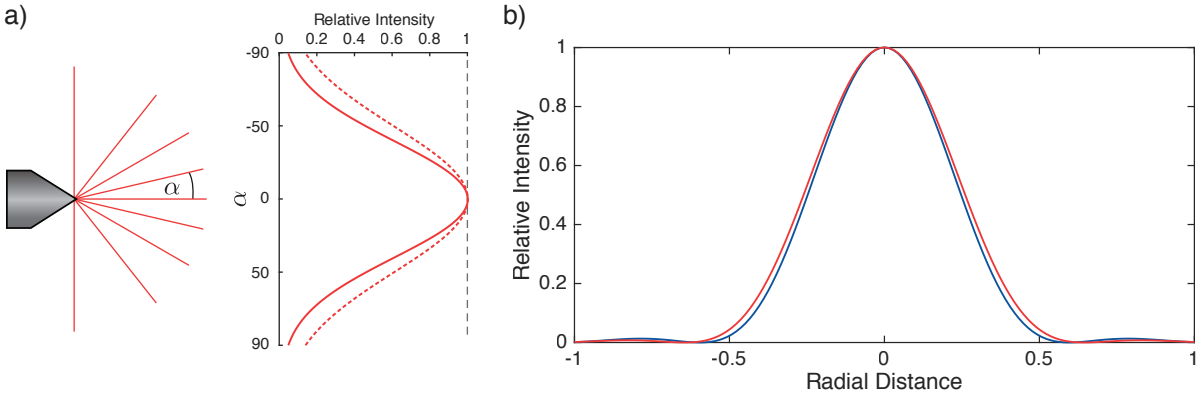

Figure 2.15: **(a)** Illustration of the Gaussian distributed radial emission from a SNOM-fiber. The solid red line represents a distribution with a RMS of $\sigma_{\parallel} = 50°$ and the dashed red line represents a distribution with RMS of $\sigma_{\perp} = 65°$, respectively. **(b)** The red line represents a cut, parallel to the dipole axis, through PSF of an NA = 0.92 objective lens, whereas the blue line represents the a cut, perpendicular to the dipole axis, through PSF. The blue curve is essentially identical to an ideal Airy disk, whereas the red line is slightly wider.

function: the collimated beam has more intensity towards the center of the beam (see fig. 2.15(a)), and hence we expect a broader central peak of the PSF. Similar to the apodization function, we can incorporate this effect by further modifying equation (2.33):

$$E_0(x, y) = E_0 \sqrt{A_{\text{Abbe}}(x, y)\, f_{\text{Gauss}}(x, \sigma_x, y, \sigma_y)}\,, \tag{2.35}$$

where f_{Gauss} is a 2D Gaussian distribution with the RMS widths σ_x and σ_y. The red solid line in figure 2.15(b) shows a cut through the PSF for an axis parallel to the linear polarization. The perpendicular axis is not shown since the curve shows visually no difference compared to the one of an Airy disc (blue line). The different emission profiles of a linear polarization, hence, lead to an asymmetric PSF. However, we can recover a symmetric PSF in our measurements by injecting a circular instead of a linear polarization into the SNOM-fibre [167], which is possible since around 97% of the injected polarization is preserved in the emission at the fibre tip [164].

Using equation (2.32) in combination with the electric field given in equation (2.35) we performed a non-linear least squares fit of the simulated PSF to the measured one shown in figure 2.13(b). Figure 2.13(c) shows the azimuthally integrated measured PSF (solid blue) as well as the azimuthally integrated one obtained from the fit (dashed red), which agree remarkably well. The fit confirms that the objective lens works diffraction limited (Strehl ratio = 0.81) for a numerical aperture of NA = (0.938 ± 0.001), and hence achieves a resolution of 453 nm. A detailed list of the Zernike coefficients is given in Tab. 2.4, which reveals that the predominant aberration comes from defocus. The defocus is not an intrinsic problem of the lens design, but instead related to the fact that the SNOM-fiber was not perfectly positioned in focus. The short depth of focus of the objective lens (500 nm) makes it indeed difficult to experimentally position the SNOM-fibre exactly in focus, since the employed translation stage has a positioning precision on the order of 100 nm. Later, when imaging atoms in the optical lattice, this problem vanishes (see [149] for more details). The solid red curve in figure 2.13(c) – obtained from our theoretical model – shows the PSF in the case where the SNOM-fiber is exactly in focus, while the other aberrations are as given in table 2.4. The corresponding Strehl ratio amounts to 0.98, which nicely agrees with the theoretical prediction from the lens design.

Table 2.4: Result of the wavefront fitting to the measured PSF expressed in terms of low-order Zernike polynomials. The overall wavefront distortion is obtained by adding the different contributions in quadrature.

	Defocus	Astigmatism	Coma	Trefoil	Spherical	secondary Astigmatism
Orders (radial, azimuthal)	(2,0)	(2,2)	(3,1)	(3,3)	(4,0)	(4,2)
RMS wavefront distortion (λ units)	0.07(3)	−0.010(1)	−0.004(1)	−0.001(1)	0.006(1)	−0.015(1)

In the presented analysis we neglected a possible contribution from the vectorial nature of the polarization, which can become important for high-NA objective lenses [155]. However, referring to the analysis presented in Novotny et al. [168], where the PSF is obtained by starting with a vectorial dyadic Greens function for a collection angle of 70°, we can conclude that the predominant changes of the PSF arise from the apodization function as well as from characteristics the radiation source. Of course, if one wants to use our high-NA objective lens to address individual atoms locally using a focussed laser beam, these effects have to be taken into consideration. However, this needs to be the subject of further studies.

2.3 Coherent Quantum State Manipulations

The ground state hyperfine levels $|F = 4\rangle$ and $|F = 3\rangle$ of cesium are ideal candidates for a qubit system since they have an extremely narrow transition [169], and hence a coherent superposition of these states can in principle last for a long time. The narrow transition is in fact the reason that since 1967 cesium is used to define the second. However, while the current cesium atomic fountain clocks reach an uncertainty down to 5×10^{-16} [170][13], recent experiments have reached an almost two orders of magnitude lower uncertainty, e.g. clocks based on a single trapped $^{171}Yb^{+}$ ion [172], or ^{87}Sr optical lattices [173, 174]. Therefore, it is expected that the definition of the second may change in the near future [175].

The two hyperfine states of cesium are separated by $\Delta\nu_{HF} = 9.19263177\,\text{GHz}$, which is convenient from an experimental point of view, since this frequency can be easily generated using off the shelf microwave generators. For most of the experiments presented in the following we require a qubit, a closed two-level system. Ideally we would choose the so-called clock states ($|F = 4, m_F = 0\rangle$ and $|F = 3, m_F = 0\rangle$), since they are to first order insensitive to magnetic field fluctuations, and hence preserve the quantum information much longer [176]. However, the concept of state-dependent transport itself requires us to choose a state with a non-vanishing angular momentum (see section 2.1.3). Therefore, we choose the outermost cesium hyperfine sublevels – $|\uparrow\rangle := |F = 4, m_F = 4\rangle$ and $|\downarrow\rangle := |F = 3, m_F = 3\rangle$ – as our qubit states, which realize a pseudo spin-1/2 system. In the following sections we will elucidate how to efficiently prepare, manipulate and detect the qubit state of atoms trapped in our optical lattice.

2.3.1 State Initialization and Detection

During the fluorescence image acquisition we deliberately cancel all residual DC magnetic fields [169] – such as the earth magnetic field – using a set of six compensation coils. The trapped atoms will, hence, undergo σ^-, π, and σ^+ transitions, which lead to an equal occupation of the nine $|F = 4\rangle$ hyperfine sublevels. Throughout the subsequent 100 ms long adiabatic lowering of the optical lattice (see sec. 2.1.2)

[13] The noise performance of atomic clocks is typically given as the Allan variance [171]

atoms further off-resonantly scatter photons from the optical lattice (see sec. 2.4.1), which then equally populates all $|F = 4\rangle$ and $|F = 3\rangle$ hyperfine sublevels. To initialize – and subsequently manipulate – atoms in $|\uparrow\rangle$ we employ optical F- and m_F-state pumping [177, 178], which reaches a fidelity of $> 99\,\%$[14]. The m_F-state pumping is achieved using a σ^+-polarized laser beam 25 MHz blue detuned from the $|F = 4\rangle \rightarrow |F' = 4\rangle$ transition, which is overlapped with the optical lattice and parallel to the quantization axis. The latter is defined using the six compensation coils to generate a guiding magnetic field with a strength of $|B_0| = (2.95 \pm 0.02)\,\mathrm{G}$. It is noteworthy that the state initialization fidelity critically depends on the overlap of the quantization axis with the laser beam and the purity of the circular polarization ($\Pi > 20\,000$[15]). The m_F-state pumping beam is generated by extracting some of the unshifted molasses cooling light, generated by the IF diode-laser locked on the crossover transition $|F = 4\rangle \rightarrow |F' = 3\rangle$ and $|F = 4\rangle \rightarrow |F' = 5\rangle$ [91] (see sec. 2.1.1). The F-state pumping is achieved by extracting light from the MOT repumping laser – locked on the $|F = 3\rangle \rightarrow |F' = 4\rangle$ transition – and by overlapping the extracted fraction with the m_F-state pumping laser beam. Using 10 nW of F- and 30 nW of m_F-state pumping light for a duration of 20 ms ensures that $> 99\,\%$ of the atoms accumulate in $|\uparrow\rangle$, which is the dark state of the optical pumping process. Further information about the optical setup can be found in Steffen [181].

The qubit state of trapped atoms can be detected either by the traditional push-out technique [182], or by a newly developed loss-free one, which utilizes the state-dependent optical lattice. The latter can only be utilized for small, well separated ensembles of atoms trapped in the optical lattice (see sec. 3.3.1), whereas the former is achieved by applying a short laser pulse resonant with the $|F = 4\rangle \rightarrow |F' = 5\rangle$ transition (40 µW for 150 µs). This pulse pushes atoms – via radiation pressure force – in the $|\uparrow\rangle$ state out of the optical lattice, while not affecting atoms in the $|\downarrow\rangle$ state with an efficiency of $> 99\,\%$. The maximum efficiency in the shortest time is obtained using a laser beam which is σ^+-polarized and perpendicular to the optical lattice [183]. However, this would require us to rotate the quantization such that it is also perpendicular to the optical lattice. While this is certainly possible, it was not possible to observe an improved efficiency using our experimental apparatus [53]. Also, by leaving the quantization axis constant we can strongly low pass filter the current that drives the compensation coils, and hence reduce fluctuations of the guiding magnetic field.

2.3.2 Coupling the Qubit States and its Representation on the Bloch Sphere

An atom initialized in $|\uparrow\rangle$ can be coupled by microwave radiation to any of the other m_F hyperfine sublevel. The interaction between the magnetic component of the oscillating microwave field and dipole moment μ of the atom is well explained by a semiclassical approximation. Since we engineered the state-dependent transport for the qubit states $|\uparrow\rangle$ and $|\downarrow\rangle$ (see sec. 2.1.3), we are only interested in coupling these two, and hence we can reduce the Hilbert space of all internal atomic states to one of a two-level system. The wave function of an arbitrary superposition state is then described by

$$|\psi\rangle = c_\uparrow |\uparrow\rangle + c_\downarrow |\downarrow\rangle \,, \tag{2.36}$$

where the complex amplitudes $c_\uparrow$ and $c_\downarrow$ fulfill $\left|c_\uparrow\right|^2 + \left|c_\downarrow\right|^2 = 1$. Experimentally, the coupling to other m_F hyperfine sublevels is prevented through the strong magnetic guiding field defining the quantization axis, which lifts the degeneracy of the m_F sublevels. For a field strength of $|B_0| = 3\,\mathrm{G}$ two consecutive levels are spectrally separated by 1.05 MHz [184]. The dynamics of such a driven pseudo spin 1/2 system are described by the optical Bloch equations [185], which are obtained from solving the Heisenberg

[14] The fidelity in this case is a measure of the accuracy to reach the desired state and not a measure of the distance between density operators as defined in [179]

[15] The purity is defined as the ratio of σ^+/σ^- polarized light, for more details see [180]

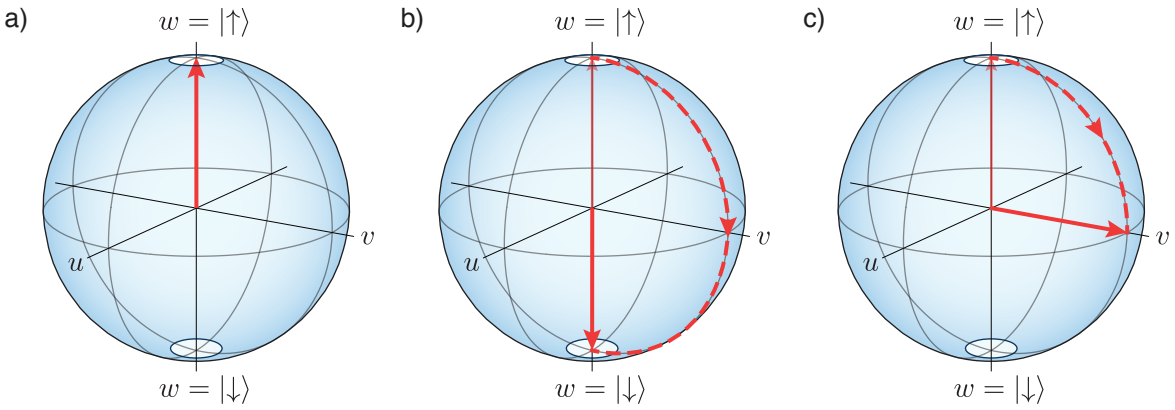

Figure 2.16: Bloch sphere representation of a two-level system. **(a)** The north pole corresponds to a $|\uparrow\rangle$ state. **(b)** Illustration of a spin-flip ($\pi-$pulse) operation which turns $|\uparrow\rangle$ into $|\downarrow\rangle$ and **(c)** of a $\pi/2-$pulse which creates an equal superposition state.

equation of motion using the rotating wave approximation. By additionally incorporating population and coherence relaxation effects as dampening terms [182] – similar to diffusion terms in nuclear magnetic resonance [186, 187] – we derive the following set of partial differential equations:

$$\langle\frac{\partial u}{\partial t}\rangle = \Omega_R \sin(\varphi_{MW})\ \langle w\rangle + \delta\langle v\rangle - \frac{\delta\langle u\rangle}{T_2}\,, \tag{2.37}$$

$$\langle\frac{\partial v}{\partial t}\rangle = -\delta\langle u\rangle + \Omega_R \cos(\varphi_{MW})\ \langle w\rangle - \frac{\delta\langle v\rangle}{T_2}\,, \tag{2.38}$$

$$\langle\frac{\partial w}{\partial t}\rangle = -\Omega_R \cos(\varphi_{MW})\ \langle v\rangle - \Omega_R \sin(\varphi_{MW})\ \langle u\rangle - \frac{\langle w\rangle - w_0}{T_1}\,, \tag{2.39}$$

where w describes the population, while u and v comprise the coherence of the qubit state. Here we introduced the detuning $\delta = \omega - \omega_0$, the Rabi frequency of the microwave field $\Omega_R = \mu B_0 \hbar$ including its phase φ_{MW}, the population relaxation time T_1, and the coherence relaxation time T_2. Please note that the Rabi frequency of the microwave field Ω_R can be time dependent. A closed two-level system – the states of which have a neglectable energy difference – would eventually decay into a statistical mixture with equal relative occurrences of $|\uparrow\rangle$ and $|\downarrow\rangle$ ($w_0 = 1/2$). However, as we will see in section 2.4.1 this does not hold true for cesium which is trapped in an optical lattice. The three constituents (w, u, and v) form the so-called Bloch vector, which enables us to visualize the temporal evolution of a qubit state on the Bloch sphere (see fig. 2.16(a)). In fact, the Bloch vector is related to the wave function given in equation (2.36) via the density matrix ρ of the two-level system:

$$u = \rho_{10} + \rho_{01}\,,\quad v = i(\rho_{01} - \rho_{10})\,,\ \text{and}\ \ w = \rho_{00} - \rho_{11}\,. \tag{2.40}$$

Let us for now consider a decoherence free system ($T_1 = T_2 = \infty$) which is resonantly driven ($\delta = 0$) with $\varphi_{MW} = 0$. The amount and physical origin of the population and the coherence relaxation time T_1 and T_2 for cesium trapped in a state-dependent optical lattice is later discussed in section 2.4. These assumptions greatly simplify the optical Bloch equations (2.37)-(2.39), such that the temporal evolution of the population can be analytically solved:

$$w(t) = -\cos(\Omega_R(t)\, t)\ . \tag{2.41}$$

Equation (2.41) is of particular experimental relevance, since a precise control of the microwave radiations field strength – and hence the Rabo frequency $\Omega_R(t)$ – for a certain duration Δt enables us to engineer any desired qubit superposition state. For instance, if we choose $\int dt\, \Omega_R(t)\, t = \pi$ we can invert the qubit state e.g. from $|\uparrow\rangle \rightarrow |\downarrow\rangle$ (see illustration in fig. 2.16(b)), while a value of $\pi/2$ puts an initial pure state in an equal superposition of $|\uparrow\rangle$ and $|\downarrow\rangle$ (see fig. 2.16(c)). The additional control of the microwave phase φ_{MW} allows us to also choose the rotation axis of the Bloch vector. This degree of freedom is used in section 2.4.2 to scan the phase in a Ramsey fringe measurement.

To create the required 9.2 GHz microwave frequency, we mix[16] the signal output of a vector generator[17], which produces 160 MHz, with a 9.04 GHz stable constant frequency from a PLDRO[18] (Phase-Locked Dielectric Resonator Oscillator). The combined signal passes through an analog PIN diode attenuator[19], is amplified to a maximum power of 41 dBm[20], and directed to the atoms by an open metallic waveguide, which is positioned in close vicinity of the vacuum glass cell. The maximally attainable Rabi frequency of this experimental setup amounts to 58 kHz. The envelope of the microwave radiation can be shaped either by the PIN diode attenuator on timescales $> 20\,\mu s$, or – in order to create shorter rectangular pulses – by using an external trigger generator[21] with a timing resolution of 100 ns. This trigger generator directly gates the output of the vector generator. Phase and frequency of the microwave radiation can be controlled through the vector generator using an analog input which is connected to the laboratory computer. More details on the experimental setup can be found in references [53, 181] and information on the incorporation of the setup in the newly developed control system is given in Zopes [188].

2.3.3 Microwave Driven Global Spin Rotations

In our laboratory, microwave spectroscopy is a routinely employed tool, which enables us to determine the exact transition frequency between the two qubit states and, furthermore, also allows a characterization of the spin flip efficiency. For experiments with single atoms we commonly employ two different types of addressing π-pulses: a fast rectangular shaped pulse and a spectrally narrow Gaussian shaped one. The former achieves a spin flip in the shortest possible time using the maximally attainable Rabi frequency ($\Omega_R = 58\,kHz$) for a duration of $t \approx 9\,\mu s$. The fast square π-pulse also has the advantage that it is spectrally broad, which makes it rather insensitive to small detunings of the qubit transition frequency. In fact, the qubit transition frequencies of different atoms are generally not expected to be equal: spatially and temporally varying magnetic fields lead to changing hyperfine splittings while the fact that atoms are not yet cooled into their vibrational ground state leads to varying light shifts [182, 189]. The Gaussian π-pulse, on the contrary, is used if we desire a better spectral resolution, as for example when locally addressing individual atoms (see sec. 2.3.4). Similar to the Fourier limit, in principle it is also possible to spectrally narrow the square pulse by reducing its Rabi frequency while adjusting the time – the effect of the Rabi frequency on the spectral resolution is generally referred to as power broadening [190]. However, this has two experimental drawbacks: The sinc-like nature of the square π-pulse spectrum (see fig. 2.17(a)) will always lead to small side peaks, which are undesirable for local addressing pulses. Furthermore, the qubit state is most sensitive to dephasing decoherence for an equal superposition while it vanishes for pure states. Hence, the Gaussian π-pulse shields the qubit against dephasing decoherence, since it spends less time in a state close to the equator of the Bloch sphere. Therefore, the qubit transfer

[16] MITEQ SSM0812LC2CDC
[17] Agilent: E4432B ESG-D
[18] MITEQ: PLDRO-10-09040-3-15P
[19] MITEQ MPAT-08001200-60-10
[20] MITEQ: AMF-6B-08500950-40-41P-TTL
[21] Agilent: 33220A Function / Arbitrary Waveform Generator

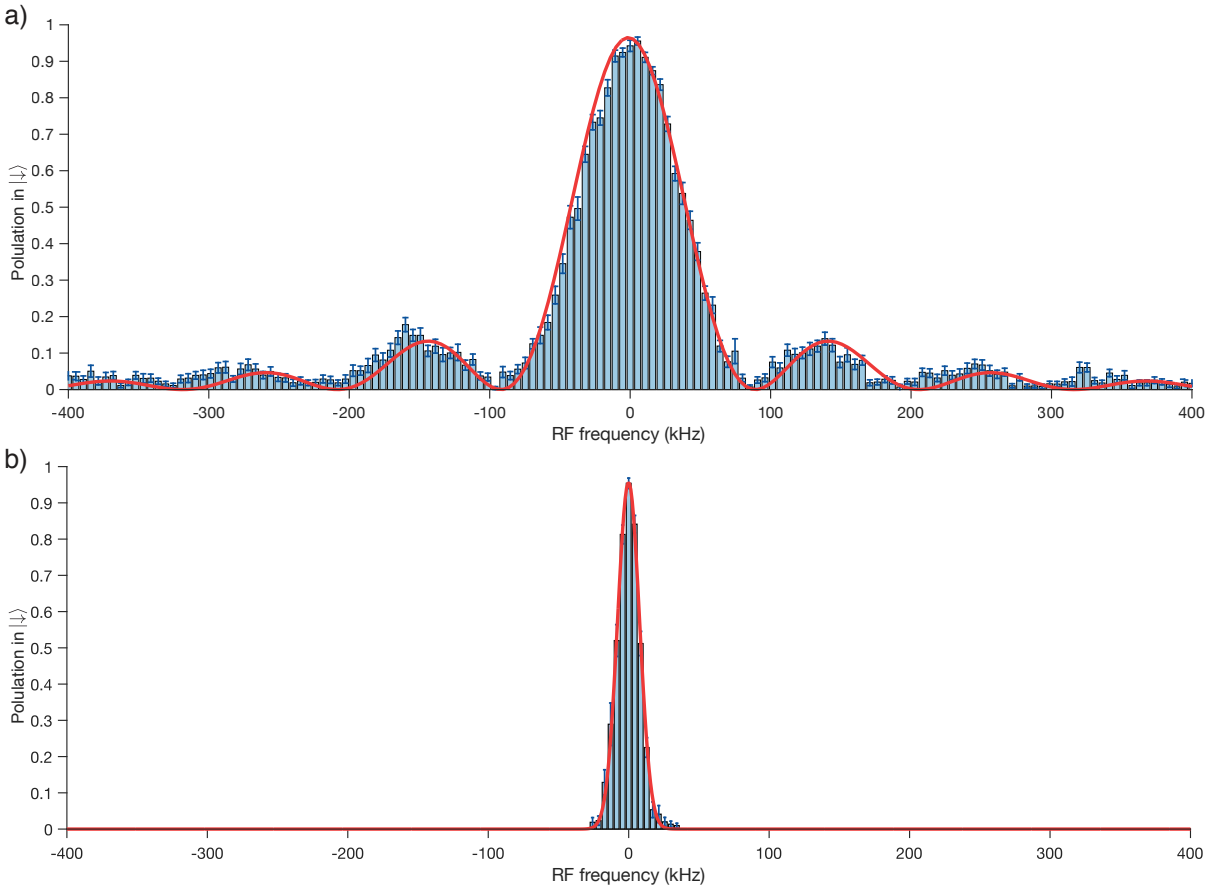

Figure 2.17: Exemplary microwave spectra obtained by **(a)** employing a 9 µs long square pulse and **(b)** employing a pulse the amplitude of which is Gaussian shaped with a RMS of 30 µs. The red lines in both figures represent simulated spectra, obtained by numerically solving the Bloch equations (2.37)-(2.39) with $T_1 = 100\,\text{ms}$ and $T_2 = 250\,\mu\text{s}$. The span of both figures is deliberately chosen to be identical in order to highlight the spectral difference of the two pulses.

efficiencies of Gaussian π-pulse are higher than those of a square π-pulse with similar spectral resolution. It is noteworthy, that while the spectral resolution of a microwave pulse can theoretically become infinitely narrow for a system without decoherence, one will ultimately always be limited by the natural line width of the qubit transition (circa 100 Hz).

The histogram in figure 2.17(a) exemplarily depicts a measured microwave spectrum using a square π-pulse, whereas the histogram in figure 2.17(b) represents a spectrum obtained from a Gaussian π-pulse. The red solid line in both figure 2.17(a) and figure 2.17(b) shows the result from a non-linear least squares fit of a simulated spectrum – obtained by numerically solving the Bloch equations (see eq. (2.37)-(2.39)) – to the measured spectrum. This fit allows us to extract the transfer efficiency and spectral width of the pulses which are summarized in table 2.5. Both microwave spectra are recorded using the following experimental procedure: we load an ensemble of atoms into the optical lattice, determine their initial number via fluorescence imaging, lower the optical lattice, and initialize the ensemble in $|\uparrow\rangle$ by means of optical pumping. Subsequently, the atoms are exposed to a microwave pulse the frequency of which varies each iteration. Using the push-out technique the qubit is then projected onto either $|\uparrow\rangle$ or $|\downarrow\rangle$ and in

Table 2.5: Summary of the fast square $\pi-$pulse and the gaussian $\pi-$pulse. The values are obtained from the microwave spectra shown in figure 2.17. The duration of the Gaussian pulse is given as the $1/\sqrt{e}$ time of the pulse.

	Square pulse	Gaussian pulse
Pulse duration Δt	9 µs	30 µs
Rabi frequency Ω_R	58 kHz	-
Transfer efficiency	(98 ± 1) %	(96 ± 1) %
Central peak FWHM	(96.0 ± 1.0) kHz	(18.0 ± 0.5) kHz

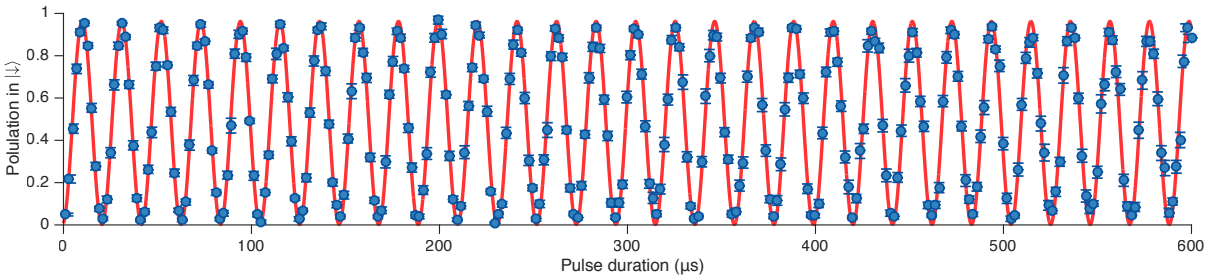

Figure 2.18: Microwave radiation induced Rabi oscillations between the $|\uparrow\rangle$ and $|\downarrow\rangle$ state with an oscillation frequency of 48 kHz. The red line represents a fit without accounting for decoherence, since the contrast of the oscillation does visibly not decay after almost 30 oscillations.

the case of the former removed from the optical lattice. To detect the remaining fraction of atoms we again rely on fluorescence imaging. The microwave frequency is increased each iteration until it reaches a user defined maximum, at which the entire procedure is repeated until a spectrum with sufficient statistics is recorded (typically 10 repetitions where on average 20 atoms are loaded into the optical lattice).

The transfer efficiency of the rectangular π-pulse is in first order insensitive to small deviations in the duration Δt (see eq. (2.41)). However, this is exactly opposite for the rectangular $\pi/2$-pulse, which is used to create an equal superposition of the qubit states. Nevertheless, e.g. the experimental violation of the Leggett Garg inequality – presented in chapter 4 – relies on a precisely adjusted $\pi/2$ condition. For this purpose we employ Rabi oscillation measurements, where we scan the pulse duration Δt, while the frequency remains on resonance. Figure 2.18 exemplarily shows the result of such a measurement for a Rabi frequency of $\Omega_R = 48$ kHz. By fitting a sinusoidal curve to the measured values (red line) we can extract the required duration Δt, which amounts to $\Delta t_{\pi/2} = (4.82 \pm 0.01)$ µs and $\Delta t_\pi = (9.60 \pm 0.01)$ µs. It is noteworthy, that the amplitude of the Rabi oscillation does visually not decrease even after more than 25 oscillations, which indicates a long coherence time. Rabi oscillations, however, are intrinsically not particularly sensitive to decoherence, since they make use of so-called dynamic decoupling [191, 192]. Therefore, we employ Ramsey spectroscopy in the following to study the decoherence time in more detail.

2.3.4 Microwave Driven Local Spin Rotations

Local addressing of individual atoms trapped in an optical lattice embodies one of the milestones on the path towards a scalable quantum computer [67]. Up until today a variety of experimental realizations achieved such addressing of individual atoms. Initially most experiments were based on incoherent methods including a focussed ion beam [193], a focussed near-resonant laser beam [194], and crossed

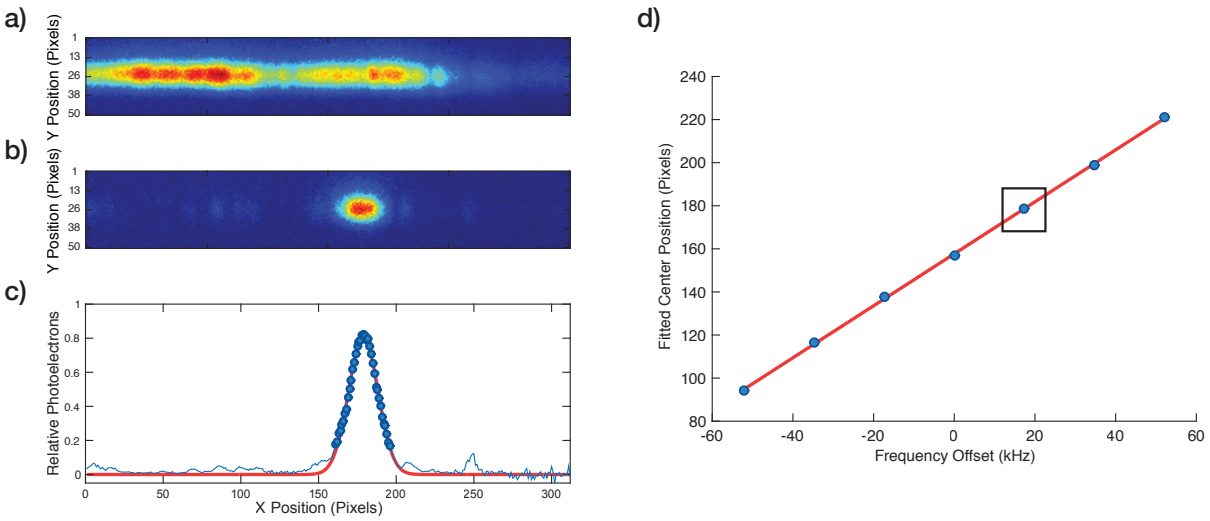

Figure 2.19: Position dependent microwave addressing of atoms using a magnetic field gradient. **(a)** Averaged image of 20 initial distributions of atoms which are trapped in the optical lattice. **(b)** Averaged image of the 20 distributions after employing a position dependent Gaussian shaped microwave $\pi-$pulse and the push out beam. **(c)** Vertically integrated image, normalized to the initial distribution. The red line represents a Gaussian fit. **(d)** Resulting magnetic field gradient calibration after repeating several position dependent microwave spectra for different transition frequencies, each represented by a blue dot. The black square represents the data shown in (a)-(c). Error bars are smaller than the blue dots.

optical lattices [195]. More recently, three common experimental strategies have been established, which also allow coherent operations: one can use a pair of focussed Raman lasers to optically induce the qubit transition [196, 197]; a magnetic field gradient to realize position dependent qubit transition frequencies, which are addressed by microwave radiation [126, 198, 199], or hybrid approach combining the advantages of both by using a focussed off-resonant laser beam to locally shift the qubit transition, which is then addressed by microwave radiation [67, 128, 200].

While the latter is of great interest for the newly developed high numerical aperture objective (see ref. [149] for details) the experiment at hand comprises a set of anti-Helmholtz coils which can be used to generate high magnetic field gradients along the optical lattice. The magnetic field gradient addressing technique was pioneered for trapped ions [198] and shortly after used by our group to imprint patterns of neutral atoms with single lattice site resolution [126]. Single site addressing, however, requires the maximally attainable magnetic field gradient of $120\,\mathrm{G\,cm^{-1}}$, which in turn requires a rather long pause ($> 50\,\mathrm{ms}$) until the field gradient is stable enough to ensure high addressing efficiencies. Since we cannot allow such long pauses e.g. for the atomic Hong-Ou-Mandel experiment (see sec. 5.2), we restrict ourself to a magnetic field gradient of $11.6\,\mathrm{G\,cm^{-1}}$ within this thesis. This enables us to raise the magnetic gradient after the state initialization within 10 ms – short enough such that only few of the qubits change their state by scattering optical lattice photons (see sec. 2.4.1).

To calibrate the magnetic field gradient we again employ microwave spectroscopy. In this case we initially load as many atoms as possible into the optical lattice (see fig. 2.19(a)), and employ the microwave spectrum sequence outlined above, with the addition that the magnetic field gradient is applied during the addressing pulse. Since the transition frequency of each atom increases linearly along the optical lattice (see also section 2.3.2), the fluorescence image recorded after the push-out operation reveals directly the entire spectrum encoded in the position along the lattice (see fig. 2.19(b)). The central

addressing position, for a certain microwave frequency, can be determined by fitting a Gaussian function to the ratio of the first and second fluorescence image (see fig. 2.19(c)) – more precisely to the average of several repetitions. Therefore, by using this method for different microwave frequencies, we can calibrate the magnetic field gradient (see fig. 2.19(d)), which amounts to $\Delta\nu_{\lambda/2} = (1.251 \pm 0.006)\,\mathrm{kHz}$ and corresponding $11.6\,\mathrm{G\,cm^{-1}}$ for a coil current of 4.1 A.

The magnetic field gradient calibration will be used in chapter 3 and chapter 5 to address individual trapped atoms, which is one of the constituents to sort neutral atoms in our state-dependent optical lattice. Unfortunately, the low magnetic field gradient prevents us from addressing atoms in neighboring lattice sites. Instead, for a Gaussian π-pulse with a FWHM of 18 kHz we require a minimal separation of $d_{\mathrm{MW}} = 19$ lattice sites to ensure a probability $< 1\%$ that local addressing pulses spin-flip a neighboring atom. Furthermore, the magnetic field gradient induces additional decoherence, and hence limits the transfer efficiency to $(86 \pm 1)\,\%$ instead of $(96 \pm 1)\,\%$ as reported above.

2.4 Population and Coherence Relaxation of Qubits in Polarization-Synthesized Optical Lattices

In the foregoing sections we already identified several mechanisms which limit the lifetime of our qubit state. We will summarize and complete the list in the following, elaborate in more detail the physical origin of spin relaxation, and discuss experimental procedures which allow us to quantitatively extract their value for the apparatus at hand. While we have not yet formally introduced the polarization-synthesized optical lattice, all of the following measurements are obtained using our novel optical lattice technique, which is introduced in chapter 3. Hence, besides our fundamental interest, they serve to benchmark the impact of polarization-synthesized optical lattices onto the qubit properties. In section 2.3.2 we phenomenologically introduced the concept of the qubits' population and coherence relaxation as dampening terms in the optical Bloch equations (2.37)-(2.39). We will maintain this discrimination in the following discussion, since it is possible to separate their physical origin.

2.4.1 The Population Relaxation Time T_1

The relaxation rate of neutral atom's hyperfine sublevels has been studied in detail over the last two decades. In fact, the spin relaxation of cesium in a magnetic trap induced by inelastic collisions prevented the first attempt of creating a BEC [201]. On the contrary, the hyperfine sublevel lifetime of neutral atoms, which are trapped in an off-resonant optical dipole potential, is not limited by collisions but instead by off-resonant scattering processes with photons of the dipole potential [202, 203]. The experimental sequence to measure these relaxations is rather straightforward with the tools we discussed earlier: similar to the microwave spectrum sequence, we load and image an ensemble of atoms in the optical lattice which is subsequently initialized in $|\uparrow\rangle$ via optical pumping in the 74 µK deep lattice. Instead of applying a microwave pulse, we hold the atoms for a certain duration, before applying the push-out pulse. Hence, those atoms whose hyperfine level has changed from $|F = 4\rangle$ to $|F = 3\rangle$ are not removed from the optical lattice and appear in the second fluorescence image. The blue dots depicted in figure 2.20 represent the fraction of atoms which occupy $|F = 3\rangle$ hyperfine sublevels for increasing hold times between state initialization and detection. It is noteworthy, that the values presented in figure 2.20 have been corrected by the atom losses one expects from heating of the optical lattice as discussed in section 2.1.2.

At first sight the decay of the qubit population seems to be exponential, and indeed, if we take a page out of the NMR (nuclear magnetic resonance) playbook [186], we can describe the population decay of a spin 1/2 system – the dynamics of which follow the Bloch equations (2.37)-(2.39) – with the following

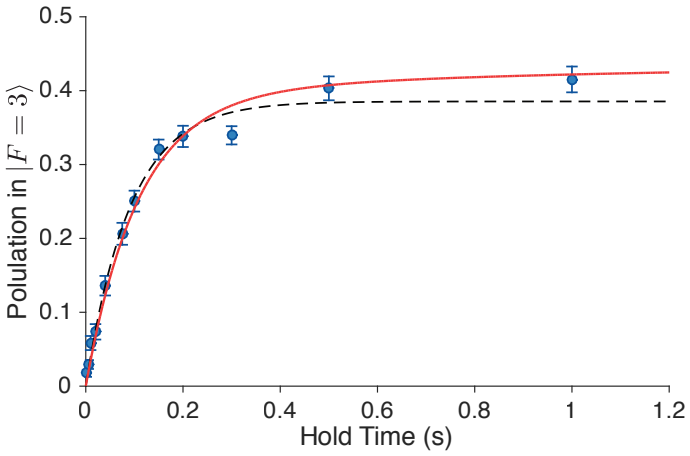

Figure 2.20: Population relaxation measurement of atoms which are initialized in $|\uparrow\rangle$. The dashed black line represents a fit using the simple model given in equation (2.42), whereas the red solid line is obtained by numerically simulating the temporal evolution of the $|\uparrow\rangle$ state using calculated scattering rates.

model:

$$P_{\uparrow}(t) = P_{\mathrm{Eq}} - \left(P_{\mathrm{Eq}} - P_{\downarrow}(0)\right) e^{-\frac{t}{T_1}}\,, \tag{2.42}$$

where $P_{\uparrow/\downarrow}(t)$ is the relative population of the $|\uparrow\rangle$ / $|\downarrow\rangle$ state at time t, P_{Eq} the equilibrium ratio of $|\uparrow\rangle$ and $|\downarrow\rangle$, and T_1 the $1/e$ population decay time. Here we already included that the initial state preparation may not be perfect, and hence a fraction of atoms starts in the opposite state ($P_{\downarrow}(0)$). For a perfect spin 1/2 system the states of which have a neglectable energy difference we would expect an equilibrium ratio of $P_{\mathrm{Eq}} = 1/2$. The dashed black line in figure 2.20 represents the result of a non-linear least squares fit of equation (2.42) to the measured data with $T_1 = (92 \pm 12)\,\mathrm{ms}$, $P_{\downarrow}(0) = (0.5 \pm 0.5)\,\%$, and $P_{\mathrm{Eq}} = (39 \pm 2)\,\%$. While the fitted curve shows a systematic discrepancy to the measured data, the extracted T_1 time agrees well with the values reported in Karski [53] for the same experimental apparatus. It is also noteworthy, that the extracted equilibrium population differs significantly from 1/2. This is, however, not surprising, since spontaneous scattering events can couple the qubit states to any other cesium hyperfine sublevel. It was shown that in the case of a linear polarized optical lattice with a parallel quantization axis spontaneous scattering of lattice photons leads to an equal population of all hyperfine sublevels, and hence for cesium $P_{\mathrm{Eq}} = 7/16$ [69]. One explanation for the discrepancy may be that the experimental procedure outlined above does not probe the qubit states, but instead only differentiates between the population in $|F = 4\rangle$ and $|F = 3\rangle$. Below we will discuss how one can instead derive the temporal evolution of all hyperfine sublevels from an *ab initio* calculation, which nicely agrees with the experimental data (see red line in fig. 2.20).

Following the path outlined in Cline et al. [203] we can derive the Kramers-Heisenberg formula for our experimental situation, which allows us then to quantitatively calculate the scattering rates of all hyperfine sublevels. Scattering of light consists in general of two processes – the absorption of an incoming photon and the emission of the scattered one – and hence, they are processes of second order radiative transitions, which are described by the generalized Fermi's golden rule [74]. Using the multilevel version of equation (2.7) and after some calculus (see appx. sec. B.4) we obtain the Kramers-Heisenberg formula given in equation (B.31). This formula depends only on the properties of the optical lattice (wavelength λ_{DT}, intensity I_{DT}, polarization $\vec{\varepsilon}_{\mathrm{DT}}$, and the direction of the quantization axis) and the matrix elements between the ground state and all possible excited levels. The latter can be

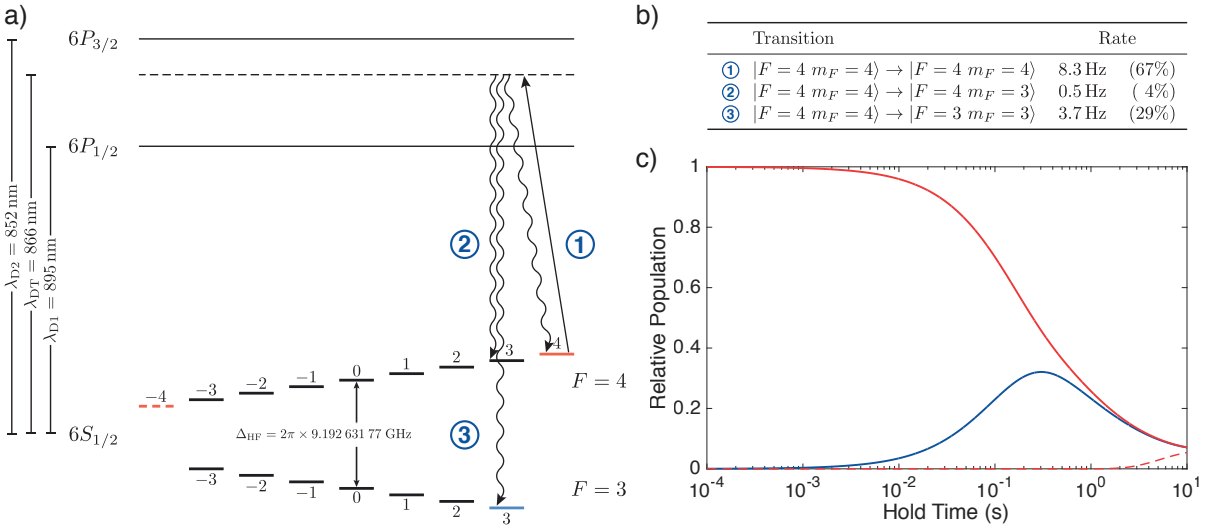

Figure 2.21: **(a)** Ground state hyperfine energy levels of cesium including the D_1 and D_2 transition. The arrows indicate all possible two-photon scattering transitions for an atom in $|\uparrow\rangle$ arising from off-resonantly scattering a photon with the state-dependent optical lattice. **(b)** Individual scattering rates, obtained from the Kramers-Heisenberg formula (see appx. sec. B.4). **(c)** The red line represents the temporal evolution of a qubit initially prepared in $|\uparrow\rangle$, the blue line shows the contribution in $|\downarrow\rangle$, and the red dashed line the contribution in $|F = 4, m_F = -4\rangle$.

calculated using the Wigner-Eckart theorem (see appx. sec. B.3) and the values of the reduced matrix elements given in Steck [184]. The optical lattice – as discussed in 2.1.1 – is formed by a pair of linear polarized counter-propagating laser beams with $\lambda_{DT} = 866$ nm, therefore, the quantization axis is perpendicular to the polarization vector. The intensity of the optical lattice at the focal position is given through the power in each laser beam $P_{DT} = 6$ mW and the waist $w_{DT} = 17\,\mu$m (see also fig. B.1(b) in appx. sec. B.1). Figure 2.21(a) shows the allowed two-photon scattering transitions for the $|\uparrow\rangle$ state (see eq. (B.28) in appx. sec. B.1 for dipole transition selection rules), whereas their absolute and relative values are summarized in table in figure 2.21(b). Correspondingly, figure 2.22(a) shows the allowed two-photon scattering transitions for the $|\downarrow\rangle$ state, whereas their absolute and relative values are summarized in table in figure 2.22(b). The total scattering rate of each qubit state amounts to 12 Hz. Conventionally, we distinguish two types of scattering events: elastic processes, also referred to as Rayleigh scattering, where the atom remains in the same state after the scattering event and inelastic processes, also referred to as Raman scattering, where the atom changes its internal state.

The calculated scattering rates, in turn, can be used to numerically simulate the temporal evolution of a trapped ensemble of atoms, which is initially prepared in $|\uparrow\rangle$. Indeed, the solid red line depicted in figure 2.20 is obtained by integrating the population of all $|F = 3\rangle$ hyperfine levels for each time step from such a numerical simulation. The agreement between the simulation and the measurement is remarkable, especially since all parameters are either fundamental or directly defined by the optical lattice. Furthermore, while the beginning of the population decay can be approximated by an exponential curve, it converges much slower to the equilibrium population. This is related to the fact that cesium is not a two-level system, and instead more back and forth scattering occurs between all hyperfine level. The numerical simulation additionally reveals that if the optical lattice polarization is perpendicular to the quantization axis, all hyperfine level become equally populated. In our specific case an equilibrium is reached after more than 10 s.

While the current state of the experimental apparatus can only probe whether an atom is in $|F = 3\rangle$

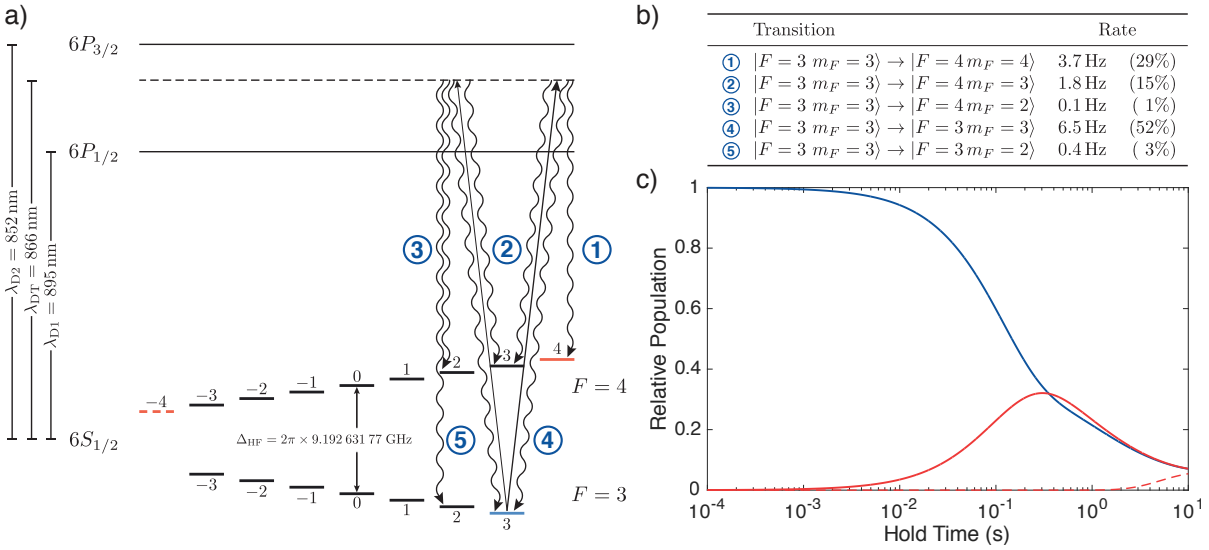

Figure 2.22: **(a)** Ground state hyperfine energy levels of cesium including the D_1 and D_2 transition. The arrows indicate all possible two-photon scattering transitions for an atom in $|\downarrow\rangle$ arising by off-resonantly scattering a photon with the state-dependent optical lattice. **(b)** Individual scattering rates, obtained from the Kramers-Heisenberg formula (see appx. sec. B.4). **(c)** The blue line represents the temporal evolution of a qubit initially prepared in $|\downarrow\rangle$, the red line shows the contribution in $|\uparrow\rangle$, and the red dashed line the contribution in $|F = 4, m_F = -4\rangle$.

or $|F = 4\rangle$, we can now capitalize on the scattering rates to study the temporal evolution of $|\uparrow\rangle$ and $|\downarrow\rangle$. This evolution is shown for $|\uparrow\rangle$ in figure 2.21(c) and for $|\downarrow\rangle$ in figure 2.21(b), respectively. In both cases, scattering events pump atoms initially from one to the other qubit state and eventually diffuse them over all attainable levels. This effect is indicated in both figures by the dashed red line which shows the population in the outermost hyperfine sublevel $|F = 4, m_F = -4\rangle$. The lifetime of our qubit states – defined by the time at which 1 % of an initial state is decayed – amounts to 2.4 ms for $|\uparrow\rangle$ and 1.7 ms for $|\downarrow\rangle$, respectively. This lifetime is two orders of magnitude longer than our average qubit operation (microwave pulses circa 10 µs, state-dependent lattice shifts circa 20 µs), and hence can be neglected for most of the experiments reported in this thesis. However, these results actually put a hard boundary on the long term perspective of experiments based on state-dependent transport of cesium. While it is possible to enhance the fidelity of our qubit operations by reducing the decoherence (as we will see in the following), off-resonant scattering events cannot be prevented unless we change the lattice wavelength, which prevents state-dependent transport, or reduce the dipole potential. The latter is also unfavorable, since it only scales linearly with the intensity of the optical lattice. This brings us back to the discussion at the end of section 2.1.3: The level structure of group III atoms may provide an answer to this dilemma, since they offer the capability to utilize state-dependent transport also for arbitrarily large detunings of the optical lattice. While considerable challenges have to tackled to before such experiments can be realized, this approach is highly promising to realize a one-million-operation quantum cellular automaton with neutral atoms.

2.4.2 The Coherence Relaxation Time T_2

The so-called "Tao of Quantum Computing" [45] is the inherent conflict which all modern quantum optics experiments need to face: we desire a qubit system which couples strongly to coherent external

drives, while at the same time we aspire it to be only weakly coupled to the environment, such that coherences are preserved for long times. Often, the choice of the former also defines the latter. For instance, experiments with ions benefit from the fact that the ions couple strongly to each other through coulomb interaction, however, this interaction cannot be turned off, and hence noisy electric fields from the environment are the prime source of decoherence [204]. Neutral atoms, on the contrary, do not *per se* have a long range interaction. Instead, one can either engineer long range interaction by means of the Rydberg blockade [205, 206], or use short range interactions via cold collisions in combination with Feshbach resonances [207]. We will discuss our first results in the direction of controlled cold collisions between neutral atoms in section 5.1, however, at the moment we will neglect their impact on the decoherence of the qubit.

Our experimental apparatus is tailored to perform experiments based on state-dependent transport. This choice enables a broad spectrum of experiments, however, it also comes at the price of opening up opportunities for the environment to interact with our qubits. In the preceding section we already discussed that both, elastic and inelastic scattering rates, are higher than those of other experiments working with far detuned optical lattices [208]. While inelastic scattering events lead to a population decay, elastic ones induce decoherence since the probability amplitudes differ for the two qubit states. Furthermore, we discussed in section 2.3 that the state-dependent transport requires us to work with magnetic sensitive hyperfine sublevels, and hence our qubit system is sensitive to magnetic field noise from the environment. A comprehensive list of the physical origin of decoherence for experiments with neutral atoms as well as a quantitative estimate can be found in Alberti et al. [189]. In essence, all decoherence sources lead to temporal or spatial varying qubit transition frequencies, which in turn lead to a dephasing. The most dominant source in our experimental apparatus arises from differential light shifts. We discussed in section 2.1.2 that the energy of molasses cooled atoms, trapped in an optical lattice, follow a Boltzmann distribution. Hence, they occupy different vibrational levels, which means that they experience different values of the light intensity (see also eq. (2.2)). We typically distinguish two types of light shifts: scalar and vectorial. The former is caused directly by the hyperfine frequency splitting Δ_{HF} [182], whereas the latter is caused by imperfections of the light polarization [209]. We will discuss in the subsequent section how one can in principle fully negate these effects by cooling the atoms into their vibrational ground state.

Ramsey spectroscopy originates from NMR experiments [210] and has since become the default choice in cold atom experiments to experimentally measure the amount of decoherence [211]. While there exist a variety of different approaches how to measure a Ramsey fringe [212, 213], in our experimental apparatus we make use of the fact that we can scan the phase of the microwave pulse, and hence the rotation axis of the Bloch vector (see sec. 2.3.2). The experimental procedure follows closely the one employed to measure microwave spectra (see sec. 2.3.3). After preparing the ensemble of atoms in $|\uparrow\rangle$, a first microwave square $\pi/2$-pulse creates an equal superposition of $|\uparrow\rangle$ and $|\downarrow\rangle$. The atoms then remain in this superposition state for a defined duration Δt before a second $\pi/2$-pulse is applied. Finally, using the push-out technique, all qubits are projected onto either $|\uparrow\rangle$ or $|\downarrow\rangle$ and the former is removed from the optical lattice. The phase of the microwave allows us now to scan the Ramsey fringe: If we are perfectly resonant and neglecting decoherence we expect that that the second $\pi/2$-pulse in the case of $\phi_{\mathrm{MW}} = 0$ transfers the equal superposition state into $|\downarrow\rangle$, whereas $\phi_{\mathrm{MW}} = \pi$ transfers all atoms back into $|\uparrow\rangle$. Figure 2.23(a) shows the result of such a Ramsey fringe measurement for $\Delta t = 50\,\mu\mathrm{s}$, which results in a contrast of $(95 \pm 1)\,\%$. Furthermore, the phase of the fringe is shifted in comparison to our discussion above. This reveals that the microwave pulse frequency was not exactly on resonance, and hence induced a precession along the equator off the Bloch sphere.

To measure the coherence relaxation time T_2 – defined as the time Δt at which the Ramsey fringe contrast is reduced to 50 % – we repeat the same procedure for increasing times Δt. The measurement

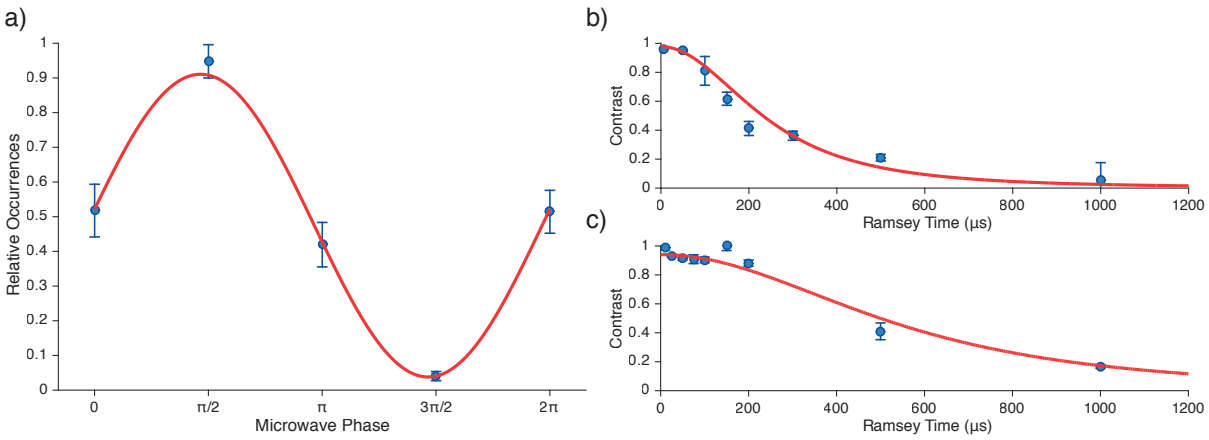

Figure 2.23: **(a)** Ramsey fringe measurement for a Ramsey time of 50 µs between the two $\pi/2-$pulses. **(b)** Coherence time measurement obtained by performing several Ramsey fringe measurements with increasing Ramsey times. The red line represents a fit of the model introduced in Kuhr et al. [212], yielding $T_2 = (240 \pm 20)\,\mu s$. **(c)** Similar coherence time measurement with an additional spin echo pulse in between the two $\pi/2-$pulses, yielding $T_2^{\text{echo}} = (530 \pm 40)\,\mu s$.

results are displayed in figure 2.23(b) together with fit of the model introduced in Kuhr et al. [212]. The fit allows us to extract a coherence time of $T_2 = (240 \pm 20)\,\mu s$, which is in good agreement with the values reported in Karski [53]. Hence, we can infer that our novel polarization-synthesized optical lattice (see chap. 3) does not introduce significantly more decoherence than the previous setup.

It is, furthermore, possible to experimentally distinguish between homogeneous (temporal varying) and inhomogeneous (spatially varying) dephasing decoherence mechanisms using spin echo techniques [210]. If we apply an additional π-pulse after $\Delta t/2$ we can refocus the effect of inhomogeneous dephasing, and hence regain contrast in a Ramsey fringe measurement. Figure 2.23(c) shows the result of such a measurement. As expected, we observe a longer coherence time, which amounts to $T_2^{\text{echo}} = (530 \pm 40)\,\mu s$.

2.5 Three-Dimensional Ground State Cooling in a Blue-Detuned Hollow Beam Dipole Trap

We discussed in the preceding sections that it is desirable to cool the atoms into the vibrational ground state of the optical lattice to enhance their coherence time. Furthermore, the cooling is an indispensable prerequirement for experiments with indistinguishable particles, such as the Hong-Ou-Mandel interference (see chap. 5). In order to cool atoms into – or close to – their vibrational ground state, the state of the art approach consists of either forming a BEC which subsequently undergoes a phase transition into a Mott insulator state [43], or through resolved vibrational sideband cooling. While the former can achieve a nearly unity filled optical lattice where each atom occupies the three dimensional (3D) ground state with a probability of $> 99\,\%$ [40, 61], realizing a Mott insulator state requires substantial experimental effort [214]. The latter, on the contrary, is particular appealing in situations where one wants to cool small ensembles of atoms. It was demonstrated that sideband cooling – for single ions in Paul traps – can achieve 3D ground state occupations of up to 99.9 % [215]. Furthermore, sideband cooling can be utilized to re-cool atoms which may have been heated during an experimental sequence – since it preserves the atoms' positions – whereas recreating a Mott insulator state will always lead to a unity

filled optical lattice, hence, erasing information stored in the atoms' positions.

All resolved sideband cooling techniques use the recoil of optical photons to dissipate the atom's vibrational energy. In the following we will discuss both Raman and microwave sideband cooling as well as how we employ both to achieve an average 3D vibrational ground state occupation of up to 80 %. Both techniques consist of a coherent sideband transition – which lowers the vibrational state – followed by the incoherent scattering of a photon. Hence, it is an inevitable prerequisite that the recoil energy of a scattered photon ($\hbar\omega_{\mathrm{Recoil}}$) is much smaller than the energy spacing of the optical potential ($h\,\nu_{\mathrm{Trap}}$), such that the atoms' vibrational state is preserved in a scattering process [216]. This condition is commonly expressed in terms of the Lamb-Dicke parameter η [204], given by

$$\eta^2 = \frac{\omega_{\mathrm{Recoil}}}{2\pi \times \nu_{\mathrm{Trap}}} \ll 1\,. \tag{2.43}$$

Using the longitudinal and transverse trapping frequencies given in equation (2.5) and (2.6), respectively, we obtain $\{\eta_{\mathrm{L}}^2, \eta_{\mathrm{T}}^2\} = \{0.02, 2.00\}$ for our one dimensional optical lattice. Hence, the transverse confinement is not sufficient to achieve ground state cooling, in fact the confinement is so weak that we would actively heat and not cool the atoms. Increasing the trapping frequencies by simply using more laser intensity is not an option, since the transverse trapping frequency scales only with the square root of the optical power (see eq. (2.6)), whereas the scattering rate due to lattice photons has a linear scaling (see eq. (2.6)). Therefore, we require another approach to increase the atoms' confinement. A blue-detuned hollow laser beam superimposed with the state-dependent optical lattice embodies an elegant solution: Since the atoms are repelled from the light we expect only a marginal difference in the total scattering rate even for high laser intensities of the hollow beam (see sec. 2.5.1). Furthermore, a coinciding hollow beam does not alter the dimensionality of our optical lattice: while a plausible alternative to the hollow beam is a three dimensional optical lattice (see ref. [149]), such a 3D optical lattice would make the 1D experiments presented in this thesis rather time consuming, since atoms would only be rarely trapped in the same line.

2.5.1 The Blue-Detuned Hollow Beam Dipole Trap

Since their first application in 1997 [217] blue-detuned hollow beam dipole traps have been employed in a variety of cold atom experiments [218–225]. While most of these never exceeded proof of principle atom trapping experiments, two realizations stand out from the others: Ozeri et al. [218, 226] characterized the population relaxation time T_1 for various detunings and Li et al. [224] proved for the first time coherent qubit manipulations by performing Ramsey fringe measurements to determine the coherence relaxation time T_2. In the following we will discuss the generation of a hollow beam and its integration in our experimental apparatus. Furthermore, we will study the impact of the combined optical potential – the polarization-synthesized optical lattice (see chap. 3) and the blue-detuned hollow dipole potential – on the qubit properties.

Hollow Beam Generation: There exist several different approaches to generate a hollow laser beam, including cylindrical lens mode converters [227, 228], axicon lens mode converters [219, 229], computer-generated holograms [230, 231], diffractive optics [232], and spiral phase plates (SPP) [233, 234]. in fact, all these techniques have been employed to trap neutral atoms. Since we aspire a strong transverse confinement it is beneficial to adjust the dipole trap's wavelength as close as possible to the atomic resonance. This, however, makes our experiment sensitive to spurious light, since off-resonant scattering events would limit the lifetime of our qubit states substantially (see sec. 2.4.1). Hence, we require a hollow laser beam with a low darkness factor – defined as the ratio between the light intensity at the

center and the intensity at the first surrounding ring [218, 226]. In fact, as we will see in the following, even for a wavelength of $\lambda_{\mathrm{HB}} = 851\,\mathrm{nm}$ – only 1 nm detuned from the cesium D_2 resonance – we still require about 1 W of optical power to attain a Lamb-Dicke parameter of $\eta^2 < 0.1$ – corresponding to $\nu_{\mathrm{T}} = 20\,\mathrm{kHz}$. A hollow beam with these parameters and darkness factor of $1/100$ would lead to a scattering rate of 250 Hz, which is more than one order of magnitude higher than the scattering rate of the optical lattice. Furthermore, 1 W of optical power with $\lambda_{\mathrm{HB}} = 851\,\mathrm{nm}$ at the position of the atoms is close to the limit which one can obtain with commercial laser systems. Hence, we desire low optical losses as the Gaussian beam of the laser system is converted to the hollow beam.

Mode conversion of a Gaussian laser beam using cylindrical lenses is fundamentally impossible, instead it requires a beam with a transverse Hermite-Gaussian mode of order $(1, 0)$. This mode can be obtained by modifying the cavity of the laser source, which however, substantially reduces the available optical power [235]. Mode conversion through an axicon lens in turn can be achieved directly by a Gaussian laser beam, however, the darkness factor is limited to about $1/100$ due to imperfections of axicon lenses [219]. Despite significant technological progress in the recent years, the darkness factor of hollow beams created by computer-generated holograms cannot reach the level of those generated by spiral phase plates [222]. Furthermore, the conversion relies on diffraction, which limits the efficiency at best to circa 80 % [236]. While diffractive optics outperform computer-generated holograms in terms of the efficiency – 93 % efficiency has been reported [232] – they also lack in terms of darkness factor – $1/33$ is the best reported value [232]. On the contrary, spiral phase plates meet both requirements: Phase plates convert > 99 % of a Gaussian into a hollow beam with darkness factors $< 1/1000$ by imprinting an azimuthally dependent phase delay on a plane wavefront [237]. Since the phase is undefined on the optical axis the intensity must be zero in the center [231]. The spiral phase delay is created by passing through an optical element the thickness of which increases around the laser beams propagation axis (see SPP illustration in fig. 2.24). While the manufacturing of optical SPPs via electron beam lithography is still a subject of ongoing research [238], we employ a commercially available SPP[22] which consists of a glass substrate coated with a polymer. The spiral structure is imprinted in the polymer through a lithographic technique with a 2π phase step optimized for a wavelength of 849.9 nm. The discrepancy between the SPP's design wavelength and the employed laser's wavelength of $\lambda_{\mathrm{HB}} = 851\,\mathrm{nm}$ causes a 0.1 % reduction of the topological charge a, defined by:

$$a = \frac{(n_{\mathrm{SPP}} - 1)\, h}{\lambda}\,, \tag{2.44}$$

where n_{SPP} is the refraction index and h the step height of the SPP. A dedicated Master project [239] verified that the darkness factor of the hollow beam is not altered by changes in the topological charge. Furthermore, it was shown that the overall beam profile starts to deform, when the topological charge deviates by more than 10 % from 1, while it remains virtually unchanged for changes around 0.1 %.

Following the path outlined in section 2.1.1 we can estimate the atomic oscillation frequencies of the hollow dipole potential by a harmonic approximation of the intensity distribution. This requires us to estimate the size of the hollow beam at the focal position inside the vacuum chamber. Unlike a Gaussian beam, the SPP generated hollow beam is no longer an eigensolution of the paraxial wave equation [240]. Therefore, in order to calculate the propagation through the focussing telescope, we cannot employ the standard ABCD formalism based on the paraxial Fresnel integral [147]. Instead, we need to use a similar ray propagation formalism for hollow beams, which is based on the Collins integral [240]. After some

[22] RPC Photonics: VPP-1a

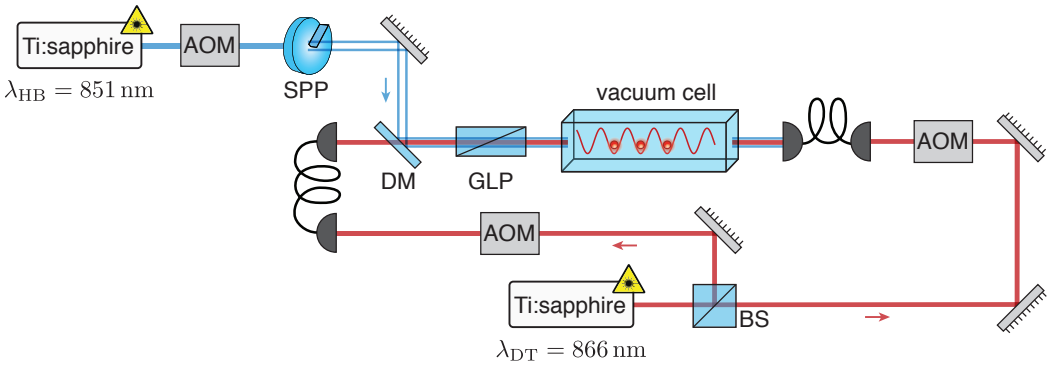

Figure 2.24: Optical setup employed to combine our one dimensional state-dependent optical lattice with the blue-detuned hollow beam dipole trap: the laser beam is generated by an additional Ti:sapphire laser source, the intensity of which is controlled by an intensity lock steering an AOM. The transverse Gaussian beam is transformed into a hollow beam by passing through a spiral phase plate (SPP) and is thereafter overlapped with the optical lattice using a dichroic mirror (DM). The polarization of both overlapped beams is cleaned by passing through an additional Glan-laser polarizer.

calculus we obtain the following expression for the transverse trapping frequencies [239]:

$$\nu_T = \sqrt{\frac{\pi^2 U_0 M^4 w_0^4}{4 m_{Cs} f^4 \lambda_{HB}^4}}, \tag{2.45}$$

where w_0 is the waist of the initial Gaussian beam, M is the magnification, and f the focal length, both determined by the focussing telescope. Using the lens parameters of the employed optics [71], we theoretically expect trapping frequencies on the order of $\nu_T \approx 20\,kHz$, for a detuning of 1 nm, 1 W optical power, and an initial Gaussian waist of 0.8 mm. The strong dependency on the initial waist w_0 – in principle – allows us to realize trapping frequencies on the same order as the longitudinal ones of the optical lattice (circa 100 kHz). However, the already large lens diameter of the employed focussing telescope prevents us from further enlarging the initial beam size.

Integrating the Hollow Beam Dipole Trap: The integration of the blue-detuned hollow beam dipole trap into the existing experimental apparatus is illustrated in figure 2.24: A second Ti-sapphire laser system[23] produces a laser beam with $\lambda_{HB} = 851\,nm$ and delivers up to 4 W optical power. This beam passes through an acousto-optic modulator, which is used to stabilize the optical power by means of an intensity feedback loop similar to the one described in section 2.1.1. A subsequent optical fiber – not shown – acts as a transverse mode filter to create a Gaussian beam, which is then converted into a hollow beam by passing through the SPP. Using a custom made dichroic mirror[24] we superimpose the hollow beam with the state-dependent optical lattice. The orientation of the hollow beam's linear polarization is chosen such that the dichroic mirror reflects around 98 % of the beam, whereas only 80 % of the 866 nm optical lattice laser beam is transmitted. Since the dichroic mirror deteriorates the purity of the linear polarization both beams pass through a Glan-laser polarizer before entering the vacuum chamber.

While small changes in the topological charge leave the intensity profile of the hollow beam virtually unaffected, it is important to align the impinging Gaussian beam precisely to the center of the SPP

[23] Coherent MBR 110 pumped by Coherent Verdi G18
[24] Laser Component: 850 nm: Rs > 97 % Rp > 65 % for 45° AOI; 866 nm: Ts > 60 % Tp > 80 % for 45° AOI

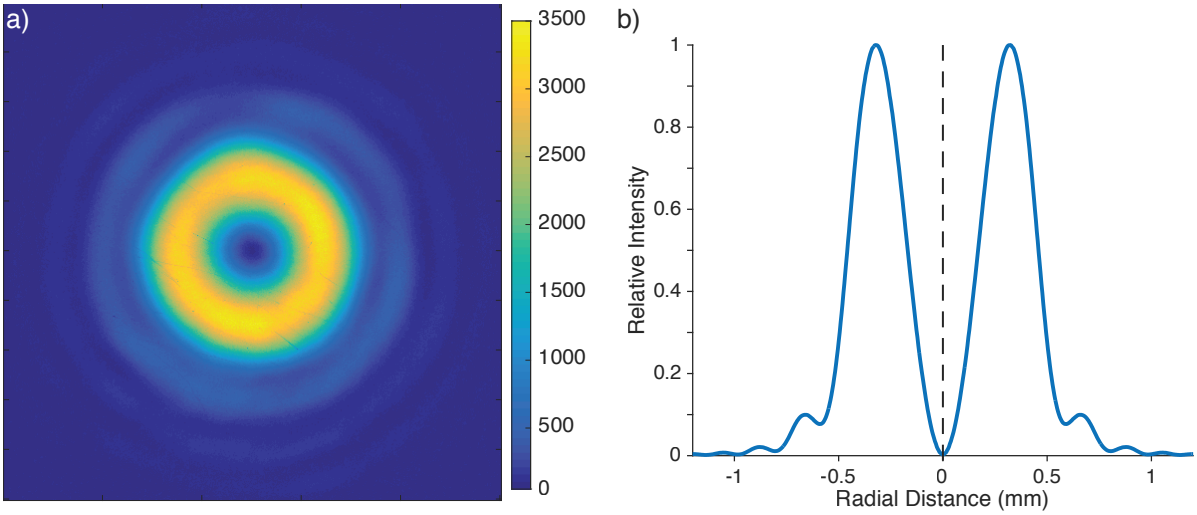

Figure 2.25: **(a)** Beam profile measurement of the hollow laser beam recorded circa 500 mm behind the spiral phase plate. **(b)** Corresponding azimuthally integrated and normalized intensity distribution. For illustration purpose the data is mirrored at the vertically dashed line.

(see Mawardi et al. [239]). For that purpose we temporarily position a CCD beam profiling camera[25] behind the dichroic mirror – about 0.5 m of free propagation – which allows us to monitor the intensity distribution of the hollow beam while aligning the SPP mounted on a precision five-axis translation stage[26]. A typical intensity distribution obtained after alignment is shown in figure 2.25(a) and attests to the desired intensity minima at the center of the beam. In addition, we extract an estimate of the darkness factor from the azimuthally integrated intensity distribution (see fig. 2.25(b)), which amounts to $< 1/450$, limited only by the dynamic range of the beam profiling camera.

The spatial overlap of the optical lattice with the hollow dipole trap is a delicate matter: already a relative angle of 0.001° between the lattice and hollow laser beam translates into a displacement between both optical potentials of 1 µm at the focal position inside the vacuum chamber. Consequently, a non vanishing transverse displacement between these two at the trapping region leads to a combined optical potential which attracts atoms neither to the maximum of the optical lattice nor to the minimum of the hollow dipole trap. While minor relative transverse displacements are expected to noticeably reduce the qubits coherence time through scalar differential light shifts (see sec. 2.4.2), larger deviations significantly increase the atoms scattering rate. These scattering events reduce the qubit lifetime (see sec. 2.4) and can in extreme cases even impact the storage time of trapped atoms. Spatial mode matching of two laser beams is typically achieved by coupling both beams through a single mode optical fiber. This technique, however, cannot be directly employed in this case, since the transverse mode of the hollow beam is orthogonal to the transverse mode which is guided by optical fibers. Instead, we first ensure a spatial overlap of both by iteratively minimizing the relative displacement between both beams in front of and behind the vacuum chamber using the CCD beam profiling camera mentioned above. Once no visual difference of the two beams central position can be detected, we can further optimize the overlap by adjusting the transmission through the optical fiber of the counter-propagating lattice beam to virtually zero. Here, we employ piezoelectric kinematic mirror mounts[27], which allow us to adjust the tilt angles

[25] Ophir: Spiricon LW230
[26] Newport: 9082-M wide five-axis aligner
[27] Radiant Dyes: MDI-H-1" Piezo-Drive

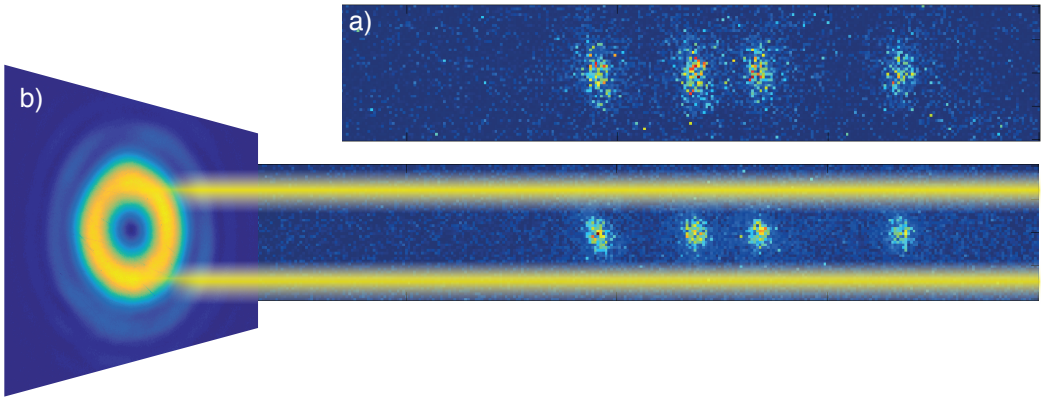

Figure 2.26: Transverse compression of atoms by hollow trap. (a) Without extra transverse confinement, thermal atoms are elongated in the transverse direction (y-axis in the figure). (b) By adding a doughnut-shaped blue-detuned laser beam, the atoms' motion is transversally squeezed. The radius of the round shape is limited by the 1.9 µm optical resolution of the microscope objective lens (NA=0.23). This figure is adapted from Robens et al. [4].

of the hollow beam with a precision of 0.0005°.

We can also make use of the atoms themselves to quantitatively determine final overlap of both optical potentials by recording the fluorescence of atoms which are trapped in the optical lattice, while gradually increasing the intensity of the hollow beam. Figure 2.26(a) exemplarily shows the fluorescence image of four atoms solely trapped by the optical lattice. The intensity distributions of these atoms exhibit a characteristic elliptical shape which arises from the vaguely focussed Gaussian beam (see sec. 2.2). Increasing the hollow dipole trap's intensity, however, decreases the ellipticity since the additional confinement restricts the atoms transverse motion. For the maximum trap depth we expect the extent of the transverse thermal motion to be on the order of 500 nm, which is well below our optical resolution of $r_A = 1.9\,\mu m$. Hence, the intensity distribution of the atoms becomes round when recording a fluorescence image, which is exemplarily shown in figure 2.26(b) for the same group of four atoms. Therefore, if both optical potentials are well overlapped, the vertical position of the atoms remains unchanged with and without the hollow beam dipole trap.

Furthermore, using the blue-detuned hollow dipole trap during fluorescence imaging enables us to shorten the image acquisition time while maintaining the same signal to noise ratio. This is of general interest since acquisition time embodies the bottleneck of all experimental sequences requiring single site detection. The additional confinement of the hollow dipole trap enables a reduction of the acquisition time, since it prevents atoms from hopping along the lattice during imaging even for larger saturation parameters (see sec. 2.2). However, to acquire fluorescence images – such as the one shown in figure 2.26(b) – we need to manually tune the wavelength of the Ti:sapphire laser system a few nanometer further away from the cesium D_2 resonance ($\lambda_{HB} \approx 848\,nm$). Otherwise, stray light arising from reflections of the hollow laser beam is no longer blocked by the interference filter in front of the EMCCD camera. Nevertheless, it is experimentally conceivable to automatize the wavelength scanning for prospective experiments.

Population and Coherence Relaxation Times: In the preceding sections we discussed how to optically verify the purity of the blue-detuned hollow laser beam and concluded that a SPP generated hollow beam should nicely integrate in the existing experimental apparatus. Therefore, it is time that we devote our attention to the properties of the qubits themselves, namely the storage time as well as the population and coherence relaxation times. The required experimental sequences were introduced in

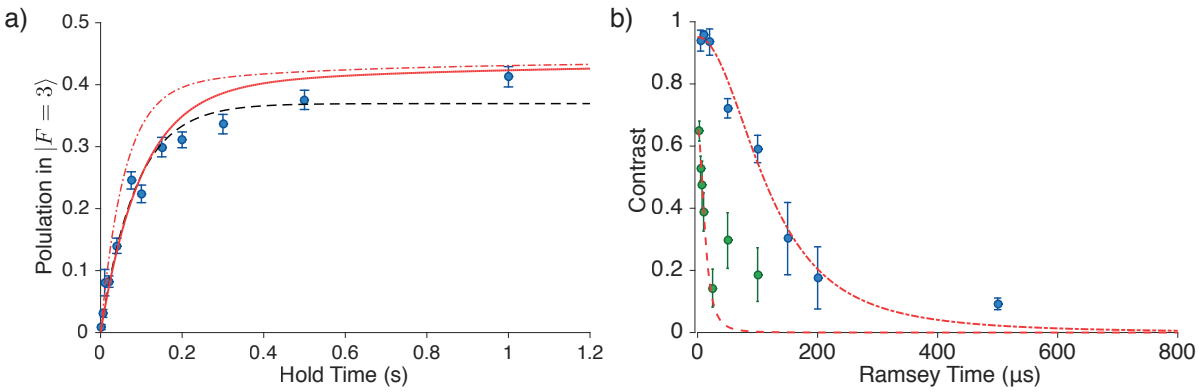

Figure 2.27: **(a)** Population relaxation measurement of atoms which are initialized in $|\uparrow\rangle$ and trapped in the combined optical potential arising from the optical lattice and the hollow beam. The dashed black line represents a fit using the simple model given in equation (2.42). The dashed red line is obtained by numerically simulating the temporal evolution of the $|\uparrow\rangle$ state using calculated scattering rates and a hollow beam darkness factor of 1/1 000, likewise the solid red line for a hollow beam darkness factor of 1/10 000. **(b)** Coherence time measurement obtained by performing several Ramsey fringe measurements with increasing Ramsey times. The green dots represent a measurement of atoms which are only molasses cooled, whereas the blue dots represent a measurement where atoms are partially cooled into their 3D ground state, using the techniques discussed in section 2.5.2. The red lines represent fits of the model introduced in Kuhr et al. [212], yielding $T_2 = (12 \pm 4)\,\mu s$ for the molasses cooled atoms and $T_2 = (115 \pm 15)\,\mu s$ for the partially 3D cooled ones.

section 2.4 and remain mostly the same as before, with the addition that the hollow beam dipole potential is adiabatically raised once the initial fluorescence image is recorded and likewise adiabatically lowered before the state detection.

During the raising of the hollow beam potential, the atoms are stored in the deep lattice potential ($U_0/k_B = 370\,\mu K$) and continuously cooled employing the optical molasses beams (see sec. 2.1.1). While at first sight it might seem irrelevant whether we increase the hollow beam dipole potential when the optical lattice is low or deep, it makes a significant difference for the subsequent ground state cooling: Without the additional transverse confinement the mean transverse vibrational occupation in the optical lattice amounts to $\bar{n}_T \approx 200$. Reducing on average 200 motional quanta to cool an atom into its vibrational ground state is a rather tedious starting point. In comparison, along the longitudinal direction of the optical lattice the mean longitudinal vibrational occupation amounts to $\bar{n}_L < 2$. While molasses cooling in the blue-detuned hollow potential does not reduce the atomic temperature it nevertheless reduces the mean transversal vibrational occupation to $\bar{n}_T \approx 10$. Hence, the strong transversal confinement enables us to remove 95 % of the transverse vibrational excitations, without any additional cooling technique.

The hollow beam must be lowered before the state detection since the push-out technique makes use of radiation pressure forces to push the atoms out of the optical lattice in the transverse direction (see sec. 2.3.1). Hence, a deeper transverse potential would lower the detection efficiency. Prior to the qubit population and coherence relaxation time measurements, we verified that the storage time of atoms in the combined optical potential for a hollow beam detuning of 1 nm and 1 W of optical power remains nearly unaffected (50 % loss storage time $\approx$ 5 s). In fact, if we do not raise the hollow beam intensity adiabatically or if we choose detunings below 1 nm, the scattering rate quickly reduces the storage time to values below 1 s.

Figure 2.27(a) shows population decay of atoms in the $|\uparrow\rangle$ state which are trapped in the combined optical potential as a function of the hold time in between state initialization and detection. The overall

shape resembles the one of the measurements where atoms were trapped solely in the optical lattice (see fig. 2.20). In fact, if we use the simplified exponential model (see eq. (2.42)) to extract the population relaxation time T_1 – represented by the dashed black curve in fig. 2.27(a) – we obtain $T_1 = (86 \pm 12)\,\mathrm{ms}$, which is in good agreement with the value obtained without the additional blue-detuned hollow potential. Furthermore, as outlined above, we can numerically calculate the scattering rates – using the Kramers-Heisenberg formula – for each of the two potentials individually and simulate the temporal evolution of an atomic ensemble prepared in $|\uparrow\rangle$. Here we make the assumption that the hollow beam is not perfectly dark at its center, which is modeled by a homogeneous background (flat-top beam profile, see fig. B.1(c) in appx. sec. B.1). It is noteworthy that possible transversal displacement of the two optical potentials cannot reduce the total scattering rate: while a displacement pushes atoms away from the intensity maximum of the optical lattice, and hence reduces the lattice induced scattering rate, it simultaneously drags atoms away from the hollow beam minima, which consequently increases the total scattering rate. The dashed red line in fig. 2.27(a) represents a numerical simulation with a hollow beam darkness factor of $1/1\,000$ (corresponding to a total scattering rate of $1/\tau = 15\,\mathrm{Hz}$), whereas the solid red line is obtained assuming a darkness factor of $1/10\,000$ (corresponding to a total scattering rate of $1/\tau = 1.5\,\mathrm{Hz}$). These simulations allow us to conclude that the hollow laser beams darkness factor is better than $1/1\,000$, which for itself is a remarkable result and attests the quality at which SPPs can create hollow laser beams. Furthermore, our findings are in good agreement with the T_1 time values reported in Ozeri et al. [218, 226], which obtained a $1/e$ population relaxation time of $T_1 \approx 150\,\mathrm{ms}$ for a hollow beam with a darkness factor of $1/750$.

While the population relaxation time shows great promise for a general application of hollow beam dipole traps in cold atom experiments, the coherence time tells a different story. The green dots shown in figure 2.27(b) represent the remaining fringe contrast obtained from Ramsey fringe measurements for increasing delay times between the two $\pi/2$ pulses (see sec. 2.4.2). Employing the same fit model as before [212] allows us to extract a coherence relaxation time of $T_2 = (12 \pm 4)\,\mu\mathrm{s}$, which is more than one order of magnitude reduced in comparison to the coherence time obtained without the hollow beam dipole potential. In fact, this coherence time is so short that it noticeably reduces the transfer efficiencies of the microwave addressing pulses to circa 85 % for the 10 µs square π-pulse and to circa 50 % for the narrow Gaussian π-pulse, respectively (see tab. 2.5 for comparison). While a full quantitive analysis of this behavior is subject of prospective studies, we can already conclude that the reduction of the coherence time is a result of differential light shifts, since the scattering rate has not increased noticeably. However, decoherence arising from differential light shifts is expected to vanish once atoms are cooled into their 3D vibrational ground state. Therefore, we repeated the coherence time measurement with atoms whose average transverse vibrational occupation was lowered to $\bar{n}_\mathrm{T} \approx 1$ using the sideband cooling techniques introduced in the following section. The result of this measurement is represented by the blue dots shown in figure 2.27(b) and the corresponding coherence time amounts to $T_2 = (115 \pm 15)\,\mu\mathrm{s}$. While the coherence time is still shorter compared to the situation where atoms are solely trapped by the optical lattice, it is sufficient to bring the microwave transfer efficiencies well above 90 %. Furthermore, we will see in the following that we can reach an average transverse vibrational occupation of $\bar{n}_\mathrm{T} < 0.25$, which should further increase the qubits coherence time. We also repeated the spin echo measurement for the sideband cooled ensemble which is trapped in the combined optical potential (data not shown) yielding a coherence time of $T_2^{\mathrm{echo}} = (340 \pm 50)\,\mu\mathrm{s}$. Unfortunately a direct comparison with the values reported in Li et al. [224] is not possible. While they also used cesium atoms, in their case, the hollow beam was 320 nm blue detuned from the cesium D_2 resonance and the qubit encoded in the clock states ($|F = 4, m_F = 0\rangle$ and $|F = 3, m_F = 0\rangle$). The far off resonance dipole trap reduces the decoherence due to the hyperfine splitting almost entirely (scalar differential light shift, see also sec. 2.4.2), whereas the clock states are only sensitive to magnetic field noise due to the quadratic Zeeman shift. Using these

parameters Li et al. [224] obtained a $1/e$ coherence time of $T_2 = 43\,\mathrm{ms}$, which is comparable to other experiments using cesium clock states.

2.5.2 Vibrational Ground State Cooling

We introduced in section 2.5 that both, Raman and microwave, sideband cooling techniques require a coherent sideband transition, which lowers the vibrational state by one quantum, $|\uparrow, n\rangle \leftrightarrow |\downarrow, n-1\rangle$. Furthermore, we introduced in section 2.5 the Lamb-Dicke parameter η and identified the condition $\eta^2 \ll 1$ as one of the prerequisites of resolved-sideband cooling. Hence, it comes at no surprise that sideband cooling using a coherent two-photon transition was first realized for single ions in Paul traps where trapping frequencies of up to 10 MHz can be engineered [241]. Nevertheless, only a few years later different groups achieved almost simultaneously sideband cooling of neutral atoms trapped in an optical lattice [242–244], which has since become a standard tool in cold atom experiments [245–249].

Coherent two-photon transitions are an alternative technique to drive the qubit transition. However, in contrast to microwave radiation, two-photon transitions can directly change the vibrational state of an atom due to the larger momentum of optical photons, as we will see in the following. To experimentally realize coherent two-photon Raman transitions we illuminate the atoms with two off-resonant laser beams (one π-, the other σ^+-polarized), the relative frequency difference of which corresponds to precisely the qubit transition frequency of 9.2 GHz. Consequently, the two qubit states are coupled by these laser beams through a virtual excited level, which is illustrated in figure 2.28(a). If the laser frequencies are detuned far enough from the atomic resonance – typically on the order of 100 GHz – the effective qubit Raman-Rabi frequency amounts to:

$$\Omega_\mathrm{R} = \frac{\Omega_\pi\,\Omega_{\sigma^+}}{2\Delta_\mathrm{R}}\,, \tag{2.46}$$

where Δ_R is laser detuning, and Ω_{π/σ^+} the single-photon Rabi frequencies of the resonant optical transition, induced by the π/σ^+ polarized laser beam. Despite the fact that we are driving the system through a third, intermediate state, we can reduce the Hilbert space to an effective two-level system the dynamics of which is again described by the optical Bloch equations introduced in section 2.3.2.

In addition to coupling the two qubit states, Raman two-photon transitions give us a tool to couple two specific vibrational levels by adjusting the relative laser frequency difference $\Delta\nu$. If we set $\Delta\nu$ exactly to the qubit transition frequency we drive the so-called carrier transition $|\uparrow, n\rangle \leftrightarrow |\downarrow, n\rangle$, which – similar to the coupling via microwave radiation as discussed in section 2.3.2 – preserves the vibrational state of our atoms. On the contrary, if we detune $\Delta\nu$ from the qubit transition resonance by the longitudinal trapping frequency ($\pm\nu_\mathrm{L}$), or by the transverse trapping frequency ($\pm\nu_\mathrm{T}$) we can couple two adjacent vibrational levels $|\uparrow, n_\mathrm{L/T}\rangle \leftrightarrow |\downarrow, n_\mathrm{L/T} \pm 1\rangle$, which is commonly referred to as a sideband transition.

At this point it is reasonable to ask whether Raman lasers allow us to couple vibrational levels in any spatial direction of a three dimensional trap – specifically, in our case, along the longitudinal and two transverse directions of the optical lattice. The answer is: in principle yes, but it depends on the orientation of the momentum which is exchanged in the two-photon process. We can gain more insight by recalling that the eigenfunctions of the quantum harmonic oscillator are orthogonal and consequently the overlap integral of two different vibrational level (n and n') amounts to zero: $\langle\uparrow, n\,|\,\downarrow, n'\rangle = 0$, for $n \neq n'$. Therefore, to couple adjacent vibrational levels we seek an operator which breaks this orthogonality such that the overlap integral differs from zero. In the case of the two-photon transition induced by the Raman lasers this operator is given by the momentum shift operator:

$$T_{\Delta k}^{\mathrm{Raman}} = e^{i\vec{x}\Delta\vec{k}}\,, \tag{2.47}$$

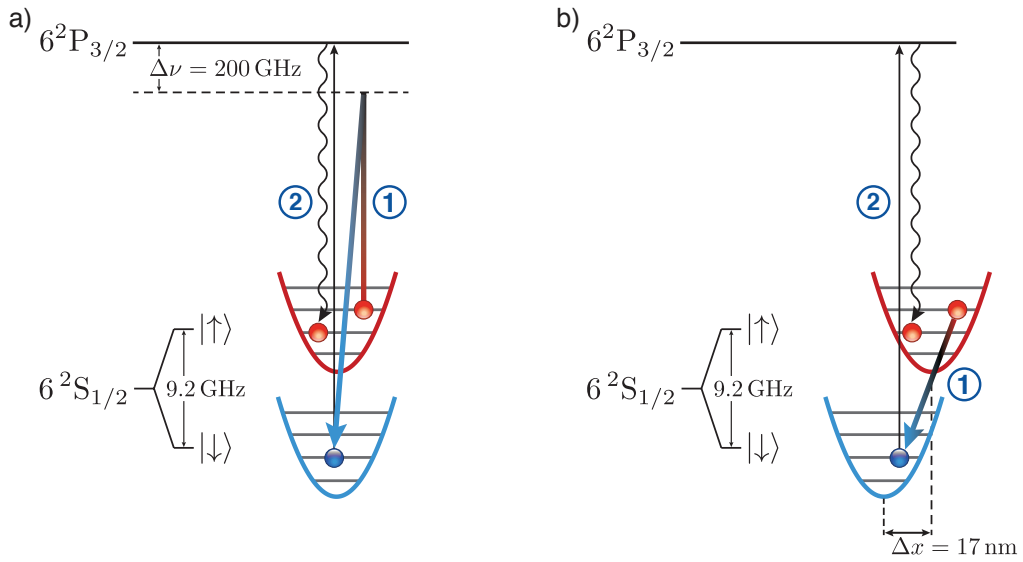

Figure 2.28: Side by side comparison of the Raman and microwave sideband cooling cycle: **(a)** A two-photon Raman transition (1) lowers the vibrational state by one quantum, $|\uparrow, n\rangle \rightarrow |\downarrow, n-1\rangle$. Subsequently the atom is transferred back into the $|\uparrow\rangle$ state through an on-resonant scattering process (2). **(b)** Since the momentum transferred by a single microwave photon is not sufficient to enable sideband transitions, we instead utilize spatially shifted potentials (see sec. 2.5.2) to drive a coherent sideband transition, which lowers the vibrational state by one quantum (1). The consecutive on-resonant scattering process (2) likewise transfers the atom back into the $|\uparrow\rangle$ state.

where Δk is the wave vector difference between the two optical photons. Hence, choosing the orientation of Δk enables us to drive sideband transitions in any desired spatial direction of the optical potential. For example, if we choose two co-propagating Raman-laser beams which are overlapped with the optical lattice, Δk is also oriented along the lattice, and hence the two-photon transition can only couple longitudinal vibrational levels. For our application we align one laser collinear with and the other perpendicular to the optical lattice (see also fig. 2.30). This way, as we will see in the following, Δk has a projection onto all spatial directions, and hence it is possible to achieve 3D ground state cooling with a single pair of Raman lasers.

The connection between coupling vibrational levels and the momentum shift operator allows us also to understand why we don't see longitudinal or transversal sideband transitions in our microwave spectra (see sec. 2.3.3), despite the fact that the spectral resolution of these pulses is high enough to resolve vibrational transitions. The momentum transferred from a single microwave photon is so small that the corresponding momentum shift operator effectively does not break the orthogonality of the wave functions, and hence:

$$\langle\uparrow, n|\, T_{\Delta k}^{\mathrm{MW}}\, |\downarrow, n'\rangle \approx 0\,. \tag{2.48}$$

However, from an experimental point of view it would be highly desirable to couple vibrational levels with microwave radiation, simply because microwave generators have proven to be extremely reliable, whereas even state of the art Raman lasers require almost daily maintenance. From a mathematical point of view, the solution is intriguingly simple: instead of using the momentum shift operator $T_{\Delta k}$ we can use the position translation operator $T_{\Delta x}$ to achieve a non-zero overlap of the wave functions:

$$I_n^{n'}(\Delta x) = \langle\uparrow, n|\, T_{\Delta x}\, |\downarrow, n'\rangle\,, \tag{2.49}$$

where the coupling strength $I_n^{n'}$ between two vibrational levels is commonly referred to as the Franck-Condon factor, in analogy to molecular physics [250]. Hence, instead of exchanging momentum through an optical photon, potential energy is exchanged through a spatial translation. To experimentally realize a position translation operator we need to spatially separate the potential minima of the $|\uparrow\rangle$ and $|\downarrow\rangle$ state, such that when we change the atoms qubit state from $|\uparrow\rangle$ to $|\downarrow\rangle$ the atom correspondingly changes its position, which is illustrated in figure 2.28(b). In general, such a state-dependent displacement is experimentally not straightforward. In fact, although this concept was theoretically already proposed in 1997 [251], it took more than ten years before it could be realized for single ions in Paul traps using strong magnetic field gradients [198], or for neutral atoms in optical lattices by our group using state-dependent transport [245]. Indeed, our state-dependent optical potentials are an ideal tool, allowing us to adjust the spatial displacement Δx with subnanometer precision, which in turn, gives a precise control of the coupling strength $I_n^{n'}(\Delta x)$. A rigorous analysis based on the Lindblad master equation formalism can be found in Belmechri et al. [252], which concludes that the ideal displacement for ground state cooling amounts to $\Delta x \approx 17\,\mathrm{nm}$.

By now we have seen that it is possible to coherently couple vibrational levels using either microwave radiation or a pair of Raman lasers, which allows us to drive a transition between adjacent vibrational levels of a trapped atom: $|\uparrow, n\rangle \leftrightarrow |\downarrow, n-1\rangle$. However, it is not possible to cool atoms into their vibrational ground state relying purely on coherent operations, since these operations – by definition – cannot remove entropy from the system. Hence, we make use of a photon scattering process – for both Raman and microwave cooling – which closes the cooling cycle by transferring atoms back into the $|\uparrow\rangle$ state, as illustrated in figure 2.28(a) for the Raman cooling scheme and in figure 2.28(b) for the microwave cooling scheme, respectively. This photon scattering process is induced by illuminating the atoms with σ^+ polarized laser light from the repumping laser, which is resonant with the $|F = 3\rangle \rightarrow |F' = 4\rangle$ transition (see sec. 2.1.1). Each cooling cycle removes one vibrational quantum from the atom until it reaches the $|\uparrow, 0\rangle$ state, where it is decoupled from the coherent transition. Thus, in the absence of a competing heating mechanism, all atoms will eventually accumulate in the ground state, which is the dark state of the cooling process [204]. However, in our experimental apparatus several heating mechanisms simultaneously pump atoms out of the dark state, and hence it is impossible for us to cool 100 % of the atoms in their vibrational ground state, which we will discuss in section 2.5.2.

In the following we will discuss separately the experimental results achieved employing microwave sideband cooling to cool the vibrational excitations along the longitudinal direction and Raman sideband cooling to cool the excitations along both transversal directions of cesium atoms which are trapped in the combined potential of the optical lattice and the blue-detuned hollow dipole potential.

Longitudinal Vibrational Microwave Cooling

Cooling the longitudinal vibrational excitations has been routinely employed in our laboratory since the first demonstration reported in Förster et al. [245]. To experimentally implement the cooling scheme depicted in figure 2.28(b), we first shift the σ^+ polarized lattice 17 nm apart from the σ^- polarized lattice using a 1 ms long adiabatic transport operation (see chap. 3 for more information on the transport). Then, we concurrently apply microwave radiation, which is resonant with the cooling sideband transition $|\uparrow, n\rangle \leftrightarrow |\downarrow, n-1\rangle$, and both F- and m_F-state pumping light (see sec. 2.3.1). So far we omitted the m_F-state pumping light in the cooling scheme. The light is required to pump atoms back into the cooling cycle which were transferred into a hyperfine sublevel other than $|\uparrow\rangle$ or $|\downarrow\rangle$, through off-resonant Raman scattering processes. The equilibrium vibrational distribution is typically achieved after 20 ms, whereupon we adiabatically shift the σ^+ lattice back, such that both lattices are again perfectly overlapped.

In order to probe the equilibrium vibrational state distribution, we perform sideband spectroscopy.

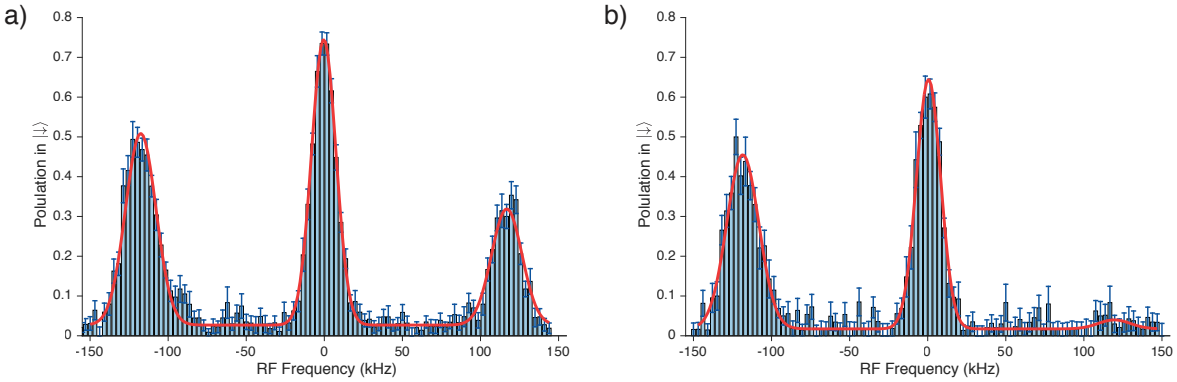

Figure 2.29: Microwave sideband spectrum of an ensemble of atoms, which is only molasses cooled **(a)** and of an ensemble, which is cooled close to the vibrational 3D ground state **(b)** by applying multiple iterations of both microwave and Raman sideband cooling as depicted in figure 2.31. The asymmetry of the cooling and heating sideband transition heights allows us to infer a longitudinal ground state occupation of $n_0^{\mathrm{L}} = (39 \pm 4)\,\%$ for the molasses cooled atoms and $n_0^{\mathrm{L}} = (95 \pm 3)\,\%$ for the 3D cooled ones.

Table 2.6: Summary of the obtained mean longitudinal vibrational occupations $\bar{n}^{\mathrm{L}}$ and corresponding ground state populations n_0^{L} employing microwave sideband cooling with different cooling sequences.

Cooling technique	$\bar{n}^{\mathrm{L}}$	n_0^{L}
Molasses cooling	(1.50 ± 0.20)	$(39 \pm 4)\,\%$
1D microwave sideband cooling [1]	(0.01 ± 0.01)	$(99 \pm 1)\,\%$
3D sideband cooling	(0.05 ± 0.03)	$(95 \pm 3)\,\%$

Sideband spectroscopy is technically equivalent to microwave spectroscopy, which we discussed in section 2.3.3, with the addition that we shift the two state-dependent lattices apart prior to applying a microwave π-pulse. The histogram displayed in figure 2.29(a) exemplarily depicts a measured microwave sideband spectrum of thermal atoms, trapped in our optical lattice, which are cooled using only the molasses cooling introduced insection 2.1.1. The three visible peaks correspond to the heating sideband transition $|\uparrow, n\rangle \rightarrow |\downarrow, n+1\rangle$, the carrier sideband transition $|\uparrow, n\rangle \rightarrow |\downarrow, n\rangle$, and cooling sideband transition $|\uparrow, n\rangle \rightarrow |\downarrow, n-1\rangle$, respectively. This measurement allows us to extract the longitudinal oscillation frequency of our optical lattice by performing a non-linear least squares fit to the measured data, the result of which is represented by the red line in figure 2.29(a). The resulting longitudinal trapping frequency amounts to $\nu_{\mathrm{L}} = (117.2 \pm 0.4)\,\mathrm{kHz}$, which is in good agreement with the theoretical value of $\nu_{\mathrm{L}}^{\mathrm{Theo}} = 110\,\mathrm{kHz}$ obtained from equation (2.5).

The histogram displayed in figure 2.29(b), on the contrary, shows a sideband spectrum, obtained after applying multiple iterations of both microwave and Raman sideband cooling to cool the atoms into their 3D ground state. The experimental details of this 3D cooling sequence are depicted in figure 2.31 and introduced in more detail in the following section. While the microwave sideband spectrum shown in figure 2.29(a) shows only a slight asymmetry in the height of the cooling and heating sideband, the sideband spectrum obtained after ground state cooling (see fig. 2.29(b)) shows almost no sign of the cooling sideband. In fact, this is precisely what we expect, since in the case where all atoms were successfully cooled into the $|\uparrow, 0\rangle$ state, there is no transition into the $|\downarrow\rangle$ state, which further lowers the vibrational quantum number. Additionally, the asymmetry of the peak heights allows us to extract the

fraction of atoms which resides in the vibrational ground state [204]:

$$R_{\mathrm{Sb}} = \frac{h_{\mathrm{CSb}}}{h_{\mathrm{HSb}}}\,, \tag{2.50}$$

where h_{CSb} is the height of the cooling sideband and h_{HSb} is the height of the heating sideband. Assuming that the vibrational states are distributed according to a thermal Boltzmann distribution and that we can neglect effects from the anharmonicity of the optical lattice – which certainly holds true for the lowest vibrational states – the following expression for the mean vibrational occupation is obtained [204]:

$$\bar{n} = \frac{R_{\mathrm{Sb}}}{1 - R_{\mathrm{Sb}}}\,. \tag{2.51}$$

There exist several other techniques how to extract the mean vibrational state occupation [97–102], however, this method is particularly convenient since it is independent of the pulse duration, the carrier Rabi frequency, and the Lamb-Dicke parameter [253]. The mean vibrational occupation $\bar{n}$ in turn allows us to determine the ground state population, according to:

$$n_0 = \frac{1}{1 + \bar{n}}\,. \tag{2.52}$$

Using the non-linear least squares fit allows us to extract the occupations for both the molasses cooled and the sideband cooled spectrum, which are summarized in table 2.6. It is noteworthy that we achieve mean longitudinal ground state occupations of up to $n_0^{\mathrm{L}} = 99\,\%$ [1] if we omit the transverse Raman sideband cooling, which is also in agreement with the theoretical prediction given in Belmechri et al. [252]. Hence, for completeness, table 2.6 comprises the values obtained employing exclusively 1D microwave sideband cooling.

Transverse Vibrational Raman Cooling

Since we cannot induce a state-dependent potential displacement in the direction which is transverse to the optical lattice, we here employ Raman sideband cooling. Hence, we need to incorporate additional laser beams into the optical setup. As depicted in figure 2.30, we use a single pair of Raman beams – one collinear with and the other perpendicular to the optical lattice – to cool both transverse directions according to the Raman cooling scheme depicted in figure 2.28(b). The collinear beam shares the optical path with the F- and m_F-state pumping beams, ensuring a circular polarization purity of $\Pi > 20\,000$[28], which hence, induces a σ^+ transition for the atoms. The perpendicular beam impinging from the top is also circular polarized, however, due to the orientation of the quantization axis, this light induces σ^+, π, and σ^- transitions. Nevertheless, only the π component leads to the desired two-photon Raman transition, whereas the other two components have no effect besides slightly increasing the off-resonant scattering rate. More details on the optical setup can be found in Boventer [104]. We achieve simultaneous cooling in both transverse directions by exploiting a slight ellipticity of the hollow beam dipole trap, which ensures vibrational coupling between the two transverse directions, so that the momentum transfer provided along a single direction by the Raman transition suffices to cool the atomic motion in both transverse directions (see inset of figure 2.30). Since the ellipticity of the hollow beam is only on the order of a few percent, likewise the trapping frequencies will differ by about 1 kHz. This frequency difference is enough to lift the degeneracy of the transverse trapping frequencies, however, it is not large enough to spectroscopically resolve the two orthogonal directions individually. Instead when performing

[28] The purity is defined as the ratio of σ^+/σ^- polarized light, for more details see [180]

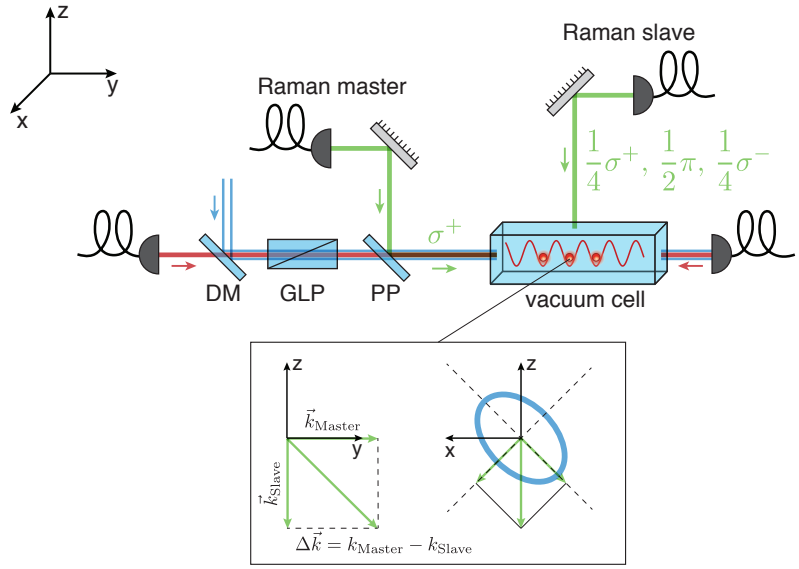

Figure 2.30: Optical setup to incorporate the two phase locked Raman lasers into the experimental apparatus: The Raman master laser shares the optical path with the F- and m_F-state pumping beams and is, hence, overlapped with the optical lattice and the hollow laser beam using a pickup plate (PP). The Raman slave laser beam impinges from the top and partially shares the optical path with the z-axis molasses beam. Consequently the beam is circular polarized. The inset visualizes the momentum transferred onto an atom which undergoes a two-photon Raman transition. The orientation of the hollow beam ellipticity – exaggeratedly drawn for illustrational purposes – enables momentum transfer along both vibrational directions.

sideband spectroscopy, we expect to see a combined peak for both transverse sideband transitions, the FWHM of which increases with the order of the sideband transition [204].

A natural prerequisite for sideband cooling is an accurate knowledge of the trap oscillation frequencies. If the frequency difference of the Raman lasers is not exactly tuned to the cooling sideband transition, we not only lower the cooling rate, but also increase the likeliness to induce an off-resonant heating transition. Hence, following the procedure outlined above, one could attempt to extract the transversal trapping frequencies by performing sideband spectroscopy on an ensemble of atoms cooled only using the molasses lasers. However, as shown in figure 2.32(a), if we perform sideband spectroscopy on purely molasses cooled atoms we observe only a single broad peak independent of the Raman-Rabi frequency. This does not come as a surprise: we have seen in section 2.5.1, that the additional hollow beam confinement leads to strong decoherence, which in turn broadens the individual sideband transitions to a point where no individual transitions can be spectrally distinguished. Figure 2.32(a) shows the sideband spectrum obtained by applying a 3 ms long Raman pulse. Contrary to microwave sideband spectroscopy, where we carefully adjusted the pulse such that it suffices the π-pulse condition, the Raman pulse length is much longer than the coherence time T_2, but still sufficiently shorter than population relaxation time T_1, which creates a statistical mixture of $|\uparrow\rangle$ and $|\downarrow\rangle$ with equal probability – in the case where the frequency difference of the Raman lasers is in resonance with the carrier transition. From an experimental point of view, choosing such a long pulse is advantageous, since it allows to perform sideband spectroscopy without precisely characterizing the Raman-Rabi frequency in advance.

In order to circumvent the problem, that we cannot resolve the transversal sidebands in an purely molasses cooled atomic ensemble, we employ unresolved sideband cooling [243] prior to the Raman

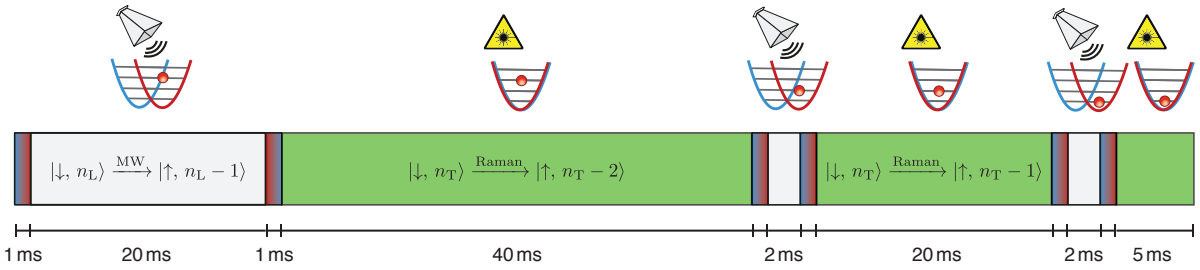

Figure 2.31: Experimental sequence employed to achieve 3D ground state cooling: The red-blue gradient symbolizes a transport operation which separates/recombines the two optical potentials by 17 nm. The grey shaded areas correspond to longitudinal microwave sideband cooling, whereas the green ones correspond to transverse Raman sideband cooling, respectively. The first 20 ms long microwave cooling sequence also initializes all atoms in $|\uparrow\rangle$. The first Raman cooling sequence drives second order transitions to remove two vibrational quanta in one cooling cycle.

sideband spectroscopy pulse. Unresolved sideband cooling means, that we use the theoretical estimate of the transversal trapping frequencies obtained from equation (2.45) and sweep the frequency difference of the Raman lasers a few kilohertz around this estimate for 40 ms. This technique cools atoms close enough to the ground state, allowing us to extract the experimental transversal trapping frequencies (spectrum not shown), which in turn can be used for resolved sideband cooling.

Knowing both, the longitudinal and transverse trapping frequencies, we can now cool atoms which are trapped in the combined potential of the optical lattice and the blue-detuned hollow dipole potential into their 3D vibrational ground state. A natural first guess would be to sequentially cool the atoms first into the longitudinal ground state using microwave sideband cooling and then into the transverse ground state using Raman sideband cooling. However, since we occasionally create an excitation in the uncooled direction either by off-resonant photon scattering or by heating from the optical lattice (see sec. 2.5.2), we need to go through several iterations of both cooling techniques, with decreasing durations, as illustrated in figure 2.31. Furthermore, we estimated in section 2.5.1, that we need to cool on average 10 transverse excitations, before the atoms reach the ground state. Hence, as depicted in figure 2.31, we first drive second order cooling transitions which lower the transverse vibrational state by two quanta per cycle, instead of by only one.

The histogram depicted in figure 2.32(b) shows the transverse spectrum obtained after applying the 3D cooling sequence shown in figure 2.31. In contrast to the sideband spectrum shown in figure 2.32(a), we now can clearly resolve the peaks of individual sideband transitions. Using a simplified fit model – consisting of several Gaussian functions – in combination with equation (2.52) and equation (2.51) allows us to extract the mean transverse vibrational occupation, which amounts to $\bar{n}^T = (0.07 \pm 0.04)$, and the corresponding transverse ground state population, which amounts to $n_0^T = (94 \pm 4)\,\%$ – for each of the two transverse directions. Combining this result with the one obtained from longitudinal sideband spectroscopy, reported in the preceding section, allows us to conclude that we can cool individual atoms into their 3D vibrational ground state with a success rate n_0^{3D} of up to 80 % (see also tab. 2.7). Furthermore, using the simplified fit model also allows us to extract a transverse trapping frequency yielding $\nu_T = (19.9 \pm 0.4)\,\text{kHz}$, which is in good agreement with the theoretical value of $\nu_T^{Theo} = 20\,\text{kHz}$ obtained from equation (2.45). It is noteworthy, that the spectrum depicted in figure 2.32(b), represents our record in terms of 3D ground state cooling for the experimental apparatus at hand. More commonly, we achieve transverse ground state cooling with a mean vibrational occupation of $\bar{n}^T = 0.25$, which corresponds to a ground state population of $n_0^T = 80\,\%$. In the following section we use a simplified

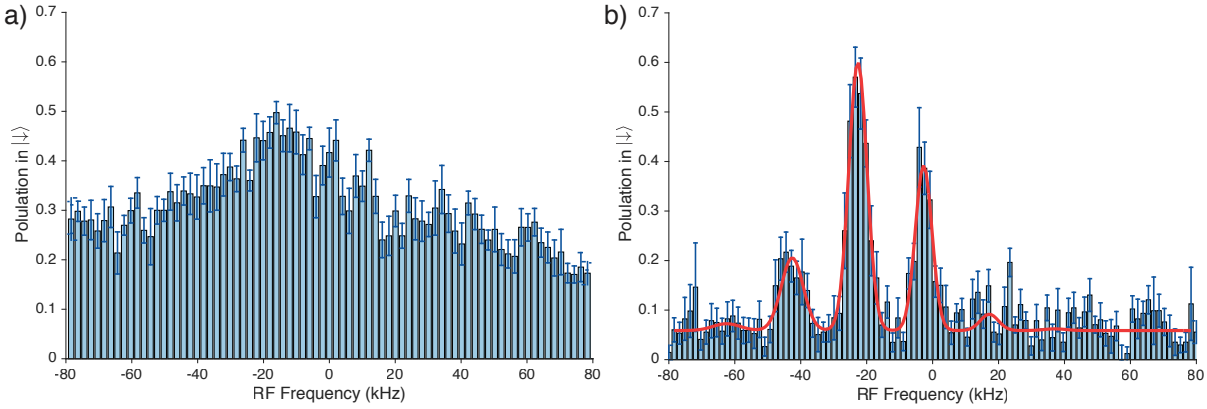

Figure 2.32: Raman sideband spectrum of an ensemble of atoms, **(a)** which is only molasses cooled and of an ensemble, **(b)** which is cooled close to the vibrational 3D ground state by applying multiple iterations of both microwave and Raman sideband cooling as depicted in figure 2.31. Without sideband cooling, decoherence broadens individual transitions to a point where basically no features can be observed. The asymmetry of the cooling and heating sideband transition heights allows us to infer a transverse ground state occupation of $n_0^{\mathrm{T}} = (94 \pm 4)\,\%$ for the 3D cooled atoms.

Table 2.7: Summary of the obtained mean vibrational occupations $\bar{n}^{\mathrm{L}}$ and corresponding ground state populations n_0^{L} employing microwave sideband cooling along the longitudinal direction and Raman sideband cooling along the transverse direction, respectively. It is noteworthy, that the values for the Raman sideband cooling represent our record in terms of 3D ground state cooling for the experimental apparatus at hand. More commonly, we achieve transverse ground state cooling with a mean vibrational occupation of $\bar{n}^{\mathrm{T}} = 0.25$ and correspondingly $n_0^{\mathrm{T}} = 80\,\%$.

	Mean vibrational occupation	Ground state population
Longitudinal	$\bar{n}^{\mathrm{L}} = (0.05 \pm 0.03)$	$n_0^{\mathrm{L}} = (95 \pm 3)\,\%$
Transverse	$\bar{n}^{\mathrm{T}} = (0.07 \pm 0.04)$	$n_0^{\mathrm{T}} = (94 \pm 4)\,\%$
3D	-	$n_0^{\mathrm{3D}} = n_0^{\mathrm{L}}(n_0^{\mathrm{T}})^2 = (84 \pm 4)\,\%$

model of the cooling and heating processes occurring during the ground state cooling to quantitatively estimate the maximal attainable mean ground state occupation, as well as the lifetime of atoms which were successfully cooled into their 3D ground state.

The carrier transition in figure 2.32(b) is spectrally well resolved with a FWHM of $(5.8 \pm 0.6)\,\mathrm{kHz}$, which in itself attests an enhancement of the coherence time. By performing a non-linear least squares fit of a simulated spectrum – obtained by numerically solving the Bloch equations (see eq. (2.37)-(2.39)) – to the measured carrier transition, we extract an estimate of both the Raman-Rabi frequency and the coherence time T_2, which amount to $\Omega_{\mathrm{R}} = (1.0 \pm 0.4)\,\mathrm{kHz}$ and $T_2 = (700 \pm 400)\,\mu\mathrm{s}$. In fact, the ratio between the cooling Rabi frequency and the trapping frequency is chosen such that we achieve a maximal cooling rate while simultaneously keeping the rate of off-resonant carrier or even heating sideband transitions at a minimum, which we will discuss in more detail in the following section. Furthermore, our Raman-Rabi frequency agrees well with the cooling Rabi frequencies typically chosen by other experiments, which are about one order of magnitude smaller than the trapping frequencies [245–249].

A cooling Rabi frequency on the order of only a few kilohertz unfortunately increases the sensitivity of the cooling efficiency to small magnetic field fluctuations. In particular magnetic field fluctuations arising from the power line frequency (50 Hz) can easily shift the qubit carrier transition frequency by a few

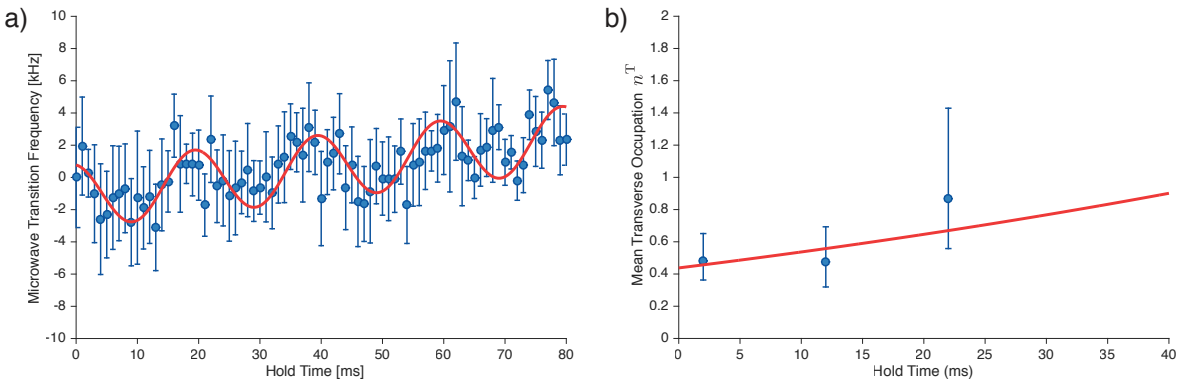

Figure 2.33: **(a)** Carrier transition frequency as a function of time. The periodic dependency of the transition frequency is caused by magnetic field fluctuations arising from the 50 Hz oscillation of the power line. The small linear drift arises from a long settling time of our magnetic coils, which generate the quantization axis. The large uncertainty on individual measurements is not intrinsic, but a consequence of choosing few repetitions. **(b)** Transverse heating rate measurement of atoms which are cooled close to their vibrational ground state. The mean transverse occupation is obtained from individual sideband spectra with increasing hold times between cooling and detection. The red line represents a fit of a simple exponential model to the measured data.

kilohertz, which hence, would significantly lower the cooling rate. In order to measure these fluctuations we perform spectrally narrow microwave spectroscopy and extract the carrier transition frequency for increasing hold times, which is summarized in the graph shown in figure 2.33(a). As expected we observe a signal with a 20 ms periodicity and a peak to peak amplitude of 4 kHz[29]. This calibration, in turn, allows us to employ feed forward control by modulating the frequency difference of the Raman lasers during the cooling process. All experiments presented within this thesis, which rely on sideband cooling, were obtained using this feed forward control method.

Cooling Limitations and Ground State Lifetime

The experimental results from the preceding sections attest that we can achieve a significant 3D ground state occupation, however, we are still considerably far away from reaching 100 %. In the following we will first obtain an estimate of the cooling rate based on a simplified model, which we then extend by incorporating all relevant sources of heating. Furthermore, some of these heating processes not only occur during the cooling process. These heating processes, hence, will determine the lifetime of the ground state, which we can also measure experimentally.

A theoretical prediction of the final vibrational state of an ensemble of atoms which is cooled via sideband cooling can be obtained following a similar route as presented in [254] where the interaction Hamiltonian is inserted into the master equation and solved numerically. However, since each cooling cycle consists of a coherent sideband transition – either Raman or microwave – followed by a repumping event, which involves spontaneous emission, coherences typically don't play a significant role. Thus, the problem can be approximately solved using rate equations [204]. Furthermore, we experimentally verified, that we achieve a significant ground state occupation. Hence we can even further simplify the calculation by restricting the rate equations to the lowest two vibrational levels. In the absence of technical heating mechanism, it can be shown that the minimal mean vibrational occupation $\bar{n}$ is limited

[29] We repeated the power line magnetic field fluctuation measurement several times over a timespan of 2 months without noticing a significant deviation from the curve presented in figure 2.33(a)

by off-resonant carrier and heating-sideband excitations [204], in which case $\bar{n}$ is given by:

$$\bar{n} \approx \left(\frac{\Omega_{\text{rep.}}}{2\nu}\right)^2 \left[\left(\frac{\tilde{\eta}}{\eta}\right)^2 + \frac{1}{4}\right], \tag{2.53}$$

where $\Omega_{\text{rep.}}$ is the Rabi frequency of the optical repumper, η the Lamb-Dicke parameter of the cooling transition, and $\tilde{\eta}$ the Lamb-Dicke parameter of the repumping transition, respectively. Hence – without additional heating sources – the final temperature is independent of the cooling Rabi frequency and instead solely determined by the repumper Rabi frequency. Consequently, an infinitely small repumper intensity theoretically, allows us to achieve virtually 100 % ground state occupation. However, we have already seen in the preceding sections that several heating mechanisms are present in our experimental apparatus, including off-resonant scattering events (see sec. 2.4.1), potential position and depth fluctuations (see sec. 2.1.2). Therefore, we need to incorporate these in our model and test whether these can explain the experimentally attainable ground state population.

Still restricting our calculations to the lowest two vibrational levels, we obtain the following generalized solution of the rate equations:

$$\bar{n} = \frac{\mathrm{H}_{\text{total}}}{\mathrm{C}_{\text{total}} + \mathrm{H}_{\text{total}}}, \tag{2.54}$$

where $\mathrm{H}_{\text{total}}$, is the total heating rate and $\mathrm{C}_{\text{total}}$ the total cooling rate. The heating rate comprises all heating mechanisms which pump the atom from the ground state into the first excited level, whereas the cooling rate acts in the opposite direction. In the following, we discuss the relevant heating rate contributions and how to obtain first order quantitate estimates for each. A summary of the individual rate components together with their scaling and quantitive estimates is provided in table 2.8. Our analysis will primarily focus on the transverse Raman sideband cooling, since the cooling limitations of the microwave sideband cooling for the experimental apparatus at hand, are rigorously discussed in Belmechri et al. [252]. This analysis concludes that we can achieve longitudinal ground state populations of up to 99 % using microwave sideband cooling, which is in agreement with our experimental findings (see tab. 2.6).

A) Raman Sideband Cooling Rate: Following the concept outlined in Leibfried et al. [204], the cooling rate is given by the product of the probability to drive a Raman cooling sideband transition $P_{\mathrm{R}}(n)$ for an atom in $|\uparrow, n\rangle$ and the repumping rate $\Omega_{\text{rep.}}$:

$$\mathrm{C}_{\mathrm{R}} = \Omega_{\text{rep.}}\, P_{\mathrm{R}}(n) = \Omega_{\text{rep.}} \frac{(\eta\sqrt{n}\,\Omega_{\mathrm{R}})^2}{2\,(\eta\sqrt{n}\,\Omega_{\mathrm{R}})^2 + \Omega_{\text{rep.}}^2}. \tag{2.55}$$

It is noteworthy that for Raman sideband cooling, the Lamb-Dicke parameter of the cooling and repumping transition are fairly similar, hence, we will use $\eta = \tilde{\eta}$ in the following. The cooling rate C_{R} depends on the vibrational level of the atom and – as expected – vanishes once the atom is in its ground state. Using the experimental parameters – $\Omega_{\text{rep.}} \approx 10\,\text{kHz}$, $\Omega_{\mathrm{R}} \approx 1\,\text{kHz}$, and $\eta_{\mathrm{T}} = 0.32$ which corresponds to $\nu_{\mathrm{T}} = 20\,\text{kHz}$ – we obtain a cooling rate of $\mathrm{C}_{\mathrm{R}} = 10.3\,\text{quanta}\,\text{s}^{-1}$. However, each cooling cycle includes a photon scattering event, which in turn may lead to an excitation through the recoil of the photon. Therefore, since our trapping frequencies are not large enough to neglect these effect, we need to incorporate this effect in the cooling rate. The likeliness to excite the atom in a scattering event is given by the squared Lamb-Dicke parameter, which amounts to an excitation probability of 2 % for the longitudinal and 10 % for the transverse direction, respectively. Furthermore, since the repumping laser beam is collinear with the optical lattice, the photon recoil arising from the absorption cannot lead to a transverse excitation. On the contrary, assuming in first order an isotropic emission, the recoil from

Table 2.8: Summary of all transverse cooling and heating processes present during the transverse Raman sideband cooling. Some heating mechanisms are also present after the cooling, which hence, limit the lifetime of the ground state. More information on each rate can be found in the corresponding section.

	Scaling	Rate	Present after cooling	Discussion in
C_R	$\Omega_{rep.}^{-1}\,\Omega_R^2\,\nu^{-1}$	10.0 quanta s^{-1}	no	2.5.2.A
H_R	$\Omega_{rep.}\,\Omega_R^2\,\nu^{-3}$	0.8 quanta s^{-1}	no	2.5.2.B
H_{ScDT}	ν^{-1}	0.8 quanta s^{-1}	yes	2.5.2.C
H_{ScHB}	ν^{-1}	0.1 quanta s^{-1}	yes	2.5.2.C
H_{ScR}	$\Omega_R\,\nu^{-1}$	0.3 quanta s^{-1}	no	2.5.2.C
H_{ScOP}	$\Omega_{rep.}\nu^{-1}$	0.1 quanta s^{-1}	no	2.5.2.C
$H_{\Delta x}$	ν^3	< 0.1 quanta s^{-1}	yes	2.5.2.D
H_{Int}	ν^2	< 0.1 quanta s^{-1}	yes	2.5.2.E
H_{OPPol}	ν^2	< 0.1 quanta s^{-1}	no	2.5.2.F
C_{total}		10.0 quanta s^{-1}		2.5.2.G
H_{total}		2.1 quanta s^{-1}		2.5.2.G
H_{dark}		0.9 quanta s^{-1}		2.5.2.G

the photon emission results in transverse excitation probability of $1/3\,\eta_T^2$, for each of the two transverse directions. The corrected transverse cooling rate then amounts to $C_R = 10.0$ quanta s^{-1}.

B) Off-Resonant Raman Sideband Heating Rate: The analysis in the preceding section shows that the cooling rate increases for larger Raman-Rabi frequencies. However, increasing the Raman-Rabi frequency also increases the likeliness to drive off-resonant sideband transitions. The first order contributions to the heating rate come from driving an off-resonant carrier transition followed by an excitation in the repumping cycle, and from driving directly an off-resonant heating transition. Following, again, the concept outlined in Leibfried et al. [204], the off-resonant transition probabilities are given by:

$$H_R = \left(\frac{\Omega_R}{2\,\nu}\right)^2 \eta^2\,\Omega_{rep.} + \left(\frac{\Omega_R}{4\,\nu}\right)^2 \eta^2\,\Omega_{rep.}\,. \tag{2.56}$$

Using the experimental parameters given above, the heating rate induced by off-resonant Raman sideband transition amounts to $H_R = 0.2$ quanta s^{-1}.

C) Off-Resonant Scattering Heating Rate: Using the tools we developed in section 2.4.1, we can numerically calculate the off-resonant scattering rates – using the Kramers-Heisenberg formula – for all laser sources which are present during the cooling process. These include: the lasers forming the optical lattice, the hollow dipole trap laser, the pair of Raman lasers themselves, and the F- and m_F-state pumping lasers. Similar to the discussion above, we need to keep in mind the geometrical orientation of each beam – with respect to the optical lattice – for the photon which is absorbed in the scattering event, whereas we will treat the emission as isotropic. Furthermore, we need to distinguish between scattering events which bring the atom back into its original qubit state and those which require additional F-, m_F-state pumping. For our analysis we will only consider first order contributions, since all higher orders

scale with η^4, and correspondingly ν^{-2}, which can be neglected even for trapping frequencies as low as 20 kHz. For example, the heating rate arising from off-resonantly scattering photons of the optical lattice is given by:

$$\mathrm{H}_{\mathrm{ScDT}} = \frac{1}{3}\eta_{\mathrm{T}}^2 \left[R_{|4,4\rangle\rightarrow|4,4\rangle} + R_{|4,4\rangle\rightarrow|4,3\rangle}(1+n_{\mathrm{ph}}) + R_{|4,4\rangle\rightarrow|3,3\rangle}(1+n_{\mathrm{ph}}) \right], \tag{2.57}$$

where n_{ph} is the average number of scattering events required until the atom is pumped back into the $|\uparrow\rangle$ state using the F-, m_F-state pumping light, which amounts to $n_{\mathrm{ph}} \approx 2$. Using the experimental parameters we obtain $\mathrm{H}_{\mathrm{ScDT}} = 0.8\,\mathrm{quanta\,s^{-1}}$, for the off-resonant scattering events induced by the optical lattice. The heating rates arising from the hollow dipole trap laser, the pair Raman lasers, and the F- and m_F-state pumping lasers can be obtained in a similar fashion and are summarized in table 2.8.

D) Optical Potential Position Fluctuation Heating Rate: In section 2.1.2 we derived the generalized transition rates (see eq. (2.16)), which arise from positional fluctuations of the potential. Using these transition rates, we obtain the following ground state heating rate:

$$\mathrm{H}_{\Delta x} = \frac{4\pi^4 \nu^3 m_{\mathrm{Cs}}}{h} S_{\Delta x}(\nu)\,. \tag{2.58}$$

Transverse potential fluctuations arise from pointing instabilities of the dipole trap lasers. A detailed description how to experimentally measure these can be found in Kuhr [169]. In this thesis, instead, we will reuse the power spectral density measurement presented in section 2.1.2 to derive an upper limit on these fluctuations. As discussed in section 2.1.2, the position fluctuations in the longitudinal direction are primarily caused by the phase noise of the frequency synthesizers driving the AOMs. This, however, cannot lead to position fluctuations in the transverse direction, and hence the noise spectral density serves only as a worst-case estimate. The ground state heating rate due to positional fluctuations of the optical potential then amounts to $\mathrm{H}_{\Delta x} = 0.02\,\mathrm{quanta\,s^{-1}}$, which is still more than an order of magnitude smaller than e.g. the heating due to off-resonant scattering events.

E) Optical Lattice Intensity Noise Heating Rate: We already concluded in section 2.1.2, that the intensity noise heating can be neglected in comparison to heating arising from positional fluctuations of the optical potential. Nevertheless, for completeness, we can use the transition rates (see eq. (2.10)) to derive the intensity noise ground state heating rate, which amounts to:

$$\mathrm{H}_{\mathrm{Int}} = \frac{\pi^2 \nu^2}{8} S_I(2\nu)\,. \tag{2.59}$$

Please note, that for our model we only consider the lowest two vibrational level, however, intensity noise produces only parametric excitations, hence, we included a factor of $1/2$ in equation (2.59). Using the experimental parameters we obtain $\mathrm{H}_{\mathrm{Int}} = 4 \times 10^{-6}\,\mathrm{quanta\,s^{-1}}$, which is – as expected – neglectable in comparison with other heating rates.

F) Imperfect Optical Pumping Polarization Heating Rate: In section 2.3.1, we demonstrated that we achieve a σ^+ polarization purity of $\Pi > 20\,000$[30] for the m_F-state pumping light. The $|\uparrow\rangle$ state is only a dark state for pure σ^+ polarized m_F-state pumping light, therefore the remaining light leads to

[30] The purity is defined as the ratio of σ^+/σ^- polarized light, for more details see [180]

resonant scattering events. However, this scattering rate amounts to less than 1 kHz – for our experimental parameters – and the corresponding heating rate to $H_{OPPol} < 0.1$ quanta s^{-1}.

G) Achievable Ground State Population and its Lifetime: Combining the individual heating rates gives us a total heating rate of $H_{total} = 2.1$ quanta s^{-1} and a cooling rate of $C_{total} = 10.0$ quanta s^{-1}. Using equation (2.54), we can, hence, determine a theoretical estimate of the mean vibrational occupation for each of the two transverse directions, which amounts to $\bar{n}^{T}_{Theo} = 0.17$ and, correspondingly, a ground state population of 85 %. This value agrees well with the 80 % ground state population we commonly observe with the experimental apparatus at hand (see sec. 2.5.2). Furthermore, the framework developed in the preceding sections allows us to investigate the transverse Raman cooling limit by varying the Raman-Rabi frequency Ω_R and the repumping rate $\Omega_{rep.}$. While the trapping frequency would be another interesting parameter, we are experimentally already at the limit of both the detuning and laser intensity, as discussed in section 2.5.1. A numerical analysis of our model yields that we should be able to reach a ground state occupation of up to 99 % for each of the two transverse directions by increasing the Raman-Rabi frequency to 5 kHz, while decreasing the repumping rate to $\Omega_{rep.} = 2$ kHz.

Furthermore, we can use our framework to extract the lifetime of atoms which were successfully cooled into their vibrational ground state by evaluating the heating mechanisms which are present even without sideband cooling. For each transverse direction we obtain a heating rate of $H^{T}_{dark} = 0.9$ quanta s^{-1}, which is primarily limited by off-resonant scattering events induced by the state-dependent optical lattice. We can also directly measure the transverse heating rate by extracting the mean transverse vibrational occupation from Raman sideband spectra for increasing hold times between cooling and detection, which is shown in figure 2.33(b). Using a simple exponential model, we extract the heating rate (red line in fig. 2.33(b)), which amounts to $H^{T}_{exp} = 8\,^{+4}_{-8}$ quanta s^{-1}. This result, however, only serves as an upper boundary. Unfortunately, our rather short population relaxation time of $T_1 \approx 100$ ms, makes it experimentally challenging to measure the transverse excitations for longer hold times. Already 10 % of the spins have decayed after 20 ms, which reduces the signal to noise ratio, and hence results in a rather large uncertainty of the mean transverse vibrational occupation (see fig. 2.33(b)).

Lastly, we can also use our framework to repeat the analysis for the longitudinal direction. Here, we obtain a heating rate of $H^{L}_{dark} = 3$ quanta s^{-1}, which is almost entirely due to the phase noise of the optical lattice (see sec. 2.1.2).

Outlook: Microwave Cooling of Transverse Vibrational Sidebands

From an experimental point of view – as discussed in section 2.5.2 – it would be desirable to also cool atoms using microwave sideband cooling along the transverse direction. We also know that microwave sideband cooling requires a transverse displacement of the $|\uparrow\rangle$ potential with respect to the $|\downarrow\rangle$ potential. In principle, such a displacement could be realized using an additional 866 nm laser beam which is e.g. σ^+ polarized and collinear with the optical lattice, however, slightly displaced in the transverse direction. Hence, controlling the intensity of the additional laser beam, would allow us to separate and recombine the optical potentials in the transverse direction.

Out of curiosity we tested whether microwave coupling along the transverse direction also in the existing experimental apparatus even without incorporating such an additional beam. Such a coupling can arise if the hollow beam is not purely π-polarized, or also from light shifts if the atoms are not in their vibrational ground state. In fact, the sideband spectra presented in figure 2.34(a) and figure 2.34(b), respectively, clearly show sideband transitions ±20 kHz next to the carrier transition. The sideband spectrum displayed in figure 2.34(a) is recorded using a Gaussian microwave π-pulse and the ensemble was cooled along the longitudinal direction using microwave sideband cooling, hence, the longitudinal

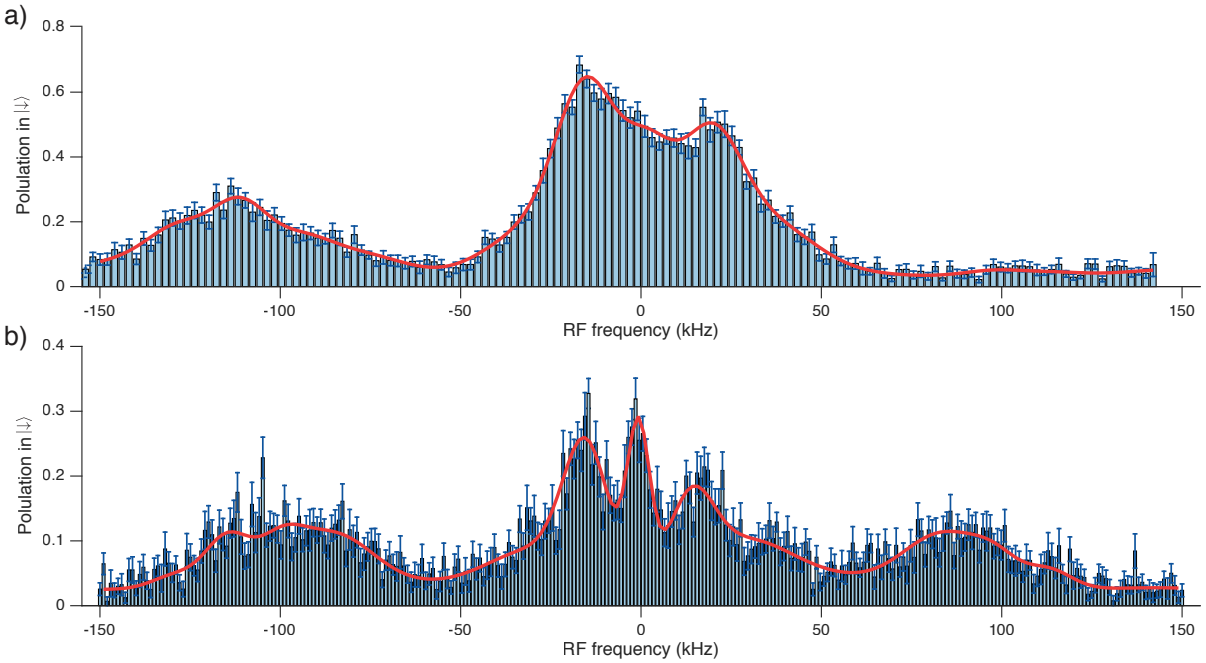

Figure 2.34: Transverse and longitudinal microwave sideband spectrum of an ensemble of atoms: Obtained using a Gaussian microwave π-pulse **(a)** and using a long – decohered – square microwave pulse with a higher spectral resolution **(b)**. In the case of the latter, we also employ transverse microwave sideband cooling, which leads to a visible asymmetry in the height of the transverse heating and cooling sideband transition.

cooling sideband transition (110 kHz) is not visible. On the contrary, the sideband spectrum depicted in figure 2.34(b) is obtained using a long – decohered – square microwave pulse with a higher spectral resolution. Furthermore, it shows a first attempt to cool the transverse vibrational excitations using microwave radiation. Using the fit model described in section 2.5.2 in combination with equations (2.52)-(2.51), we extract the mean transverse vibrational occupation, which amounts to $\bar{n}^{\mathrm{T}} = 1.6\,^{+0.8}_{-0.5}$, and the corresponding transverse ground state population, which amounts to $n_0^{\mathrm{T}} = (40 \pm 10)\,\%$. While these results are a first indication of microwave transverse sideband cooling, prospective experiments need to investigate the potential and limits of 3D microwave sideband cooling.

CHAPTER 3

Low-Entropy States of Neutral Atoms in Polarization-Synthesized Optical Lattices

Compared to other quantum systems, optical lattice potentials stand out for being naturally scalable. They offer thousands of sites, arranged in periodic arrays, in which quantum particles, such as atoms, can be confined and manipulated [255]. The idea of employing the multitude of sites available as a well-controlled Hilbert space has influenced modern research frontiers ranging from quantum metrology [174], quantum information processing [16, 67, 110, 127, 256, 257], discrete-time quantum walks [66], up to quantum simulations of strongly correlated condensed-matter systems [42, 43, 258] with single lattice-site resolution [132, 259]. Substantial experimental effort has recently been devoted to creating low-entropy states of atoms in the lattice, with each site being occupied by an integer number of atoms. Low-entropy states play an essential role in a host of quantum applications, including the creation of highly entangled cluster states for quantum information processing [113], investigation of Hong-Ou-Mandel-like quantum correlations in many-body systems [17, 40], and the quantum simulation of quantum spin liquids in frustrated systems [260, 261].

To date, the approach that has proven most effective to generate low-entropy states in optical lattices relies on a Mott insulator phase [42, 43]. This is denoted as a top-down approach since ultracold atoms, due to interactions, self-organize in domains with integer filling factors. Other approaches [262] relying only on laser cooling techniques have recently demonstrated filling factors beyond the one-half limit imposed by inelastic light-assisted collisions [263, 264], though without providing a fully deterministic method. In contrast, a bottom-up approach generating arbitrary low-entropy states from individual atoms has long been desired [110, 256], yet never been experimentally realized.

In the following chapter, we discuss a bottom-up approach to generate arbitrary atom patterns, including unity filling of lattice sites, in a one-dimensional (1D) optical lattice. Inspired by the seminal work by Jaksch et al. [110] proposing spin-dependent optical lattices to control individual atoms' positions, our work realizes the atom sorting scheme proposed by Weiss et al. [265]. The experimental challenge consists in developing spin-dependent optical lattices able to shift atoms by any amount of lattice sites conditioned to their spin state. Previous implementations [113, 114] of spin-dependent optical lattices were limited to only relative displacements of the two spin components and to relative shift distances of one site at most. To overcome these limitations, we devised a scheme for spin-dependent transport based on a high precision, large bandwidth synthesizer of light polarization. Hence, we refer to our new implementation of spin-dependent optical potentials as polarization-synthesized (PS) optical lattices. In contrast to the atom sorting technique formerly demonstrated by our group [266], which cannot resolve single lattice sites, PS optical lattices allow us to reposition individual atoms with a precision of 1 Å,

reducing thereby the positional entropy of a randomly distributed ensemble to virtually zero. In addition, the novel approach requires no post-selection, which have limited the success rates in earlier efforts to create ordered patterns from a thermal ensemble [126, 195].

3.1 A Novel Approach to State-Dependent Transport

The key elements in realizing the spin-dependent optical-lattice potentials, which we introduced in section 2.1.3, are two superimposed, yet independently controllable optical standing waves with opposite circular polarization, σ^+ and σ^-,

$$U_\uparrow(x,t) = U_\uparrow^0 \cos^2\{k_{\mathrm{DT}}[x - x_\uparrow(t)]\}\,, \tag{3.1}$$

$$U_\downarrow(x,t) = U_\downarrow^0 \cos^2\{k_{\mathrm{DT}}[x - x_\downarrow(t)]\}\,, \tag{3.2}$$

with identical lattice constant $a_{\mathrm{DT}} = \pi/k_{\mathrm{DT}}$. We operate both optical standing waves at a so-called magic wavelength λ_{DT} of cesium, allowing atoms in $|\uparrow\rangle$ and $|\downarrow\rangle$ state to be trapped in the maximum-intensity regions of the σ^+- and σ^--polarized light field, respectively (see sec. 2.1.3). Such a magic wavelength was already employed in earlier implementations of spin-dependent optical lattices, for example in Mandel et al. [113] and by our group [114]. However, these implementations permitted only relative displacements and, most importantly, maximum shift distances of one lattice site, thereby precluding the possibility of sorting randomly distributed atoms into predefined patterns. In contrast, PS optical lattices entirely overcome these limitations by relying on two fully independent optical standing waves (see fig. 2.9). In order to create the standing waves, we let two co-propagating laser beams with opposite circular polarization each interfere with a linearly-polarized, counter-propagating beam, as illustrated in figure 3.1(a). We employ an optical fiber to ensure that the resulting standing waves are perfectly matched to the same transverse mode, and thereby that atoms in both spin states, $|\uparrow\rangle$ and $|\downarrow\rangle$, experience an identical transverse potential. Transverse-mode filtering is essential to ensure long spin-coherence times for spectrally-narrow coherent pulses (e.g., spin-flips for single-atom addressing, see section 2.3.4), or else thermal atoms would undergo inhomogeneous spin dephasing in a few microseconds due to a strong differential light shift [189]. We have seen in section 2.4.2 – using Ramsey interferometry – that our PS optical lattice does not affect the spin-coherence time T_2. Instead, spin-coherence time is limited rather by other spin-dephasing sources, including stray magnetic fields and hyperfine-interaction-mediated differential light shifts [182].

While in the transverse directions the two standing waves are perfectly overlapped, they are *a priori* free to fluctuate in the lattice direction due to environmental disturbances (e.g., acoustic waves, mechanical vibrations, and air currents). Fluctuations of their relative position must be suppressed with interferometric precision[1] to avoid vibrational excitations when we spin-flip the atoms. Otherwise, as discussed in section 2.5.2, the Franck-Condon factor would not amount to zero [252], hence, allowing microwave operations to also change the vibrational state of an atom. Furthermore, the position of each standing wave must be controlled to ensure that atoms are transported to the desired position. We achieve this by employing two independent optical phase-locked loops (PLLs) that actively stabilize the phases of each circularly-polarized beam, $\phi_\uparrow$ and $\phi_\downarrow$, with respect to a common optical reference beam. As shown in figure 3.1(b), each optical phase $\phi_{\uparrow/\downarrow}$ is referenced to a low-phase-noise RF signal (DDS). Varying the phase of the RF signals according to a digitally programmed profile allows us to independently steer $\phi_{\uparrow/\downarrow}$,

[1] The relative position jitter must be much smaller than the harmonic oscillator length $\sqrt{\frac{\hbar}{4\pi m_{\mathrm{Cs}}\nu_{\mathrm{L}}}}$.

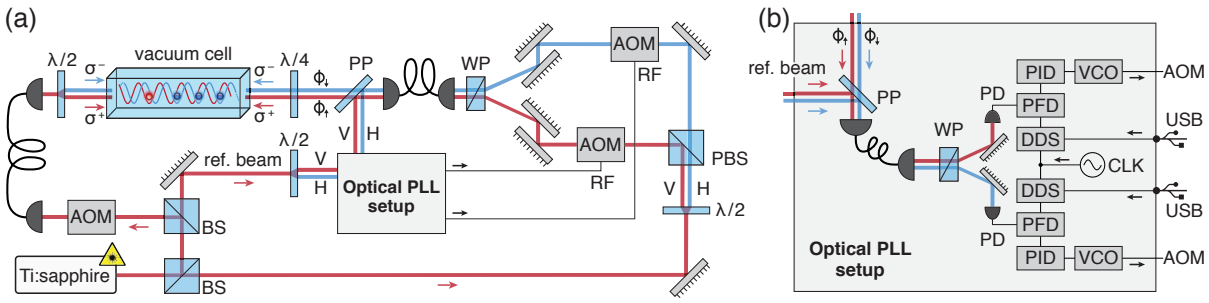

Figure 3.1: Schematic illustration of the experimental setup for polarization-synthesized optical lattices. **(a)** The linearly polarized output of a Ti:sapphire laser is split by beam splitters (BS) into the reference beam, which is used for the optical phase-locked loops (PLLs), and the beams forming the lattice in the vacuum cell. While the polarization of the left lattice beam is static and linear, the polarization of the right lattice beam is synthesized by overlapping two beams of opposite circular polarizations. The latter are combined by a Wollaston prism (WP) in linear polarization basis (vertical V, horizontal H), spatially mode matched by a polarization maintaining optical fiber (high polarization extinction ratio > 50 dB [267]), and transformed into circular polarizations by a $\lambda/4$ plate. A fraction of light is diverted by a pickup plate (PP) into the optical PLL setup, which controls the optical phases $\phi_\uparrow$ and $\phi_\downarrow$ by feeding RF signals back to the acousto-optic modulators (AOMs). **(b)** Optical PLL setup: the diverted light is overlapped with a common reference beam. The resulting beat signals are independently recorded by fast photodiodes (PD) after the WP. The phase of each beat signal is compared with a RF reference signal (DDS) using a digital phase-frequency discriminator (PFD), and fed to a PID controller (10 MHz bandwidth), which steers the corresponding AOM through a voltage-controlled oscillator (VCO). The DDS RF sources are phase referenced to the same 400 MHz clock signal (CLK) and interfaced via USB with a computer. Three additional control-loop setups (see sec. 2.1.1) independently regulate the intensity of each lattice beam by controlling the RF power of the corresponding AOM. This figure is originally published in Robens et al. [3]

and thereby the position of the respective optical potential $U_{\uparrow/\downarrow}$:

$$x_{\uparrow/\downarrow}(t) = \frac{\lambda_{\mathrm{DT}}}{2}\frac{\phi_{\uparrow/\downarrow}(t)}{2\pi}\,. \tag{3.3}$$

Since we are working with deep trapping potentials ($U^0 \approx k_B \times 75\,\mu\mathrm{K}$, see sec. 2.1.1), a spatial displacements of the sub-lattice in turn leads to a translation of atoms occupying the related spin state.

In addition, we note that PS optical lattices not only allow us to arbitrarily steer the positions $x_{\uparrow/\downarrow}$ but also the lattice depths $U^0_{\uparrow/\downarrow}$ for each spin species individually. To that purpose, we employ separate PID servo loops controlling the intensity $I_{\uparrow/\downarrow}$ of both co-propagating and the counter-propagating beams, which we introduced in section 2.1.1. While the individual control of $U^0_{\uparrow/\downarrow}$ plays no role for the production of low-entropy states, it constitutes a crucial component in future applications, including quantum optical control of atom transport [6](see sec. 3.4.2), non-equilibrium quantum thermodynamics experiments [268], non-equilibrium localization experiments [269], and the quantum simulation of quantum electrodynamics [51] and of impurity models [270, 271].

3.2 High Precision Polarization Synthesizer

In view of future quantum applications, where particles are in fragile quantum states delocalized over many lattice sites, it is crucial to determine the precision attained by PS optical lattices. Ultimately, their precision depends on the optoelectronic setup developed to coherently combine the two laser beams of

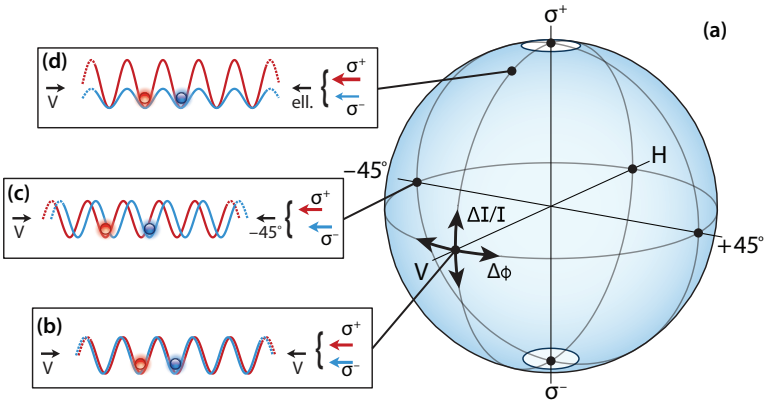

Figure 3.2: Representation of the synthesized polarization state on the Poincaré sphere (see appx. sec. B.2.3) **(a)**. The effect of noise sources on the polarization state is also displayed. Circular regions close to the poles represent exclusion regions not accessible by the polarization synthesizer due to the limited dynamic range of intensity servo loops. The points represent three synthesized polarizations corresponding to two spin-dependent lattice that are overlapped **(b)**, relatively shifted by a quarter-period **(c)**, and of different depths **(d)**. This figure is originally published in Robens et al. [3]

opposite circular polarization, which form the lattice potentials in equations (3.1)-(3.2). In essence, this setup constitutes a polarization synthesizer capable of generating arbitrary polarization states, as shown in figure 3.2. We quantify the precision of the synthesized polarization by measuring, independently, both the relative intensity noise and the relative phase noise of the two circularly polarized beams. The details of these measurements are discussed in section 3.2.2. Besides noise sources, we also consider static imperfections originating from spatial polarization inhomogeneities over the cross section of the synthesized beam, which is discussed insection 3.2.3. The results, summarized in table 3.1, show that static polarization inhomogeneities are the dominating contribution degrading the polarization purity. They also show that the measured phase noise $\Delta\phi$ is particularly small, corresponding to a jitter of the relative position between the two standing waves equal to $\Delta x = 1.20\,\text{Å}$ (see eq. (3.3)). This is more than two orders of magnitude smaller than the extent of the atomic wave function in the vibrational ground state (20 nm).

Static polarization imperfections produce spin-dependent deformation of the lattice potentials, one of the main sources of inhomogeneous spin dephasing for thermal atoms [189]. In contrast, fluctuations of the synthesized polarization due to phase and intensity noise can produce spin dephasing also for atoms cooled to the vibrational ground state. In addition, fluctuations can also cause vibrational excitations, as we have seen in section 2.5.2. However, we carried out independent measurements based on microwave (see sec. 2.5.2) and Raman sideband spectroscopy (see sec. 2.5.2), obtaining less than ten vibrational quanta per second (see sec. 2.5.2). This result is consistent with our analysis in sec. 2.1.2, where we estimated the heating rate from the power spectral densities of phase and intensity noise [95, 96], revealing in addition that the intensity-noise contribution is negligible on the scale of seconds.

Concerning the dynamical control of PS optical lattices, we measured the response function of the polarization synthesizer for both the phase and intensity servo loops, obtaining a bandwidth of 800 kHz, which is discussed insection 3.2.4. Such a high bandwidth allows us to perform arbitrary spin-dependent lattice operations on the microsecond timescale, similar in magnitude to the typical timescales in trapped ion experiments and orders of magnitude shorter than in typical neutral atom experiments. By sideband spectroscopy, we furthermore observe that all transport operations employed for atom sorting leave 99 %

Table 3.1: Sources limiting the precision of polarization synthesized states. For comparison purpose, we choose the polarization extinction ratio η as a measure of the polarization purity. The details of the intensity noise measurement and of the phase noise measurement are discussed in section 3.2.2, those of the spatial inhomogeneities in section 3.2.3, respectively. The degree of polarization is abbreviated with DOP (see appx. sec. B.2.3)

				η
Intensity noise	$\Delta I/I$	=	0.04 %	4×10^{-8}
Phase noise	$\Delta\phi$	=	0.1°	8×10^{-7}
Spatial inhomogeneities	DOP	=	99.990 %	5×10^{-5}

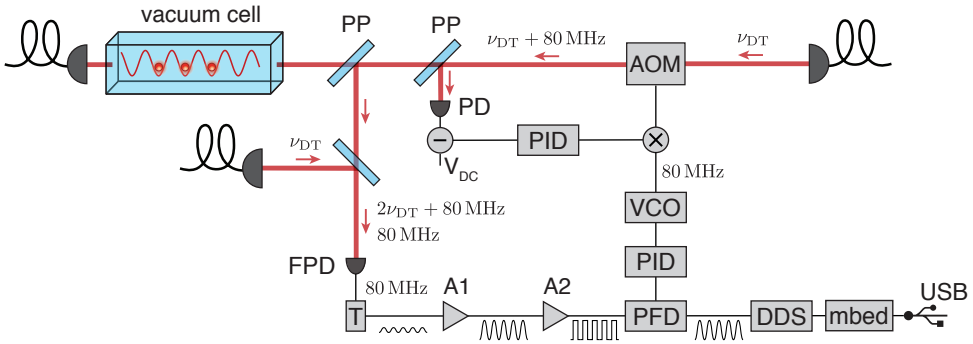

Figure 3.3: Illustration of electro-optical setup employed to simultaneously stabilize the phase and intensity of σ^+ optical lattice. The same setup is also used for the σ^- optical lattice, which is not displayed for illustrational purposes. See section 3.2.1 for more details. Used abbreviations: acousto-optic modulator (AOM), pickup plate (PP), photo diode (PD), fast photo diode (FPD), proportional–integral–derivative controller (PID), bias tee (T), low noise amplifier (A1), limiting amplifier (A2), phase frequency discriminator (PDF), direct digital synthesizer (DDS), ARM Cortex-M microcontroller (mbed), voltage controlled oscillator (VCO).

of the atoms in the longitudinal and transversal vibrational ground state, which is discussed insection 3.3.1. This is even the case for non-adiabatic spin-dependent transport operations, taking 20 µs per single-site shift using a bang-bang-like transport pulse [272], which we use e.g. to realize discrete-time quantum walks (see sec. 3.4.1).

3.2.1 Electro-Optical Setup of the Phase Lock

In the preceding section we introduced the experimental apparatus required to generate two independent spin-dependent optical lattices, which is shown in figure 3.1. However, for simplicity, we omitted some of the experimental details of the employed hardware. In this section we will rigorously introduce all relevant components for one of the two optical phase locks as well as how we achieve both, phase and intensity locks, using the same AOM. In fact, during recent years four Master projects have been dedicated to study different aspects of the optical phase lock loop: one achieved a first proof of principle version of the optical phase lock loop [77], one aimed to improve the phase lock photodiode [273], another investigated the usage of digital instead of analog feedback controller [106], and the most recent one developed a new frequency synthesizer [274].

The electro-optical setup for the σ^+ polarized optical lattice is illustrated in figure 3.3: We employ an

AOM[2], which shifts the frequency of the laser beam by 80 MHz. Subsequently, a fraction of the laser beam is extracted for the intensity feedback loop, using a custom coated pickup plate[3]. The intensity control loop corresponds chiefly to the one we introduced in section 2.1.1. However, now we mix[4] the output of the analog PID controller[5] with the signal from the phase lock, instead of using a static 80 MHz signal, to control the corresponding AOM. Additionally another fraction of the laser beam is extracted for the optical phase lock loop[3], as discussed in section 3.1. This fraction is overlapped with a reference beam, the laser frequency of which is not shifted by an AOM. Hence, we create an optical beat signal with sum frequency $2 \times \nu_{\mathrm{DT}} + 80\,\mathrm{MHz}$ and difference frequency 80 MHz. The difference frequency is detected using an ultrafast AC photodiode[6], which has a bandwidth of 10 GHz. This bandwidth is significantly higher than beat signal we intend to observe. However, when employing photodiodes with a bandwidth of 150 MHz, we noticed a phase sensitivity to ambient light. Typically this is of no concern, however, since we want to stabilize the optical phase with a precision below 1°, also small amplitude to frequency conversions become critical. We use a bias tee[7] to provide the required bias voltage of the fast photodiode, which guarantees a DC free RF signal behind the bias tee. Subsequently, the signal is amplified in two stages: first by a low noise amplifier[8] and then by a limiting amplifier[9]. The former is specifically designed to amplify signals with low amplitudes, such as our beat signal. The latter is employed to "digitize" the RF signal, which is indicated by the square wave in figure 3.3. This digitalization prevents possible amplitude to phase conversions, which can occur when we change the depth of the optical lattice. The phase of the digitized signal is then compared to the one from the DDS[10], using a phase frequency discriminator[11], as discussed in section 3.1. More information on the circuit diagram of the PFD, which was designed by Professor Marco Prevedelli, can be found in Hild [275]. The resulting error signal is fed to an analog PID controller[5], which controls the phase and frequency of the voltage-controlled oscillator[12]. The VCO signal is then mixed[4] with the previously introduced signal from the intensity control loop. Its is possible to stabilize the phase and intensity of the optical beam independently since these are orthogonal parameters. Nevertheless, in the experimental setup, we notice a marginal crosstalk between the locks. However, this crosstalk has no significant impact on the atoms since it is barely above the noise floor.

3.2.2 Intensity and Phase Noise

A differential intensity noise between the σ^+ polarized and the σ^- polarized laser beams leads to time dependent fluctuations of the desired polarization state. Differential intensity noise can be visualized as a rotation in the plane which is perpendicular to the equatorial plane of the Poincaré sphere (see fig. 3.2). However, if these intensity fluctuations are faster than our detection technique, they will "wash out" and instead appear as a reduction of the degree of polarization (DOP, see appx. sec. B.2.3), and correspondingly a reduced linear extinction ratio η. These two quantities are mathematically related

[2] Gooch & Housego: AOM 3080-122
[3] Altechna: BK7 glass plate, 2° wedge, coating side 1: AR, coating side 2: PRs, PRp = 12 % for 45° AOI
[4] Mini-Circuits: ZLW-6+ frequency mixer
[5] Vescent Photonics: D2-125 laser servo
[6] HAMAMATSU: G4176-03 ultrafast MSM photodetector
[7] Mini-Circuits: ZX85-12G+ bias tee
[8] Mini-Circuits: ZFL-500HLN+ low noise amplifier
[9] Analog Devices: EVAL-AD8306 high precision limiting-logarithmic amplifier evaluation board
[10] Analog Devices: EVAL-AD9954 400 Msps, 14-Bit, direct digital synthesizer
[11] On Semiconductor: MC100EP140 phase-frequency detector
[12] Mini-Circuits: ZX95-78+ voltage-controlled oscillator

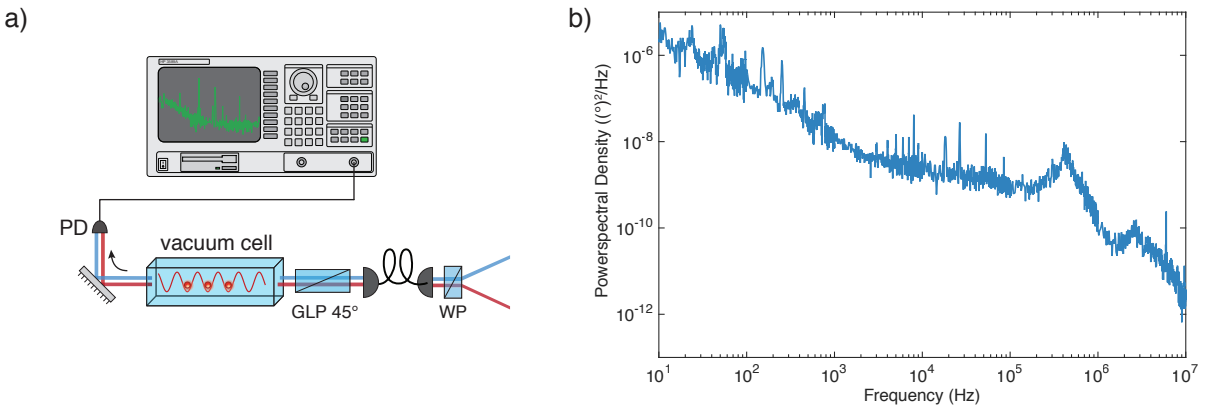

Figure 3.4: **(a)** Opto-electrical setup to measure the differential phase noise between the σ^+ and the σ^- polarized laser beam: The phase noise is inferred from the transmission of a synthesized linear polarization through a 45°-oriented analyzer. The resulting intensity fluctuations are recorded using a fast photodiode, the signal of which is analyzed with a spectrum analyzer. **(b)** Obtained phase noise spectral density yielding a total differential phase noise of $\Delta\phi = 0.1°$.

by [180]:

$$\mathrm{DOP} = 1 - 2\eta. \tag{3.4}$$

Likewise a differential phase noise between the σ^+ polarized and the σ^- polarized laser beams can be visualized as a rotation in the equatorial plane of the Poincaré sphere (see fig. 3.2), which similarly leads to a degradation of the linear extinction ratio η [180].

We introduced in section 2.1.2 an experimental procedure, which allows us to measure the intensity noise spectral density of laser beams in our experimental apparatus. After performing such a measurement for each of the two laser beams, we obtain the relative intensity noise (RIN) by integrating the noise spectral density from 1 Hz to 25 MHz. The relative differential intensity noise $\Delta I/I$, given in table 3.1, is then defined by:

$$\Delta I/I = (I_\uparrow - I_\downarrow)/(I_\uparrow + I_\downarrow)\,, \tag{3.5}$$

and the corresponding contribution to linear extinction ratio η by [180]:

$$\eta \approx (\Delta I/I)^2/4\,. \tag{3.6}$$

Hence, we obtain a RIN of 0.04 %, per laser beam, which limits the linear extinction ratio of our polarization synthesizer to $\eta = 4 \times 10^{-8}$.

The differential phase noise is measured as outlined in figure 3.4(a): both beams (σ^+ and σ^-) are adjusted to have the same phase and intensity to create a synthesized linear polarization. Since we cannot measure the differential phase noise directly, we instead convert phase noise into intensity noise using a 45°-oriented Glan-laser polarizer, as illustrated in figure 3.4(a). The resulting intensity fluctuations of the transmission through the polarizer is, thus, recorded using the spectrum analyzer[13] we employed to measure the intensity noise spectral density. The desired phase noise spectral density, which is displayed in figure 3.4(b), is then obtained by converting the intensity to phase. Integrating the noise spectral density from 1 Hz to 25 MHz gives us the total differential phase noise $\Delta\phi = \phi_\uparrow - \phi_\downarrow$, which amounts to 0.1°. This phase noise, in turn, leads to a reduced linear extinction ratio of $\eta = 8 \times 10^{-7}$, according

[13] HP: 3589A Spectrum/Network Analyzer, 10 Hz to 150 MHz

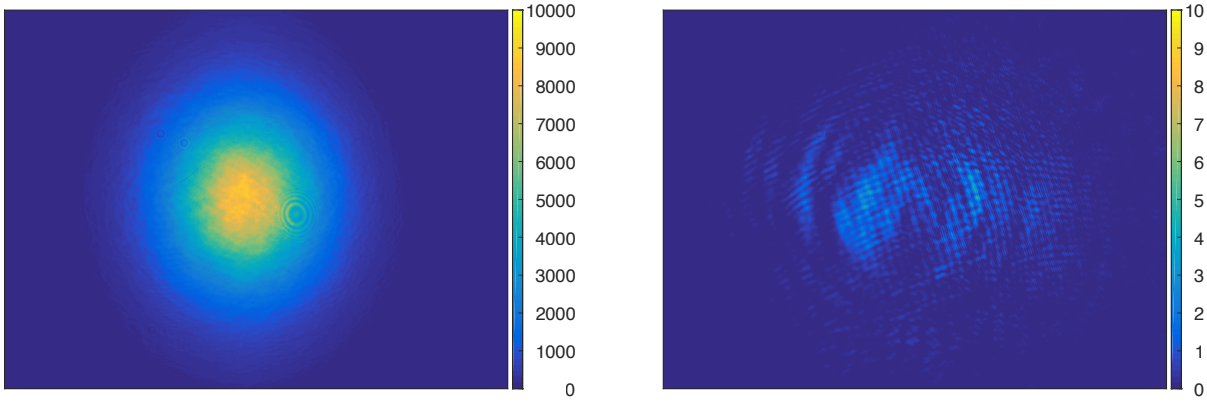

Figure 3.5: **(a)** Beam profile measurement of a synthesized linear polarization. Please note: the ring-like structures are caused by small dust particles on the CCD sensor. **(b)** Beam profile measurement of the same synthesized linear polarization, which passes through a linear polarizer set to extinction. The remaining transmission shows ring-like structures, which originate from the optical fiber coupler.

to [180]:

$$\eta \approx (\Delta\phi)^2/4\,. \tag{3.7}$$

3.2.3 Spatial Polarization Inhomogeneities

The analysis of the preceding section concluded that our polarization synthesizer should be able to generate a linear polarization with an extinction ratio of $\eta < 1 \times 10^{-6}$. However, the extinction ratio we measure by a linear polarizer[14] in extinction configuration, amounts to $\eta \approx 5 \times 10^{-5}$. This discrepancy, in fact, is caused by spatial polarization inhomogeneities, which we neglected so far. Spatial polarization inhomogeneities can be characterized with a beam profile CCD-camera[15] by recording the synthesized beam which passes through a linear polarizer in extinction configuration. Figure 3.5(b) shows the result of such a measurement. By additionally also recording the beam profile without polarizer (see fig. 3.5(a)), we estimate the degradation of the extinction ratio as a result of spatial inhomogeneities, which amounts to $\eta = 2 \times 10^{-4}$. At first sight it might be surprising that the estimated extinction ratio is worse than the one we obtain from the first measurement, where we used a power meter instead of the beam profile camera. However, this can be explained: When we use the beam profile camera, we measure the extinction of a collimated beam, whereas in the other case we measure the extinction ratio of a focussed beam – also the atoms are located in the focus of the optical beam. Most of the light, which passes through the polarizer, shows ringlike structures. Since these ring structures become equally distributed in the focus of the beam, we consequently obtain a lower extinction ratio.

At the current time, we do not fully understand the physical mechanism which causes these ringlike spatial polarization inhomogeneities. Nevertheless, we could experimentally verify that they originate from the optical fiber coupler, which combines the σ^+ and σ^- polarized beam (see fig. 3.1).

[14] we verified separately that the polarizer itself is capable of producing and detecting polarizations on the order of $\eta = 1 \times 10^{-7}$
[15] Ophir: Spiricon LW230

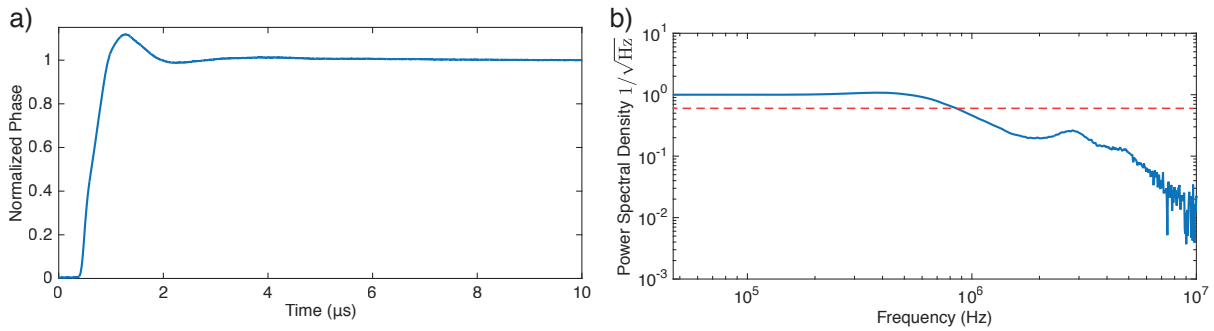

Figure 3.6: **(a)** Closed loop step response of the optical phase lock controlling the σ^+ polarized laser beam. At time $t = 0\,\mu s$ the reference phase of the corresponding DDS is increased by 10°. **(b)** Corresponding bode plot which reveals the spectral response of the control loop: the gain stays close to unity up to the lowpass-like cut-off at 800 kHz.

3.2.4 Control Bandwidth of the Polarization-Synthesized Optical Lattice

We infer the control loop bandwidth of all intensity and phase control loops by recording the systems response to step like change in the control parameter. Figure 3.6(a) exemplarily shows the response of the phase lock, which controls the phase of the σ^+ polarized laser beam. The displayed time trace is obtained using a similar setup as depicted in figure 3.4. However, this time we record the voltage signal of the photodiode with an oscilloscope and not with the spectrum analyzer. To create a step like change for the phase lock loop, we increase the phase of the corresponding DDS by 10°, at time $t = 0\,\mu s$, and record the response of the optical phase lock. In order to extract the bandwidth of the corresponding phase lock, we need to convert the step response into an impulse response. The impulse response can then be used to obtain the spectral response of the control loop through a Fourier transformation [274]. The bode plot, corresponding to the time trace shown in figure 3.6(a), is displayed in figure 3.6(b), from which we infer a 3 dB cut-off at 800 kHz (dashed red line). The 3 dB cut-off is commonly referred to as the bandwidth of the control loop [274]. The bandwidth of the phase lock is primarily limited by the finite dead time of the AOM, which amounts to 300 ns [77].

The phase lock loop of the σ^- polarized laser beam, as well as both intensity control loops, have a similar spectral response, hence, we omit these measurements here. Nevertheless, it is noteworthy that the application of internal model control theory promises to extend the bandwidth even further up to 10 MHz by compensating for the dead time of the AOMs [274, 276].

3.3 Sorting Individual Atoms in Polarization-Synthesized Optical Lattices

In the following we will discuss, how we use our PS optical lattice in combination with techniques we introduced in chapter 2 to rearrange individual cesium atoms from a dilute thermal ensemble into a predefined, ordered distribution. This atom sorting procedure works akin to Maxwell's demon [265]. In essence, an automated feedback-based experimental setup acquires the initial location of atoms through fluorescence imaging with single site precision, and it uses this information to subsequently shift the atoms, one by one, to form the desired pattern. We will keep the σ^+ polarized optical lattice fixed, which serves as a *storage register* for atoms in $|\uparrow\rangle$, while the σ^- polarized one is mobile, providing a *shift register* for atoms in $|\downarrow\rangle$.

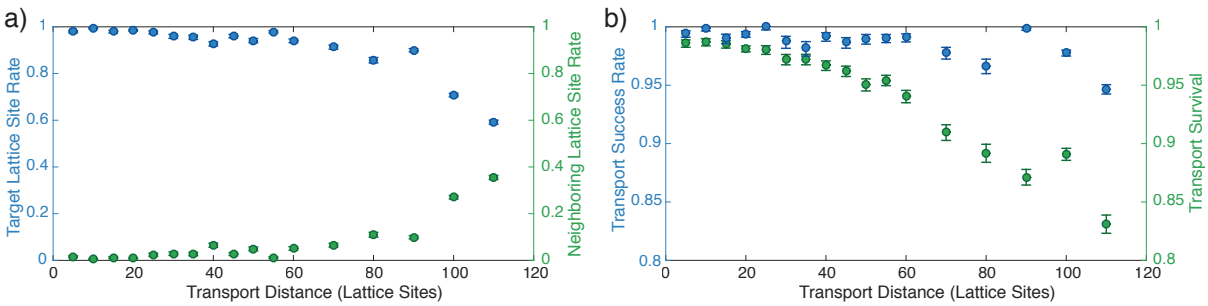

Figure 3.7: Transport success rate measurements: **(a)** The blue dots represent the fraction of atoms which reaches the exact target location for increasing transport distances, whereas the green dots represent the fraction of atoms which are detected in one of the neighboring lattice sites. **(b)** The blue dots represent the combined transport success rate (target and neighboring lattice sites), whereas the green dots indicate the probability of a single atom to remain trapped during the transport operation.

In section 3.3.1 we will verify that our PS optical lattice allows us to transport atoms over several tens of lattice sites with single lattice site precision without creating vibrational excitations. These transport operations embody a crucial part in the generation of low-entropy states, which are discussed in sec. 3.3.3. Furthermore, the preparation of low-entropy states or also pairs of atoms (see sec. 3.3.4) requires us to employ real time feedback. For this purpose we developed a novel control software for the experimental apparatus, which allows us not only to realize real time feedback, but also fully automizes most experimental sequences. This control software and specifically the part which is utilized to sort individual atoms is introduced insection 3.3.2.

3.3.1 Classical Atom Transport

Our newly developed PS optical lattice overcomes the shortcomings of previous implementations [113, 277] which e.g. were limited to a simultaneous displacement of both sub-lattices in opposite direction by rotating the linear polarization of one of two counter-propagating laser beams with an electro-optical modulator (EOM). The EOM based spin-dependent transport, furthermore, also suffers from a maximum achievable separation of the σ^+ and σ^- lattice by one lattice site. Therefore, additional spin-flips are required to transport an atom over several lattice sites [277]. These in turn substantially limit the transport efficiency as it decreases exponentially with the number of transported lattice sites. Even with the best reported efficiency of 99 % per shift operation [277], the transport efficiency over 20 sites had never exceeded $0.99^{2 \cdot 20} \approx 67\,\%$.

In order to attest the reliability of our PS optical lattice – in comparison to previous implementations – we measure the transport efficiency by translating spin-polarized atoms in $|\uparrow\rangle$ using a single adiabatic transport operation over 20 lattice sites. The atoms are initialized in $|\uparrow\rangle$ employing optical m_F-state pumping (see sec. 2.3.1) and their position determined before and after the transport operation using fluorescence imaging, as discussed in section 2.2.3. Using this procedure we obtain a transport efficiency of $(97.4 \pm 3)\,\%$, where the remaining unsuccessful events can be attributed to optical pumping errors (0.4 %), spin-flips during transport (0.6 %) and position reconstruction errors (1.6 %).

Additional measurements, summarized in figure 3.7, show that the transport efficiency remains well above 95 % for transport distances of up to 100 lattice sites. Each dot in figure 3.7(a) represents the result from a single transport efficiency measurement: the blue dots represents the fraction of atoms which reaches exactly the target lattice site, whereas the green dots represent the fraction of atoms which are

detected in one of the neighboring lattice sites. The decreasing transport efficiency for larger distances is not a result of the PS optical lattice not being shifted far enough, instead this reduction is caused by an outdated version of the position reconstruction algorithm, which was not reliable for distances of more than 50 lattice sites. In fact, these results inspired an improvement of the reconstruction algorithm, which we reported in Alberti et al. [2]. Instead of using a single LSF for the entire field of view, the improved algorithm accounts for spatially varying optical aberrations by reconstructing the atoms' positions with different LSFs, depending on their absolute position in the optical lattice. Figure 3.7(b) shows the combined – target and neighboring lattice site – transport efficiency (blue dots) as well as the probability of an atom to survive the transport operation (green dots). We notice an increased probability to lose an atom during the transport operation for distances over 50 lattice sites. This is not an intrinsic problem of the employed transport operations, but rather a direct consequence arising from the discretization of the transport ramp generated by the DDS. The currently employed DDS is limited to 1024 phase points per transport operation, hence, when transporting atoms over larger distances the atoms no longer "feel" a smooth ramp, but instead receive individual kicks each time the phase is updated. Our newly developed versatile digital frequency synthesizer [106] will hurdle down this shortcoming, since it is capable of storing two orders of magnitude more phase points.

Measuring Transport Excitations Using Sideband Spectroscopy

In the following section we will make use of the sideband spectroscopy tools we introduced in section 2.5.2 to quantitatively measure the probability to create a longitudinal or transverse excitation as a result of the transport itself. For this purpose we first cool the atoms into – or close to – their vibrational ground state (see sec. 2.5.2), which also initializes all atoms in $|\uparrow\rangle$. Then we translate the σ^+ lattice using a 1 ms long sinusoidal phase ramp, which leads to an adiabatic acceleration and deceleration of the transported atoms. Directly after the translation we employ either microwave radiation to probe the longitudinal vibrational occupation (see sec. 2.5.2), or Raman laser radiation to probe the transverse vibrational occupation (see sec. 2.5.2). The resulting mean vibrational occupation (see eq. (2.51)), as a function of the transport distance, is displayed in figure 3.8(a) for the longitudinal direction and in figure 3.8(b) for the transverse direction, respectively. It is noteworthy that we have to be careful when trying to interpret the mean vibrational occupation according to equation (2.51): if we cool all atoms truly into their vibrational 3D ground state, the corresponding distribution would no longer be described by a thermal Boltzmann distribution, which is one of the assumptions in the derivation of equation (2.51). Furthermore, excitations caused by transport operations cannot be classified as a thermal heating process, instead they need to be regarded as a coherent operation, which raise the vibrational level. However, we will use $\bar{n}^{\mathrm{L/T}}$ as a measure for the analysis summarized in figure 3.8, since we measure no impact of the transport on the vibrational excitations along the longitudinal direction and only a marginal one in the transverse one ($< (9 \pm 3) \times 10^{-3}$ excitations per transported lattice site), .

Loss-Free State Detection

Our PS optical lattice also opens up a way to infer the atoms' qubit state, without removing some of the atoms from the lattice. This is achieved by mapping the spin information onto the position of the atom which enables us to detect both internal states for every probed atom, thus eliminating the shortcoming of push-out detection (see sec. 2.3.1) typical of single atom interferometers [114]. Furthermore, this state detection technique allows us to infer the qubit state during an experimental sequence, which is a fundamental prerequisite for the experiments presented in chapter 4. Lastly, we can also use the transport fidelity measurements – presented above – to precisely characterize the m_F-state pumping success rate.

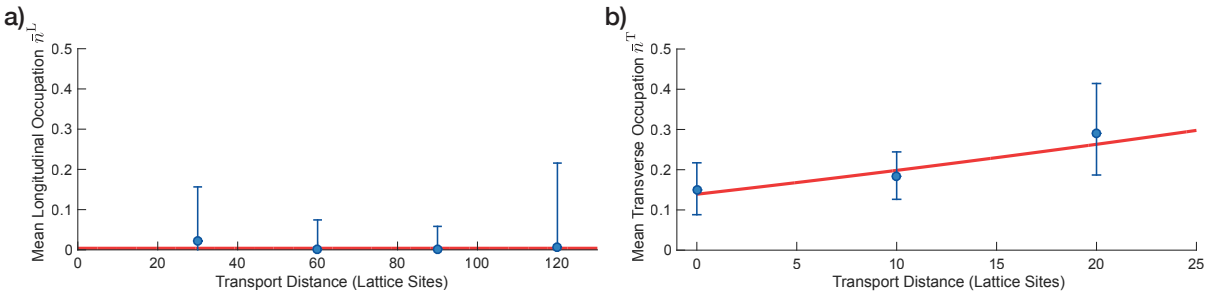

Figure 3.8: Mean longitudinal **(a)** and transverse **(b)** vibrational occupation as a function of the transport distance. Obtained by performing sideband spectroscopy on an ensemble of atoms, which is initialized in $|\uparrow\rangle$, cooled close to the 3D ground state, and subsequently adiabatically transported by shifting the σ^+ lattice.

We analyze the fraction of atoms which remain in their initial position after the transport operation. The resulting state preparation success rate amounts to $(99.6 \pm 0.4)\,\%$.

3.3.2 A Novel Control Software and the Feedback Algorithm

Almost all experiments carried out with the experimental apparatus at hand, prior to those presented in this thesis, were obtained by employing static experimental sequences [66, 114, 126, 245]. However, the sorting of individual atoms in our PS optical lattice – and all experiments based on this technology – require real-time feedback, since we need to reprogram the hardware depending on the atoms' positions. For this purpose Jonathan Zopes and myself developed a novel control software – using Matlab [109] – which is not only capable of controlling all experimental hardware[16], but furthermore, also acquires and analyses data in real-time. In its current version it can conduct nearly all experimental sequences presented within this thesis automatically. This also includes periodically verifying that all required hardware is operational (e.g. laser locks) and several fully automized calibration methods, spanning from simple task (e.g. the optical lattice depth, or adjusting the relative phase of our PS optical lattice) to more complex ones (e.g. calibrating the magnetic field gradient using the method introduced in sec. 2.3.4) [188]. Such an automatization of the measurement and analysis procedure is inevitable, considering that modern experiments are becoming increasingly complex [278]. In the following we will discuss the feedback algorithm, which is employed to control the position of individual atoms utilizing our PS optical lattice. This algorithm essentially consists of two stages: the first stage of this algorithm ensures that N well separated atoms are stored in the optical lattice, whereas the second stage rearranges these atoms until the target ensemble is generated.

Initially, the atoms are stochastically loaded from a magneto-optical trap into the spin-dependent optical lattice (see sec. 2.1). The feedback algorithm infers the number and position of these atoms by recording fluorescence image, which is analyzed using the super-resolution algorithm introduced in section 2.2.3. If more than the required number of atoms are loaded into the optical lattice the qubit state of the rightmost N atoms is flipped from $|\uparrow\rangle$ to $|\downarrow\rangle$, which allows us to remove all additional atoms from the optical lattice with the spin selective push out laser beam (see sec. 2.3.1). The local addressing of individual atoms is achieved by the spectrally narrow microwave pulses in combination with a weak magnetic field gradient, which we introduced in section 2.3.4. Alternatively, if the number of atoms is lower than required by the desired target ensemble, or if the interatomic separations are below $d_{\mathrm{MW}} = 20$

[16] Up until today more than 16 different devices are controlled through a variety of interfaces, including PCI, PCIe, ethernet, USB, GPIB, and serial port [188].

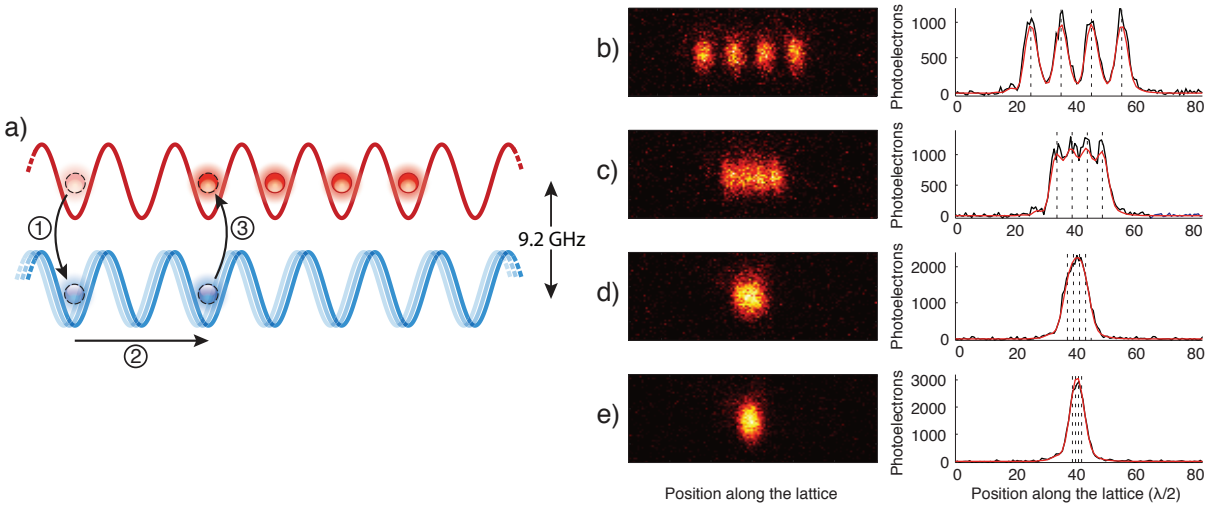

Figure 3.9: Atom sorting in polarization-synthesized optical lattices. **(a)** Central building block of the atom sorting procedure: (1) the leftmost atom (marked by the dashed circle) is transferred from the *storage register* (upper lattice) into the *shift register* (lower lattice) by a microwave pulse, (2) transported by two sites to the right by shifting the lower lattice, (3) and transferred back into the storage register. **(b)** - **(e)** From top to bottom, four atoms deterministically placed at equidistant separations of $d_{\text{target}} = (10, 5, 2, 1)$ lattice sites. Left panels: recorded single-shot fluorescence images. Right panels: vertically integrated distributions with the fitted intensity profiles (continuous red curves) and the reconstructed positions (vertical dashed lines). This figure is originally published in Robens et al. [3]

lattice sites, the algorithm automatically loads a new ensemble of atoms into the optical lattice. The minimal separation d_{MW} in between atoms ensures a probability $< 1\,\%$ that local addressing pulses spin-flip a neighboring atom (see sec. 2.3.4).

The second stage of the feedback algorithm consecutively rearranges the separated N atoms by first computing the required transport operations from a fluorescence image and then iteratively repeating the following procedure, which is illustrated in 3.9(a): Optical m_F-state pumping prepares all atoms in the storage register (σ^+ lattice). Subsequently one atom is transferred from the storage register into the shift register (σ^- lattice) using the local MW addressing technique. Finally the transferred atom is repositioned to its target location by translating the shift register. A total of $N - 1$ addressing and shift operations are required to generate the target ensemble, since the translational invariance of the optical lattice allows us to define the rightmost atom as a reference point. After resorting all atoms the feedback algorithm records a final fluorescence image to verify whether the atom positions coincide with the target ensemble. If errors are detected in the final distribution (e.g., imperfect spin-flips, wrong position reconstruction, atom losses), the feedback algorithm attempts to correct them.

3.3.3 Unity Filling in Polarization-Synthesized Optical Lattices

The principal result of the atom sorting is shown in figure 3.9: four cesium atoms from a dilute thermal ensemble are rearranged into a predefined, ordered distribution inside a 1D optical lattice. The fluorescence images in figure 3.9(b-e) show the final distribution of atoms for four different target patterns, including unity filling of a region of the lattice, which were obtained by employing the feedback algorithm described in the preceding section

Since we require N atoms to remain trapped during $O(N-1)$ addressing and positioning operations, the efficiency of the sorting procedure scales as P^{N^2}, yielding a super-exponential decay with the probability P of a single atom to remain trapped in the optical lattice after each operation. Similarly, we find an exponential decay with the addressing and transport fidelities. While the number of atoms that can be prepared in arbitrary positions, is fundamentally not limited, experimental imperfections currently restrict the attainable ensemble size to $N \approx 4$, with a success rate of circa 10 % for $N = 4$. The main limitations of this success rate arise from heating of atoms (see section 2.1.2), a limited addressing fidelity of the local MW addressing pulses ($A \approx 86\,\%$, see section 2.3.4) arising from decoherence by differential light-shifts [189], and transport errors resulting from position detection errors (see section 3.3.1). Heating of atoms is not only caused by the previously mentioned phase noise of the DDS but also by a discretization problem arising from a limitation of 1024 phase points per transport operation, which we discussed in section 3.3.1. Utilizing the latest generation of DDS chips we expect to reach a probability for a single atom to remain trapped in our PS optical lattice of $P > 99\,\%$.

So far we have not considered using a reservoir of atoms, which provides compensation for those atoms that get lost during the sorting. However, in our one dimensional optical lattice and relying on a magnetic field gradient to realize local addressing of atoms we cannot benefit much from an additional reservoir. Even in the best possible case we will be limited to 10 well isolated atoms, since we require a minimal addressing separation of $d_{\mathrm{MW}} = 20$ lattice sites. A theoretical investigation conducted by Weiss et al. [265] concluded that atoms can be compactified more efficiently in higher dimensions. According to their work, the scaling of the required number of sorting operations for N atoms in d dimensions is given by $N^{\frac{1}{d}}$. This would require us to carry out 25 sorting operations to compactify 100 atoms in a two dimensional lattice [279]. However, their algorithm was developed at a time, where state-dependent transport over several tens of lattice sites was not conceivable and, hence, it does not include the transport operations our PS optical lattices can perform. In the following, we will briefly discuss an efficient sorting algorithm which is tailored to the next generation experimental apparatus utilizing a two-dimensional PS optical lattice [149]. In comparison, our algorithm requires on average only 3 sorting operations to create a region of 10×10 lattice sites with unity occupation.

Outlook: Sorting Atoms in a Two-Dimensional State-Dependent Optical Lattice

Before we discuss the idea of the algorithm let us first make both a conservative and an optimistic estimate of the expected addressing fidelity and atom storage time of the new experimental apparatus. This apparatus will host our new high-NA objective lens, which we introduced in section 2.2.4. The objective lens achieves a diffraction limited resolution of 460 nm, which significantly boosts the localization precision (see sec. 2.2). Consequently, we expect to determine the lattice-site positions of single atoms with high reliability even for image acquisition times below 50 ms. Furthermore, the high-NA objective lens enables us to utilize state of the art single addressing of individual atoms by using a focussed laser beam to create local AC-Stark shifts [200]. It was just recently demonstrated by Wang et al. [67] that the fidelity of this technique can exceed 99 %. Consequently, we will assume a fidelity of 90 % for our conservative estimate and 99 % for the optimistic one. Since the storage time is essentially only limited by the rate at which atoms collide with the background vapor, we can estimate a storage time between 60 s and 360 s (see sec. 2.1.2). Initially the atoms are randomly distributed the 2D optical lattice, which we will assume to be 100×100 lattice sites [149]. The filling factor of the lattice can vary from 20 % to 65 % – determined by how many atoms are initially captured by the magneto-optical trap. Anticipating the results presented in the following section, in our experimental apparatus, light-assisted collisions can lead to initial filling factors of 65 %. Furthermore, Grünzweig et al. [280] demonstrated that filling factors exceeding 80 % can be realized using an additional blue-detuned laser beam.

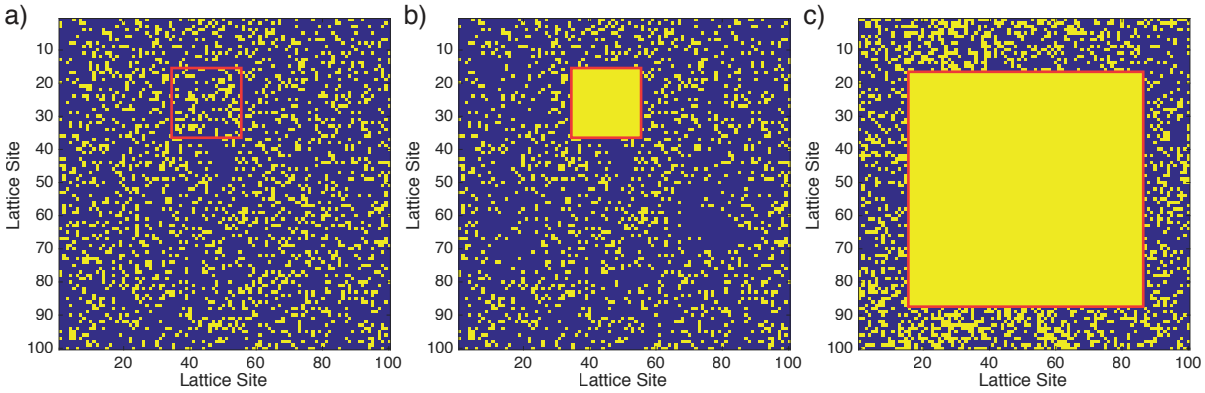

Figure 3.10: **(a)** Randomly distributed atoms in a 2D optical lattice with 20 % filling. The red square represents the densest 21×21 region. **(b)** Conservative estimate: unity occupation of 400 atoms (21×21) obtained after 12 sorting operations. **(c)** Optimistic estimate: unity occupation of 5 000 atoms (71×71) obtained after 16 sorting operations.

The first step of the 2D sorting algorithm is to analyze the initial atom distribution and identify the densest region, which is illustrated by the red square in figure 3.10(a). In the iterative stage the algorithm creates a mask of the remaining holes in the ensemble and searches the reservoir for a region which best matches the hole pattern. Single site addressing transfers all required atoms from the storage into the shift register, which are then shifted to the target location using a single transport operation. A subsequent fluorescence image detects possible errors, before the algorithm enters the next iteration. For a filling factor of 50 %, each iteration will reduce the remaining holes in the target assemble by $1/2$, leading hence, to a logarithmic scaling of the algorithm. However, due to entropy, occasionally there exist a pattern of atoms in the reservoir which matches particularly well with the holes in the target, allowing the algorithm to converge even faster.

In the case of our conservative estimate (addressing fidelity 90 %, storage time 60 s, initial filling 20 %) it is conceivable to create unity filling in a region of 21×21 lattice sites in less than one second (on average 12 iterations), which is illustrated in figure 3.10(b). Furthermore, figure 3.10(c) displays the outcome for the optimistic estimate (addressing fidelity 99 %, storage time 360 s, initial filling 65 %), which allows us to achieve unity filling in a region of 71×71 lattice sites in less than one second (on average 16 iterations). While it is likely that there exist even further optimized sorting algorithms, these results highlight the scalability of our PS optical lattices, especially in comparison to recent results using micro potentials [18, 19].

3.3.4 Pair Production and Parity Projection in Polarization-Synthesized Optical Lattices

Beyond preparing unity filling, we demonstrate that the same atom sorting technique can be applied to deterministically prepare a pair of atoms in the same lattice site. We will see in the following, that our measured efficiencies ($P_{\text{succ.}} > 90\,\%$) exceed state of the art results, obtained by overlapping two micro-potentials via spatial light modulators [281]. An efficient method of generating atom pairs is of particular interest, since it embodies one of the two indispensable building blocks of our Hong-Ou-Mandel experiment (see section 5.2) and, further, represents a fundamental prerequisite to study atom-atom interactions occurring via ground-state collisions [110, 113].

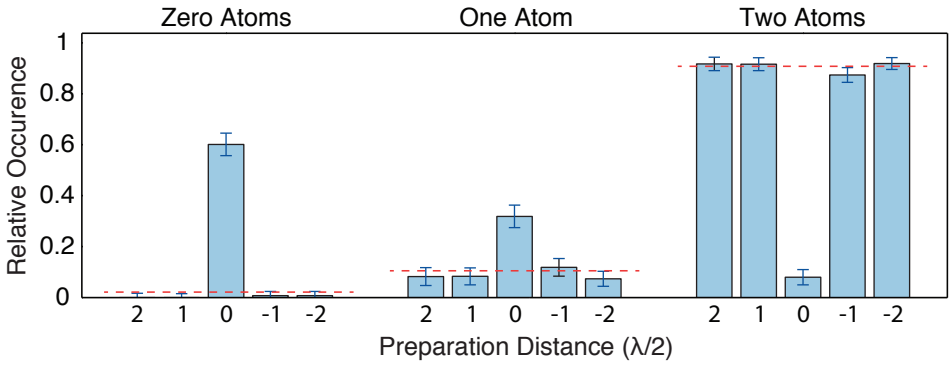

Figure 3.11: Probability of zero-, one-, and two-atom events for final interatomic separations $d_{\text{final}} = [\pm 2, \pm 1, 0]$. The dashed red line corresponds to the theoretical expectation of losses, which are uncorrelated with light-assisted collisions. The errors are estimated using the Clopper-Pearson method ($\alpha = 0.32$) and each preparation distance comprises approximately 150 individual measurements. This figure is adapted from Zopes [188]

In the preceding section we discussed that our position reconstruction algorithm becomes less reliable for interatomic distances beyond 100 lattice sites. For the pair production, we circumvent this shortcoming by first preparing two atoms at fixed absolute positions in our PS optical lattice with an interatomic separation of $d_{\text{initial}} = 20$ lattice sites. Once the initial configuration is achieved, both atoms are optically pumped, the left atom transferred into the shift register, which is then transported to position of the right atom. We probe the final distribution by recording a fluorescence image. It is not possible to directly observe two atoms in the same lattice site using the fluorescence imaging. During the imaging process atoms in a common lattice site undergo collisions, which are induced by the illumination lasers themselves [282]. These light-assisted collisions lead to the loss of either one or both of the collision partners on timescales much shorter (100 µs [283]) than the exposure time which is on the order of 1 s [284]. In fact, in a variety of experimental setups from other groups (e.g. [17, 259, 283]) light-assisted collisions lead to a nearly perfect parity projection of the atom number which occupies a single lattice potential well: if the atom number is even all atoms are lost, while an odd number leaves always a single atom behind. However, this strongly depends on the experimental parameters, including the atom species, the depth of the optical potential, as well as frequency and intensity of the illumination lasers [284]. Therefore, we additionally conduct reference measurements by transporting the left atom not exactly into the same lattice site as the right one, but displaced by $d_{\text{final}} = [\pm 2, \pm 1]$ lattice sites.

Figure 3.11 displays the relative occurrences at which we observe either two, one, or zero atoms in the last fluorescence images for both the pair production and reference measurements. These rates show a significant discrepancy between the pair production and the reference measurements. However, our measurements reveal that light-assisted collisions for the experimental apparatus at hand do not lead to flawless parity projection. Instead, we observe significantly more cases where a single atom remains in the optical lattice.

The reference measurements agree well with the probability for k out of 2 atoms to remain trapped in the optical lattice – uncorrelated with light-assisted collisions. The probability is given by the following binomial distribution (see dashed lines in fig. 3.11):

$$S(k) = \binom{2}{k} (1 - S)^k S^{2-k}. \tag{3.8}$$

Furthermore, we can use the uncorrelated probability S of a single atom to remain trapped, to construct a simple model for the pair production events. This model, in turn, allows us to extract the rate P_{LAC}, at which we loose either one or both atoms due to light-assisted collisions, as well as the success rate $P_{\mathrm{succ.}}$ of successfully generating an atom pair:

$$\text{Probability that:} \begin{cases} 0 \text{ atoms survive} = (1-S)^2 + S^2 P_{\mathrm{succ.}} P_{\mathrm{LAC}} \\ 1 \text{ atom survives} = 2S(1-S) + S^2\, P_{\mathrm{succ.}}(1-P_{\mathrm{LAC}}) \\ 2 \text{ atoms survive} = S^2(1-P_{\mathrm{succ.}}) \end{cases} \tag{3.9}$$

Applying this model to the data presented in figure 3.11, yields a success rate of $P_{\mathrm{succ.}} = (91 \pm 3)\,\%$ and $P_{\mathrm{LAC}} = (71 \pm 5)\,\%$. Therefore, if we image two atoms in the same lattice site, we have a 70 % chance to loose both atoms due to light-assisted collisions, whereas in the remaining cases a single atom remains in the optical lattice. The extracted success rate $P_{\mathrm{succ.}}$, to create a pair of atoms in a common lattice site using our PS optical lattice, demonstrates a significantly improvement in comparison to previous results achieved by our group. Using the EOM based spin-dependent transport the best reported success rate is $P_{\mathrm{succ.}} = (37 \pm 8)\,\%$ [53] and by employing two crossed optical lattices $P_{\mathrm{succ.}} = (16 \pm 4)\,\%$ [266].

3.4 Coherent Delocalization of the Atomic Wave Function

The transport operations we discussed in the preceding sections can all be classified as classical transport: we transported a single atom trapped in a quantized optical potential, however, so far coherences did not play an essential role in the transport, since we exclusively transported atoms in pure states ($|\uparrow\rangle$ and $|\downarrow\rangle$). In the following we will discuss how we utilize our PS optical lattice to achieve quantum transport, which allows us to coherently delocalize the atomic wave function. However, for coherent transport we cannot make use of the adiabatic transport operations we employed so far, simply because they last longer than our coherence relaxation time T_2 ($250\,\mu\mathrm{s} < 1\,\mathrm{ms}$). Instead, we make use of the so-called bang-bang technique [272], which allows us to transport an atom over one lattice site within $20\,\mu\mathrm{s}$ without creating motional excitations. This technique has been routinely employed by our group for several years [66, 116, 209]. In its core, it consists of two well timed delta-like kicks onto the atoms by abruptly accelerating and decelerating the optical lattice. The time in between the two kicks must be chosen exactly as an integer multiple of the atoms' longitudinal oscillation period $1/\nu_{\mathrm{L}}$. More recently, we investigated optimal control theory, which allows us to decrease the transport time even further (see sec. 3.4.2).

3.4.1 Discrete-Time Quantum Walks

Introduced by Richard Feynman to model the one-dimensional motion of a spin-1/2 particle [285], discrete-time quantum walks can be regarded as the archetype of quantum transport experiments. While quantum walks share many similarities with classical random walks, the behavior of these two transport paradigms is strongly different [286].

In a "classical", one dimensional, random walk scenario, a particle moves in discrete steps, either leftward or rightward, with the direction determined by the result of a coin toss. After iterating the sequence of coin toss and subsequent displacement n times, one finds the binomial distribution $\binom{n}{x}/2^n$ describing the motion of the particle simply by enumerating the trajectories terminating in position x. The Brownian motion of colloidal particles suspended in a liquid is a well-known example of this type of diffusive classical transport. Discrete-time quantum walks are the quantum analog of "classical" random walks. As shown in figure 3.12(a), a quantum walker, rather than tossing a real coin, is put at every time

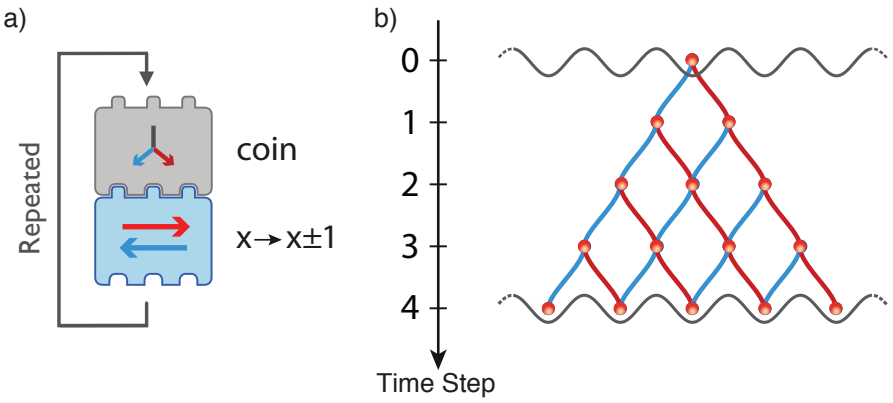

Figure 3.12: Discrete-time quantum walks in position space. **(a)** Discrete unitary operations defining the quantum walk's step. **(b)** Delocalization of the quantum walker over multiple paths. The number of paths increases exponentially with the number of time steps. This figure is originally published in Robens et al. [4]

step in a coherent superposition (coin operation) of the qubit states, $|\uparrow\rangle$ and $|\downarrow\rangle$, and it is subsequently shifted by one lattice site in a direction subject to the spin state (spin-dependent shift operation), e.g., $|\uparrow\rangle$ to the left and $|\downarrow\rangle$ to the right. Since the first realization of quantum walks by our group [66, 116], quantum walks were experimentally realized by several other groups using different physical systems, including trapped ions [287, 288] and photons [289–291].

In our experimental apparatus, we realize the coin operation by using microwave radiation that resonantly couples the two hyperfine states (see sec. 2.3.3). This allows us to achieve any arbitrary unitary transformation of the pseudo spin-1/2 with the coin operation. The most frequently used coin, however, is the Hadamard coin, which produces an equal superposition of the two spin states (coin angle equal to $\pi/2$). The spin-dependent shift operation is realized by employing our PS optical lattice, which moves the atom by one site rightward or leftward depending on the internal state. After applying both operations the trajectory of an atom will thus be split, giving rise to a beam splitter operation of a single atom interferometer [209].

After iteratively repeating the coin and shift operation, the matter wave spreads over multiple trajectories in position space, as illustrated in figure 3.12(b), producing a complex multi-path interference effect. The resulting probability distribution measured after a twenty-step quantum walk is shown in figure 3.13, where originally the walker was prepared in site $x = 0$ and in the $|\uparrow\rangle$ state. The prominent peak on the left-hand side provides signature of multi-path interference. Furthermore, the quantum walk spreads ballistically with the number of time steps n in contrast to a classic random walk, which spreads diffusively with a Gaussian distribution of width $\sqrt{n}$. Decoherence reduces the interference contrast, turning the quantum walk into a classical random walk. The number of coherent steps is primarily limited by decoherence arising from light shifts [189], which is expected to vanish with the atoms cooled to the three-dimensional ground state of the optical lattice (see section 2.5).

3.4.2 Outlook: Speeding It up with Optimal Control

All experimental results presented in this thesis, which make use of coherent transport operations (e.g. the quantum walk presented in figure 3.13), were obtained using the bang-bang technique [272]. However, from an experimental point of view it would be desirable to improve upon two characteristics of this technique: (1) While the transport operation using the bang-bang technique is significantly faster than the

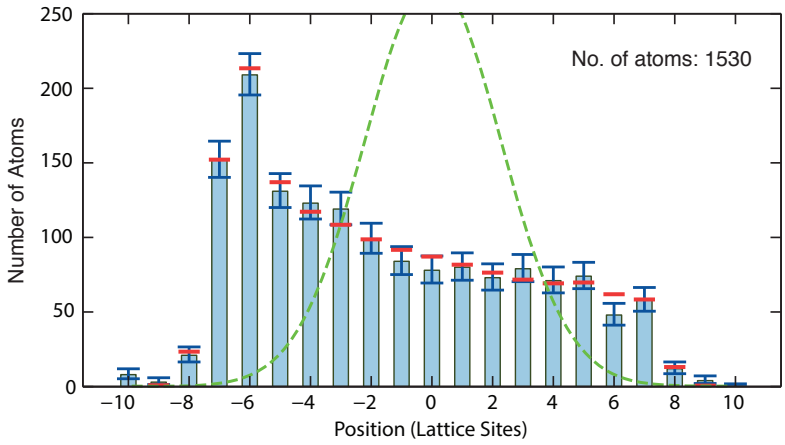

Figure 3.13: Discrete-time quantum walks of single cesium atoms. Probability distribution of single atoms after 20-step quantum walks. Bars with confidence intervals are the experimental data, short horizontal lines are the theoretical prediction with about 5% coherence loss per step [189]. Dashed line is the prediction for a random walk (no coherence). This figure is originally published in Robens et al. [4]

adiabatic transport operations we discussed in section 3.3.1 ($20\,\mu s \ll 1$ ms), any further reduction of the transport time directly allows us to increase the number of coherent operations (e.g. the number of steps in a quantum walks) in an experimental sequence. (2) The bang-bang technique is particularly sensitive to small changes in the trap depth [53], which, in turn, requires us to frequently readjust the transport operation. With the ever increasing complexity of prospective experiments, it is therefore beneficial if the transport operation would be intrinsically insensitive to deviations of experimental parameters.

A promising candidate to further improve the transport operation performance is optimal control, namely an open-loop approach, where external parameters are optimally shaped in order to steer the dynamics of the system in a predetermined way [292]. Since the dynamics of our system are well described by the Schrödinger equation, and furthermore, the response of our control parameters is experimentally accessible (see sec. 3.2), we can directly resort to methods from classical control theory [292]. Additionally, since we are optimizing a quantum system we specifically use the interference of several paths in the Hilbert space, which leads to excitation free transport, faster than what could be achievable with classical physics. Over the recent years several theoretical investigations have been carried out to optimize the transport of quantum particles, including optimal control methods [293], inverse engineering techniques based on Lewis-Riesenfeld invariants [294, 295], and via the spatial adiabatic passage technique [296–298] – the analog of the stimulated Raman adiabatic passage [299]. However, so far it is unclear whether these techniques lead to the fastest possible transport operation.

Antonio Negretti – with experimental support from our side – carried out an optimization [6], making use of the chopped random basis (CRAB) optimization algorithm [300], which aimed to improve the transport operations of neutral atoms the dynamics of which are controlled by our PS optical lattice. The CRAB optimization uses a truncated basis of randomized functions for the control parameters to reduce the dimensionality of the search space. In our case, we utilize the CRAB algorithm to optimize the overlap of the atomic wave function before and after the transport operation by adjusting the optical phases $\phi_{\uparrow/\downarrow}$ (see eq. (3.3)) and the potential depths $U^0_{\uparrow/\downarrow}$ (see eqns. (3.1)-(3.2)) of the PS optical lattice during the transport. The algorithm directly incorporates the finite response of all parameters using the response functions we obtained in sec. 3.2. Further details on the optimization can be found in Negretti

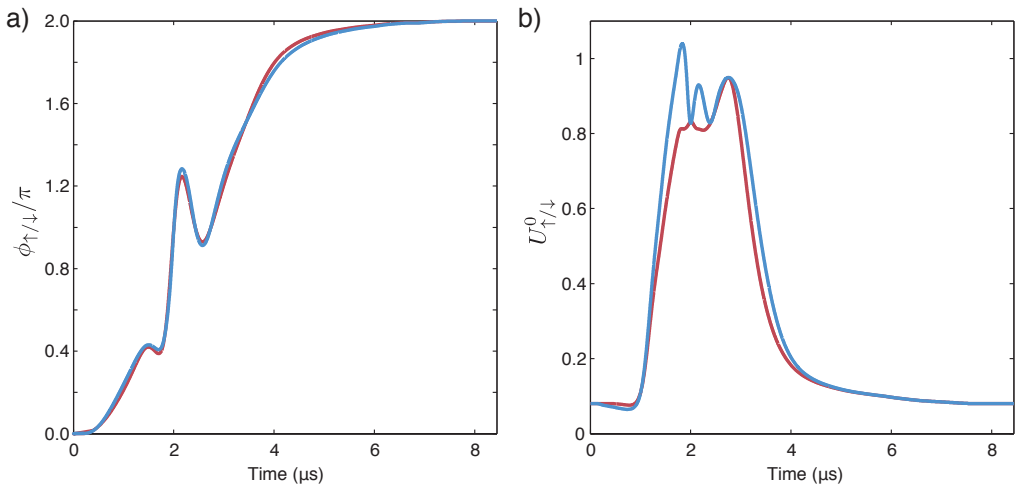

Figure 3.14: **(a)** Optimal phases as a function of time for a single lattice site transport. The red line corresponds to $\phi_\uparrow$, whereas the blue line to $\phi_\downarrow$. **(b)** Optimal lattice depths as a function of time for a single lattice site transport. The red line corresponds to $U^0_\uparrow$, whereas the blue line to $U^0_\downarrow$. The optimal transport time for this operation amounts to $T_{\mathrm{OPT}} \simeq 8.4\,\mu\mathrm{s}$. This figure is originally published in Negretti et al. [6]

et al. [6].

Figure 3.14 displays the optimized optical phases $\phi_{\uparrow/\downarrow}$ and potential depths $U^0_{\uparrow/\downarrow}$ for a transport operation, which shifts the two spin dependent potentials by one lattice site apart. The small differences in the curves for the σ^+ and σ^- lattice arise from the residual coupling crosstalk of the $|\downarrow\rangle$ state, which we discussed in section 2.1.3. The entire operation requires only 8.4 μs – more than a factor of two faster than the bang-bang like transport we employed so far. However, this is merely the starting point of what can be achieved with optimal control transport ramps: for example, we can also employ the algorithm to optimize transport operations which coherently delocalize the atomic wave function over several tens – or even hundreds – of lattice sites. At the current state, optimal control theory predicts that we can achieve excitation free transport over 10 lattice sites in 20 μs [6]. Such transport long distance transport operations make it feasible to realize a single atom interferometer with a macroscopic splitting of up to 1 mm.

CHAPTER 4

Ideal Negative Measurements in Quantum Walks Test Single-Atom Trajectories

The superposition principle is one of the pillars of quantum theory and it also constitutes a central resource in quantum metrology [301], quantum communication technologies [302], and quantum information processing [15]. Yet the same principle has been the source of heated discussions since the inception of quantum theory [303–313]: the central question of the long-standing debate is about the physical origin of the observed "definiteness" of macroscopic physical objects. In fact, while it is widely accepted that microscopic systems can live in superposition states, the fact that in a physical apparatus individual measurements always yield single, definite outcomes has so far eluded a comprehensive explanation [31]. For instance, the macroscopic apparatus of a Stern-Gerlach experiment always measures a definite orientation of the electron's spin, although the electron is, according to quantum mechanics, in a superposition of both spin orientations. To reconcile the definiteness of measurements with the Schrödinger equation, two plausible explanations have been advanced [33]: (1) Quantum superposition applies at all scales, even for macroscopic objects, and environment-induced decoherence is responsible for the emergence of so-called pointer states, to which the wavefunction is reduced ("collapses") with probabilities determined by Born's rule. (2) There exists a deeper, underlying theory which gives rise to coherent quantum evolution at the micro scale and yet well-defined trajectories at the macroscopic level, independently of the environment's influence. This second explanation advocates a "macrorealistic" description of nature as it implies that macroscopic physical objects follow classical trajectories.

In order to put the latter idea of "macrorealism" to the experimental test, Leggett and Garg (LG) derived a set of inequalities bounding the linear combinations of two-time correlation measurements [29]. In recent years, violation of LG inequalities has been shown in a wide range of physical systems spanning from superconducting qubits [314, 315] to photons [316–319], nitrogen-vacancy centers in diamond [320], nuclear spins [321], and phosphorus impurities in silicon [322]. However, these experiments are confined to test superposition states in a simple qubit system, which exhibits Rabi oscillations – far away from Leggett and Garg's original intention to probe macroscopic quantum superpositions.

Performing LG tests in more complex systems including also mechanical degrees of freedom – mechanical superposition states are the essential component of most macrorealistic models [323–325] – constitutes a major challenge: not only quantum superposition states become very fragile, but also new experimental methods must be developed to realize so-called 'ideal negative measurements' in these systems. Ideal negative measurements – namely, the ability to measure the physical object yet avoiding any direct interaction with it – are a prerequisite for any rigorous LG test, as without it, violations can

simply be attributed to an unwitting invasiveness on behalf of the experimenter, rather than to the absence of a realistic description [326]. Despite their importance, a rigorous implementation of this type of measurement has been demonstrated in just one of the many LG tests reported in the literature [322].

We will see in the following section, that we can achieve a 6σ (standard deviation) violation of LG inequality for a cesium atom performing a quantum walk (see sec. 3.4.1), in which the atom is coherently transported along a line in discrete steps in space and time. We obtain the violation by measuring the correlation between the atom's positions at successive times with measurements of the ideal negative type, which a devout realist would perceive as non-invasive. The capability of PS optical lattice, allowing state-dependent displacements of atoms over arbitrary large distances enables us to remove atoms depending on their position state and to realize, thus, a negative position measurement on the unshifted atoms.

Criteria for the assessment of the degree of macroscopicity of superposition states have long been discussed in the literature [327, 328]. There is a general agreement that the macroscopicity of a mechanical system increases with heavier masses and larger spatial separations of the superposition states. Although the atomic wavefunction of the cesium atom in our experiment spreads, at most, over a distance of 5 sites (2 μm), our results set the stage for future experiments testing the LG inequalities with objects of thousands of proton masses split over macroscopic distances (for a review see [329]). Furthermore, we remark that this work extends the experimental study of LG violations to quantum transport systems [330] with dynamics far richer than those of the hitherto-considered qubit systems.

4.1 The Leggett-Garg Inequality

The reconstructed probability distribution of a quantum walk (e.g. fig. 3.4.1) can be precisely explained with quantum mechanics in terms of interference of all trajectories that the particle is allowed to follow while moving from the initial to the final point. The agreement with experimental observations, in the spirit of Francis Bacon's inductive thinking, serves as an important piece of validation of quantum theory itself. However, according to Karl Popper's point of view, one must acknowledge that the remarkable fit between observations and quantum theory does not itself constitute a 'falsification' of the 'other' hypothesis – that an underlying probability distribution could conceivably describe, at all times, the position and the spin of the atom as elements of objective reality. Here is where the LG inequality becomes important, as it subjects the idea of realism to a rigorous, objective test by looking for violation of

$$K = \langle Q(t_2)Q(t_1)\rangle + \langle Q(t_3)Q(t_2)\rangle - \langle Q(t_3)Q(t_1)\rangle \leq 1, \tag{4.1}$$

where $Q(t_i)$ are real values with $|Q(t_i)| \leq 1$ assigned to the outcomes of a measurement performed at time t_i with $t_i < t_{i+1}$, and where $\langle \ldots \rangle$ denotes the average over many repetitions of the experiment. The derivation of this inequality essentially rests on two assumptions [331]: (A1) realism, as discussed above; and (A2) non-invasive measurability, which asserts the possibility to measure the system without affecting its future evolution. Both these assumptions are implicit in a realistic view of nature [29]; but of course, quantum mechanics holds to neither [332, 333]. However, to be a valid test of the LG inequality, it is sufficient to persuade whom already believes in (A1) that the measurement scheme used in the experiment complies with (A2). Otherwise, violations of equation (4.1) may be attributed to a trivial invasivity of the measurement [326]. To ensure this, Leggett and Garg put forward the concept of "ideal negative measurements" [29], which are well illustrated by the following example: Imagine that a physical object, like the atom, can be found in only two positions, $x = \pm 1$, and that we check the presence of the object at $x = +1$ without looking at $x = -1$. From the point of view of a realist, the absence of the object at $x = +1$ necessarily implies that $x = -1$ without ever having influenced the object during the measurement. By

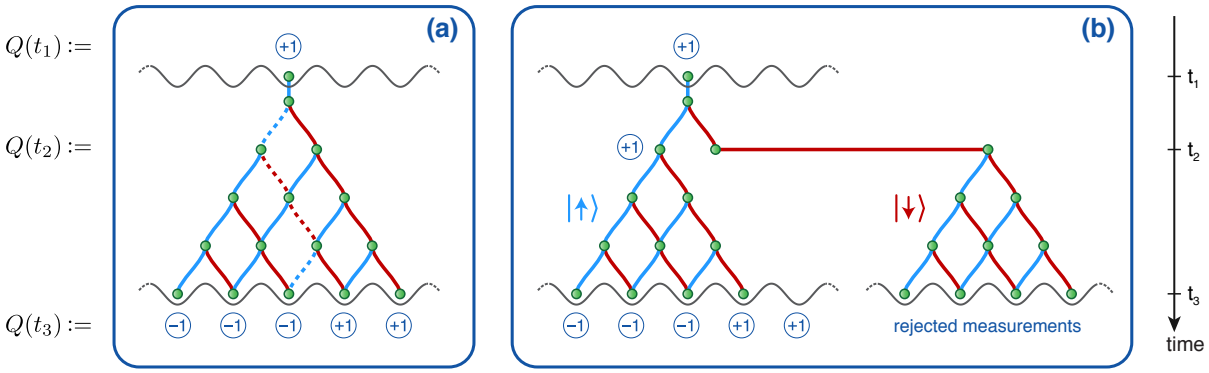

Figure 4.1: Ideal negative measurements test the non-classicality of quantum walks. **(a)** Schematic representation of a four-step quantum walk containing 16 possible trajectories, which according to quantum mechanics the cesium atom simultaneously follows. Conversely, upholders of realism believe that in each experiment the atom follows a definite trajectory connecting the initial and final point, *e.g.*, the dashed line shown in figure. The outcomes ± 1 of $Q(t_i)$ measurements are indicated with circles, where $Q(t_1)$ is identified with the initial state preparation, whereas $Q(t_2)$ and $Q(t_3)$ are related to position measurements. For instance, measurements at times t_1 and t_3 yields the correlation function $\langle Q(t_3)Q(t_1)\rangle$. **(b)** To measure the correlation function $\langle Q(t_3)Q(t_2)\rangle$, we use at time t_2 an ideal negative measurement scheme, which ensures the non-invasiveness of $Q(t_2)$: On condition that only atoms in $\downarrow$ state are transported at t_2 far away to the right, atoms in $\uparrow$ continue afterwards their walk undisturbed. In the case $Q(t_2)$ measurement has not removed the atom, measuring at t_3 the atom's position yields $Q(t_3)$ conditioned to the state $(\uparrow, x = -1)$ at t_2. Likewise, we obtain $Q(t_3)$ conditioned to $(\downarrow, x = +1)$ by transporting at t_2 the atom in $\downarrow$ far away to the left (not shown in the figure). This figure is originally published in Robens et al. [1]

repeating this measurement many times, probing the object either at $x = +1$ or $x = -1$ and discarding all measurements that directly reveal the object, we can thus measure correlations functions like $\langle Q(t_3)Q(t_2)\rangle$ without having ever meddled with the object itself at time t_2. Hence, any violation of equation (4.1) that arises from ideal negative measurements must imply a violation of the realist principles (A1) or (A2) – or both.

4.2 Quantum Walks Falsify Classical Trajectories

We base our experiment on a four-step quantum walk probed at times $t_1 = 0$, $t_2 = 1$, and $t_3 = 4$ steps, as displayed in the panels of Figure 4.1, where each step lasts around 26 µs. The three different measurements are defined as follows. We equate the first measurement $Q(t_1)$ with the state preparation in $(\uparrow, x = 0)$: fluorescence imaging first determines the initial position of the atom with single site resolution (see sec. 2.2), while sideband cooling slows the atom's motion to the lowest longitudinal vibrational state and concurrently polarizes the atom in $\uparrow$ state (see sec. 2.5.2). The translational symmetry of the optical standing wave allows us to safely label the initial position with $x = 0$. We designate $Q(t_1) = 1$. At time t_2, we measure the atoms' state, which is restricted to two possibilities, either $(\uparrow, x = -1)$ or $(\downarrow, x = +1)$, and we assign to this measurement the value $Q(t_2) = 1$ independently of the atom's internal state or position. The assignment of $Q(t_2)$ to a constant value is, in fact, one of the legitimate choices that are consistent with the condition $|Q(t_i)| \leq 1$ in the derivation of LG inequalities [331]. Finally, $Q(t_3)$ measures the atom's position at the end of the walk and returns the value -1 for $x \leq 0$ and value $+1$ for $x > 0$. According to quantum mechanics, with this definition of $Q(t_i)$ we expect a violation of the LG inequality yielding $K = 1.5$ (see sec. 4.2.1).

Quantum mechanics also shows that other designations of $Q(t_2)$ are possible to produce a violation of equation (4.1), for instance, by assigning the measurement outcome $(\downarrow, x = +1)$ to 1 and $(\uparrow, x = -1)$ to a certain value ξ with $|\xi| \leq 1$. While previous experiments [314–322] have adopted a dichotomic designations of $Q(t_2)$ (analogous to set here $\xi = -1$), we intentionally dropped such an extra condition to permit larger violations of the LG inequality as fewer constraints are imposed (cf. eq. (4.3) and eq. (4.4) in sec. 4.2.1). Such a constant designation especially reveals that the essential requisite to violate equation (4.1) is that the particle is measured at t_2, even though the result of the measurement itself is then discarded.

Because the measurement $Q(t_1)$ is a state preparation, and because we are not concerned about the atom's evolution after time t_3, only the measurement $Q(t_2)$ must be performed non-invasively. Since we are not allowed to directly image the atom at time t_2 because it would be invasive, we adopt an ideal negative measurement strategy that hinges on state-selective removal of atoms. This measurement scheme draws direct inspiration from the experimental realization of interaction-free measurements of the state of single photons [334]. The measurement scheme, which is illustrated in figure 4.1(b), proceeds as follows: if we want to non-invasively detect the atom's presence, say, in $x = -1$, we remove the atoms in the state $(\downarrow, x = +1)$ by transporting them far to the right, whereas we leave the atoms in the state $(\uparrow, x = -1)$ untouched. Providing this shift (set here to 5 sites) is larger than the distance covered by the atom between t_2 and t_3, the atom's position at the later time t_3 allows us to unequivocally mark the shifted atoms (which though remain trapped in the lattice potential) as effectively removed with confidence better than 99 %. Hence, the state-selective removal of atoms provides information about the atom's position at time t_2 and, at the same time, postselects those measurements that are carried out non-invasively.

In order to measure the LG correlation function, we note that with our assignment of $Q(t_i)$, the correlation function $K_{12} \equiv \langle Q(t_2)Q(t_1)\rangle$ is trivially equal to one. Furthermore, we have $K_{13} \equiv \langle Q(t_3)Q(t_1)\rangle = \langle Q(t_3)\rangle$, which quantifies the asymmetry of the final position distribution. Figure 4.2(a) shows the measured probability distribution of a four-step quantum walk with fair coin toss ($\theta = \pi/2$). The distribution is characterized by a pronounced skew to the left, which translates into a non-zero value $K_{13} = -0.57 \pm 0.05$. Although this asymmetry itself is often interpreted as a hallmark of "quantumness" [66, 287], we would rather eschew similar premature conclusions here. Using the law of total probability under assumptions (A1) and (A2), the final correlation function may be obtained as

$$K_{23} = \sum_{x=\pm 1} P(t_2; x)\langle Q(t_3)\rangle_x, \tag{4.2}$$

where $P(t_2; x)$ is the probability of finding the atom in x at t_2, and $\langle \ldots \rangle_x$ is the average over the distribution conditioned on a negative detection of the atom in x at t_2. Hence, we perform two separate experiments to measure K_{23}, one for each term of the sum in equation (4.2), as shown in figure 4.2(c). After rejecting all measurements during which atoms have provably been perturbed, we find $P(t_2; x = -1) = 0.506 \pm 0.026$ and $P(t_2; x = +1) = 0.494 \pm 0.026$. Averaging $Q(t_3)$ with the two conditioned distributions yields a value $K_{23} = -0.14 \pm 0.05$ close to zero. Taken together, the three correlation functions yield $K = 1.435 \pm 0.074 > 1$, which violates the LG inequality by about $6\,\sigma$ (standard deviation). The uncertainty is estimated to be purely statistical (see appx. sec. A).

4.2.1 Quantum Mechanical Prediction

A quantum mechanical calculation shows that, among the possible designations of $Q(t_i)$, the maximal violation of LG inequality is obtained by associating the measurements' results to the extremal values in the permitted range, that is, either $+1$ or -1. Other designations, e.g. $Q(t_3) = x/2$, would lead to a smaller upper bound for K.

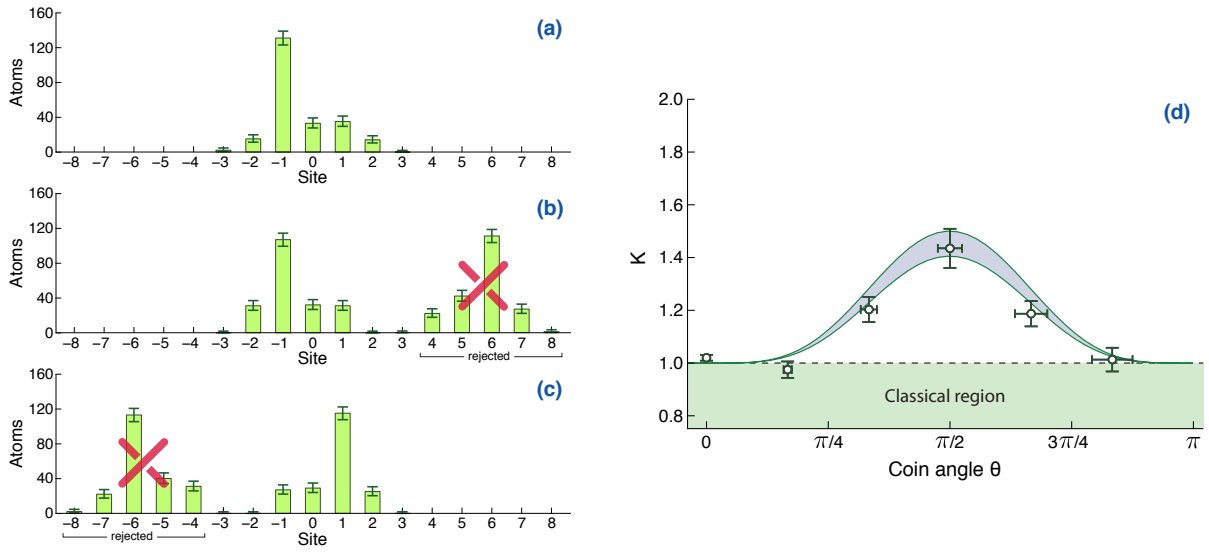

Figure 4.2: Violation of Leggett-Garg inequality probing a four-step quantum walk. The spatial distribution of single atoms is reconstructed by measuring their positions at time t_3: **(a)** If we do not observe which trajectory the atom has taken at t_2, the distribution exhibits a pronounced peak on the left hand side. However, when we conclude from an ideal negative result whether the atom at time t_2 was in **(b)** $x = -1$ or **(c)** $x = 1$, we obtain two distributions which resemble the mirror image of one other. The events in which the atom's position has been affected by $Q(t_2)$ measurement are recognized through the larger displacement and, thus, rejected. Because the overall number of probed atoms, 404, is the same in **(b)** and **(c)**, the retained events can be added together to produce the position distribution at t_3 conditioned on having measured the position at t_2. The sum distribution (not shown) is symmetric and differs strongly from the asymmetric distribution in (a). The vertical error bars represent 68 % Clopper-Pearson confidence intervals. (d) Leggett-Garg correlation measurement witnessing the degree of quantumness. Maximum violation occurs for a fair coin ($\theta = \pi/2$), while no violation occurs for classical transport at $\theta = 0$ and $\theta = \pi$. The solid lines is the theoretical prediction based on quantum mechanics of the LG correlation function K for a decoherence free quantum walk (upper curve) and for a quantum walk with 10 % decoherence per step (lower curve). The vertical error bars represent 1 σ uncertainty, while the horizontal error bars denotes a systematic uncertainty on the coin angle. This figure is originally published in Robens et al. [1]

With our prescription of $Q(t_i)$, we find for a four-step quantum walk an analytic expression of K as a function of the coin angle θ,

$$K = \frac{1}{16}\left[19 - 4\cos(2\theta) + \cos(4\theta)\right], \tag{4.3}$$

which is the curve plotted as the upper line in figure 4.2. Alternatively, with a dichotomic assignment of $Q(t_2)$ equal to -1 for $(\uparrow, x = -1)$ and to $+1$ for $(\downarrow, x = +1)$, we obtain

$$K = \frac{1}{32}\left[33 - 4\cos(\theta) - 4\cos(2\theta) + 4\cos(3\theta) + 3\cos(4\theta)\right], \tag{4.4}$$

which reaches the maximum value of approximately 1.31, in contrast to 1.5 corresponding to equation (4.3).

4.3 Measuring the Quantumness of a Quantum Walk

Besides the fundamental interest, LG inequalities also find application in quantifying the degree of "quantumness" of a system. This requires, however, that we abandon the standpoint of realists and, from now on, embrace quantum mechanics instead. Intuitively, the LG correlation function K may serve as an indicator, say a witness, of the amount of superposition involved in the system's dynamics. This idea of 'quantum witnesses' has recently been proposed as a method to discern quantum signatures in systems like biological organisms [335].

Owing to our particular definition of $Q(t_2)$, which is constantly mapped to 1, we prove a direct connection (see sec. 4.3.1) between LG inequalities and quantum witness formalism by identifying $W \equiv |K-1|$ with the first quantum witness introduced in Li et al. [335]. The deviation of W from zero indicates the degree of "quantumness" in the system's dynamics.

We provide demonstration of the quantum witness W in the four-step quantum walk by testing different types of coins, which differ in the probability of tails $p = \cos^2(\theta/2)$ and heads $q = 1-p$. For instance, $p = q = 1/2$ corresponds to the fair coin's situation, which has hitherto been considered. As displayed in Figure 4.2(d), we measure the LG correlation function K for different values of the coin angle θ, which is tuned by setting the duration of the coin's microwave pulse. The violation is maximal for $\theta = \pi/2$ (fair coin), when the coin maximally splits the walker's state at each step in an equal superposition of states. Instead, the violation vanishes for $\theta = 0$ and $\theta = \pi$, when the walk reduces to classic transport with no superposition involved.

4.3.1 Quantum Witness

The assignment $Q(t_2) = 1$, together with $Q(t_1) = 1$ by preparation, implies that the LG inequality (see eq. (4.1)) can be written in general terms as

$$K - 1 = \left(\sum_{x=\pm 1} P(t_2; x) \langle Q(t_3) \rangle_x \right) - \langle Q(t_3) \rangle \leq 0 \,. \tag{4.5}$$

This inequality is but one of a family of inequalities, and $K' = \langle Q(t_2)Q(t_1)\rangle - \langle Q(t_3)Q(t_2)\rangle + \langle Q(t_3)Q(t_1)\rangle \leq 1$ defines a similar, though independent inequality built from the same correlation terms [331]. With the choice of $Q(t_i)$ discussed here, we find that $K' - 1 = -(K-1)$. Taken together, these two inequalities imply that $W = |K-1| = 0$. The comparison with Li et al. [335] allows us to identify W as the first quantum witness in that work.

4.4 Witnessing the Decoherence of a Quantum State

Decoherence is ubiquitous in quantum systems [309] and, if controllable, offers a tuning knob to set the amount of "quantumness". We now employ the LG inequality as a tool to study spin decoherence – one of the most basic mechanisms that affect atoms trapped in optical potentials. To this end, we consider a Ramsey *in-situ* interferometry experiment for the spin, with the position degree of freedom being used only as part of the measurement scheme (see sec. 2.4.2). In this case, the lower dimensionality of the system (spin only) allows us to better illustrate the relationship between the violation of LG inequality and the fringe visibility of an interferogram [336, 337]. The system evolution is depicted in figure 4.3(a): We first prepare the atom in a certain lattice site in state $\uparrow$ (time t_1 with $Q(t_1) = +1$). We then apply a microwave $\pi/2$ pulse. In particular, when measuring the correlation term K_{23}, the internal state at time t_2 is non-invasively detected with the same ideal negative measurement scheme described above, except

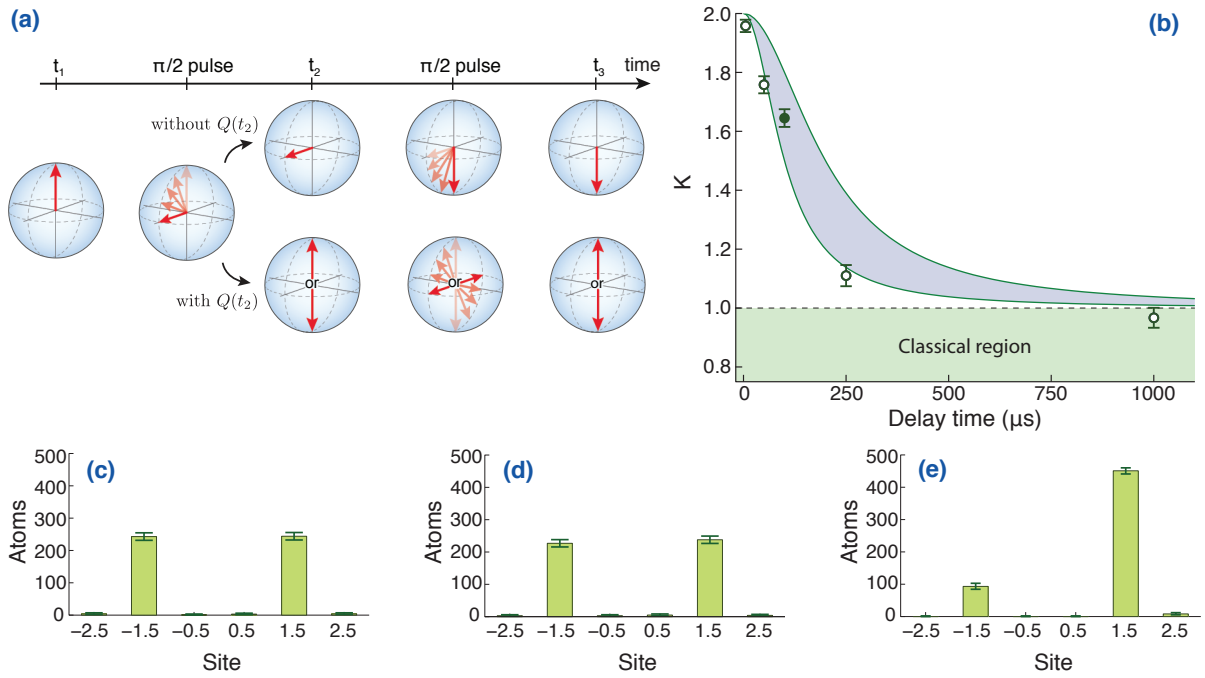

Figure 4.3: Leggett-Garg correlation measurement witnessing quantum-to-classical transition: **(a)** Evolution of the spin degree of freedom on the Bloch sphere during the Ramsey sequence detailed in the text (double arrows pointing in opposite directions indicate two equally probable spin orientations). **(b)** We measure a violation of LG inequality for an increasing amount of decoherence, which is controlled by varying the delay time between the two $\pi/2$ pulses. The upper and lower curve represent the theoretical prediction for coherence times of 75 µs and 200 µs, respectively, accounting solely for decoherence due to differential scalar light shift. Referring to the point indicated with a solid circle in **(b)**: **(c)** distribution of atoms' positions at t_3 in the case atoms in $\downarrow$ state are shifted apart at time t_2 (rejected atoms are not shown). **(d)** The same but with atoms in $\uparrow$ shifted apart. (e) Distribution of atoms' positions at t_3 with $Q(t_2)$ measurement omitted. Atoms occur at $x = -1.5$ because of spin decoherence. Error bars are defined as in figure 4.2. This figure is originally published in Robens et al. [5]

that here atoms are state-dependently transported away by 7 lattice sites. As done for quantum walks, we also map both values of the detected spin to the value $Q(t_2) = +1$. The dynamics of the atom is resumed with a second microwave $\pi/2$ pulse, after which the atom is shifted depending on the spin state to two separate positions in the lattice, 3 sites apart. Finally, the atom's position is detected and observable $Q(t_3)$ obtained: $Q(t_3) = +1$ for $x > 0$ and $Q(t_3) = -1$ for $x < 0$. Mapping the spin information onto the positions enables us to detect both internal states for every probed atom, thus eliminating the shortcoming of push-out detection typical of single atom interferometers (see sec. 3.3.1).

To investigate the effect of spin decoherence, we record the LG correlation function K while varying the time elapsed between the two Ramsey $\pi/2$ pulses. The results are shown in figure 4.3(b). For a minimum delay time of 5 µs, we record a value of $K = 1.958 \pm 0.033$, which violates the LG inequality by 21 σ (standard deviation). While this point lies very close to the decoherence-free prediction of $K = 2$, the recorded value of K decreases at longer delay times (i.e., larger decoherence) until it reaches the classical limit of 1.

The analysis of the experimental results help us understand the relation between K and the interference contrast C of the corresponding Ramsey interferometer, thus providing intuition about the quantum-to-classical transition of the LG correlation measurement. The measurement of K_{23} yields a vanishing value

independent of the delay time. In fact, according to quantum mechanics, the negative measurement $Q(t_2)$ provides complete which-way information and precludes interference at time t_3, see figure 4.3(c,d). As a result, $K = 1 + K_{23} - K_{13}$ is essentially determined only by the measurement of K_{13}, shown in figure 4.3e. Because this term is equal to the contrast C[1], the LG correlation function K of this experiment can be recast in the suggestive form $K = 1 + C$. This insight allows us to compare the experimental points in figure 4.3(b) with the fringes' visibility that is predicted for our system in the presence of dephasing due to differential scalar light shift in an optical standing wave [189], which we discussed in sec. 2.4.2.

4.5 Macroscopicity Measure and the Venalty

Our violation of the LG inequality proves that the concept of a well-defined, classical trajectory is incompatible with the results obtained in a quantum walk experiment. Yet, the concept of well-defined trajectories in position space can, in part, still be rescued providing one renounces locality. An example is provided by Bohmian mechanics, the predictions of which are equivalent to those of non-relativistic quantum mechanics [338]. In this interpretation of quantum theory, physical objects follow precise trajectories, which are guided by the universe's pilot wavefunction, that is, by a physical entity constituting a non-local hidden variable. It is therefore clear that Bohmian mechanics is not in contradiction with our findings since, from that point of view, assumption (A2) is not fulfilled.

Recently, a minimal macrorealistic extension of (non-relativistic) quantum mechanics has been put forward under general assumptions [328], which proposes a universal objective measure of macroscopicity accounting for both the mass and spatial separation of the superposition states. Within this model, we estimate a measure of macroscopicity for our experiment (see sec. 4.5) that lies in the range of typical cold atom experiments [329] – whether those be performed with thermal atoms or with a Bose-Einstein condensate. We remark, moreover, that the macroscopicity of our experiment is, coincidentally, on the same order of magnitude of experiments testing superpositions of macroscopic persisting currents [314, 329, 339]. In spite of the yet microscopic nature of the present LG tests, our result gives a conceptual demonstration that non-invasive measurement techniques can be applied to test the LG inequality, e.g., in double-slit experiments with genuinely massive particles by alternatively blocking at time t_2 either one of the two slits.

Unlike the test of Bell inequalities, where a loophole-free violation seems in reach [340], LG experiments remain susceptible to the so-called clumsiness loophole – even employing negative measurements. This loophole refers to the impossibility on behalf of the experimenter to exclude an invasivity of the measurements. Hence, it is appropriate to comment on the three main instances which can hinder the fulfillment of (A2) in our experimental set-up. (1) In the measurement of $Q(t_2)$, the state-dependent shift could cause vibrational excitations to the unshifted atoms. To avoid this problem, we deliberately set the shift duration to a time of 200 µs, which is much longer than than the period of the longitudinal motion of circa 10 µs. We measured the fraction of atoms that are left in the ground state by the shift process for both shifted and unshifted internal states (see sec. 3.3.1). In both cases, we obtained a fraction > 99 %, which is consistent with the precision of the initial preparation, thus confirming that no excitation is produced. The concept of venality, which has been introduced in Briggs et al. [322] to account for non-ideal negative measurements, can be applied to this effect as well, which is discussed in section 4.5. However, four our experimental apparatus the upper limit imposed on K is only slightly changed. (2) The duration of measurement $Q(t_2)$ is comparable to the spin coherence time. In principle, an equal delay

[1] The contrast of a Ramsey fringe, which is centered in the interval $[0, 1]$ is given by $C = 2p_\uparrow - 1$ (see also sec. 2.4.2), where $p_\uparrow$ is the maximum probability of detecting $|\uparrow\rangle$. Since the two Ramsey $\pi/2$ pulses are experimentally set to have the same phase, the correlation function reads $K_{13} = \langle Q(t_3)\rangle = p_\uparrow - (1 - p_\uparrow) = C$

time should also be included in the sequence when no measurement is performed at t_2. However, we have seen in section 4.4, using a Ramsey interferometer – instead of a quantum walk – produces also a violation of the LG inequality. (3) At time t_1, the motion of the atom in the transverse direction is prepared according to a Boltzmann-like distribution, which extends over the first hundred vibrational states. A statistical mixture is not a problem *per se*, providing the statistical properties are maintained constant. A realist, though, could raise the objection that the experiment "knows" which correlation term, either K_{13} or K_{23}, is being measured and exploits this information to prepare the transverse motion *ad hoc* in a way to counterfeit the violation of the LG inequality (cf. the hypothesis of so-called induction discussed by Leggett [327]). More generally, the same argument can also be invoked in the case of any hidden variable η, which, from an epistemological point of view, is tantamount to the transverse motion of the atoms. Eventually, to blunt this criticism, one could base the choice which correlation term to measure upon random events that are uncorrelated from the initial preparation [341, 342].

There is one further aspect of this LG test that must be emphasized, namely that we test single, individual copies of the system by probing one Cesium atom at a time. Prior experiments in NMR systems [321, 322] took an alternative approach by substituting individual measurements with measurements on a large ensemble of identical systems instead. Our approach *a priori* eliminates the need for the extra assumption that multiple copies of the system – even when positioned in near proximity – do not interact with each other. However plausible this hypothesis is in NMR systems, ignoring it would allow a realist to argue that the several copies of the system have interacted with each other – in particular with those copies that have been invasively measured, thus invalidating hypothesis (A2). In addition, employing ensembles instead of individual systems can lead to controversial interpretations, as is illustrated by the following examples. A wave-like analogue of quantum walks based on coherent electromagnetic waves (*e.g.* a laser beam [290]) is expected to produce a violation of the LG inequality similar to the one obtained with individual photons. In a similar way, even acoustic or surface waves could be used to measure a violation. However, it is certainly debatable whether an experiment hinging on Maxwell equations or mechanical waves can indeed rule out realism. In fact, to reach this conclusion, a realist should be first persuaded that light is composed of photons and waves of phonons.

In conclusion, our experiment gives a rigorous, quantitative demonstration of the non-classicality of a massive-particle quantum walk. The experiment also sets the basis for a test of LG inequality probing the positional degree of freedom over macroscopic distances. The interaction-free detection method of the atom's position can well be adapted to other systems like matter wave interferometers with large spatial splitting [343–345]. The ten-dimensional Hilbert space (5 lattice sites with 2 internal states each) of this LG test constitutes a significant advance beyond the simple two-level system, which has been so far investigated. Moreover, the multidimensionality of the Hilbert space [346] can be used in the future to approach the algebraic limit of the correlation function K, which is equal to 3. Finally, we should remark the illustrative value of this violation of the LG inequality, which puts the particle's trajectories in position space at the center stage.

Macroscopicity Measure

Nimmrichter et al. [328] have suggested a universal, objective measure μ that quantifies the amount of macroscopicity of a mechanical superposition state. In the proposed model, μ sets a lower limit for the time (expressed in logarithmic scale) during which an electron – chosen as the reference particle – behaves like a "wave" delocalized over distances larger than a certain critical classicalization length scale ℓ, which represents a phenomenological parameter. The length scale ℓ is defined in the model such that quantum superpositions of paths separated by less than ℓ preserve their coherence. We estimate for our experiment $\mu = \log_{10}(T\, M_{\mathrm{Cs}}^2/m_{\mathrm{e}}^2) \approx 6.8$ for values of ℓ shorter than the maximal separation,

2 µm, reached during the 4-step quantum walk. Here, M_{Cs} and m_{e} denote the masses of the cesium atom and of an electron, respectively, and T represents the overall duration of the quantum walk. For values of ℓ larger than 2 µm, the measure μ as a function of ℓ itself behaves, up to an additive constant, as $-2\log_{10}(\ell/2\,\mu\mathrm{m})$ [328].

Venalty

Knee et al. [322] have introduced the concept of venality ζ to quantify how often a non-ideal negative measurement, *i.e.* a measurement that could potentially violate (A2), has been performed. In our experiment, it occurs with a relative frequency of 1 % (estimated as the upper limit) that vibrational excitations of the unshifted atoms are produced during the measurement of $Q(t_2)$ (see sec. 3.3.1). In addition, spontaneous flips (see sec. 2.4.1) of the internal state happening during the 200 µs-long $Q(t_2)$ measurement could also invalidate hypothesis (A2). This second process, however, occurs with an even smaller relative frequency of circa 0.2 %. Hence, we quantify the relative frequency of non-ideal negative measurements with $\zeta = 1\,\%$.

Along the lines of Knee et al. [322], the correlation function K measured in our experiment can be decomposed as $K = 1 + (1-\zeta)K_{23}^{\mathrm{ideal}} + \zeta K_{23}^{\mathrm{corrupt}} - K_{13}$, where K_{23}^{ideal} and $K_{23}^{\mathrm{corrupt}}$ denote the correlation function $\langle Q(t_3)Q(t_2)\rangle$ which has been measured with an ideal negative measurement $Q(t_2)$ and with a corrupted one, respectively. Taking into account the venality ζ, the Leggett-Garg inequality, which is derived from (A1) and (A2), reads $K \leq 1 + \zeta(K_{23}^{\mathrm{corrupt}} - K_{13})$. From this we obtain a new upper bound for $K \leq 1 + 2\zeta = 1.02$, which is only slightly displaced from the ideal case of 1.

CHAPTER 5

Testing the Quantumness of Two-Atom Trajectories

The capability to control the position of individual cesium atoms with high fidelity (see chap. 3) combined with 3D ground state cooling (see sec. 2.5.2) gives us a versatile tool to probe quantum interference effects of two-atom trajectories. In this chapter we will discuss our recent results on collisional losses due to inelastic collisions occurring at high two-atom densities (see sec. 5.1) and demonstrate a Hong-Ou-Mandel interference with massive particles (see chap. 5.2). The former represents a first step in the direction of measuring atomic properties such as the scattering length between different spin combinations using exactly two atoms, whereas the latter is of particular interest since our two-particle interference demonstrates the fundamental building block e.g. to realize controlled two-atom phase gates [347] or to study correlated discrete-time quantum walks with indistinguishable particles [348]. Continuous-time analogues of DTQWs with correlated boson particles have similarly been observed [61, 349].

Our experimental apparatus embodies an ideal testing environment to study the Bose statistics of exactly two particles. Bose statistics provides particles a "nonclassical" way to interfere due to the exchange symmetry, which reflects the fact that quantum systems are symmetric by exchange of identical particles. This symmetry is at the heart of the famous Hong-Ou-Mandel experiment [30], in which two indistinguishable photons (with identical polarization and transverse mode) impinging simultaneously upon a beam splitter emerge in an entangled quantum state. Both photons exit from the beam splitter either through one or the other output port, but not from separate ones. The analysis, provided in section 5.2.1, reveals that our microwave Hong-Ou-Mandel experiment with neutral atoms achieves a signature of the two-particle interference with a statistical significance of $4\,\sigma$ (standard deviation).

5.1 Probing Two-Atom Collisions at High Densities

Shortly after the first observation of a BEC in an ultracold gas of rubidium atoms by Anderson et al. [350] and of sodium atoms by Davis et al. [351], researchers started to investigate whether a BEC could be achieved with cesium atoms. However, the first attempts resulted unsuccessful due to inelastic collisions [201] and it took a few more years before the first BEC of cesium could be realized by adjusting the interaction through a Feshbach resonance [352]. During this period several groups investigated the collisional properties of cesium trapped in a magneto-optical trap [282]. For example, it was demonstrated that a dense cloud of cesium atoms undergoes hyperfine state-changing collisions on a time scale of a

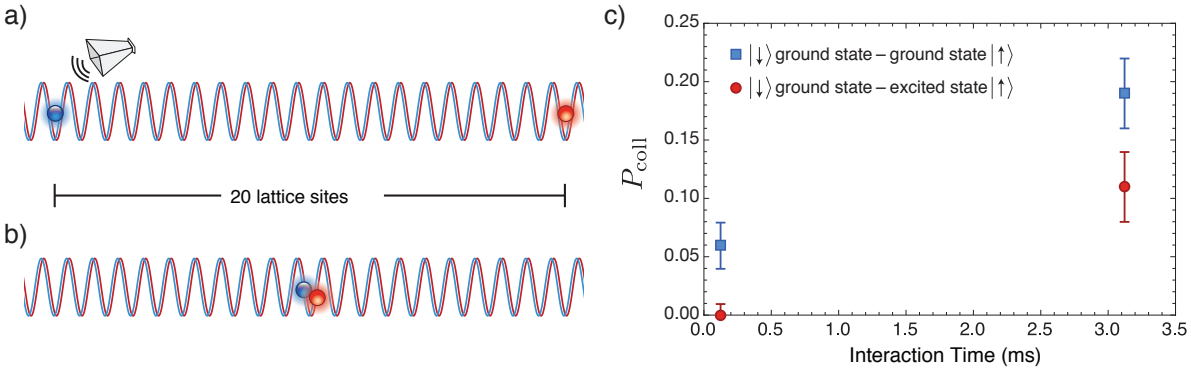

Figure 5.1: Probing two-atom collisions in state-dependent optical lattices. **(a)** Two atoms are initially placed at a relative distance of 20 sites and cooled to the motional ground state. Using an addressing magnetic field gradient, one of the two atoms has its spin flipped by a microwave π pulse (see sec. 2.3.4). **(b)** Both atoms are transported to the same lattice site by a single adiabatic spin-dependent shift operation lasting circa 1 ms (see sec. 3.3.1). Subsequently the two atoms are again separated. **(c)** Based on the model in equation (5.1), we determine the probability P_{coll} for two atoms to be lost due to a hyperfine changing collision. By exciting selectively the atom in $|\uparrow\rangle$ (see sec. 5.1.1), we observe a reduced probability of collisional losses. This figure is originally published in Robens et al. [4]

minute for densities $n \approx 10^{10}\,\mathrm{cm}^{-3}$ [201]. Our experimental apparatus enables us to realize densities six orders of magnitude higher by transporting two 3D-cooled atoms into the same lattice site according to the scheme illustrated in figure 5.1(a). In contrast to the pair production measurements discussed in section 3.3.4 where two thermal atoms were imaged in the same lattice site, we now bring two 3D vibrational ground state cooled particles together and let them interact for a controllable amount of time. After the interaction time we split the particles again to observe whether one or both of them were lost as a result of an inelastic collision event by recording a fluorescence image.

The energy released in the inelastic collision is on the order of $\Delta E = k_{\mathrm{B}} \times 400\,\mathrm{mK}$ [353], which is more than three orders of magnitude larger than the depth of the optical potential. Hence, we expect to loose both atoms in the case where they undergo a hyperfine state-changing collision. By recording the occurrences where both, one, or no atom remains in the optical lattice after a variable interaction time, we can extract the probability of inelastic collisional losses P_{coll} using a simple model:

$$\text{Probability that} \begin{cases} 0 \text{ atom survives} = S^2\, P_{\mathrm{coll}} + (1-S)^2 \\ 1 \text{ atom survives} = 2S(1-S) \\ 2 \text{ atoms survive} = S^2(1-P_{\mathrm{coll}}) \end{cases} \tag{5.1}$$

where S is the uncorrelated probability for a single atom to remain trapped in the optical lattice during the experimental sequence in the absence of collisions. Independent measurements show that the survival probability S amounts to $S \approx 91\%$, which is mainly limited by technical reasons (timing of the experimental sequence) and additional losses experienced due to transverse cooling. Experiments with tighter transverse confinement are expected to reach single-atom survival probabilities close to 99 %.

These preliminary results already exhibit losses detectable for interaction times on the ms scale, shown by the blue squares in figure 5.1(c). We further verify that the inelastic collision probability P_{coll} depends on the two-atom density. For that purpose, we excite the atom in $|\uparrow\rangle$ with a spin-dependent shaking of the σ^+ optical lattice (see sec. 5.1.1), which increases the volume of the atom's wave function. The

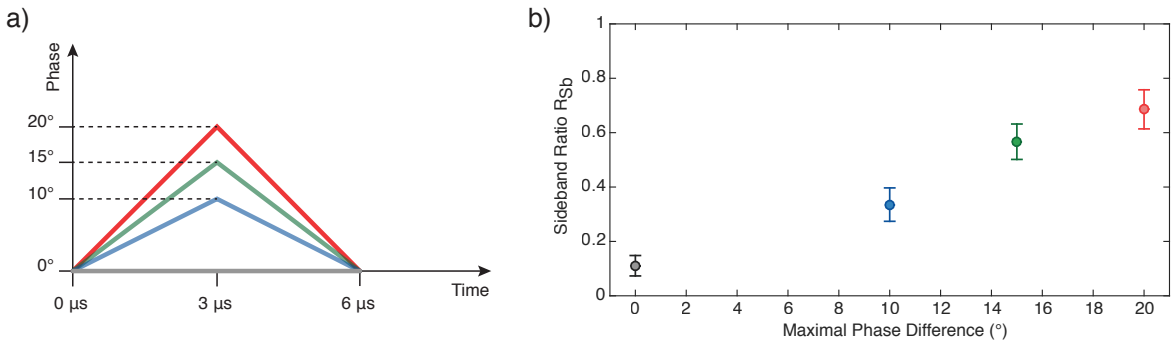

Figure 5.2: **(a)** Linear phase ramps employed to create state dependent vibrational excitations with different maximal phase differences (blue: 10°, green: 15°, red: 20°). **(b)** Ratio of the cooling and heating sideband transition (see sec. 2.5.2) obtained by performing longitudinal microwave sideband spectroscopy after shaking the σ^+ polarized optical lattice using the linear phase ramps depicted in **(a)**.

reduced probability of collisional losses in this case is shown by the red circle points in figure 5.1(c). In the following section we will briefly discuss how to create spin-dependent excitations with our polarization-synthesized optical lattice.

5.1.1 State-Dependent Vibrational Excitations

In chapter 3 we spend considerable effort on ensuring and verifying that our transport operations do not lead to accidental longitudinal or transverse vibrational excitations (see sec. 3.3.1). Nevertheless, deliberately causing vibrational excitations is an interesting tool to fine-tune the volume of the atom's wave function, as we have seen in the preceding section. Furthermore, this technique can also be of use to controllably make two indistinguishable atoms distinguishable again, which is an interesting perspective for the Hong-Ou-Mandel experiment with massive particles discussed in section 5.2.

Figure 5.2(a) depicts the phase ramps we employ in order to excite atoms in the $|\uparrow\rangle$ state. At first sight they look identical to the bang-bang technique transport ramps discussed section 3.4. However, here we specifically choose the time between the first and the second delta-like kick, such that it is incommensurable with the longitudinal oscillation frequency of a trapped atom. Hence, after the shaking procedure we expect atoms in $|\uparrow\rangle$ to be in a vibrational excited level, which can be verified by probing the ground state population through sideband spectroscopy (see sec. 2.5.2). Figure 5.2(b) shows the ratio of the cooling and heating sideband transition of atoms, which were prepared in the $|\uparrow\rangle$ state, longitudinally cooled close to their ground state, and then excited using the corresponding shaking operation depicted in 5.2(a). The observable revival of the cooling sideband transition attests that most of the atoms were transferred to an excited state. Conducting additional experiments, we verified that atoms in the $|\downarrow\rangle$ state remain in their vibrational ground state for all shaking operations depicted in 5.2(a) (data not shown). An alternative and perhaps more precise method would be to employ local microwave sideband pulses which also change the vibrational level of the atom as discussed in Belmechri et al. [252]. However, the shaking method does not require a magnetic field gradient and, in addition, is more robust since the delta-like kick is almost guaranteed to cause vibrational excitations.

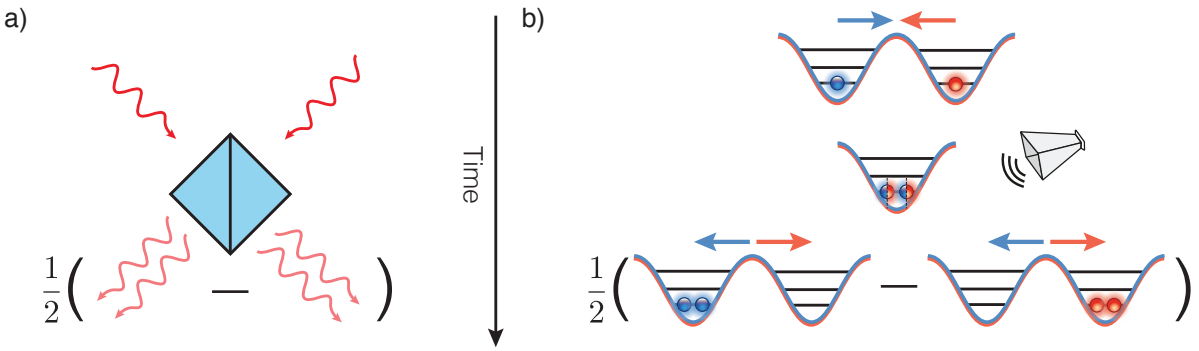

Figure 5.3: Side by side comparison of the historical Hong-Ou-Mandel effect **(a)** with photons and **(b)** the atomic analog using our polarization-synthesized optical lattice. In the case of the latter, two atoms with opposite spin states are transported into the same lattice site in an analogous fashion as in depicted in figure 5.1. A microwave $\pi/2$ pulse mixes the two indistinguishable atoms like in the beam splitter in the optical realization. A final state dependent shift separates the two spin species. A two-particle interference leads to both atoms either emerging on the left or right hand side. For identical atoms, no event is expected with the two atoms in distinct sites.

5.2 Microwave Hong-Ou-Mandel Interferometer with Massive Particles

Ultracold atoms in the vibrational ground state of an optical lattice allow us to explore fascinating quantum-mechanical interference effects between the trajectories of two (or more) indistinguishable neutral atoms. Quantum mechanics shows that quantum correlated states of two particles can be produced even if particles are non-interacting. The most prominent example is provided by the Hong-Ou-Mandel experiment [30], which is illustrated in figure 5.3(a). The quantum correlation of this experiment results from quantum interference of two-particle trajectories, and applies in general to any indistinguishable boson particles, including massive ones. Only recently, independent groups achieved the first demonstration of the Hong-Ou-Mandel interference with massive particles using tunneling between potential wells in micro potentials [17, 40] and in an atom interferometer-like experiment with metastable helium [41]. Our experimental apparatus is well suited to implement a direct analogue of the original HOM experiment, which is illustrated by a direct comparison in figure 5.3(a)-(b). In the following we will first discuss the experimental sequence of our atomic HOM interferometer, then construct a simple model to extract an estimate of the anti-bunching probability, and finally use a Monte Carlo simulation to rigorously analyze our data.

Similar to the experimental sequence outlined in section 5.1, we initially prepare two atoms separated by twenty lattice sites and cool them into the 3D ground state. A local microwave addressing pulse (see sec. 2.3.4) flips the spin of the left atom (see fig. 5.4(a)), which is then transported twenty lattice sites to the right (see sec. 3.3.1), such that both atoms coincide in the same potential well (see fig. 5.4(b)). Instead of letting atoms interact on a millisecond time scale (see sec. 5.1), we directly apply a 4.8 µs long $\pi/2-$pulse (see sec. 2.3.3). This pulse removes the "which-way" information by transforming each atom into an equal superposition of $|\uparrow\rangle$ and $|\downarrow\rangle$ (see fig. 5.4(c)). If both atoms are indistinguishable, interference of the two bosons leads to the entangled NOON state which is best understood by making a small detour through quantum optics: So far in this thesis we have exclusively dealt with the physics of single particle trajectories, for which it was convenient to express the atomic state in terms of $|\uparrow\rangle$ and $|\downarrow\rangle$. However, in the following, we will adopt a slightly different notation, where $a^\dagger_{\uparrow,0}$ denotes the creation operator of $|\uparrow\rangle$

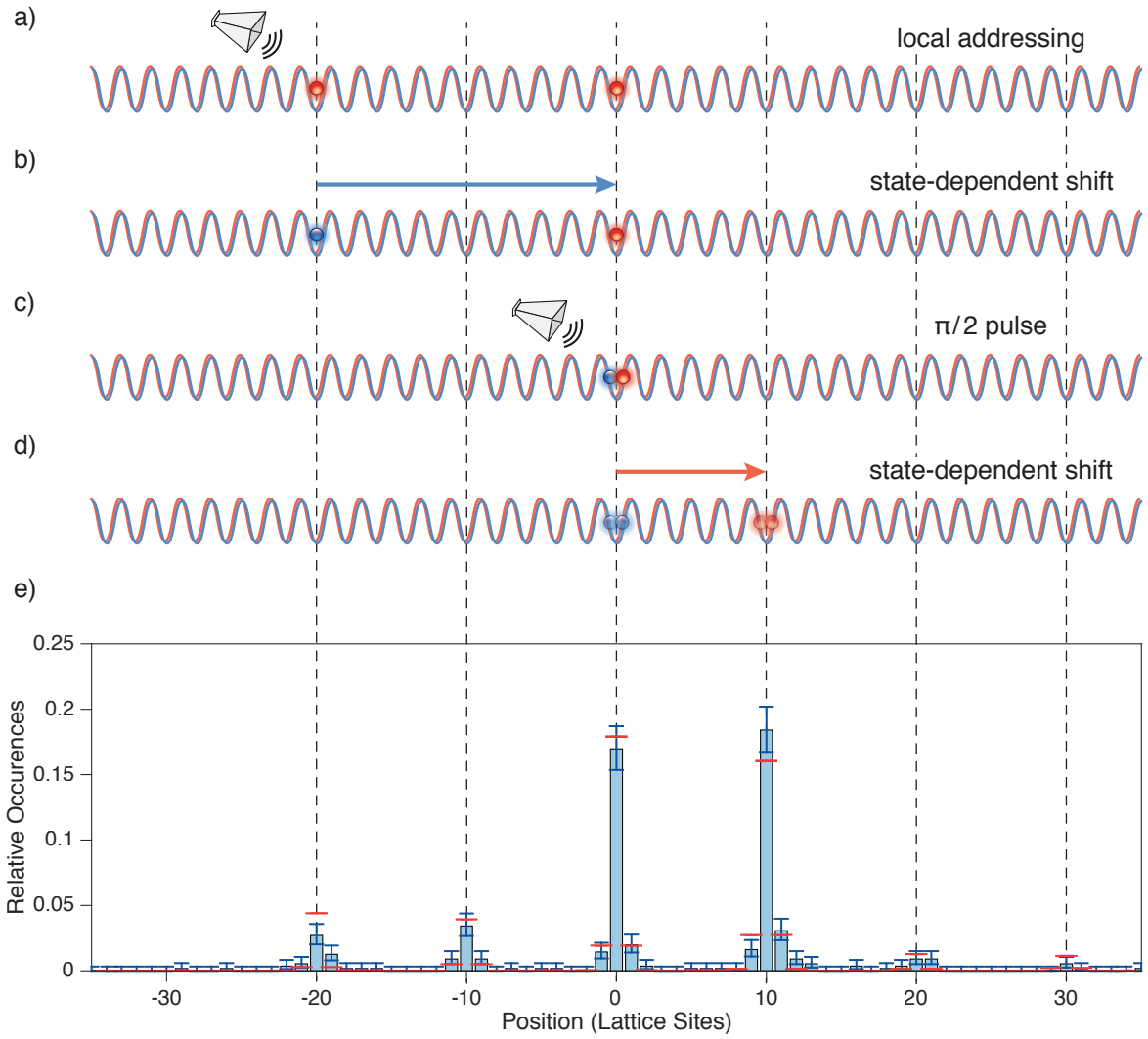

Figure 5.4: **(a)-(d)** Experimental sequence of the atomic HOM interferometer. Please note that for illustrational purposes only every second potential well of the optical lattice is depicted. Initially atoms are prepared 20 lattice sites apart and cooled into the 3D ground state. **(a)** A local microwave addressing pulse flips the spin of the left atom, then **(b)** the $|\downarrow\rangle$ potential is translated by 20 lattice sites. **(c)** Once both atoms are in the same lattice site, a $\pi/2-$pulse turns each atom into an equal superposition of $|\uparrow\rangle$ and $|\downarrow\rangle$. If both atoms are indistinguishable, interference between the two bosons leads to $1/2\,(a^\dagger_{\uparrow,0}a^\dagger_{\uparrow,0} - a^\dagger_{\downarrow,0}a^\dagger_{\downarrow,0})\,|0\rangle$. **(d)** A final translation of the $|\uparrow\rangle$ potential separates the two spin components. **(e)** Reconstructed atoms' positions obtained from 277 repetitions of **(a)-(d)**. Most of the atoms are located either at lattice site 0 or 10, however, several experimental imperfections lead to atoms also appearing in other locations (see discussion in text). The solid red horizontal lines are the result from a Monte Carlo simulation, which is discussed in section 5.2.1. The error bars are estimated using the Clopper-Pearson method. It is noteworthy that these error bars serve only as an illustration, since the Clopper-Pearson method is in principle not suited for correlated two atom events.

at lattice site zero, $a^\dagger_{\downarrow,0}$ the creation operator $|\downarrow\rangle$ at lattice site zero, and $|0\rangle$ the vacuum state. Using this notation we can express the action of the microwave operation in the following way:

$$a^\dagger_{\uparrow,0}a^\dagger_{\downarrow,0}|0\rangle \xrightarrow{\pi/2-\text{pulse}} \frac{1}{\sqrt{2}}\left(a^\dagger_{\uparrow,0}+a^\dagger_{\downarrow,0}\right)\frac{1}{\sqrt{2}}\left(a^\dagger_{\uparrow,0}-a^\dagger_{\downarrow,0}\right)|0\rangle = \frac{1}{2}\left(a^\dagger_{\uparrow,0}a^\dagger_{\uparrow,0}-a^\dagger_{\downarrow,0}a^\dagger_{\downarrow,0}\right)|0\rangle\,, \tag{5.2}$$

where in the last step we used the indistinguishability of the particles to commute the operators $a^\dagger_{\uparrow,0}$ and $a^\dagger_{\downarrow,0}$. The microwave $\pi/2-$pulse is, hence, the analogue of the balanced beamsplitter in the photonic HOM experiment. A subsequent translation of the $|\uparrow\rangle$ potential by ten lattice sites (see fig. 5.4(d)) separates the two spin components $\frac{1}{2}(a^\dagger_{\uparrow,10}a^\dagger_{\uparrow,10}-a^\dagger_{\downarrow,0}a^\dagger_{\downarrow,0})|0\rangle$. This allows us to experimentally detect the state of the atoms. Analogous to the original detection method [30], we obtain an experimental signature of the two-particle interference by recording the suppression of events where two atoms are detected at different lattice sites in a fluorescence image.

So far, we have simply assumed that the two cesium atoms are indistinguishable. In terms of their atomic structure, all cesium atoms are naturally indistinguishable, since ^{133}Cs is the only stable isotope of cesium. However, according to quantum mechanics, the indistinguishability of particles is determined by the overlap of both particles' wave functions. As discussed in section 2.1.1, the wave functions of atoms trapped in an optical lattice are to good approximation given by the quantum harmonic oscillator's eigenfunctions. Therefore, in order to be indistinguishable, both atoms need to be in the exact same 3D vibrational state, which can be efficiently achieved by the vibrational ground state cooling introduced in sec. 2.5.2. Hence, to first order, the indistinguishability of our atoms – and correspondingly the probability to create the desired NOON – is given by $(n_0^{3D})^2$, where n_0^{3D} is the probability of a single atom to be in the 3D vibrational ground state, as defined in table 2.7. Consequently, the probability to observe an anti-bunched pair of atoms after the experimental sequence is given by

$$P_{\uparrow/\downarrow} = \frac{1}{2}\left[1-\left(n_0^{3D}\right)^2\right]. \tag{5.3}$$

The first contribution in equation (5.3) arises from the statistical probability of distinguishable particles: Without particles being indistinguishable we cannot commute the creation and annihilation operators in equation (5.2). Therefore each atom has an uncorrelated probability of 50 % to be found either at lattice site zero or ten, which results in $P_{\uparrow/\downarrow} = 50\,\%$ for fully distinguishable particles.

Thus, by experimentally observing a significantly lower anti-bunching probability, we can prove[1] our capability to generate the desired entangled NOON state. Unfortunately, this probability is not directly accessible using the experimental sequence depicted in figure 5.4. Instead, recording a fluorescence image of the final atomic distribution allows us to extract the probabilities of observing two-, one-, or zero-atoms in one of the target locations. Figure 5.4(e) displays the reconstructed atoms' positions obtained from 277 repetitions of the experimental sequence outlined in figure 5.4(a)-(d) and the relative occurrences of the two-, one-, and zero-atom events are summarized in table 5.1. For our analysis we include atoms which are found in the neighboring lattice sites, however, we initially disregard all events where atoms are found in other locations (see sec. 5.2.1 for the Monte Carlo analysis).

Intuitively one might be tempted to associate the probability to observe a two atom event P_{2A} directly with the anti-bunching probability $P_{\uparrow/\downarrow}$. However – neglecting for now all experimental imperfections besides the uncorrelated probability S of a single atom to remain trapped – P_{2A} also includes uncorrelated loss events which do not unveil information about the HOM interference. Instead, we can extract $P_{\uparrow/\downarrow}$

[1] Please note, that in contrast to chapter 4, we here argue in the spirit of Francis Bacon's inductive thinking, where the agreement between quantum theory and experimental observations serves as a validation of the theory itself.

Table 5.1: Probability of zero-, one-, and two-atom events from 277 events and their corresponding anti-bunching probability $P_{\uparrow/\downarrow}$ obtained from the simple model given in equation (5.4).

	2 atom events	1 atom events	0 atom events
Relative occurrence	$P_{2A} = (19 \pm 3)\,\%$	$P_{1A} = (48 \pm 4)\,\%$	$P_{0A} = (33 \pm 4)\,\%$
Anti-bunching probability	$P^{2A}_{\uparrow/\downarrow} = 27\,^{+4}_{-4}\,\%$	$P^{1A}_{\uparrow/\downarrow} = 27\,^{+15}_{-17}\,\%$	$P^{0A}_{\uparrow/\downarrow} = 27\,^{+10}_{-11}\,\%$

from a simple model, which incorporates the uncorrelated survival probability S and the probability P_{LAC}, with which we lose either one or both atoms due to light-assisted collisions, if both atoms occupied the same lattice site (see sec. 3.3.4):

$$\text{Probability that} \begin{cases} \text{2 atoms survive} = P_{2A} = S^2\, P_{\uparrow/\downarrow} \\ \text{1 atom survives} = P_{1A} = 2S(1-S) + S^2\,(1 - P_{\mathrm{LAC}})\,(1 - P_{\uparrow/\downarrow}) \\ \text{0 atoms survive} = P_{0A} = (1-S)^2 + S^2\, P_{\mathrm{LAC}}\,(1 - P_{\uparrow/\downarrow}) \end{cases} \tag{5.4}$$

The light-assisted collisions branching ratio P_{LAC} was discussed in section 3.3.4 and amounts to $P_{\mathrm{LAC}} = (71 \pm 5)\,\%$. To determine the uncorrelated survival probability S, we carried out an independent measurement repeating the experimental sequence outlined in figure 5.4(a)-(d), however, omitting the $\pi/2-$pulse. This makes the experiment purely classical, and thus both atoms will always be separated in the fluorescence image – one at lattice site zero, the other at ten. Therefore, counting all atoms in the final image enables us to extract the uncorrelated survival probability S, which amounts to $S = (84 \pm 1)\,\%$. The unusually low survival can be attributed to: (a) technical limitations which require us to keep the atoms longer than usual in the low lattice before executing the experimental sequence depicted in figure 5.4 and (b) during the vibrational sideband cooling some atoms escape from the trap – through off-resonant heating sideband transitions or photon recoil excitations – before they are cooled into their vibrational ground state. Knowing both P_{LAC} and S together with the relative occurrences of the two-, one-, and zero-atom events allows us to extract $P_{\uparrow/\downarrow}$, which is summarized in table 5.1. Since the equations of our simple model are not independent, the occurrences of the two-, one-, and zero-atom events result in the same anti-bunching probability $P_{\uparrow/\downarrow}$. However, each case has a different sensitivity on the anti-bunching probability $P_{\uparrow/\downarrow}$ which manifests in different confidence intervals. We will investigate this sensitivity in more detail in the following section. Nevertheless, according to our simple model we obtain a $5.8\,\sigma$ (standard deviation) decreased anti-bunching probability $P_{\uparrow/\downarrow}$ which can only be caused by indistinguishable particles. Using equation (5.3), the HOM interference measurement also enables us to extract the single atom ground state probability n_0^{3D} yielding $n_0^{3D} = (67 \pm 6)\,\%$, which is in good agreement with the results discussed in section 2.5.2. In fact, modern photonic experiments often use the Hong-Ou-Mandel interference to quantify the indistinguishability of their single photon source [36–39].

5.2.1 Monte Carlo Analysis of the Atomic Hong-Ou-Mandel Experiment

So far, we have excluded all events where atoms were found in lattice sites other than the two target ones. While this was convenient to develop the simple model, it is, strictly speaking, not correct since we might create artificial false positive of false negative events, when interpreting the measurement data using our simple model. For example, it is possible that we did not flip the spin of the left atom, and hence the two atoms would never meet at the same lattice site. In some of these cases, additionally, the left atom gets lost, which leads to a one atom event. This example, therefore, represents a false negative event when

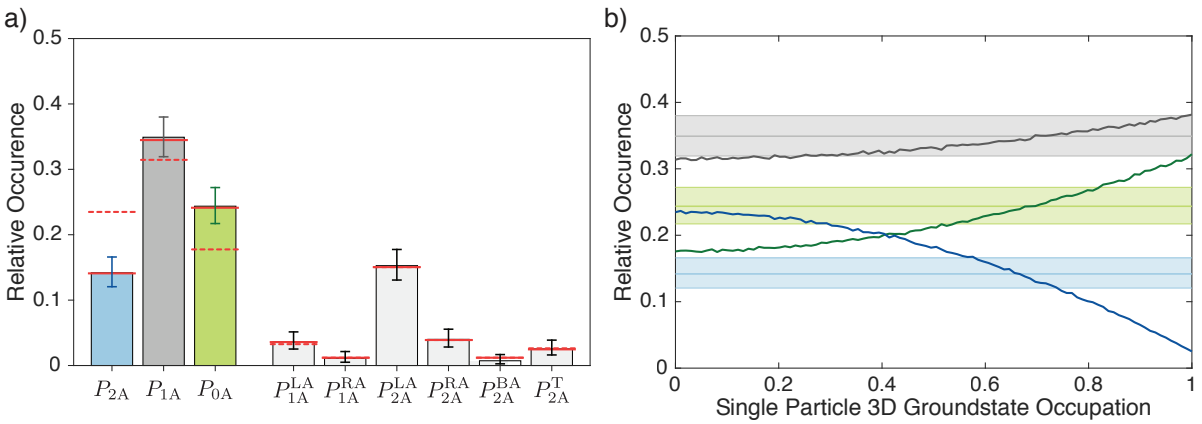

Figure 5.5: **(a)** Relative occurrences of all nine distinct cases, obtained from 277 events. The different cases are defined in appendix section C. The blue, grey, and green bars correspond to the two-, one-, and zero-atom events, respectively. Errors are estimated using the Clopper-Pearson method ($\alpha = 0.32$). The solid red line is the result from a least squares fit of generated Monte Carlo events to the measured ones with $n_0^{3D} = 67\,\%$ and the dashed red line represents Monte Carlo data obtained from fully distinguishable particles ($n_0^{3D} = 0\,\%$). **(b)** Study of the sensitivity of the two-, one-, and zero-atom events in dependency of the single atom ground state probability n_0^{3D}. The colored areas represent the 68 % confidence interval of the two-, one-, and zero-atom events displayed in **(a)**.

interpreting the measurement data using our simple model. Furthermore, the events we have discarded so far contain valuable information on the experimental parameters and it would be wasteful to simply neglect this information. In fact, we can identify five additional distinct cases for these events, the details of which are given in the appendix section C. The distribution we obtain after separating our 277 events into all nine distinct cases is displayed in figure 5.5(a).

To rigorously analyze the distribution depicted figure 5.5(a) we resort to a Monte Carlo analysis instead of extending our simple model to a more complex one. For this purpose we devised a Monte Carlo simulation, which mimics the experimental sequence outlined in figure 5.4. The input parameters of this Monte Carlo simulation are (a) the single atom ground state probability n_0^{3D}, (b) the uncorrelated survival probability S, (c) the light-assisted collisions branching ratio P_{LAC}, (d) the probability to address the left atom, (e) the probability to accidentally address the right atom, and (f) the probability to successfully reconstruct the position of the atoms. By performing a non-linear least squares fit of the generated Monte Carlo events – separated into the nine distinct cases, see appendix section C – to the measured ones, we can extract the underlying experimental parameters, which are summarized in table 5.2. The resulting event distribution is further indicated by the solid red horizontal lines in figure 5.5(a), which all agree remarkably well with the measured ones. In addition, the extracted values of the uncorrelated survival probability S and the light-assisted collision branching ratio P_{LAC} agree within one standard deviation with the independently measurement ones. Furthermore, the Monte Carlo simulation allows us to gain more insight on the sensitivity of the two-, one- and zero-atom events. For this purpose, the relative occurrence of the two-, one- and zero-atom events as a function of the single atom ground state probability n_0^{3D} are displayed in figure 5.5(b).

While the Monte Carlo simulation reproduces the measured distribution perfectly, the obtained confidence intervals of the non-linear least squares fit are not representative. The employed fit routine extracts the confidence intervals from local deviations of the function (in our case the Monte Carlo simulation) without properly accounting for an experimental uncertainty of the function. However, we can extract the confidence intervals using the so-called bootstrapping method [354]. For this purpose,

Table 5.2: Result from fitting the Monte Carlo generated events to the measured distribution displayed in figure 5.5 and the bootstrapping analysis. We have additionally performed a global non-linear least squares fit with 40 randomized starting parameters to ensure a local minimum (data not shown).

	Fit	Bootstrapping	Independent measurement
(a) Single atom ground state probability n_0^{3D}	(67 ± 2) %	(69 ± 9) %	
(b) Uncorrelated survival probability S	(83 ± 1) %	(84 ± 4) %	(84 ± 1) % see sec. 5.2
(c) Light-assisted collisions P_{LAC}	(68 ± 2) %	(68 ± 10) %	(71 ± 5) % see sec. 3.3.4
(d) Right atom addressing probability	(76 ± 1) %	(76 ± 3) %	
(e) Left atom addressing probability	(8 ± 1) %	(7 ± 2) %	
(f) Successful position reconstruction	(89 ± 2) %	(89 ± 4) %	

we resample our 277 measured events into 1 500 bootstrap samples which each contain 277 events. Performing a non-linear least squares fit with each one of them gives us a statistic distribution for each parameter. From the spread of these distributions we can then determine the 68 % confidence intervals, which are summarized in table 5.2. The bootstrapping method is in general applicable as long as the measured distribution accurately represents the true underlying distribution, which is a justified assumption for our 277 events. Using equation (5.3) we can finally extract the anti-bunching probability yielding $P_{\uparrow/\downarrow} = (27 \pm 6)\,\%$, which corresponds to a 4.1 σ (standard deviation) discrepancy between our measurement and the prediction using distinguishable particles.

5.2.2 Outlook: Further Enhancing the Hong-Ou-Mandel Signature

In the preceding chapter we have discussed our atomic Hong-Ou-Mandel experiment and obtained a signature of the two-particle interference with a statistical significance of 4 σ. Furthermore, we have discussed that the anti-bunching probability of the experiment is only determined by the indistinguishability of the particles, which in our case is given by the 3D vibrational ground state probability. Following the discussion of section 2.5.2, it is feasible to reach 3D vibrational ground state probabilities of up to 97 % with the experimental apparatus at hand, which in turn leads to an anti-bunching rate of only 3 %. Additionally, a higher 3D vibrational ground state occupation should also significantly boost the coherence time leading to an improved spin-flip success rate, when addressing individual atoms (see sec. 2.5.1). The HOM results presented in this thesis also reflect a rather low uncorrelated survival probability of individual atoms. However, we expect to reach $S = 99\,\%$ by adjusting the cooling sequence employed to achieve 3D vibrational ground state cooling (see fig. 2.31) and further by exchanging the arbitrary waveform generator controlling the optical lattice depth, which causes unnecessarily long hold times before executing the experimental sequence depicted in figure 5.4. These improvements combined will allow us to measure the signature of the two-particle interference with an enhanced significance.

Additionally we plan to incorporate two changes to the experimental sequence outlined in figure 5.4: (a) Utilizing our capability to create state-dependent vibrational excitations (see sec. 5.1.1) allows to controllably make two indistinguishable atoms distinguishable again. This tool enables us to create a reference measurement for our HOM experiment, without resorting to a Monte Carlo analysis. (b) It is a bit unsatisfying that we can only directly observe the anti-bunched state, whereas in the case where the atoms are bunched we need to extract the information indirectly through the one- and zero-atom events. In principle it is possible to split atoms located in the same lattice site by exploiting a controllable phase shift induced by coherent cold collisions. However, this technique is experimentally rather demanding. Instead, we can also make use of a statistical method – namely, our quantum walks – to split the bunched

pair of atoms: conducting a three step quantum walk already reduces the probability of the two atoms being in the same lattice site from 1 to 3/8. In fact, utilizing our newly developed versatile digital frequency synthesizer [106] allows us to directly incorporate this protocol into the experimental sequence of our atomic HOM experiment depicted in figure 5.4. A similar approach was recently demonstrated using tunneling instead of discrete time quantum walks [355].

CHAPTER 6

Outlook

This thesis presents a novel concept of state-dependent transport, which gives us an unprecedented control over the position of individual atoms in optical lattices. This control lies at the heart of the experimental violation of the Leggett Garg inequality (see chap. 3), our bottom-up approach of generating arbitrary low-entropy states with neutral atoms (see chap. 4), and the Hong-Ou-Mandel interference with massive particles (see chap. 5).

Furthermore, parts of this thesis were devoted to develop several experimental tools and techniques: Three dimensional ground state cooling of single atoms which are trapped in the combined potential of the polarization-synthesized optical lattice and the blue-detuned hollow dipole potential (see sec. 2.5). An automated feedback-based experimental control system, which rearranges individual atoms into predefined, ordered distributions (see sec. 3.3.2). Interaction free – ideal negative – measurements, which entangle the position of atoms with their internal state (see sec. 4.2). A high-NA (0.92) objective lens achieving a diffraction limited resolution of 460 nm (see sec. 2.2.4). And an improved super-resolution algorithm, which resolves the position of individual atoms in small clusters at high filling factors, even when each lattice site is occupied (see sec. 2.2.3).

Throughout this thesis I have discussed several ideas how to extend the *status quo* of our research. In the following paragraphs I will recapitulate some of these and, further, give an outlook on prospective experiments, which become feasible with the newly developed tools and techniques.

Optimal Control Theory and Split Step Quantum Walks: At the end of chapter 3 we introduced quantum optimal control theory as a tool to improve the transport operations carried out with our polarization-synthesized optical lattices. We concluded that using these optimized transport operations, it becomes attainable to transport atoms significantly faster over greater distances, while these operations are simultaneously also more robust against deviations of experimental parameters. At the current stage we are implementing the newly developed versatile digital frequency synthesizer [106] into the electro-optical setup of our polarization-synthesized optical lattice (see sec. 3.2.1). With this device in place we can put the optimal control transport operations to the test.

While a proof of principle experiment attesting the predominance of quantum optimal control is interesting in itself, these ramps are crucial for all upcoming experiments which rely on coherent interference of atom trajectories. For example, they find application in studying the topological properties of discrete time quantum walks (DTQWs) [49, 356, 357]. To reveal the nontrivial topological character of DTQWs we need to modify the iterative walk protocol introduced in section 3.4.1. Instead of shifting the $|\uparrow\rangle$ and $|\downarrow\rangle$ potential at the same time, in a so-called split step DTQW, we split both the coin and the

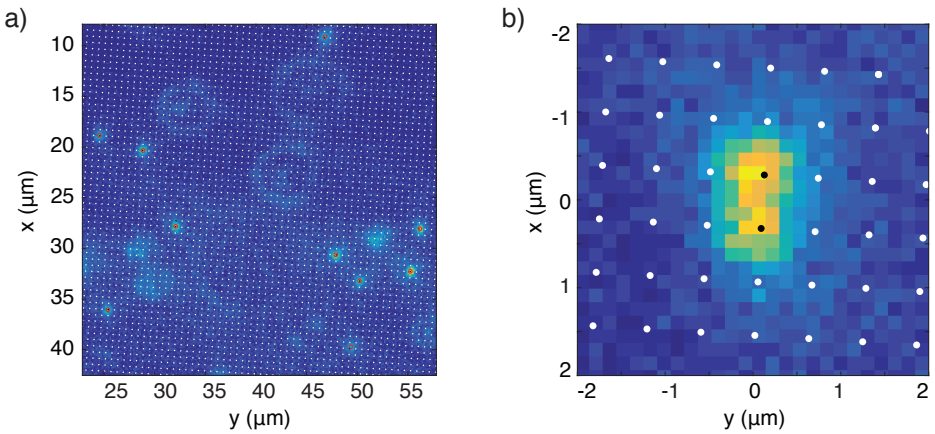

Figure 6.1: Preliminary images of single atoms trapped in a 3D optical lattice, obtained with the high-NA objective lens. **(a)** Image of several atoms distributed in the 3D optical lattice. Atoms trapped at different vertical layers appear as rings. **(b)** A pair of atoms in neighboring lattice sites. Courtesy of Stefan Brakhane [149]

shift operation [356]:

$$W = S^{\downarrow} C(\theta_1)\, S^{\uparrow} C(\theta_2)\,, \tag{6.1}$$

where $C(\theta)$ is the coin operator and $S^{\uparrow/\downarrow}$ the state dependent shift operator which translates the corresponding $|\uparrow\rangle$ / $|\downarrow\rangle$ potential. In fact, without our new polarization-synthesized optical lattices such an independent translation of the two potentials would not be possible. Topologically protected edge states of the split step DTQW can be observed by realizing spatially distinct coin angles [49]. While this may be rather intricate with the experimental apparatus at hand, the high-NA objective lens of the new apparatus makes this straightforward [49]. Nevertheless, even without distinct topological domains we can unveil some of the topological properties of DTQWs. For this purpose we further modify the split step DTQW protocol and make use of the ideal negative measurement we introduced in chapter 4:

$$R = C(\pi/2)\, R^{\uparrow} C(-\pi/2)\,, \tag{6.2}$$

where $R^{\uparrow}$ is the ideal negative measurement which removes all atoms in $|\uparrow\rangle$. Iteratively repeating this protocol and keeping track of the exact lattice site at which the atoms are removed allows us to extract the average position at which an atom is removed from the walk. It can be shown that the average removal position – after sufficient iterations – is always an integer number which represents the sum of the topological invariants of a split step quantum walk as defined in Groh et al. [49].

Two-Dimensional State-Dependent Transport and Topology: The construction of the next generation experimental apparatus, which utilizes the high-NA objective lens (see sec. 2.2.4) and a two-dimensional polarization-synthesized optical lattice, is nearly completed. The experimental details of this apparatus can be found in Brakhane [149]. Figure 6.1 represents preliminary results showing the fluorescence image of single atoms trapped in a 3D optical lattice. The scheme to implement spin-dependent discrete shift operations in a two-dimensional optical lattice is described in a recent publication by our group [49]. Two-dimensional state-dependent transport allows us to directly implement the sorting algorithm we introduced in sec. 3.3.3 with the prospect of creating low-entropy states with more than one thousand atoms in a bottom-up approach. Yet, this is merely the beginning. The capabilities of the new experimental apparatus open a variety of interesting physical phenomena that can be studied.

For example, a recent publication by Groh et al. [49] describes how one can realize spatial boundaries between distinct topological phases and observe the emerging topologically protected edge states using two-dimensional quantum walks. Furthermore, Muhammad Sajid and Andrea Alberti in collaboration with Reinhard Werner with are currently investigating how one can realize synthetic magnetic fields by utilizing position- and state-dependent AC-Stark shifts [358].

Contact-Free Entanglement of Indistinguishable Particles: When we think about entanglement of massive particles, we typically have a picture in mind where the particles interact in a certain region in space and time. However, the Hong-Ou-Mandel interference already hints that entanglement *per se* does not require interaction. In fact, using photons it was demonstrated that it is possible to realize a Hong-Ou-Mandel two particle interference, despite the fact that the photons never "meet" in the beamsplitter [359]. Recently, Andrea Alberti and Dieter Meschede in collaboration with Christian Roos and Hartmut Häffner devised a new two-particle interferometer scheme, which demonstrates that two particles both prepared and detected at separate places, can be entangled [50]. The particular symmetry of the proposed scheme makes the interferometer intrinsically robust against all typical decoherence sources like spin-dependent as well as spin-independent potential gradients. With the 3D vibrational ground state cooling and our polarization-synthesized optical lattice, it is within reach to test this scheme with the experimental apparatus at hand.

Towards a One-Million-Operation Quantum Cellular Automaton: This thesis demonstrates the potential of polarization-synthesized optical lattices for future experiments. In particular, the capability to precisely rearrange individual atoms over large distances in a few microseconds, has interesting applications in quantum information processing [110, 256]. However, throughout this thesis it has also become apparent that reaching the grand goal of building a universal quantum computer using alkali atoms in state-dependent optical lattices may not be conceivable. Relying on alkali atoms, state-dependent optical potentials can only be realized by choosing a wavelength which is in between two excited P orbitals. This, in turn, leads to comparably high off-resonant scattering rates (see sec. 2.4.1), which correspondingly set a hard boundary on the time where we can use our qubit states, before they loose their information to the environment. For the experimental apparatus at hand, after only 1 ms already 1 % of the information stored in the qubits is lost. In principle one can extend the qubit lifetime by reducing the optical potential, however, this simultaneously slows down our transport operations (see sec. 3.4.2), which does not solve our problem either. This brings us back to the discussion at the end of section 2.1.3: the level structure of group III atoms posses the particularity of an inverse energy level structure, which is illustrated for Indium in figure 6.2. The ground state P orbital enables us to realize far off-resonant state-dependent optical potentials, which are opposite compared to their cesium counterpart: atoms with $m_J = -1/2$ are attracted only by σ^+ polarized light, whereas atoms with $m_J = +1/2$ are attracted by σ^- polarized light. We estimate, that it is conceivable to reach longitudinal trapping frequencies of up to 1 MHz and a scattering rate of only 0.5 Hz using a 532 nm laser source with an output power of 5 W [360]. The challenge with indium lies in the development of technologies, which are standard tools for cesium, e.g. creating a magneto-optical trap. In previous work, our group demonstrated efficient sub-Doppler cooling of indium [361], which at the time, was limited by the available laser power. However, with recent developments in semiconductor laser diodes, magneto-optical trapping of indium becomes feasible. This would be an important step and should naturally lead to trapping of indium atoms in a far off-resonant optical lattice.

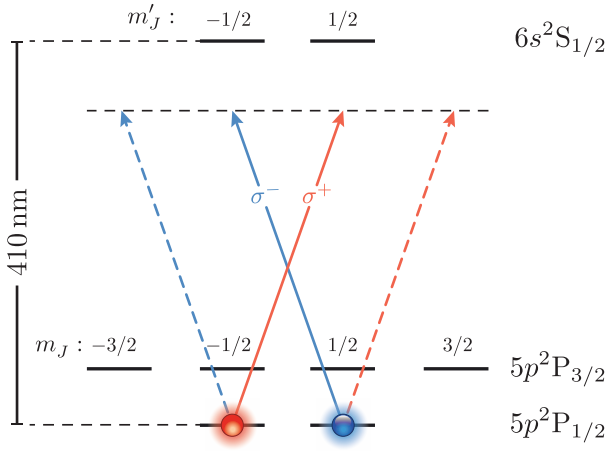

Figure 6.2: Ground state and first excited level of indium. Due to the inverse level structure it is possible to create far off-resonant state-dependent optical potentials: atoms with $m_J = -1/2$ are attracted only by σ^+ polarized light, whereas atoms with $m_J = +1/2$ are attracted by σ^- polarized light.

Lastly: whether we call it the second [8, 362] or even the third quantum revolution [363], one thing is beyond doubt: it is a marvelous time for quantum optics, so let us see what we can achieve with our combined effort.

Bibliography

[1] C. Robens, W. Alt, D. Meschede, C. Emary and A. Alberti, "Ideal Negative Measurements in Quantum Walks Disprove Theories Based on Classical Trajectories", Physical Review X 5.1 (2015) 011003 (cit. on pp. iv, 18, 56, 57, 89, 91).

[2] A. Alberti, C. Robens, W. Alt, S. Brakhane, M. Karski, R. Reimann, A. Widera and D. Meschede, "Super-resolution microscopy of single atoms in optical lattices", New Journal of Physics 18.5 (2016) 053010 (cit. on pp. iv, 3, 4, 10, 19–21, 23–25, 77).

[3] C. Robens, J. Zopes, W. Alt, S. Brakhane, D. Meschede and A. Alberti, "Low-entropy states of neutral atoms in polarization-synthesized optical lattices", arXiv.org (2016), arXiv: 1608.02410v1 [quant-ph] (cit. on pp. iv, 69, 70, 79).

[4] C. Robens, S. Brakhane, D. Meschede and A. Alberti, "Quantum Walks With Neutral Atoms: Quantum Interference Effects of One and Two Particles", arXiv.org (2015), arXiv: 1511.03569v1 [quant-ph] (cit. on pp. iv, 50, 84, 85, 98).

[5] C. Robens, W. Alt, D. Meschede, C. Emary and A. Alberti, "Atomic "bomb testing": the Elitzur-Vaidman experiment violates the Leggett-Garg inequality", In preparation (2016) (cit. on pp. iv, 93).

[6] A. Negretti, C. Robens, D. Meschede, T. Calarco and A. Alberti, "Optimal and fast transport control for coherent splittings of trapped atoms", In preparation (2016) (cit. on pp. iv, 2, 69, 85, 86).

[7] G. Webster, *University of Chicago Press Staff: The Chicago Manual of Style*, 2012, ISBN: 9780226104201 (cit. on p. iv).

[8] J. P. Dowling and G. J. Milburn, "Quantum technology: the second quantum revolution", Philosophical transactions. Series A, Mathematical, physical, and engineering sciences 361.1809 (2003) 1655 (cit. on pp. 1, 110).

[9] A. Einstein, "Strahlungs-Emission und Absorption nach der Quantentheorie", Deutsche Physikalische Gesellschaft 18 (1916) (cit. on p. 1).

[10] T. H. Maiman, "Stimulated Optical Radiation in Ruby", Nature 187.4736 (1960) 493 (cit. on p. 1).

[11] P. A. M. Dirac, "A Theory of Electrons and Protons", Proceedings of the Royal Society A: Mathematical, Physical and Engineering Sciences 126.801 (1930) 360 (cit. on p. 1).

[12] "The Transistor: Selected Reference Material on Characteristics and Applications", Prepared by Bell Telephone Laboratories, Inc for Western Electric Co, New York, 1952 (cit. on p. 1).

[13] E. Schrödinger, "Are there quantum jumps?", The British Journal for the Philosophy of science III.10 (1952) 109 (cit. on p. 1).

[14] D. Deutsch,
"Quantum theory, the Church-Turing principle and the universal quantum computer",
Proceedings of the Royal Society A: Mathematical, Physical and Engineering Sciences 400.1818 (1985) 97 (cit. on p. 1).

[15] T. D. Ladd, F. Jelezko, R. Laflamme, Y. Nakamura, C. Monroe and J. L. O'Brien,
"Quantum computers", Nature 464.7285 (2010) 45 (cit. on pp. 1, 87).

[16] I. Bloch, "Quantum coherence and entanglement with ultracold atoms in optical lattices",
Nature 453.7198 (2008) 1016 (cit. on pp. 1, 19, 67).

[17] A. M. Kaufman, B. J. Lester, C. M. Reynolds, M. L. Wall, M. Foss-Feig, K. R. A. Hazzard,
A. M. Rey and C. A. Regal,
"Two-particle quantum interference in tunnel-coupled optical tweezers.",
Science 345.6194 (2014) 306 (cit. on pp. 1, 2, 4, 67, 82, 100).

[18] D. Barredo, S. de Léséleuc, V. Lienhard, T. Lahaye and A. Browaeys,
"An atom-by-atom assembler of defect-free arbitrary 2d atomic arrays", arXiv.org (2016),
arXiv: 1607.03042v1 [quant-ph] (cit. on pp. 1, 81).

[19] M. Endres, H. Bernien, A. Keesling, H. Levine, E. R. Anschuetz, A. Krajenbrink, C. Senko,
V. Vuletić, M. Greiner and M. D. Lukin, "Cold Matter Assembled Atom-by-Atom",
arXiv.org (2016), arXiv: 1607.03044v1 [quant-ph] (cit. on pp. 1, 81).

[20] H. Häffner, C. F. Roos and R. Blatt, "Quantum computing with trapped ions",
Physics Reports (2008) (cit. on p. 1).

[21] E. Knill, R. Laflamme and G. J. Milburn,
"A scheme for efficient quantum computation with linear optics.", Nature 409.6816 (2001) 46
(cit. on p. 1).

[22] J. Wrachtrup and F. Jelezko, "Processing quantum information in diamond",
Journal of Physics: Condensed Matter (2006) (cit. on p. 1).

[23] J. R. Weber, W. F. Koehl, J. B. Varley, A. Janotti, B. B. Buckley, C. G. Van de Walle and
D. D. Awschalom, "Quantum computing with defects",
Proceedings of the National Academy of Sciences 107.19 (2010) 8513 (cit. on p. 1).

[24] J. Clarke and F. K. Wilhelm, "Superconducting quantum bits", Nature 453.7198 (2008) 1031
(cit. on p. 1).

[25] M. D. Reed, L. DiCarlo, S. E. Nigg, L. Sun, L. Frunzio, S. M. Girvin and R. J. Schoelkopf,
"Realization of three-qubit quantum error correction with superconducting circuits",
Nature 482.7385 (2012) 382 (cit. on pp. 1, 2).

[26] N. Ofek, A. Petrenko, R. Heeres, P. Reinhold, Z. Leghtas, B. Vlastakis, Y. Liu, L. Frunzio,
S. M. Girvin, L. Jiang, M. Mirrahimi, M. H. Devoret and R. J. Schoelkopf,
"Extending the lifetime of a quantum bit with error correction in superconducting circuits",
Nature (2016) 1 (cit. on p. 1).

[27] P. J. J. O'Malley, R. Babbush, I. D. Kivlichan, J. Romero, J. R. McClean, R. Barends, J. Kelly,
P. Roushan, A. Tranter, N. Ding, B. Campbell, Y. Chen, Z. Chen, B. Chiaro, A. Dunsworth,
A. G. Fowler, E. Jeffrey, E. Lucero, A. Megrant, J. Y. Mutus, M. Neeley, C. Neill, C. Quintana,
D. Sank, A. Vainsencher, J. Wenner, T. C. White, P. V. Coveney, P. J. Love, H. Neven,
A. Aspuru-Guzik and J. M. Martinis, "Scalable Quantum Simulation of Molecular Energies",
Physical Review X 6.3 (2016) 031007 (cit. on p. 1).

[28] M. Wallquist, K. Hammerer, P. Rabl and M. Lukin,
"Hybrid quantum devices and quantum engineering", Physica Scripta (2009) (cit. on p. 1).

[29] A. Leggett and A. Garg,
"Quantum mechanics versus macroscopic realism: Is the flux there when nobody looks?",
Physical Review Letters 54.9 (1985) 857 (cit. on pp. 1, 2, 87, 88).

[30] C. Hong, Z. Ou and L. Mandel,
"Measurement of subpicosecond time intervals between two photons by interference.",
Physical Review Letters 59.18 (1987) 2044 (cit. on pp. 1, 97, 100, 102).

[31] A. J. Leggett, "Realism and the physical world",
Reports on progress in physics 71.2 (2008) 022001 (cit. on pp. 1, 87).

[32] M. Schlosshauer,
"Decoherence, the measurement problem, and interpretations of quantum mechanics",
Reviews of Modern Physics 76.4 (2005) 1267 (cit. on p. 1).

[33] A. Bassi, K. Lochan, S. Satin, T. P. Singh and H. Ulbricht,
"Models of wave-function collapse, underlying theories, and experimental tests",
Reviews of Modern Physics 85.2 (2013) 471 (cit. on pp. 1, 87).

[34] G. Knee, "Do Quantum Superpositions Have a Size Limit?", Physics 8 (2015) 6 (cit. on p. 2).

[35] C. Emary, J. P. Cotter and M. Arndt,
"Testing macroscopic realism through high-mass interferometry",
Physical Review A 90.4 (2014) 042114 (cit. on p. 2).

[36] C. Santori, D. Fattal, J. Vučković, G. S. Solomon and Y. Yamamoto,
"Indistinguishable photons from a single-photon device", Nature 419.6907 (2002) 594
(cit. on pp. 2, 103).

[37] M. Halder, A. Beveratos, N. Gisin, V. Scarani, C. Simon and H. Zbinden,
"Entangling independent photons by time measurement", Nature Physics 3.10 (2007) 692
(cit. on pp. 2, 103).

[38] Y.-M. He, Y. He, Y.-J. Wei, D. Wu, M. Atatüre, C. Schneider, S. Höfling, M. Kamp, C.-Y. Lu and J.-W. Pan,
"On-demand semiconductor single-photon source with near-unity indistinguishability",
Nature Nanotechnology (2013) 1 (cit. on pp. 2, 103).

[39] M. Müller, S. Bounouar, K. D. Jöns, M. Glässl and P. Michler,
"On-demand generation of indistinguishable polarization-entangled photon pairs",
Nature Photonics 8.3 (2014) 224 (cit. on pp. 2, 103).

[40] R. Islam, R. Ma, P. M. Preiss, M. Eric Tai, A. Lukin, M. Rispoli and M. Greiner,
"Measuring entanglement entropy in a quantum many-body system", Nature 528.7580 (2015) 77
(cit. on pp. 2, 45, 67, 100).

[41] R. Lopes, A. Imanaliev, A. Aspect, M. Cheneau, D. Boiron and C. I. Westbrook,
"Atomic Hong-Ou-Mandel experiment.", Nature 520.7545 (2015) 66 (cit. on pp. 2, 100).

[42] D. Jaksch, C. Bruder, J. I. Cirac, C. W. Gardiner and P. Zoller,
"Cold bosonic atoms in optical lattices", Physical Review Letters 81.15 (1998) 3108
(cit. on pp. 2, 67).

[43] M. Greiner, O. Mandel, T. Esslinger, T. W. Hänsch and I. Bloch,
"Quantum phase transition from a superfluid to a Mott insulator in a gas of ultracold atoms",
Nature 415.6867 (2002) 39 (cit. on pp. 2, 4, 45, 67).

[44] P. Zoller, T. Beth, D. Binosi, R. Blatt, H. Briegel, D. Bruss, T. Calarco, J. I. Cirac, D. Deutsch, J. Eisert, A. Ekert, C. Fabre, N. Gisin, P. Grangiere, M. Grassl, S. Haroche, A. Imamoglu, A. Karlson, J. Kempe, L. Kouwenhoven, S. Kröll, G. Leuchs, M. Lewenstein, D. Loss, N. Lütkenhaus, S. Massar, J. E. Mooij, M. B. Plenio, E. Polzik, S. Popescu, G. Rempe, A. Sergienko, D. Suter, J. Twamley, G. Wendin, R. Werner, A. Winter, J. Wrachtrup and A. Zeilinger, "Quantum information processing and communication",
European Physical Journal D 36.2 (2005) 203 (cit. on p. 2).

[45] I. H. Deutsch, G. K. Brennen and P. S. Jessen,
"Quantum Computing with Neutral Atoms in An Optical Lattice",
Wiley-VCH Verlag GmbH & Co. KGaA, Weinheim, FRG, 2005 (cit. on pp. 2, 43).

[46] B. M. Terhal, "Quantum error correction for quantum memories",
Reviews of Modern Physics 87.2 (2015) 307 (cit. on p. 2).

[47] A. G. Fowler, M. Mariantoni, J. M. Martinis and A. N. Cleland,
"Surface codes: Towards practical large-scale quantum computation",
Physical Review A 86.3 (2012) 032324 (cit. on p. 2).

[48] J. Chiaverini, D. Leibfried, T. Schaetz, M. D. Barrett, R. B. Blakestad, J. Britton, W. M. Itano, J. D. Jost, E. Knill, C. Langer, R. Ozeri and D. J. Wineland,
"Realization of quantum error correction.", Nature 432.7017 (2004) 602 (cit. on p. 2).

[49] T. Groh, S. Brakhane, W. Alt, D. Meschede, J. K. Asbóth and A. Alberti, "Robustness of topologically protected edge states in quantum walk experiments with neutral atoms",
Physical Review A 94.1 (2016) 013620 (cit. on pp. 2, 25, 26, 107–109).

[50] C. F. Roos, A. Alberti, D. Meschede, P. Hauke and H. Häffner,
"Unravelling quantum statistics with a pair of distant atoms", In preparation (2016)
(cit. on pp. 2, 109).

[51] I. de Vega, D. Porras and J. Ignacio Cirac,
"Matter-Wave Emission in Optical Lattices: Single Particle and Collective Effects",
Physical Review Letters 101.26 (2008) 260404 (cit. on pp. 2, 69).

[52] S. Murmann, F. Deuretzbacher, G. Zürn, J. Bjerlin, S. M. Reimann, L. Santos, T. Lompe and S. Jochim,
"Antiferromagnetic Heisenberg Spin Chain of a Few Cold Atoms in a One-Dimensional Trap",
Physical Review Letters 115.21 (2015) 215301 (cit. on p. 2).

[53] M. Karski, "State-selective transport of single neutral atoms", PhD thesis, 2010
(cit. on pp. 3, 34, 36, 41, 45, 83, 85).

[54] W. Alt, "An objective lens for efficient fluorescence detection of single atoms",
Optik - International Journal for Light and Electron Optics 113.3 (2002) 142
(cit. on pp. 4, 20, 27).

[55] B. Huang, H. Babcock and X. Zhuang,
"Breaking the Diffraction Barrier: Super-Resolution Imaging of Cells", Cell 143.7 (2010) 1047
(cit. on p. 4).

[56] M. A. Thompson, M. D. Lew and W. E. Moerner,
"Extending Microscopic Resolution with Single-Molecule Imaging and Active Control",
Annual Review of Biophysics 41.1 (2012) 321 (cit. on p. 4).

[57] A. Pertsinidis, Y. Zhang and S. Chu,
"Subnanometre single-molecule localization, registration and distance measurements",
Nature 466.7306 (2010) 647 (cit. on p. 4).

[58] M. W. Zwierlein, C. A. Stan, C. H. Schunck, S. M. F. Raupach, S. Gupta, Z. Hadzibabic and W. Ketterle, "Observation of Bose-Einstein Condensation of Molecules",
Physical Review Letters 91.25 (2003) 250401 (cit. on p. 4).

[59] T. Stöferle, H. Moritz, C. Schori, M. Köhl and T. Esslinger,
"Transition from a strongly interacting 1d superfluid to a Mott insulator.",
Physical Review Letters 92.13 (2004) 130403 (cit. on p. 4).

[60] P. Soltan-Panahi, J. Struck, P. Hauke, A. Bick, W. Plenkers, G. Meineke, C. Becker, P. Windpassinger, M. Lewenstein and K. Sengstock,
"Multi-component quantum gases in spin-dependent hexagonal lattices",
Nature Physics 7.5 (2011) 434 (cit. on p. 4).

[61] P. M. Preiss, R. Ma, M. E. Tai, A. Lukin, M. Rispoli, P. Zupancic, Y. Lahini, R. Islam and M. Greiner, "Strongly correlated quantum walks in optical lattices", Science (2015) (cit. on pp. 4, 45, 97).

[62] M. D. Barrett, J. A. Sauer and M. S. Chapman,
"All-Optical Formation of an Atomic Bose-Einstein Condensate",
Physical Review Letters 87.1 (2001) 010404 (cit. on p. 4).

[63] M. W. Zwierlein, C. A. Stan, C. H. Schunck, S. M. F. Raupach, A. J. Kerman and W. Ketterle,
"Condensation of Pairs of Fermionic Atoms near a Feshbach Resonance",
Physical Review Letters 92.12 (2004) 120403 (cit. on p. 4).

[64] R. Jördens, N. Strohmaier, K. Günter, H. Moritz and T. Esslinger,
"A Mott insulator of fermionic atoms in an optical lattice", Nature 455.7210 (2008) 204 (cit. on p. 4).

[65] D. Greif, M. F. Parsons, A. Mazurenko, C. S. Chiu, S. Blatt, F. Huber, G. Ji and M. Greiner,
"Site-resolved imaging of a fermionic Mott insulator.", Science 351.6276 (2016) 953 (cit. on pp. 4, 26).

[66] M. Karski, L. Förster, J.-M. Choi, A. Steffen, W. Alt, D. Meschede and A. Widera,
"Quantum walk in position space with single optically trapped atoms.",
Science 325.5937 (2009) 174 (cit. on pp. 4, 17–19, 67, 78, 83, 84, 90).

[67] Y. Wang, A. Kumar, T.-Y. Wu and D. S. Weiss,
"Single-qubit gates based on targeted phase shifts in a 3D neutral atom array.",
Science 352.6293 (2016) 1562 (cit. on pp. 4, 19, 38, 39, 67, 80).

[68] S. Haroche and J.-M. Raimond, "Exploring the Quantum", Oxford University Press, 2006 (cit. on p. 4).

[69] R. Grimm, M. Weidemüller and Y. B. Ovchinnikov, *Optical Dipole Traps for Neutral Atoms*, vol. 42, Advances In Atomic, Molecular, and Optical Physics, Elsevier, 2000,
ISBN: 9780120038428 (cit. on pp. 4, 41).

[70] M. Martınez-Dorantes,
"Fast non-destructive internal state detection of neutral atoms in optical potentials",
PhD thesis, 2016 (cit. on p. 5).

[71] L. Förster, "Microwave control of atomic motion in a spin dependent optical lattice",
PhD thesis, 2010 (cit. on pp. 5, 48).

[72] D. J. Wineland and W. M. Itano, "Laser cooling of atoms", Physical Review A 20.4 (1979) 1521
(cit. on p. 6).

[73] S. Wolf, S. J. Oliver and D. S. Weiss, "Suppression of Recoil Heating by an Optical Lattice",
Physical Review Letters 85.20 (2000) 4249 (cit. on p. 6).

[74] Y. R. Shen, *Principles of nonlinear optics*, 1984, ISBN: 9789971511067 (cit. on pp. 7, 41, 146).

[75] R. Loudon, *The quantum theory of light*, Clarendon Press and Oxford University Press,
ISBN: 9780198511526 (cit. on p. 7).

[76] K. D. Nelson, X. Li and D. S. Weiss, "Imaging single atoms in a three-dimensional array",
Nature Physics 3.8 (2007) 556 (cit. on p. 7).

[77] A. Hambitzer, "Direct Synthesis of Light Polarization for State-Dependent Transport",
MA thesis, 2012 (cit. on pp. 7, 71, 75).

[78] T. W. Hänsch and A. L. Schawlow, "Cooling of gases by laser radiation",
Optics Communications 13.1 (1975) 68 (cit. on p. 8).

[79] D. Wineland and H. G. Dehmelt,
"Proposed Laser Fluorescence Spectroscopy on Tl+ Mono-Ion Oscillator III ",
Bull. Am. Phys. Soc (1975) (cit. on p. 8).

[80] C. G. Townsend, N. H. Edwards, C. J. Cooper, K. P. Zetie, C. J. Foot, A. M. Steane, P Szriftgiser,
H. Perrin and J. Dalibard, "Phase-space density in the magneto-optical trap",
Physical Review A 52.2 (1995) 1423 (cit. on p. 9).

[81] A. M. Steane, M. Chowdhury and C. J. Foot, "Radiation force in the magneto-optical trap",
Journal of the Optical Society of America B 9.12 (1992) 2142 (cit. on p. 9).

[82] M. Greiner, I. Bloch, T. W. Hänsch and T. Esslinger,
"Magnetic transport of trapped cold atoms over a large distance",
Physical Review A 63.3 (2001) 031401 (cit. on p. 9).

[83] X. Baillard, A. Gauguet, S. Bize, P. Lemonde, P. Laurent, A. Clairon and P. Rosenbusch,
"Interference-filter-stabilized external-cavity diode lasers",
Optics Communications 266.2 (2006) 609 (cit. on p. 9).

[84] G. Genty, A. Grohn, H. Talvitie, M. Kaivola and H. Ludvigsen,
"Analysis of the linewidth of a grating-feedback GaAlAs laser",
IEEE Journal of Quantum Electronics 36.10 (2000) 1193 (cit. on p. 9).

[85] T. M. Hard, "Laser Wavelength Selection and Output Coupling by a Grating",
Applied Optics 9.8 (1970) 1825 (cit. on p. 9).

[86] M. G. Littman and H. J. Metcalf, "Spectrally narrow pulsed dye laser without beam expander.",
Applied Optics 17.14 (1978) 2224 (cit. on p. 9).

[87] C. J. Hawthorn, K. P. Weber and R. E. Scholten,
"Littrow configuration tunable external cavity diode laser with fixed direction output beam",
Review of Scientific Instruments 72.12 (2001) 4477 (cit. on p. 9).

[88] J. J. Snyder, "Paraxial ray analysis of a cat's-eye retroreflector", Applied Optics 14.8 (1975) 1825 (cit. on p. 9).

[89] M. L. Biermann, W. S. Rabinovich, R. Mahon and G. C. Gilbreath, "Design and analysis of a diffraction-limited cat's-eye retroreflector", Optical Engineering 41.7 (2002) 1655 (cit. on p. 9).

[90] C. P. Pearman, C. S. Adams, S. G. Cox, P. F. Griffin, D. A. Smith and I. G. Hughes, "Polarization spectroscopy of a closed atomic transition: applications to laser frequency locking", Journal of Physics B: Atomic, Molecular and Optical Physics 35.24 (2002) 5141 (cit. on p. 9).

[91] T. Udem, J. Reichert, T. W. Hänsch and M. Kourogi, "Absolute optical frequency measurement of the cesium D 2 line", Physical Review A 62.3 (2000) 031801 (cit. on pp. 9, 34).

[92] J. Dalibard and C. Cohen-Tannoudji, "Laser cooling below the Doppler limit by polarization gradients: simple theoretical models", Journal of the Optical Society of America B 6.11 (1989) 2023 (cit. on p. 10).

[93] J. E. Bjorkholm, "Collision-limited lifetimes of atom traps", Physical Review A 38.3 (1988) 1599 (cit. on p. 10).

[94] T. A. Savard, K. M. O'Hara and J. E. Thomas, "Laser-noise-induced heating in far-off resonance optical traps", Physical Review A 56.2 (1997) R1095 (cit. on pp. 11, 12).

[95] M. E. Gehm, K. M. O'Hara, T. A. Savard and J. E. Thomas, "Dynamics of noise-induced heating in atom traps", Physical Review A 58.5 (1998) 3914 (cit. on pp. 11, 13, 15, 70).

[96] M. E. Gehm, K. M. O'Hara, T. A. Savard and J. E. Thomas, "Erratum: Dynamics of noise-induced heating in atom traps [Phys. Rev. A 58, 3914 (1998)]", Physical Review A 61.2 (2000) 029902 (cit. on pp. 11, 13, 15, 70).

[97] M. J. Gibbons, S. Y. Kim, K. M. Fortier, P. Ahmadi and M. S. Chapman, "Achieving very long lifetimes in optical lattices with pulsed cooling", Physical Review A 78.4 (2008) 043418 (cit. on pp. 11, 57).

[98] S. Blatt, A. Mazurenko, M. F. Parsons, C. S. Chiu, F. Huber and M. Greiner, "Low-noise optical lattices for ultracold Li6", Physical Review A 92.2 (2015) 021402 (cit. on pp. 11, 57).

[99] P. Lett, R. Watts, C. Westbrook, W. Phillips, P. Gould and H. Metcalf, "Observation of atoms laser cooled below the Doppler limit.", Physical Review Letters 61.2 (1988) 169 (cit. on pp. 11, 57).

[100] T. M. Brzozowski, M. Maczynska, M. Zawada, J. Zachorowski and W. Gawlik, "Time-of-flight measurement of the temperature of cold atoms for short trap-probe beam distances", Journal of Optics B: Quantum and Semiclassical Optics 4.1 (2002) 62 (cit. on pp. 11, 57).

[101] W. Alt, D. Schrader, S. Kuhr, M. Müller, V. Gomer and D. Meschede, "Single atoms in a standing-wave dipole trap", Physical Review A 67.3 (2003) 033403 (cit. on pp. 11, 16, 57).

[102] M. Hohmann, F. Kindermann, T. Lausch, D. Mayer, F. Schmidt and A. Widera, "Single-atom thermometer for ultracold gases", Physical Review A 93.4 (2016) 043607 (cit. on pp. 11, 57).

[103] D. Halford, J. H. Shoaf and A. S. Risley, "Spectral Density Analysis: Frequency Domain Specification and Measurement of Signal Stability", 27th Annual Symposium on Frequency Control (1973) 421 (cit. on p. 12).

[104] I. R. Boventer, "Characterisation of Phase Noise for the Preparation of Atoms in the Motional Ground State", MA thesis, 2015 (cit. on pp. 13, 57).

[105] R. Reimann, "Cooling and Cooperative Coupling of Single Atoms in an Optical Cavity", PhD thesis, 2014 (cit. on p. 14).

[106] G. Ramola, "A versatile digital frequency synthesizer for state-dependent transport of trapped neutral atoms", MA thesis, 2016 (cit. on pp. 14, 16, 71, 77, 106, 107).

[107] F. Reif, *Fundamentals of Statistical and Thermal Physics*, McGraw-Hill series in fundamentals of physics, Waveland Press, 2009, ISBN: 9781577666127 (cit. on p. 15).

[108] L. D. Landau and E. M. Lifshitz, *Mechanics, Third Edition: Volume 1 (Course of Theoretical Physics)*, 3rd ed., Butterworth-Heinemann, 1976, ISBN: 0750628960 (cit. on p. 16).

[109] MATLAB, *version 8.4.0 (R2014b)*, Natick, Massachusetts: The MathWorks Inc., 2014 (cit. on pp. 16, 27, 78, 137).

[110] D. Jaksch, H. J. Briegel, J. I. Cirac, C. W. Gardiner and P. Zoller, "Entanglement of atoms via cold controlled collisions", Physical Review Letters 82.9 (1999) 1975 (cit. on pp. 17, 67, 81, 109).

[111] I. H. Deutsch and P. S. Jessen, "Quantum-state control in optical lattices", Physical Review A 57.3 (1998) 1972 (cit. on p. 17).

[112] O. Mandel, M. Greiner, A. Widera, T. Rom, T. W. Hänsch and I. Bloch, "Coherent Transport of Neutral Atoms in Spin-Dependent Optical Lattice Potentials", Physical Review Letters 91.1 (2003) 010407 (cit. on pp. 17, 18).

[113] O. Mandel, M. Greiner, A. Widera, T. Rom, T. W. Hänsch and I. Bloch, "Controlled collisions for multi-particle entanglement of optically trapped atoms", Nature 425.6961 (2003) 937 (cit. on pp. 17, 67, 68, 76, 81).

[114] A. Steffen, A. Alberti, W. Alt, N. Belmechri, S. Hild, M. Karski, A. Widera and D. Meschede, "Digital atom interferometer with single particle control on a discretized space-time geometry", Proceedings of the National Academy of Sciences 109.25 (2012) 9770 (cit. on pp. 17, 18, 67, 68, 77, 78).

[115] D. Doring, "Ein Experiment zum zustandsabhängigen Transport einzelner Atome", MA thesis, 2007 (cit. on p. 18).

[116] M. Genske, W. Alt, A. Steffen, A. H. Werner, R. F. Werner, D. Meschede and A. Alberti, "Electric Quantum Walks with Individual Atoms", Physical Review Letters 110.19 (2013) 190601 (cit. on pp. 18, 83, 84).

[117] T. Kuwamoto, K. Honda, Y. Takahashi and T. Yabuzaki, "Magneto-optical trapping of Yb atoms using an intercombination transition", Physical Review A 60.2 (1999) R745 (cit. on p. 19).

[118] V. V. Ivanov, A. Khramov, A. H. Hansen, W. H. Dowd, F. Münchow, A. O. Jamison and S. Gupta, "Sympathetic Cooling in an Optically Trapped Mixture of Alkali and Spin-Singlet Atoms", Physical Review Letters 106.15 (2011) 153201 (cit. on p. 19).

[119] S. Dörscher, A. Thobe, B. Hundt, A. Kochanke, R. Le Targat, P. Windpassinger, C. Becker and K. Sengstock, "Creation of quantum-degenerate gases of ytterbium in a compact 2D-/3D-magneto-optical trap setup", Review of Scientific Instruments 84.4 (2013) 043109 (cit. on p. 19).

[120] A. Kawasaki, B. Braverman, Q. Yu and V. Vuletić, "Two-color magneto-optical trap with small magnetic field for ytterbium", Journal of Physics B: Atomic, Molecular and Optical Physics 48.15 (2015) 1 (cit. on p. 19).

[121] M. Miranda, R. Inoue, Y. Okuyama, A. Nakamoto and M. Kozuma, "Site-resolved imaging of ytterbium atoms in a two-dimensional optical lattice", Physical Review A 91.6 (2015) 063414 (cit. on pp. 19, 26).

[122] R. Yamamoto, J. Kobayashi, T. Kuno, K. Kato and Y. Takahashi, "An ytterbium quantum gas microscope with narrow-line laser cooling", New Journal of Physics 18.2 (2016) 1 (cit. on p. 19).

[123] C. Zhang, S. L. Rolston and S. Das Sarma, "Manipulation of single neutral atoms in optical lattices", Physical Review A 74.4 (2006) 042316 (cit. on p. 19).

[124] P. Lee, M. Anderlini, B. Brown, J. Sebby-Strabley, W. Phillips and J. Porto, "Sublattice Addressing and Spin-Dependent Motion of Atoms in a Double-Well Lattice", Physical Review Letters 99.2 (2007) 020402 (cit. on p. 19).

[125] M. Karski, L. Förster, J. M. Choi, W. Alt, A. Widera and D. Meschede, "Nearest-Neighbor Detection of Atoms in a 1D Optical Lattice by Fluorescence Imaging", Physical Review Letters 102.5 (2009) 053001 (cit. on pp. 19, 24).

[126] M. Karski, L. Förster, J.-M. Choi, A. Steffen, N. Belmechri, W. Alt, D. Meschede and A. Widera, "Imprinting patterns of neutral atoms in an optical lattice using magnetic resonance techniques", New Journal of Physics 12.6 (2010) 065027 (cit. on pp. 19, 21, 39, 68, 78).

[127] J. H. Lee, E. Montano, I. H. Deutsch and P. S. Jessen, "Robust site-resolvable quantum gates in an optical lattice via inhomogeneous control", Nature Communications 4 (2013) 1 (cit. on pp. 19, 67).

[128] Y. Wang, X. Zhang, T. A. Corcovilos, A. Kumar and D. S. Weiss, "Coherent Addressing of Individual Neutral Atoms in a 3D Optical Lattice", Physical Review Letters 115.4 (2015) 043003 (cit. on pp. 19, 25, 39).

[129] T. Xia, M. Lichtman, K. Maller, A. W. Carr, M. J. Piotrowicz, L. Isenhower and M. Saffman, "Randomized Benchmarking of Single-Qubit Gates in a 2D Array of Neutral-Atom Qubits", Physical Review Letters 114.10 (2015) 100503 (cit. on p. 19).

[130] I. Bloch, J. Dalibard and S. Nascimbène, "Quantum simulations with ultracold quantum gases", Nature Physics 8.4 (2012) 267 (cit. on p. 19).

[131] W. S. Bakr, J. I. Gillen, A. Peng, S. Fölling and M. Greiner, "A quantum gas microscope for detecting single atoms in a Hubbard-regime optical lattice", Nature 461.7269 (2009) 74 (cit. on pp. 19, 26).

[132] J. F. Sherson, C. Weitenberg, M. Endres, M. Cheneau, I. Bloch and S. Kuhr, "Single-atom-resolved fluorescence imaging of an atomic Mott insulator", Nature 467.7311 (2010) 68 (cit. on pp. 19, 26, 67).

[133] E. Haller, J. Hudson, A. Kelly, D. A. Cotta, B. Peaudecerf, G. D. Bruce and S. Kuhr, "Single-atom imaging of fermions in a quantum-gas microscope", Nature Physics 11.9 (2015) 738 (cit. on p. 19).

[134] L. W. Cheuk, M. A. Nichols, M. Okan, T. Gersdorf, V. V. Ramasesh, W. S. Bakr, T. Lompe and M. W. Zwierlein, "Quantum-Gas Microscope for Fermionic Atoms", Physical Review Letters 114.19 (2015) 193001 (cit. on pp. 19, 26).

[135] M. F. Parsons, F. Huber, A. Mazurenko, C. S. Chiu, W. Setiawan, K. Wooley-Brown, S. Blatt and M. Greiner, "Site-resolved imaging of fermionic Li 6 in an optical lattice.", Physical Review Letters 114.21 (2015) 213002 (cit. on p. 19).

[136] A. Omran, M. Boll, T. A. Hilker, K. Kleinlein, G. Salomon, I. Bloch and C. Gross, "Microscopic Observation of Pauli Blocking in Degenerate Fermionic Lattice Gases", Physical Review Letters 115.26 (2015) 263001 (cit. on p. 19).

[137] N. Bobroff, "Position measurement with a resolution and noise-limited instrument", Review of Scientific Instruments 57.6 (1986) 1152 (cit. on p. 19).

[138] R. E. Thompson, D. R. Larson and W. W. Webb, "Precise Nanometer Localization Analysis for Individual Fluorescent Probes", Biophysical journal 82.5 (2002) 2775 (cit. on p. 19).

[139] R. J. Ober, S. Ram and E. S. Ward, "Localization Accuracy in Single-Molecule Microscopy", Biophysical journal 86.2 (2004) 1185 (cit. on p. 19).

[140] T. Quan, S. Zeng and Z.-L. Huang, "Localization capability and limitation of electron-multiplying charge-coupled, scientific complementary metal-oxide semiconductor, and charge-coupled devices for superresolution imaging", Journal of Biomedical Optics 15.6 (2010) 066005 (cit. on p. 19).

[141] Y. Miroshnychenko, W. Alt, I. Dotsenko, L. Förster, M. Khudaverdyan, A. Rauschenbeutel and D. Meschede, "Precision preparation of strings of trapped neutral atoms", New Journal of Physics 8.9 (2006) 191 (cit. on p. 20).

[142] A. Fuhrmanek, R. Bourgain, Y. R. P. Sortais and A. Browaeys, "Free-Space Lossless State Detection of a Single Trapped Atom", Physical Review Letters 106.13 (2011) 133003 (cit. on p. 20).

[143] D. B. Hume, I. Stroescu, M. Joos, W. Muessel, H. Strobel and M. K. Oberthaler, "Accurate Atom Counting in Mesoscopic Ensembles", Physical Review Letters 111.25 (2013) 253001 (cit. on p. 20).

[144] P. Seitz, "Fundamentals of Noise in Optoelectronics", *Single-Photon Imaging*, ed. by P. Seitz and A. J. Theuwissen, Springer Berlin Heidelberg, 2011 1, ISBN: 978-3-642-18443-7; (cit. on p. 20).

[145] J. Anderson and I. R. King, "Toward High-Precision Astrometry with WFPC2. I. Deriving an Accurate Point-Spread Function", Publications of the Astronomical Society of the Pacific 112.776 (2000) 1360 (cit. on p. 22).

[146] M. Born and E. Wolf, *Principle of optics*, 7th, Cambridge, UK: Cambridge University Press, 2003, ISBN: 9781139632607 (cit. on p. 24).

[147] J. W. Goodman, *Introduction to Fourier Optics*, McGraw-Hill, New York, 1996, ISBN: 9788130908205 (cit. on pp. 24, 47).

[148] G. Cennini, C. Geckeler, G. Ritt, T. Salger and M. Weitz, "Two-dimensional Bose-Einstein condensates in a CO2-laser optical lattice", Fortschritte der Physik 54.8-10 (2006) 719 (cit. on p. 25).

[149] S. Brakhane, "The Quantum Walk Microscope", PhD thesis, 2016 (cit. on pp. 26, 29, 32, 39, 46, 80, 108).

[150] E. Roth, *private communication*, Director Development Optical Systems Carl Zeiss Jena GmbH, 2012 (cit. on p. 26).

[151] Q. Wu, L. P. Ghislain and V. B. Elings, "Imaging with solid immersion lenses, spatial resolution, and applications", Proceedings of the IEEE 88.9 (2000) 1491 (cit. on pp. 26, 29).

[152] S. AG, "SCHOTT-N-SF10-Optical-Glass", (2014) 1 (cit. on p. 27).

[153] S. Brakhane, W. Alt, D. Meschede, C. Robens, G. Moon and A. Alberti, "Note: Ultra-low birefringence dodecagonal vacuum glass cell.", Review of Scientific Instruments 86.12 (2015) 126108 (cit. on p. 27).

[154] T. Gissibl, S. Thiele, A. Herkommer and H. Giessen, "Two-photon direct laser writing of ultracompact multi-lens objectives", Nature Photonics (2016) 1 (cit. on p. 29).

[155] R. Juškaitis, "Measuring the real point spread function of high numerical aperture microscope objective lenses", Handbook of biological confocal microscopy Chapter 11 (2006) 239 (cit. on pp. 29, 33).

[156] F. Kleißler, "Assembly and Characterization of a High Numerical Aperture Microscope for Single Atoms", MA thesis, 2014 (cit. on p. 29).

[157] E. Betzig and R. J. Chichester, "Single molecules observed by near-field scanning optical microscopy.", Science 262.5138 (1993) 1422 (cit. on p. 29).

[158] E. Betzig and R. J. Chichester, "Corrections and clarifications.", Science 263.5144 (1994) 159 (cit. on p. 29).

[159] J. A. Veerman, M. F. Garcia-Parajo, L. Kuipers and N. F. van Hulst, "Single molecule mapping of the optical field distribution of probes for near-field microscopy", Journal of Microscopy-Oxford 194.Pt 2-3 (1999) 477 (cit. on p. 29).

[160] S. U. Hwang and Y. G. Lee, "Simulation of an oil immersion objective lens: a simplified ray-optics model considering Abbe's sine condition", Optics Express 16.26 (2008) 21170 (cit. on p. 30).

[161] J. H. Burge, C. Zhao and M. B. Dubin, "Use of the Abbe Sine Condition to Quantify Alignment Aberrations in Optical Imaging Systems", *International Optical Design Conference*, Washington, D.C.: OSA, 2010 ITuD5, ISBN: 978-1-55752-893-3 (cit. on p. 30).

[162] C. J. R. Sheppard and M. Gu, "Imaging by a High Aperture Optical System", Journal of Modern Optics 40.8 (1993) 1631 (cit. on p. 31).

[163] J. J. M. Braat, "Abbe sine condition and related imaging conditions in geometrical optics", Fifth International Topical Meeting on Education and Training in Optics 3190 (1997) 59 (cit. on p. 31).

[164] C. Obermüller and K. Karrai, "Far field characterization of diffracting circular apertures", Applied Physics Letters 67.23 (1995) 3408 (cit. on pp. 31, 32).

[165] C. Obermuller, K. Karrai, G. Kolb and G. Abstreiter, "Transmitted radiation through a subwavelength-sized tapered optical fiber tip", Ultramicroscopy 61.1-4 (1995) 171 (cit. on p. 31).

[166] A. Drezet, J. C. Woehl and S. Huant, "Diffraction by a small aperture in conical geometry: Application to metal-coated tips used in near-field scanning optical microscopy", Physical Review E 65.4 (2002) 046611 (cit. on p. 31).

[167] T. Wilson, R. Juškaitis and P. Higdon, "The imaging of dielectric point scatterers in conventional and confocal polarisation microscopes", Optics Communications 141.5-6 (1997) 298 (cit. on p. 32).

[168] L. Novotny and B. Hecht, *Principles of Nano-optics*, Cambridge: Cambridge University Press, ISBN: 9781107005464 (cit. on p. 33).

[169] S. Kuhr, "A controlled quantum system of individual neutral atoms", PhD thesis, 2003 (cit. on pp. 33, 64).

[170] T. P. Heavner, E. A. Donley, F. Levi, G. Costanzo, T. E. Parker, J. H. Shirley, N. Ashby, S. Barlow and S. R. Jefferts, "First accuracy evaluation of NIST-F2", Metrologia 51.3 (2014) 174 (cit. on p. 33).

[171] D. W. Allan, "Statistics of atomic frequency standards", Proceedings of the IEEE 54.2 (1966) 221 (cit. on p. 33).

[172] N. Huntemann, C. Sanner, B. Lipphardt, C. Tamm and E. Peik, "Single-Ion Atomic Clock with 3 times 10-18 Systematic Uncertainty", Physical Review Letters 116.6 (2016) 063001 (cit. on p. 33).

[173] T. L. Nicholson, S. L. Campbell, R. B. Hutson, G. E. Marti, B. J. Bloom, R. L. McNally, W. Zhang, M. D. Barrett, M. S. Safronova, G. F. Strouse, W. L. Tew and J. Ye, "Systematic evaluation of an atomic clock at 2 times 10-18 total uncertainty", Nature Communications 6 (2015) 1 (cit. on p. 33).

[174] I. Ushijima, M. Takamoto, M. Das, T. Ohkubo and H. Katori, "Cryogenic optical lattice clocks", Nature Photonics (2015) (cit. on pp. 33, 67).

[175] M. Gurov, J. J. McFerran, B. Nagorny, R. Tyumenev, Z. Xu, Y. Le Coq, R. Le Targat, P. Lemonde, J. Lodewyck and S. Bize, "Optical Lattice Clocks as Candidates for a Possible Redefinition of the SI Second", IEEE Transactions on Instrumentation and Measurement 62.6 (2013) 1568 (cit. on p. 33).

[176] S. Olmschenk, R. Chicireanu, K. D. Nelson and J. V. Porto, "Randomized benchmarking of atomic qubits in an optical lattice", New Journal of Physics 12.11 (2010) 113007 (cit. on p. 33).

[177] W. Happer, "Optical pumping", Reviews of Modern Physics 44.2 (1972) 169 (cit. on p. 34).

[178] A. Omont, "Irreducible components of the density matrix. Application to optical pumping", Progress in quantum electronics 5 (1977) 69 (cit. on p. 34).

[179] R. Jozsa, "Fidelity for Mixed Quantum States", Journal of Modern Optics 41.12 (1994) 2315 (cit. on p. 34).

[180] S. Brakhane and A. Alberti, "Technical Note: Stress-Induced Birefringence in Vacuum Systems", (2016) 1 (cit. on pp. 34, 57, 64, 73, 74).

[181] A. Steffen, "Single atom interferometers and Bloch oscillations in quantum walks", PhD thesis, 2013 (cit. on pp. 34, 36).

[182] S. Kuhr, W. Alt, D. Schrader, I. Dotsenko, Y. Miroshnychenko, A. Rauschenbeutel and D. Meschede, "Analysis of dephasing mechanisms in a standing-wave dipole trap", Physical Review A 72.2 (2005) 023406 (cit. on pp. 34–36, 44, 68).

[183] D. Schrader, "A neutral atom quantum register", PhD thesis, 2004 (cit. on p. 34).

[184] D. A. Steck, "Cesium D line data", Theoretical Division (2008) (cit. on pp. 34, 42, 145).

[185] L. Allen and J. H. Eberly, *Optical Resonance and Two-Level Atoms*, Wiley, New York, 1987, ISBN: 9780486655338 (cit. on p. 34).

[186] F. Bloch, "Nuclear Induction", Physical Review 70.7-8 (1946) 460 (cit. on pp. 35, 40).

[187] H. C. Torrey, "Bloch Equations with Diffusion Terms", Physical Review 104.3 (1956) 563 (cit. on p. 35).

[188] J. Zopes, "Sorting atoms in spin-dependent optical lattices", MA thesis, 2015 (cit. on pp. 36, 78, 82).

[189] A. Alberti, W. Alt, R. Werner and D. Meschede, "Decoherence models for discrete-time quantum walks and their application to neutral atom experiments", New Journal of Physics 16.12 (2014) 1 (cit. on pp. 36, 44, 68, 70, 80, 84, 85, 94).

[190] M. L. Citron, H. R. Gray, C. W. Gabel and C. R. Stroud Jr, "Experimental study of power broadening in a two-level atom", Physical Review A 16.4 (1977) 1507 (cit. on p. 36).

[191] L. Viola and S. Lloyd, "Dynamical suppression of decoherence in two-state quantum systems", Physical Review A 58.4 (1998) 2733 (cit. on p. 38).

[192] W. Yang, Z.-Y. Wang and R.-B. Liu, "Preserving qubit coherence by dynamical decoupling", Frontiers of Physics 6.1 (2010) 2 (cit. on p. 38).

[193] P. Würtz, T. Langen, T. Gericke, A. Koglbauer and H. Ott, "Experimental Demonstration of Single-Site Addressability in a Two-Dimensional Optical Lattice", Physical Review Letters 103.8 (2009) 080404 (cit. on p. 38).

[194] R. Scheunemann, F. S. Cataliotti, T. W. Hänsch and M. Weitz, "Resolving and addressing atoms in individual sites of a CO2-laser optical lattice", Physical Review A 62.5 (2000) pages (cit. on p. 38).

[195] D. Schrader, I. Dotsenko, M. Khudaverdyan, Y. Miroshnychenko, A. Rauschenbeutel and D. Meschede, "Neutral Atom Quantum Register", Physical Review Letters 93.15 (2004) 150501 (cit. on pp. 39, 68).

[196] M. P. A. Jones, J. Beugnon, A. Gaëtan, J. Zhang, G. Messin, A. Browaeys and P. Grangier, "Fast quantum state control of a single trapped neutral atom", Physical Review A 75.4 (2007) 040301 (cit. on p. 39).

[197] D. Hanneke, J. P. Home, J. D. Jost, J. M. Amini, D. Leibfried and D. J. Wineland, "Realization of a programmable two-qubit quantum processor", Nature Physics 6.1 (2009) 13 (cit. on p. 39).

[198] M. Johanning, A. Braun, N. Timoney, V. Elman, W. Neuhauser and C. Wunderlich, "Individual Addressing of Trapped Ions and Coupling of Motional and Spin States Using rf Radiation", Physical Review Letters 102.7 (2009) 073004 (cit. on pp. 39, 55).

[199] N. Lundblad, J. M. Obrecht, I. B. Spielman and J. V. Porto, "Field-sensitive addressing and control of field-insensitive neutral-atom qubits", Nature Physics 5.8 (2009) 575 (cit. on p. 39).

[200] C. Weitenberg, M. Endres, J. F. Sherson, M. Cheneau, P. Schauß, T. Fukuhara, I. Bloch and S. Kuhr, "Single-spin addressing in an atomic Mott insulator", Nature 471.7338 (2011) 319 (cit. on pp. 39, 80).

[201] J. Söding, D. Guéry-Odelin, P. Desbiolles, G. Ferrari and J. Dalibard, "Giant Spin Relaxation of an Ultracold Cesium Gas", Physical Review Letters 80.9 (1998) 1869 (cit. on pp. 40, 97, 98).

[202] J. D. Miller, R. A. Cline and D. J. Heinzen, "Far-off-resonance optical trapping of atoms", Physical Review A 47.6 (1993) R4567 (cit. on p. 40).

[203] R. A. Cline, J. D. Miller, M. R. Matthews and D. J. Heinzen, "Spin relaxation of optically trapped atoms by light scattering.", Optics Letters 19.3 (1994) 207 (cit. on pp. 40, 41).

[204] D. Leibfried, R. Blatt, C. Monroe and D. Wineland, "Quantum dynamics of single trapped ions", Reviews of Modern Physics 75.1 (2003) 281 (cit. on pp. 44, 46, 55, 57, 58, 61–63).

[205] E. Urban, T. A. Johnson, T. Henage, L. Isenhower, D. D. Yavuz, T. G. Walker and M. Saffman, "Observation of Rydberg blockade between two atoms", Nature Physics 5.2 (2009) 110 (cit. on p. 44).

[206] L. Isenhower, E. Urban, X. L. Zhang, A. T. Gill, T. Henage, T. A. Johnson, T. G. Walker and M. Saffman, "Demonstration of a Neutral Atom Controlled-NOT Quantum Gate", Physical Review Letters 104.1 (2010) 010503 (cit. on p. 44).

[207] C. Chin, R. Grimm, P. Julienne and E. Tiesinga, "Feshbach resonances in ultracold gases", Reviews of Modern Physics 82.2 (2010) 1225 (cit. on p. 44).

[208] R. Ozeri, C. Langer, J. Jost, B. DeMarco, A. Ben-Kish, B. Blakestad, J. Britton, J. Chiaverini, W. Itano, D. Hume, D. Leibfried, T. Rosenband, P. Schmidt and D. Wineland, "Hyperfine Coherence in the Presence of Spontaneous Photon Scattering", Physical Review Letters 95.3 (2005) 030403 (cit. on p. 44).

[209] A. Steffen, W. Alt, M. Genske, D. Meschede, C. Robens and A. Alberti, "Note: In situ measurement of vacuum window birefringence by atomic spectroscopy", Review of Scientific Instruments 84.12 (2013) 126103 (cit. on pp. 44, 83, 84).

[210] E. L. Hahn, "Spin echoes", Physical Review 80.4 (1950) 580 (cit. on pp. 44, 45).

[211] M. F. Andersen, A. Kaplan and N. Davidson, "Echo Spectroscopy and Quantum Stability of Trapped Atoms", Physical Review Letters 90.2 (2003) 023001 (cit. on p. 44).

[212] S. Kuhr, W. Alt, D. Schrader, I. Dotsenko, Y. Miroshnychenko, W. Rosenfeld, M. Khudaverdyan, V. Gomer, A. Rauschenbeutel and D. Meschede, "Coherence Properties and Quantum State Transportation in an Optical Conveyor Belt", Physical Review Letters 91.21 (2003) 213002 (cit. on pp. 44, 45, 51, 52).

[213] S. Kuhr, W. Alt, D. Schrader, I. Dotsenko, Y. Miroshnychenko, W. Rosenfeld, M. Khudaverdyan, V. Gomer, A. Rauschenbeutel and D. Meschede, "Erratum: Coherence Properties and Quantum State Transportation in an Optical Conveyor Belt [Phys. Rev. Lett. 91, 213002 (2003)]", Physical Review Letters 95.9 (2005) 099901 (cit. on p. 44).

[214] J. I. Gillen, "The Quantum Gas Microscope", PhD thesis, 2009 (cit. on p. 45).

[215] C. Roos, T. Zeiger, H. Rohde, H. C. Nägerl, J. Eschner, D. Leibfried, F. Schmidt-Kaler and R. Blatt, "Quantum State Engineering on an Optical Transition and Decoherence in a Paul Trap", Physical Review Letters 83.23 (1999) 4713 (cit. on p. 45).

[216] M. Lindberg, "Resonance Fluorescence of a Laser-Cooled Trapped Ion in the Lamb-Dicke Limit", Physical Review A 34.4 (1986) 3178 (cit. on p. 46).

[217] T. Kuga, Y. Torii, N. Shiokawa, T. Hirano, Y. Shimizu and H. Sasada, "Novel Optical Trap of Atoms with a Doughnut Beam", Physical Review Letters 78.25 (1997) 4713 (cit. on p. 46).

[218] R. Ozeri, L. Khaykovich and N. Davidson, "Long spin relaxation times in a single-beam blue-detuned optical trap", Physical Review A 59.3 (1999) R1750 (cit. on pp. 46, 47, 52).

[219] S. Kulin, S. Aubin, S. Christe and B. Peker, "A single hollow-beam optical trap for cold atoms", Journal of Optics B: Quantum and Semiclassical Optics 3.6 (2001) 353 (cit. on pp. 46, 47).

[220] K. Bongs, S. Burger, S. Dettmer, D. Hellweg, J. Arlt, W. Ertmer and K. Sengstock, "Waveguide for Bose-Einstein condensates", Physical Review A 63.3 (2001) 031602 (cit. on p. 46).

[221] F. K. Fatemi, M. Bashkansky and Z. Dutton, "Dynamic high-speed spatial manipulation of cold atoms using acousto-optic and spatial light modulation", Optics Express 15.6 (2007) 3589 (cit. on p. 46).

[222] P. Xu, X. He, J. Wang and M. Zhan, "Trapping a single atom in a blue detuned optical bottle beam trap", Optics Letters 35.13 (2010) 2164 (cit. on pp. 46, 47).

[223] J. A. Pechkis and F. K. Fatemi, "Cold atom guidance in a capillary using blue-detuned, hollow optical modes", Optics Express 20.12 (2012) 13409 (cit. on p. 46).

[224] G. Li, S. Zhang, L. Isenhower, K. Maller and M. Saffman, "Crossed vortex bottle beam trap for single-atom qubits", Optics Letters 37.5 (2012) 851 (cit. on pp. 46, 52, 53).

[225] S. A. Kennedy, G. W. Biedermann, J. T. Farrar, T. G. Akin, S. P. Krzyzewski and E. R. I. Abraham, "Confinement of ultracold atoms in a Laguerre–Gaussian laser beam created with diffractive optics", Optics Communications 321.C (2014) 110 (cit. on p. 46).

[226] R. Ozeri, L. Khaykovich and N. Davidson, "Erratum: Long spin relaxation times in a single-beam blue-detuned optical trap [Phys. Rev. A 59, R1750 (1999)]", Physical Review A 65.6 (2002) 069903 (cit. on pp. 46, 47, 52).

[227] E. Abramochkin and V. Volostnikov, "Beam Transformations and Nontransformed Beams", Optics Communications 83.1-2 (1991) 123 (cit. on p. 46).

[228] M. Padgett, J. Arlt, N. Simpson and L. Allen, "An experiment to observe the intensity and phase structure of Laguerre–Gaussian laser modes", American Journal of Physics 64.1 (1996) 77 (cit. on p. 46).

[229] L. Cacciapuoti, M. de Angelis, G. Pierattini and G. M. Tino, "Single-beam optical bottle for cold atoms using a conical lens", European Physical Journal D 14.3 (2001) 373 (cit. on p. 46).

[230] V. Y. Bazhenov, M. S. Soskin and M. V. Vasnetsov, "Screw Dislocations in Light Wavefronts", Journal of Modern Optics 39.5 (1992) 985 (cit. on p. 46).

[231] N. R. Heckenberg, R. McDuff, C. P. Smith and A. G. White, "Generation of Optical-Phase Singularities by Computer-Generated Holograms", Optics Letters 17.3 (1992) 221 (cit. on pp. 46, 47).

[232] S. A. Kennedy, M. J. Szabo, H. Teslow, J. Z. Porterfield and E. R. I. Abraham, "Creation of Laguerre-Gaussian laser modes using diffractive optics", Physical Review A 66.4 (2002) 043801 (cit. on pp. 46, 47).

[233] S. N. Khonina, V. V. Kotlyar, M. V. Shinkaryev, V. A. Soifer and G. V. Uspleniev, "The Phase Rotor Filter", Journal of Modern Optics 39.5 (1992) 1147 (cit. on p. 46).

[234] M. W. Beijersbergen, R. Coerwinkel, M. Kristensen and J. P. Woerdman, "Helical-wavefront laser beams produced with a spiral phaseplate", Optics Communications 112.5-6 (1994) 321 (cit. on p. 46).

[235] M. W. Beijersbergen, L. Allen, H. E. L. O. van der Veen and J. P. Woerdman, "Astigmatic laser mode converters and transfer of orbital angular momentum", Optics Communications 96.1-3 (1993) 123 (cit. on p. 47).

[236] J. Arlt, K. Dholakia, L. Allen and M. J. Padgett, "The production of multiringed Laguerre–Gaussian modes by computer-generated holograms", Journal of Modern Optics 45.6 (1998) 1231 (cit. on p. 47).

[237] A. M. Yao and M. J. Padgett, "Orbital angular momentum: origins, behavior and applications", Advances in Optics and Photonics 3.2 (2011) 161 (cit. on p. 47).

[238] M. Massari, G. Ruffato, M. Gintoli, F. Ricci and F. Romanato, "Fabrication and characterization of high-quality spiral phase plates for optical applications", Applied Optics 54.13 (2015) 4077 (cit. on p. 47).

[239] A. Mawardi, "Generation of a donut beam for a tight radial confinement of atoms in a one-dimensional optical lattice", MA thesis, 2010 (cit. on pp. 47–49).

[240] A. Mawardi, S. Hild, A. Widera and D. Meschede, "ABCD-treatment of a propagating doughnut beam generated by a spiral phase plate", Optics Express 19.22 (2011) 21205 (cit. on p. 47).

[241] C. Monroe, D. M. Meekhof, B. E. King, S. R. Jefferts, W. M. Itano, D. J. Wineland and P. Gould, "Resolved-Side-Band Raman Cooling of a Bound Atom to the 3d Zero-Point Energy", Physical Review Letters 75.22 (1995) 4011 (cit. on p. 53).

[242] S. E. Hamann, D. L. Haycock, G. Klose, P. H. Pax, I. H. Deutsch and P. S. Jessen, "Resolved-sideband Raman cooling to the ground state of an optical lattice", Physical Review Letters 80.19 (1998) 4149 (cit. on p. 53).

[243] H. Perrin, A. Kuhn, I. Bouchoule and C. Salomon, "Sideband cooling of neutral atoms in a far-detuned optical lattice", Europhysics Letters 42.4 (1998) 395 (cit. on pp. 53, 58).

[244] V. Vuletić, C. Chin, A. J. Kerman and S. Chu, "Degenerate Raman sideband cooling of trapped cesium atoms at very high atomic densities", Physical Review Letters 81.26 (1998) 5768 (cit. on p. 53).

[245] L. Förster, M. Karski, J.-M. Choi, A. Steffen, W. Alt, D. Meschede, A. Widera, E. Montano, J. H. Lee, W. Rakreungdet and P. S. Jessen, "Microwave Control of Atomic Motion in Optical Lattices", Physical Review Letters 103.23 (2009) 233001 (cit. on pp. 53, 55, 60, 78).

[246] D. J. Han, S. Wolf, S. Oliver, C. McCormick, M. T. DePue and D. S. Weiss, "3D Raman sideband cooling of cesium atoms at high density", Physical Review Letters 85.4 (2000) 724 (cit. on pp. 53, 60).

[247] A. M. Kaufman, B. J. Lester and C. A. Regal, "Cooling a Single Atom in an Optical Tweezer to Its Quantum Ground State", Physical Review X 2.4 (2012) 041014 (cit. on pp. 53, 60).

[248] X. Li, T. A. Corcovilos, Y. Wang and D. S. Weiss, "3D Projection Sideband Cooling", Physical Review Letters 108.10 (2012) 103001 (cit. on pp. 53, 60).

[249] J. D. Thompson, T. G. Tiecke, A. S. Zibrov, V. Vuletić and M. D. Lukin, "Coherence and Raman Sideband Cooling of a Single Atom in an Optical Tweezer", Physical Review Letters 110.13 (2013) 133001 (cit. on pp. 53, 60).

[250] P. F. Bernath, *Spectra of Atoms and Molecules*, 3rd Edition, Oxford University Press, 2015, ISBN: 9780199382576 (cit. on p. 55).

[251] D. S. Weiss, S. L. Winoto and M. T. DePue, "Cooling atoms in a far-detuned optical lattice", 2995 (1997) 156 (cit. on p. 55).

[252] N. Belmechri, L. Förster, W. Alt, A. Widera, D. Meschede and A. Alberti, "Microwave control of atomic motional states in a spin-dependent optical lattice", Journal of Physics B: Atomic, Molecular and Optical Physics 46.10 (2013) 104006 (cit. on pp. 55, 57, 62, 68, 99).

[253] Q. A. Turchette, Kielpinski, B. E. King, D. Leibfried, D. M. Meekhof, C. J. Myatt, M. A. Rowe, C. A. Sackett, C. S. Wood, W. M. Itano, C. Monroe and D. J. Wineland, "Heating of trapped ions from the quantum ground state", Physical Review A 61.6 (2000) 063418 (cit. on p. 57).

[254] J. I. Cirac, L. J. Garay, R. Blatt, A. S. Parkins and P. Zoller, "Laser cooling of trapped ions: The influence of micromotion", Physical Review A 49.1 (1994) 421 (cit. on p. 61).

[255] I. Bloch and P. Zoller, "Chapter 5 - Ultracold Atoms and Molecules in Optical Lattices", *Ultracold Bosonic and Fermionic Gases*, ed. by A. L. F. Kathryn Levin and D. M. Stamper-Kurn, Elsevier, 2012 121, ISBN: 9786613625984 (cit. on p. 67).

[256] G. K. Brennen, C. M. Caves, P. S. Jessen and I. H. Deutsch,
"Quantum logic gates in optical lattices", Physical Review Letters 82.5 (1999) 1060
(cit. on pp. 67, 109).

[257] R. Raussendorf and H. J. Briegel, "A One-Way Quantum Computer",
Physical Review Letters 86.22 (2001) 5188 (cit. on p. 67).

[258] M. Lewenstein, A. Sanpera and V. Ahufinger,
Ultracold atoms in optical lattices: simulating quantum many-body systems,
Oxford: Oxford University Press, 2012, ISBN: 9780199573127 (cit. on p. 67).

[259] W. S. Bakr, A. Peng, M. E. Tai, R. Ma, J. Simon, J. I. Gillen, S. Fölling, L. Pollet and M. Greiner,
"Probing the superfluid-to-Mott insulator transition at the single-atom level.",
Science 329.5991 (2010) 547 (cit. on pp. 67, 82).

[260] A. J. Leggett,
Quantum liquids : Bose condensation and Cooper pairing in condensed-matter systems,
Oxford; New York: Oxford University Press, 2006, ISBN: 9780198526438 (cit. on p. 67).

[261] T. Esslinger, "Fermi-Hubbard Physics with Atoms in an Optical Lattice",
Annual Review of Condensed Matter Physics 1.1 (2010) 129 (cit. on p. 67).

[262] Y. Fung, P. Sompet and M. Andersen,
"Single Atoms Preparation Using Light-Assisted Collisions", Technologies 4.1 (2016) 4
(cit. on p. 67).

[263] M. T. DePue, C. McCormick, S. L. Winoto, S. Oliver and D. S. Weiss,
"Unity occupation of sites in a 3D optical lattice", Physical Review Letters 82.11 (1999) 2262
(cit. on p. 67).

[264] A. Fuhrmanek, R. Bourgain, Y. R. P. Sortais and A. Browaeys,
"Light-assisted collisions between a few cold atoms in a microscopic dipole trap",
Physical Review A 85.6 (2012) 062708 (cit. on p. 67).

[265] D. S. Weiss, J. Vala, A. V. Thapliyal, S. Myrgren, U. Vazirani and K. B. Whaley,
"Another way to approach zero entropy for a finite system of atoms",
Physical Review A 70.4 (2004) 040302 (cit. on pp. 67, 75, 80).

[266] Y. Miroshnychenko, W. Alt, I. Dotsenko, L. Förster, M. Khudaverdyan, D. Meschede,
D. Schrader and A. Rauschenbeutel, "Quantum engineering: An atom-sorting machine",
Nature 442.7099 (2006) 151 (cit. on pp. 67, 83).

[267] F. M. Sears,
"Polarization-maintenance limits in polarization-maintaining fibers and measurements",
Journal of Lightwave Technology 8.5 (1990) 684 (cit. on p. 69).

[268] R. Dorner, S. R. Clark, L. Heaney, R. Fazio, J. Goold and V. Vedral,
"Extracting Quantum Work Statistics and Fluctuation Theorems by Single-Qubit Interferometry",
Physical Review Letters 110.23 (2013) 230601 (cit. on p. 69).

[269] B. Horstmann, S. Dürr and T. Roscilde,
"Localization of Cold Atoms in State-Dependent Optical Lattices via a Rabi Pulse",
Physical Review Letters 105.16 (2010) 160402 (cit. on p. 69).

[270] Z. Lan and C. Lobo, "Optical lattices with large scattering length: Using few-body physics to
simulate an electron-phonon system", Physical Review A 90.3 (2014) 033627 (cit. on p. 69).

[271] T. Shi, Y.-H. Wu, A. González-Tudela and J. I. Cirac, "Bound States in Boson Impurity Models", Physical Review X 6.2 (2016) 021027 (cit. on p. 69).

[272] A. Walther, F. Ziesel, T. Ruster, S. T. Dawkins, K. Ott, M. Hettrich, K. Singer, F. Schmidt-Kaler and U. Poschinger, "Controlling Fast Transport of Cold Trapped Ions", Physical Review Letters 109.8 (2012) 080501 (cit. on pp. 71, 83, 84).

[273] S. Shestovyy, "Entwicklung eines hochstabilen optischen Phasendetektors für Licht-Polarisationssynthese", MA thesis, 2015 (cit. on p. 71).

[274] F. Seidler, "Digital high bandwidth feedback controller", MA thesis, 2015 (cit. on pp. 71, 75).

[275] S. Hild, "Resolved Raman sideband cooling in a doughnut-shaped optical trap", MA thesis, 2011 (cit. on p. 72).

[276] Z. J. Palmor, "Time-delay compensation—Smith predictor and its modifications", *The control handbook*, ed. by W. S. Levine, USA: CRC Press, 2011, ISBN: 9781420073669 (cit. on p. 75).

[277] M. Karski, L. Förster, A. Alberti, W. Alt, A. Widera and D. Meschede, "Direct Observation and Analysis of Spin Dependent Transport of Single Atoms in a 1D Optical Lattice", Journal of the Korean Physical Society 59.41 (2011) 2947 (cit. on p. 76).

[278] R. Koningstein, *private communication*, Engineering Director Emeritus, Google Research, 2016 (cit. on p. 78).

[279] J. Vala, A. V. Thapliyal, S. Myrgren, U. Vazirani, D. S. Weiss and K. B. Whaley, "Perfect pattern formation of neutral atoms in an addressable optical lattice", Physical Review A 71.3 (2005) 032324 (cit. on p. 80).

[280] T. Grünzweig, A. Hilliard, M. McGovern and M. F. Andersen, "Near-deterministic preparation of a single atom in an optical microtrap", Nature Physics 6.12 (2010) 951 (cit. on p. 80).

[281] X. He, P. Xu, J. Wang and M. Zhan, "High efficient loading of two atoms into a microscopic optical trap by dynamically reshaping the trap with a spatial light modulator", Optics Express 18.13 (2010) 13586 (cit. on p. 81).

[282] J. Weiner, V. S. Bagnato, S. Zilio and P. S. Julienne, "Experiments and theory in cold and ultracold collisions", Reviews of Modern Physics 71.1 (1999) 1 (cit. on pp. 82, 97).

[283] C. Weitenberg, "Single-Atom Resolved Imaging and Manipulation in an Atomic Mott Insulator", (2011) 1 (cit. on p. 82).

[284] P. Sompet, A. V. Carpentier, Y. H. Fung, M. McGovern and M. F. Andersen, "Dynamics of two atoms undergoing light-assisted collisions in an optical microtrap", Physical Review A 88.5 (2013) 051401 (cit. on p. 82).

[285] R. P. Feynman and A. R. Hibbs, *Quantum Mechanics and Path Integrals*, New York: McGraw-Hill, 1965, ISBN: 978-0486477220 (cit. on p. 83).

[286] C. Cedzich, T. Rybár, A. H. Werner, A. Alberti, M. Genske and R. F. Werner, "Propagation of Quantum Walks in Electric Fields", Physical Review Letters 111.16 (2013) 160601 (cit. on p. 83).

[287] H. Schmitz, R. Matjeschk, C. Schneider, J. Glueckert, M. Enderlein, T. Huber and T. Schaetz, "Quantum Walk of a Trapped Ion in Phase Space", Physical Review Letters 103.9 (2009) 090504 (cit. on pp. 84, 90).

[288] F. Zähringer, G. Kirchmair, R. Gerritsma, E. Solano, R. Blatt and C. F. Roos, "Realization of a Quantum Walk with One and Two Trapped Ions", Physical Review Letters 104.10 (2010) 100503 (cit. on p. 84).

[289] M. A. Broome, A. Fedrizzi, B. P. Lanyon, I. Kassal, A. Aspuru-Guzik and A. G. White, "Discrete Single-Photon Quantum Walks with Tunable Decoherence", Physical Review Letters 104.15 (2010) 153602 (cit. on p. 84).

[290] A. Schreiber, K. N. Cassemiro, V. Potocek, A. Gabris, P. J. Mosley, E. Andersson, I. Jex and C. Silberhorn, "Photons Walking the Line: A Quantum Walk with Adjustable Coin Operations", Physical Review Letters 104.5 (2010) 050502 (cit. on pp. 84, 95).

[291] L. Sansoni, F. Sciarrino, G. Vallone, P. Mataloni, A. Crespi, R. Ramponi and R. Osellame, "Two-Particle Bosonic-Fermionic Quantum Walk via Integrated Photonics", Physical Review Letters 108.1 (2012) 010502 (cit. on p. 84).

[292] D. E. Kirk, *Optimal control theory*, Mineola, New York: Dover Publicatications, Inc., 2004, ISBN: 978-0486434841 (cit. on p. 85).

[293] G. De Chiara, T. Calarco, M. Anderlini, S. Montangero, P. J. Lee, B. L. Brown, W. D. Phillips and J. V. Porto, "Optimal control of atom transport for quantum gates in optical lattices", Physical Review A 77.5 (2008) 052333 (cit. on p. 85).

[294] E. Torrontegui, S. Ibáñez, X. Chen, A. Ruschhaupt, D. Guéry-Odelin and J. G. Muga, "Fast atomic transport without vibrational heating", Physical Review A 83.1 (2011) 013415 (cit. on p. 85).

[295] X. Chen, E. Torrontegui, D. Stefanatos, J.-S. Li and J. G. Muga, "Optimal trajectories for efficient atomic transport without final excitation", Physical Review A 84.4 (2011) 043415 (cit. on p. 85).

[296] K. Eckert, M. Lewenstein, R. Corbalán, G. Birkl, W. Ertmer and J. Mompart, "Three-level atom optics via the tunneling interaction", Physical Review A 70.2 (2004) 023606 (cit. on p. 85).

[297] A. Negretti, A. Benseny, J. Mompart and T. Calarco, "Speeding up the spatial adiabatic passage of matter waves in optical microtraps by optimal control", Quantum Information Processing 12.3 (2012) 1439 (cit. on p. 85).

[298] M. Gajdacz, T. Opatrný and K. K. Das, "Transparent nonlocal species-selective transport in an optical superlattice containing two interacting atom species", Physical Review A (2011) (cit. on p. 85).

[299] K. Bergmann, H. Theuer and B. W. Shore, "Coherent population transfer among quantum states of atoms and molecules", Reviews of Modern Physics 70.3 (1998) 1003 (cit. on p. 85).

[300] T. Caneva, T. Calarco and S. Montangero, "Chopped random-basis quantum optimization", Physical Review A 84.2 (2011) 022326 (cit. on p. 85).

[301] V. Giovannetti, S. Lloyd and L. Maccone, "Quantum-enhanced measurements: beating the standard quantum limit.", Science 306.5700 (2004) 1330 (cit. on p. 87).

[302] J. L. O'Brien, A. Furusawa and J. Vučković, "Photonic quantum technologies", Nature Photonics 3.12 (2009) 687 (cit. on p. 87).

[303] E. Schrödinger, "Die gegenwärtige Situation in der Quantenmechanik", Naturwissenschaften 23.48 (1935) 807 (cit. on p. 87).

[304] M. Born, "Statistical Interpretation of Quantum Mechanics", Science 122.3172 (1955) 675 (cit. on p. 87).

[305] E. P. Wigner, "Remarks on the mind-body question", *The Scientist Speculates*, ed. by G. I. J, London: Heinemann, 1962, ISBN: 978-0465074549 (cit. on p. 87).

[306] H. Everett, *Many-worlds Interpretation of Quantum Mechanics*, ed. by B. S. DeWitt and N. Graham, Princeton series in physics, United States: Princeton University Press, 1973, ISBN: 978-0691618951 (cit. on p. 87).

[307] J. A. Wheeler and W. H. Zurek, *Quantum Theory and Measurement*, Princeton Series in Physics, United States: Princeton University Press, 1983, ISBN: 978-0691613161 (cit. on p. 87).

[308] A. Bassi and G. Ghirardi, "A General Argument Against the Universal Validity of the Superposition Principle", Physics Letters A 275.5-6 (2000) 373 (cit. on p. 87).

[309] W. H. Zurek, "Decoherence and the transition from quantum to classical - Revisited", Los Alamos Science 27 (2002) (cit. on pp. 87, 92).

[310] A. J. Leggett, "The Quantum Measurement Problem", Science 307.5711 (2005) 871 (cit. on p. 87).

[311] S. L. Adler and A. Bassi, "Is Quantum Theory Exact?", Science 325.5938 (2009) 275 (cit. on p. 87).

[312] N. D. Mermin, "Commentary Quantum mechanics: Fixing the shifty split", Physics Today 65.7 (2012) 8 (cit. on p. 87).

[313] M. F. Pusey, J. Barrett and T. Rudolph, "On the reality of the quantum state", Nature Physics 8.6 (2012) 1 (cit. on p. 87).

[314] A. Palacios-Laloy, F. Mallet, F. Nguyen, P. Bertet, D. Vion, D. Esteve and A. N. Korotkov, "Experimental violation of a Bell's inequality in time with weak measurement", Nature Physics 6.6 (2010) 442 (cit. on pp. 87, 90, 94).

[315] J. P. Groen, D. Ristè, L. Tornberg, J. Cramer, P. C. de Groot, T. Picot, G. Johansson and L. DiCarlo, "Partial-Measurement Backaction and Nonclassical Weak Values in a Superconducting Circuit", Physical Review Letters 111.9 (2013) 090506 (cit. on pp. 87, 90).

[316] M. E. Goggin, M. P. Almeida, M. Barbieri, B. P. Lanyon, J. L. O'Brien, A. G. White and G. J. Pryde, "Violation of the Leggett-Garg inequality with weak measurements of photons", Proceedings of the National Academy of Sciences 108.4 (2011) 1256 (cit. on pp. 87, 90).

[317] J.-S. Xu, C.-F. Li, X.-B. Zou and G.-C. Guo, "Experimental violation of the Leggett-Garg inequality under decoherence", Scientific Reports 1 (2011) 1 (cit. on pp. 87, 90).

[318] J. Dressel, C. J. Broadbent, J. C. Howell and A. N. Jordan, "Experimental Violation of Two-Party Leggett-Garg Inequalities with Semiweak Measurements", Physical Review Letters 106.4 (2011) 040402 (cit. on pp. 87, 90).

[319] M. Iinuma, Y. Suzuki, G. Taguchi, Y. Kadoya and H. F. Hofmann, "Weak measurement of photon polarization by back-action-induced path interference", New Journal of Physics 13.3 (2011) 033041 (cit. on pp. 87, 90).

[320] G. Waldherr, P. Neumann, S. F. Huelga, F. Jelezko and J. Wrachtrup, "Violation of a Temporal Bell Inequality for Single Spins in a Diamond Defect Center", Physical Review Letters 107.9 (2011) 090401 (cit. on pp. 87, 90).

[321] V. Athalye, S. S. Roy and T. S. Mahesh, "Investigation of the Leggett-Garg Inequality for Precessing Nuclear Spins", Physical Review Letters 107.13 (2011) 130402 (cit. on pp. 87, 90, 95).

[322] G. C. Knee, S. Simmons, E. M. Gauger, J. J. L. Morton, H. Riemann, N. V. Abrosimov, P. Becker, H.-J. Pohl, K. M. Itoh, M. L. W. Thewalt, G. A. D. Briggs and S. C. Benjamin, "Violation of a Leggett-Garg inequality with ideal non-invasive measurements", Nature Communications 2 (2012) 606 (cit. on pp. 87, 88, 90, 94–96).

[323] G. Ghirardi, A. Rimini and T. Weber, "Unified dynamics for microscopic and macroscopic systems.", Physical review D: Particles and fields 34.2 (1986) 470 (cit. on p. 87).

[324] P. Pearle, "Combining stochastic dynamical state-vector reduction with spontaneous localization.", Physical review. A, General physics 39.5 (1989) 2277 (cit. on p. 87).

[325] R. Penrose, "On Gravity's role in Quantum State Reduction", General Relativity and Gravitation 28.5 (1996) 581 (cit. on p. 87).

[326] M. M. Wilde and A. Mizel, "Addressing the Clumsiness Loophole in a Leggett-Garg Test of Macrorealism", Foundations of Physics 42.2 (2011) 256 (cit. on p. 88).

[327] A. J. Leggett, "Probing Quantum Mechanics Towards the Everyday World: Where do we Stand?", Physica Scripta T102.1 (1999) 69 (cit. on pp. 88, 95).

[328] S. Nimmrichter and K. Hornberger, "Macroscopicity of Mechanical Quantum Superposition States", Physical Review Letters 110.16 (2013) 160403 (cit. on pp. 88, 94–96).

[329] M. Arndt and K. Hornberger, "Testing the limits of quantum mechanical superpositions", Nature Physics 10.4 (2014) 271 (cit. on pp. 88, 94).

[330] N. Lambert, C. Emary, Y.-N. Chen and F. Nori, "Distinguishing Quantum and Classical Transport through Nanostructures", Physical Review Letters 105.17 (2010) 176801 (cit. on p. 88).

[331] C. Emary, N. Lambert and F. Nori, "Leggett–Garg inequalities", Reports on progress in physics 77.1 (2013) 016001 (cit. on pp. 88, 89, 92).

[332] J. von Neumann, *Mathematical Foundations of Quantum Mechanics*, United States of America: Princeton University Press, 1955, ISBN: 978-0691028934 (cit. on p. 88).

[333] G. Lüders, "Concerning the state-change due to the measurement process", Annalen der Physik 15.9 (2006) 663 (cit. on p. 88).

[334] P. Kwiat, H. Weinfurter, T. Herzog, A. Zeilinger and M. A. Kasevich, "Interaction-free measurement", Physical Review Letters 74.24 (1995) 4763 (cit. on p. 90).

[335] C.-M. Li, N. Lambert, Y.-N. Chen, G.-Y. Chen and F. Nori, "Witnessing Quantum Coherence: from solid-state to biological systems", Scientific Reports 2 (2012) 1 (cit. on p. 92).

[336] C. Emary, N. Lambert and F. Nori, "Leggett-Garg inequality in electron interferometers", Physical Review B 86.23 (2012) 235447 (cit. on p. 92).

[337] J. Kofler and Č. Brukner, "Condition for macroscopic realism beyond the Leggett-Garg inequalities", Physical Review A 87.5 (2013) 052115 (cit. on p. 92).

[338] D. Dürr and S. Teufel, *Bohmian Mechanics: The Physics and Mathematics of Quantum Theory*, Berlin: Springer, 2009, ISBN: 978-3-540-89344-8 (cit. on p. 94).

[339] J. I. Korsbakken, F. K. Wilhelm and K. B. Whaley, "Electronic structure of superposition states in flux qubits", Physica Scripta (2009) 014022 (cit. on p. 94).

[340] Z. Merali, "Quantum mechanics braces for the ultimate test.", Science 331.6023 (2011) 1380 (cit. on p. 94).

[341] T. Scheidl, R. Ursin, J. Kofler, S. Ramelow, X. S. Ma, T. Herbst, L. Ratschbacher, A. Fedrizzi, N. K. Langford, T. Jennewein and A. Zeilinger, "Violation of local realism with freedom of choice", Proceedings of the National Academy of Sciences 107.46 (2010) 19708 (cit. on p. 95).

[342] J. Gallicchio, A. S. Friedman and D. I. Kaiser, "Testing Bell's Inequality with Cosmic Photons: Closing the Setting-Independence Loophole", Physical Review Letters 112.11 (2014) 110405 (cit. on p. 95).

[343] A. Alberti, V. V. Ivanov, G. M. Tino and G. Ferrari, "Engineering the quantum transport of atomic wavefunctions over macroscopic distances", Nature Physics 5.8 (2009) 547 (cit. on p. 95).

[344] H. Müntinga, H. Ahlers, M. Krutzik, A. Wenzlawski, S. Arnold, D. Becker, K. Bongs, H. Dittus, H. Duncker, N. Gaaloul, C. Gherasim, E. Giese, C. Grzeschik, T. W. Hänsch, O. Hellmig, W. Herr, S. Herrmann, E. Kajari, S. Kleinert, C. Lämmerzahl, W. Lewoczko-Adamczyk, J. Malcolm, N. Meyer, R. Nolte, A. Peters, M. Popp, J. Reichel, A. Roura, J. Rudolph, M. Schiemangk, M. Schneider, S. T. Seidel, K. Sengstock, V. Tamma, T. Valenzuela, A. Vogel, R. Walser, T. Wendrich, P. Windpassinger, W. Zeller, T. van Zoest, W. Ertmer, W. P. Schleich and E. M. Rasel, "Interferometry with Bose-Einstein Condensates in Microgravity", Physical Review Letters 110.9 (2013) 093602 (cit. on p. 95).

[345] S. M. Dickerson, J. M. Hogan, A. Sugarbaker, D. M. S. Johnson and M. A. Kasevich, "Multiaxis Inertial Sensing with Long-Time Point Source Atom Interferometry", Physical Review Letters 111.8 (2013) 083001 (cit. on p. 95).

[346] C. Budroni and C. Emary, "Temporal Quantum Correlations and Leggett-Garg Inequalities in Multilevel Systems", Physical Review Letters 113.5 (2014) 050401 (cit. on p. 95).

[347] D. Jaksch, J. I. Cirac, P. Zoller, S. L. Rolston, R. Cote and M. D. Lukin, "Fast quantum gates for neutral atoms", Physical Review Letters 85.10 (2000) 2208 (cit. on p. 97).

[348] A. Ahlbrecht, A. Alberti, D. Meschede, V. B. Scholz, A. H. Werner and R. F. Werner, "Molecular binding in interacting quantum walks", New Journal of Physics 14.7 (2012) 073050 (cit. on p. 97).

[349] A. Peruzzo, M. Lobino, J. C. F. Matthews, N. Matsuda, A. Politi, K. Poulios, X. Q. Zhou, Y. Lahini, N. Ismail, K. Worhoff, Y. Bromberg, Y. Silberberg, M. G. Thompson and J. L. O'Brien, "Quantum Walks of Correlated Photons", Science 329.5998 (2010) 1500 (cit. on p. 97).

[350] M. H. Anderson, J. R. Ensher, M. R. Matthews, C. E. Wieman and E. A. Cornell, "Observation of bose-einstein condensation in a dilute atomic vapor.", Science 269.5221 (1995) 198 (cit. on p. 97).

[351] K. Davis, M. Mewes, M. Andrews, van Druten NJ, D. Durfee, D. Kurn and W. Ketterle, "Bose-Einstein condensation in a gas of sodium atoms", Physical Review Letters 75.22 (1995) 3969 (cit. on p. 97).

[352] T. Weber, J. Herbig, M. Mark, H. C. Nägerl and R. Grimm, "Bose-Einstein condensation of cesium", Science (2003) (cit. on p. 97).

[353] E. Tiesinga, B. Verhaar and H. Stoof, "Threshold and resonance phenomena in ultracold ground-state collisions", Physical Review A 47.5 (1993) 4114 (cit. on p. 98).

[354] B. Efron and R. J. Tibshirani, *An Introduction to the Bootstrap*, New York: Chapman Hall, 1993, ISBN: 9781439879054 (cit. on p. 104).

[355] P. M. Preiss, R. Ma, M. E. Tai, J. Simon and M. Greiner, "Quantum gas microscopy with spin, atom-number, and multilayer readout", Physical Review A 91.4 (2015) 041602 (cit. on p. 106).

[356] T. Kitagawa, M. S. Rudner, E. Berg and E. Demler, "Exploring topological phases with quantum walks", Physical Review A 82.3 (2010) 033429 (cit. on pp. 107, 108).

[357] J. K. Asbóth, "Symmetries, topological phases, and bound states in the one-dimensional quantum walk", Physical Review B 86.19 (2012) 195414 (cit. on p. 107).

[358] M. Sajid, P. Arnault, D. Meschede, R. Werner and A. Alberti, "Topological edge modes of discrete-time quantum walks in synthetic magnetic fields", In preparation (2016) (cit. on p. 109).

[359] T. Pittman, D. Strekalov, A. Migdall, M. Rubin, A. Sergienko and Y. Shih, "Can Two-Photon Interference be Considered the Interference of Two Photons?", Physical Review Letters 77.10 (1996) 1917 (cit. on p. 109).

[360] X. Cui, B. Lian, T.-L. Ho, B. L. Lev and H. Zhai, "Synthetic gauge field with highly magnetic lanthanide atoms", Physical Review A 88.1 (2013) 011601 (cit. on p. 109).

[361] J.-I. Kim, D. Haubrich and D. Meschede, "Efficient sub-Doppler laser cooling of an Indium atomic beam", Optics Express 17.23 (2009) 21216 (cit. on p. 109).

[362] A. de Touzalin, C. Marcus, F. Heijman, I. Cirac, R. Murray and T. Calarco, *Quantum Manifesto*, 2016 (cit. on p. 110).

[363] A. Celi, A. Sanpera, V. Ahufinger and M. Lewenstein,
"Quantum optics and frontiers of physics: The third quantum revolution", arXiv.org (2016),
arXiv: 1601.04616v2 [cond-mat.quant-gas] (cit. on p. 110).

[364] H. H. Ku, "Notes on the use of propagation of error formulas", Journal of Research of the National Bureau of Standards, Section C: Engineering and Instrumentation 70C.4 (1966) 263 (cit. on p. 137).

[365] C. J. Clopper and E. S. Pearson,
"The Use of Confidence or Fiducial Limits Illustrated in the Case of the Binomial",
Biometrika 26.4 (1934) 404 (cit. on p. 139).

[366] D. H. Goldstein, *Polarized Light*, Marcel Dekker, Inc., 2003, ISBN: 0-8247-4053-X
(cit. on p. 144).

APPENDIX A

Error Propagation Using Monte Carlo Samples

Error analysis and error propagation is a central aspect experimental physics. In most cases, when correlations between parameters can be neglected, error propagation is performed by using the variance method [364] assuming Gaussian distributed parameters x with a 1σ spread of σ_x. This method works well for linear functions or functions that can well be approximated by a linear function within the range of the parameters and their errors. However, this method breaks down for non linear functions, which will be demonstrated in the following. Furthermore, the variance method is also limited to Gaussian distributed parameters, which for instance makes it impossible to combine the errors from binomial a distributed parameter with a Gaussian distributed parameter. For this purpose Stefan Brakhane and myself developed a Matlab [109] toolbox which performs the error propagation with Monte Carlo generated parameter values to generate a confidence interval even for arbitrarily distributed parameters. The toolbox consists of two parts: (a) generation of Monte Carlo samples and (b) propagation of the generated samples using an analytic function and producing the corresponding function value distribution. The confidence interval (CI) for a confidence threshold of $\alpha = 1 - 0.68$ (in case of a 68% CI) is generated by integrating the function value distribution from $\pm\infty$ until $\alpha/2$ is reached. The resulting interval contains then 68% of the function value distribution, whereas the remaining 32% are equally distributed to the left and right. Unless explicitly stated differently, all error propagations presented in this thesis are performed using this toolbox for a confidence interval of 68%. In a lot of cases the resulting function value distribution is symmetric, in which the Monte Carlo CI method reproduces exactly the 1σ error from the variance method. In the following I will give list a few examples to highlight the differences to the variance method.

A.1 Example 1: Linear Function (Symmetric CI)

Let us assume we have the simple linear function $f(a, b) = a + b$ with the Gaussian distributed parameters $a = 2.0 \pm 0.2$ (MC generated parameter distribution exemplarily shown in fig. A.1(a)) and $b = 0.5 \pm 0.2$. It is straight forward to calculate the error using the variance method:

$$\sigma_f = \sqrt{\left(\frac{\partial f}{\partial a}\sigma_a\right)^2 + \left(\frac{\partial f}{\partial b}\sigma_b\right)^2} = 0.28\,. \tag{A.1}$$

Hence, we obtain $f = 2.50 \pm 0.28$. To compare this result to the Matlab Monte Carlo error propagation method we run the following code:

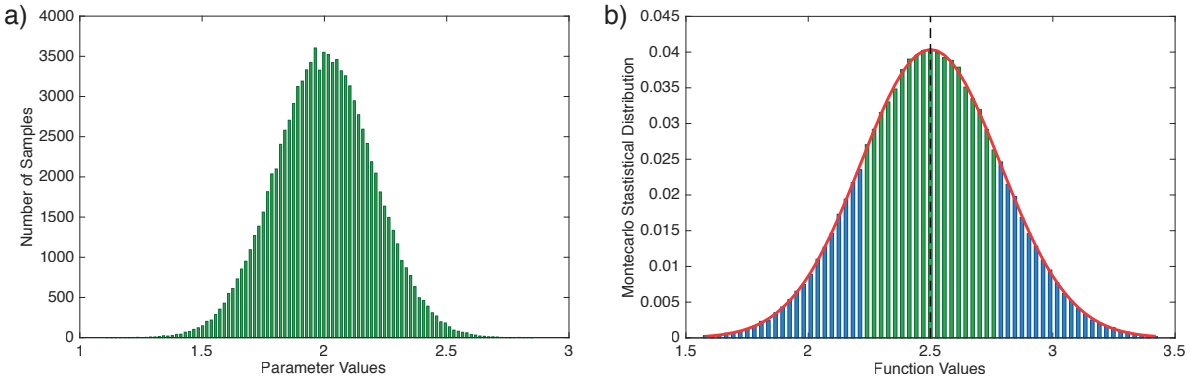

Figure A.1: (a) Histogram of generated Monte Carlo samples for a Gaussian distributed parameter $a = 2.0 \pm 0.2$; (b) Histogram of the generated MC function values of $f(a,b) = a + b$ for $a = 2.0 \pm 0.2$ and $b = 0.5 \pm 0.2$. The red solid curve shows the result from the variance method, the vertical dashed black line represents the median of the function values

```
A = generateMCparameters('gaussian',[2,0.2]);
B = generateMCparameters('gaussian',[0.5,0.2]);
paramMatrix = [A;B];
funToProp = @(x) x(1)+x(2);
[funValue,funCI,funSamples] = propagateErrorWithMC(funToProp, paramMatrix);
```

This gives us a median value of $f = 2.50$ and a 68% CI $[2.22,\ 2.78]$, which agrees perfectly with the variance method. The histogram in figure A.1(b) shows the resulting function value distribution, where the green shaded bars represent the values which lie within the 68% CI and the vertical dashed black line represents the median of the function values. The red solid line represents the result from the variance method and shows the perfect agreement of the two methods.

A.2 Example 2: Non Linear Function (Asymmetric CI)

The previous example shows that the Monte Carlo error propagation method can nicely reproduce the 1σ error from the variance method, therefore let us now consider a non linear function $f(a,b) = a/b$ with the same Gaussian distributed parameters $a = 2.0 \pm 0.2$ and $b = 0.5 \pm 0.2$. Using the variance method we obtain $f = 4.00 \pm 0.69$, while the following code produces the Matlab Monte Carlo CI:

```
A = generateMCparameters('gaussian',[2,0.2]);
B = generateMCparameters('gaussian',[0.5,0.2]);
paramMatrix = [A;B];
funToProp = @(x) x(1)./x(2);
[funValue,funCI,funSamples] = propagateErrorWithMC(funToProp, paramMatrix);
[funValue,funCI,funSamples] = propagateErrorWithMC(funToProp,
    paramMatrix,'method','maximum');
```

The histogram in figure A.2(a) shows the resulting function value distribution, which shows an asymmetric distribution and a clear distinction from the red solid line representing the result from the variance method. The corresponding median function value is $f = 3.97$ with a 68% CI $[2.79,\ 6.58]$. This example shows

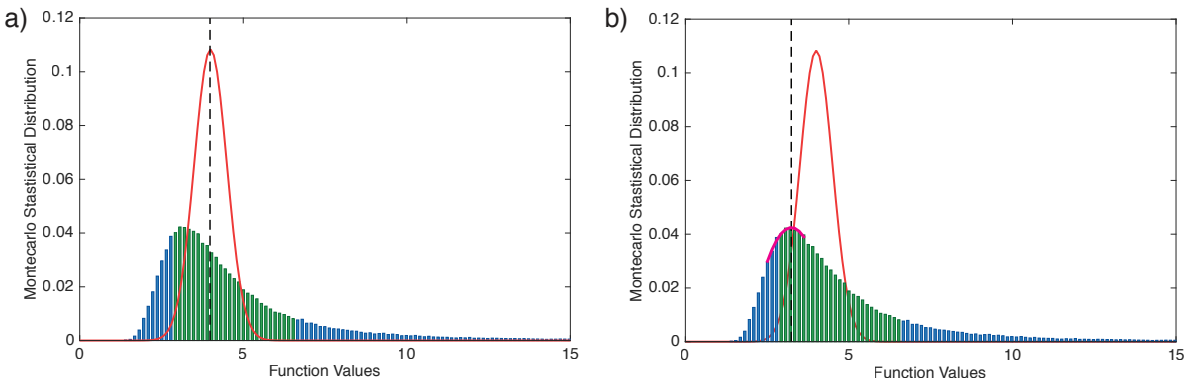

Figure A.2

nicely that the variance method cannot be used in general for all functions, while the Monte Carlo error propagation method allows an exact determination of the CI. It is noteworthy that in case of an asymmetric function value distribution the exact definition of a function value f becomes unclear. The vertical dashed black line in figure A.2(a) shows the median of the distribution which agrees well with the value one obtains from the variance method and represents the on average measured value. However, this value does no longer correspond to the most likely measured value (maximum of the function value distribution). The developed Matlab toolbox allows to specify the method to generate the function value. The vertical dashed black line in figure A.2(a) shows the result of the default median method, while the vertical dashed black line in figure A.2(b) indicates the maximum if the function value distribution, which is obtained from by fitting a polynomial to the function value distribution (cyan solid line).

A.3 Example 3: Combining Gaussian and Binomial Distributions

This following example shows that the Monte Carlo error propagation method also allows to combine parameters which are not Gaussian distributed. Let us assume we have the following function $f(a,b) = a \cdot b$, where a is again a Gaussian distributed error with $a = 2.000 \pm 0.035$, however, b comes from a survival measurement of single atoms where 18 out of 20 atoms survived. Therefore, we need to generate Monte Carlo samples which follow a binomial distribution with $n = 18$ and $k = 20$ (see fig. A.3(a)). While the variance method is not capable to handle these two distributions without modifications, the error propagation using the Monte Carlo method is straight forward:

```
A = generateMCparameters('gaussian',[2,0.035],'plot',true);
B = generateMCparameters('binomial',[20,18],'plot',true);
paramMatrix = [A;B];
funToProp = @(x) x(1).*x(2);
[funValue,funCI,funSamples] = propagateErrorWithMC(funToProp, paramMatrix);
```

In fact, the Monte Carlo method can be used for arbitrary distributions. The histogram in figure A.3(b) shows the resulting function value distribution. The parameters a and b have been chosen such that the remnants of the binomial distribution are still visible. For the given parameter values the Monte Carlo method generates a function value $f = 1.81$ with a 68% CI $[1.67,\ 1.93]$. It is noteworthy that the MC error propagation method does not converge to the Clopper Pearson CI [365] in case the error of a becomes significantly smaller. The CIs presented in this thesis, in cases where the error is either purely

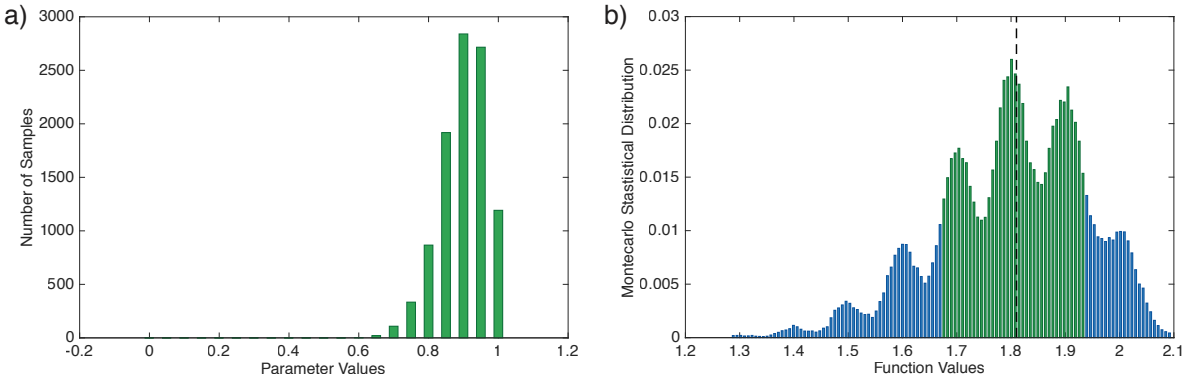

Figure A.3

binomial or all other error sources are orders of magnitude smaller, are all obtained using the Clopper Pearson method.

APPENDIX B

Useful Calculations in Quantum Optics

B.1 Electric Field, Intensity and Laser Power

In calculations presented in this thesis, where the light from a monochromatic laser source with angular frequency ω can be modeled by a classical plane wave, it takes the following form:

$$\vec{E} = \vec{\varepsilon} E_0 \cos(\omega t) \tag{B.1}$$

$$= \frac{1}{2}\vec{\varepsilon} E_0 (e^{i\vec{k}\vec{x}} e^{-i\omega t} + e^{-i\vec{k}\vec{x}} e^{i\omega t}) , \tag{B.2}$$

where E_0 is the amplitude of the electric field and $\vec{\varepsilon}$ the polarization unit vector. The decomposition into a positive- and a negative-rotating component ($e^{-i\omega t}$ and $e^{i\omega t}$) is often advantageous in calculations.

The intensity from the electric field of a single laser beam given by:

$$I = \frac{c\epsilon_0}{2} E_0^2 , \tag{B.3}$$

where ϵ_0 is the vacuum permittivity and c the speed of light.

In experiments the intensity of laser beams is typically only indirectly accessible through the power (measured with a power meter) and waist of the corresponding laser beam. The relations between intensity, power, and waist, which are relevant for different calculations within this thesis, are summarized in figure B.1. In case of a standing wave formed by two linear polarized counter propagating Gaussian laser beams we can, hence, express the squared amplitude of the electric field E_0^2 by the laser power (P_{total}) and the waist (w_0):

$$E_0^2 = \frac{2I}{c\epsilon_0} = \frac{8P_{\text{total}}}{c\epsilon_0 \pi w_0^2} . \tag{B.4}$$

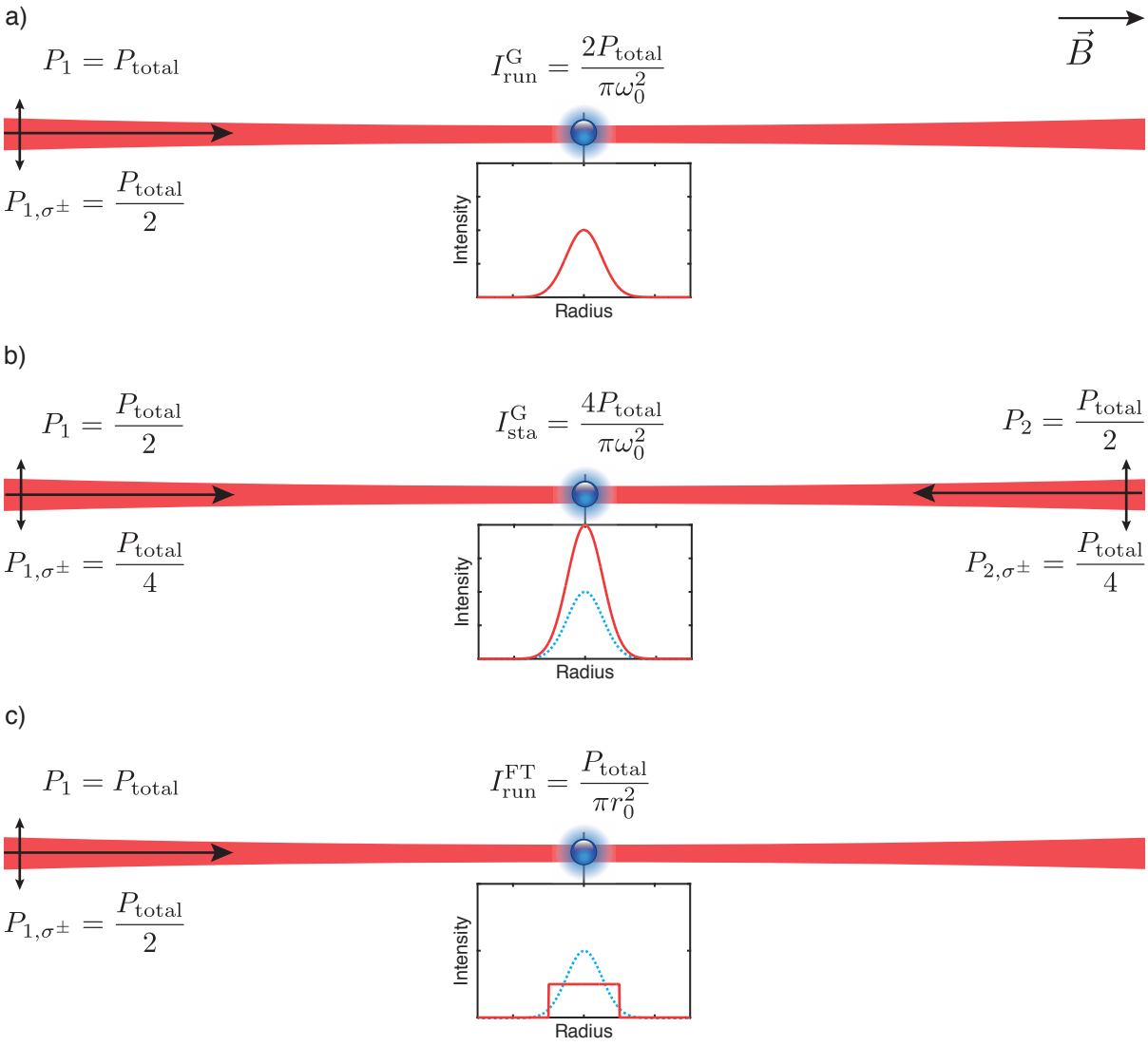

Figure B.1: Relevant laser intensity, power, and waist relations used in this thesis. The intensity is always given for an atom (blue sphere) which is located at the focus of the beam. The quantization axis is parallel to the laser axis and the polarization of all involved beams is assumed vertical. (a) Running wave with transversal Gaussian profile (waist = w_0), (b) standing wave of two counter propagating laser beams with transversal gaussian profile (waist = w_0), (c) running wave with flat-top profile (radius = r_0). The blue dashed curve in the intensity profile insets (b) and (c) shows a comparison to the single gaussian beam intensity profile

B.2 Different Mathematical Descriptions of Light Polarization

B.2.1 Cartesian and Spherical Coordinates

Any homogeneously polarized laser beam which propagates in free space (homogeneous, isotropic, and non-attenuating) can be described by the following polarization unit vector $\vec{\varepsilon}$ in Cartesian coordinates:

$$\vec{\varepsilon} = \begin{pmatrix} e^{i\phi_x} \\ e^{i\phi_y} \\ 0 \end{pmatrix}, \tag{B.5}$$

where for simplicity the light propagation direction is chosen along the z axis. In atomic physics it is often of most interest to determine which type of transition (σ^+, π, and σ^-) the polarization drives for an atom whose spin is oriented along a given quantization axis. Therefore the laser light polarization needs to be decomposed into the different components depending on the orientation of the quantization axis. In the following we assume the quantization axis of the atom to be oriented along the z axis. The following matrix converts the polarization vector from Cartesian to spherical coordinates:

$$M^{\text{cart}}_{\text{spher}} = \begin{pmatrix} \frac{1}{\sqrt{2}} & \frac{i}{\sqrt{2}} & 0 \\ 0 & 0 & 1 \\ -\frac{1}{\sqrt{2}} & \frac{i}{\sqrt{2}} & 0 \end{pmatrix}, \tag{B.6}$$

such that the resulting polarization unit vector corresponds to:

$$\vec{\varepsilon}^{\text{spher}} = \begin{pmatrix} \sigma^+ \\ \pi \\ \sigma^- \end{pmatrix}. \tag{B.7}$$

B.2.2 Jones Vector Representation

Since the polarization, in case of a homogeneously polarized laser beam in free space is always perpendicular to the propagation axis we can rewrite equation (B.5):

$$\vec{\varepsilon}_{\text{Jones}} = \begin{pmatrix} e^{i\phi_x} \\ e^{i\phi_y} \end{pmatrix}. \tag{B.8}$$

The resulting two component vector is called Jones vector. Hence, a vertically linear polarized laser beam ist described by the Jones vector $\begin{pmatrix} 0 & 1 \end{pmatrix}^T$ and a right-handed circular polarized one by $1/\sqrt{2}\begin{pmatrix} 1 & i \end{pmatrix}^T$.

B.2.3 The Poincaré Sphere and Stokes Parameter Representation

The Poincaré sphere is a useful tool to visualize different polarization states and shares a strong similarity with the Blochs sphere (see fig. B.2(a)). All linear polarizations lay on the equator of the sphere, whereas a right/left-handed polarization is represented by the north/south pole. It is noteworthy that two orthogonal polarizations (e.g. vertical and horizontal) have a relative angle of 180° and not 90° to each other. Any other elliptically polarized laser beam is oriented on the sphere. Besides pure polarizations it is also possible to display partially polarized beams by a reduction of the vector length (degree of polarization). A vector on the poincare sphere, given in spherical coordinates, can also be expressed by the Stokes

parameters, another convention used to describe polarization, in the following way:

$$S_1 = I \tag{B.9}$$
$$S_2 = I\,\mathrm{DOP}\,\cos(2\psi)\cos(2\chi) \tag{B.10}$$
$$S_3 = I\,\mathrm{DOP}\,\sin(2\psi)\cos(2\chi) \tag{B.11}$$
$$S_4 = I\,\mathrm{DOP}\,\sin(2\psi)\,, \tag{B.12}$$

where I DOP is the radial distance, 2ψ the azimuthal angle, and χ the polar angle from the equator which represent the spherical coordinates (see also fig. B.2(a)), I the total intensity of the electric field, and DOP the degree of polarization. The Stokes parameters can also be obtained directly from the electric field. If we assume again a laser beam which propagates in free space along the z direction the stokes parameter that describe its polarization are given by [366]:

$$S_1 = \frac{c\epsilon_0}{2}E_0^2(\varepsilon_x\varepsilon_x^* + \varepsilon_y\varepsilon_y^*) \tag{B.13}$$
$$S_2 = \frac{c\epsilon_0}{2}E_0^2(\varepsilon_x\varepsilon_x^* - \varepsilon_y\varepsilon_y^*) \tag{B.14}$$
$$S_3 = \frac{c\epsilon_0}{2}E_0^2(\varepsilon_x\varepsilon_y^* + \varepsilon_x\varepsilon_y^*) \tag{B.15}$$
$$S_4 = \frac{c\epsilon_0}{2}E_0^2 i(\varepsilon_x\varepsilon_y^* - \varepsilon_x\varepsilon_y^*), \tag{B.16}$$

A concrete example is given in figure B.2(b) for a vertical linear polarization (triangle), horizontal linear polarization (square), and right handed circular polarization (circle). Depending on the concrete application it might be useful to either express the polarization of a laser beam in terms of the Jones vector or through the Stokes parameters. For both, Jones and Stokes representation, there exist a set of matrix operations [366] (Jones or Mueller matrices), which mathematically describe the effect of e.g. wave plates or polarizers. The relation to the electrical field also allows to convert between the two conventions.

B.3 Wigner-Eckart Theorem, Wigner Three and Six J Symbols, and Their Application

When calculating matrix elements of tensor operators, the Wigner-Eckart theorem is an extremely useful relation, which allows to factor out the angular part of the matrix element. This element can then be expressed in terms of a Clebsch-Gordan coefficient. Let us assume we have an angular-momentum state $|\alpha\, j\, m\rangle$, where α is a quantum number without angular dependence, and we want to calculate the following matrix element of a tensor-operator $T^{(k)}$. The Wigner-Eckart theorem states then:

$$\langle \alpha\, j\, m|\, T_q^{(k)}\, |\alpha'\, j'\, m'\rangle = (-1)^{2k}\,\langle \alpha\, j||T^{(k)}||\alpha'\, j'\rangle\,\langle j\, m|j'\, m';\, k\, q\rangle\ . \tag{B.17}$$

Here, we assume spherical coordinates, such that the labeling index q, which goes from $-1\ldots 1$, represents the σ^+, π, or σ^+ component (see also eq. (B.7)).

Any light matter interaction involves calculating matrix elements of the dipole operator $\vec{d}$, which is of rank $k = 1$. For instance, using the Wigner-Eckert theorem we can calculate the strength of the interaction between two hyperfine levels of cesiums which are coupled by the dipole operator through a near resonant laser beam:

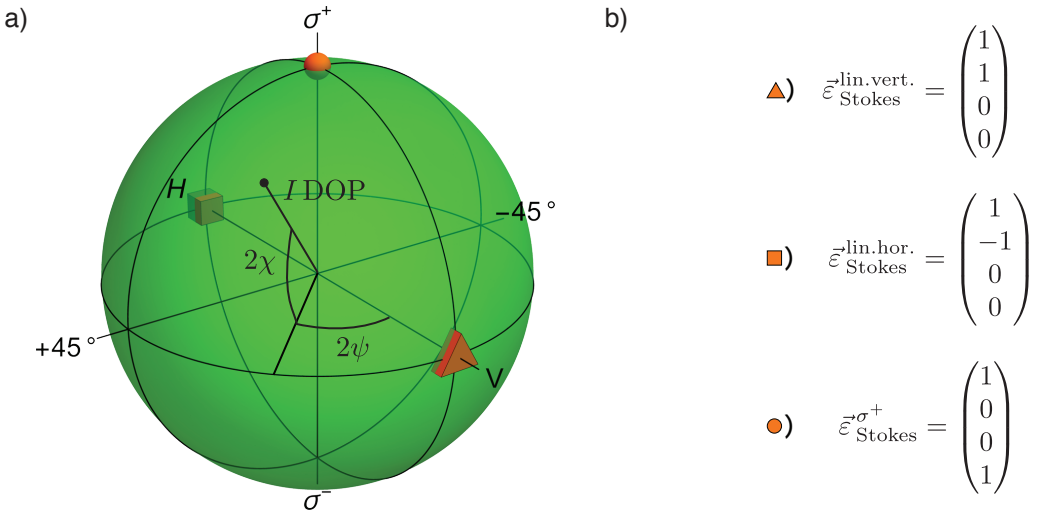

Figure B.2: (a) Poincaré sphere with three exemplarily chosen polarization states (triangle, square, circle); (b) corresponding Stokes vector for a vertical linear polarization (triangle), horizontal linear polarization (square), and right handed circular polarization (circle).

$$\langle F\, m_F|\, d_q\, |F'\, m'_F\rangle = \langle F||\,\vec{d}\,||F'\rangle\,\langle F\, m_F|F'\, 1\, m'_F\, q\rangle \tag{B.18}$$

$$= \langle J||\,\vec{d}\,||J'\rangle\,\langle J\, 1\, F|J'\, I\, F'\rangle\,\langle F\, m_F|F'\, 1\, m'_F\, q\rangle\ , \tag{B.19}$$

where F is the magnitude of the total atomic angular momentum (hyperfine structure), m_F the projection on the total angular momentum axis, J the magnitude of the total electron angular momentum (fine structure), and I the nuclear spin (for cesium $I = 7/2$). Hence, the matrix element is the product of two coefficients and the reduced matrix element $\langle J||\varepsilon_q d_q||J'\rangle$, which only depends on the quantum number J. The numerical value of the reduced matrix elements for the cesium D2 and D1 transitions ($\langle J = 1/2||\,\vec{d}\,||J' = 3/2\rangle$ and $\langle J = 1/2||\,\vec{d}\,||J' = 1/2\rangle$) can be calculated from their measured lifetimes [184]. The Clebsch-Gordan coefficient $\langle F\, m_F|F'\, 1\, m'_F\, q\rangle$ can be directly calculated using the Wigner-3j symbols:

$$\langle F\, m_F|F'\, 1\, m'_F\, q\rangle = (-1)^{F'-1+m_F}\,\sqrt{2F+1}\begin{pmatrix}F' & 1 & F\\ m'_F & q & m_F\end{pmatrix}, \tag{B.20}$$

whereas the other coefficient can be similarly obtained using the Wigner-6j symbols:

$$\langle J\, 1\, F|J'\, I\, F'\rangle = (-1)^{F'-1+J+1+I}\,\sqrt{(2F+1)(2J+1)}\begin{Bmatrix}J & J' & 1\\ F' & F & I\end{Bmatrix}. \tag{B.21}$$

Using these relations one can for example easily calculate the coupling strength between the ground state $|F = 4\, m_F = 4\rangle$ and the excited state $|F' = 5\, m'_F = 5\rangle$ for σ^+ polarized light ($q = -1$) resonant with the D2 transition:

$$\langle F = 4\, m_F = 4|\, d_{-1}\, |F' = 5\, m'_F = 5\rangle = \sqrt{\frac{1}{2}}\,\langle J = 1/2||\,\vec{d}\,||J' = 3/2\rangle\ . \tag{B.22}$$

B.4 Calculation of Scattering Rates Using the Kramers-Heisenberg Formula

Scattering of light consists in general of two processes: (a) the absorption of an incoming photon with energy ω and (b) the emission of the scattered photon with energy ω_{sc}. Hence, they are processes of second order radiative transitions, which in contrary to first order transitions go through a virtual intermediate state. The first and second order scattering rate can be described by the generalized Fermi's golden rule [74]:

$$\frac{1}{\tau} = \frac{2\pi}{\hbar} \sum_{\mathrm{final}} \left| \langle \mathrm{final} | \mathcal{H}_{\mathrm{int}} | \mathrm{initial} \rangle + \sum_{\mathrm{virt}} \frac{1}{\hbar} \frac{\langle \mathrm{final} | \mathcal{H}_{\mathrm{int}} | \mathrm{virt} \rangle \langle \mathrm{virt} | \mathcal{H}_{\mathrm{int}} | \mathrm{initial} \rangle}{\omega_{\mathrm{initial}} - \omega_{\mathrm{virt}}} \right|^2 \frac{1}{\hbar} \delta(\omega_{\mathrm{final}} - \omega_{\mathrm{initial}}) \,. \quad \text{(B.23)}$$

Here the initial state of the system (atom and photon) is denoted as $|\mathrm{initial}\rangle$ and correspondingly its final state by $|\mathrm{final}\rangle$. The first term of the absolute value describes direct (first order) transitions from the initial to the final state whereas the second one corresponds to the second order scattering events. The delta function at the end of equation (B.23) ensures that the energy is conserved after the entire process. The energy of the virtual intermediate state, however, is not restricted. Since we are only interested in second order transitions we can neglect the first term in equation (B.23). It is important to note that the sum over all virtual intermediate states is within the absolute value, while the sum over the final states is outside. The reason comes directly from quantum mechanics, since all transitions through intermediate states that lead to the same final state can interfere constructively and destructively, while the final state is measured by the environment and, hence, no interference between different final states is possible.

In our explicit case we want to calculate the total scattering rate of a cesium atom depending on its initial hyperfine state $|F\, m_F\rangle$, therefore, we need to replace the sum over all final states by one over all accessible final hyperfine states:

$$\sum_{\mathrm{final}} \langle \mathrm{final} | \longrightarrow \sum_{F_{\mathrm{final}}=3}^{4} \sum_{m_{F,\,\mathrm{final}}=-F_{\mathrm{final}}}^{F_{\mathrm{final}}} \langle \mathrm{F}_{\mathrm{final}}, \mathrm{m}_{\mathrm{F,\,final}} | \,. \quad \text{(B.24)}$$

Furthermore, the scattered photon can be emitted into any spatial mode k with a σ^+, π, or σ^+ polarization. Therefore we have to extend the sum from the precious equation to:

$$\sum_{\mathrm{final}} \langle \mathrm{final} | \longrightarrow \sum_{k} \sum_{q_{\mathrm{final}}=-1}^{1} \sum_{F_{\mathrm{final}}=3}^{4} \sum_{m_{F,\,\mathrm{final}}=-F_{\mathrm{final}}}^{F_{\mathrm{final}}} \langle \mathrm{F}_{\mathrm{final}}, \mathrm{m}_{\mathrm{F,\,final}} | \,. \quad \text{(B.25)}$$

The sum over all spatial modes k is a bit unpractical and can be replaced in general by an integration over the mode densities (number of modes per unit volume):

$$\sum_{k} \longrightarrow \frac{V}{(2\pi^3)} \int d\Omega \int d\omega_{\mathrm{sc}} \frac{\omega_{\mathrm{sc}^2}}{c^3} \,, \quad \text{(B.26)}$$

where $d\Omega$ is the integration of the solid angle. In our specific application we are interested in the scattering rate of a single cesium atom, which is trapped in an optical lattice inside a vacuum chamber. This means that there is no preferred spatial mode for the emission (the story would be different for an atom trapped in an optical cavity). Nevertheless, the emission is not isotropic in wavevector space, owing to the polarization of the emitted photon, as we will see in the following. Therefore we cannot directly compute the integral of the solid angle, while the integration over the energy of the scattered photon $d\omega_{\mathrm{sc}}$

is straight forward thanks to the delta function in equation (B.23).

Following the same logic, the sum over all virtual intermediate states can be expressed by a sum over all possible intermediate hyperfine states. This means that we also have to sum over the two components of the exited state fine-structure doublet (D1 $J' = 1/2$ and D2 $J' = 3/2$ transition):

$$\sum_{\text{virt}} \langle \text{virt}| \longrightarrow \sum_{J_{\text{virt}}=1/2}^{3/2} \sum_{F_{\text{final}}=|J_{\text{virt}}-I|}^{J_{\text{virt}}+I} \sum_{m_{F,\,\text{virt}}=-F_{\text{virt}}}^{F_{\text{virt}}} \langle \text{F}_{\text{virt}}, \text{m}_{\text{F, virt}}| \tag{B.27}$$

The selection rules for dipole transitions simplify the sum over all states significantly, since only some contributions are allowed:

$$\Delta F = 0,\, \pm 1,\; q = \Delta m_F = 0,\, \pm 1,\; \text{if } \Delta m_F = 0 \rightarrow \Delta F = \pm 1\,. \tag{B.28}$$

The remaining missing ingredient is the interaction Hamiltonian. In our example we want to calculate the rate of photons which a single trapped cesium atom scatterers from a laser beam, this allows us to treat the absorption with a semiclassical approach, while we require the full second quantization for emission of the scattered photon. This gives us the following interaction Hamiltonian:

$$\mathcal{H}_{\text{int}} = \mathcal{H}_{\text{absorption}} + \mathcal{H}_{\text{emission}} \tag{B.29}$$

$$\begin{aligned} &= \vec{d}\cdot\vec{E}\;|\text{F}_{\text{virt}}, \text{m}_{\text{F, virt}}\rangle\langle \text{F}_{\text{initial}}, \text{m}_{\text{F, initial}}| \\ &\quad + \vec{d}\cdot\vec{\varepsilon}_{\text{sc}}\sqrt{\frac{\hbar\omega_{\text{sc}}}{2V\epsilon_0}}\left(a(k)\,e^{i\vec{k}\cdot\vec{x}}e^{-i\omega_{\text{sc}}t} - a^\dagger(k)\,e^{-i\vec{k}\cdot\vec{x}}e^{i\omega_{\text{sc}}t}\right)|\text{F}_{\text{final}}, \text{m}_{\text{F, final}}\rangle\langle \text{F}_{\text{virt}}, \text{m}_{\text{F, virt}}|\;, \end{aligned} \tag{B.30}$$

where $\vec{d}$ is the dipole operator, $\vec{E}$ the electric field as defined in equation (B.2), $\vec{\varepsilon}_{\text{sc}}$ the polarization vector of the emitted photon, V the volume in which the photon is emitted, and $a^\dagger(k)$ ($a(k)$) the creation (annihilation) operator of a single photon.

Inserting the interaction Hamiltonian in the scattering rate given in equation (B.23) combined with the replacements of the final and virtual intermediate sums we obtain the following total rate for a cesium atom in its hyperfine state $|\text{F}_{\text{initial}}, \text{m}_{\text{F, initial}}\rangle$ which scatters a photon from a laser beam with polarization $\vec{\varepsilon}_{\text{laser}}$:

$$\begin{aligned} \frac{1}{\tau} = \frac{1}{2^3\pi\hbar\epsilon_0 c^4}\omega_{\text{sc}}^3\, I_{\text{DT}} \int d\Omega \sum_{F_{\text{final}}=3}^{4} \sum_{m_{F,\,\text{final}}=-F_{\text{final}}}^{F_{\text{final}}} \Bigg| \sum_{q_{\text{initial}}=-1}^{1} \sum_{q_{\text{final}}=-1}^{1} \sum_{J_{\text{virt}}=1/2}^{3/2} \sum_{F_{\text{final}}=|J_{\text{virt}}-I|}^{J_{\text{virt}}+I} \sum_{m_{F,\,\text{virt}}=-F_{\text{virt}}}^{F_{\text{virt}}} \\ \times \vec{\varepsilon}_{\text{DT},\,q_{\text{initial}}}\,\vec{\varepsilon}_{\text{sc},\,q_{\text{final}}}\,\frac{\langle \text{F}_{\text{final}}, \text{m}_{\text{F, final}}|\,d_{q_{\text{final}}}\,|\text{F}_{\text{virt}}, \text{m}_{\text{F, virt}}\rangle\langle \text{F}_{\text{virt}}, \text{m}_{\text{F, virt}}|\,d_{q_{\text{initial}}}\,|\text{F}_{\text{initial}}, \text{m}_{\text{F, initial}}\rangle}{\hbar(\omega_{\text{sc}} - \omega_{\text{virt}}(J_{\text{virt}}, F_{\text{virt}}))}\Bigg|^2\,, \end{aligned} \tag{B.31}$$

where in the simplification of the absorption matrix element we have made use of the rotating wave approximation. The laser intensity can again be expressed in dependence of the laser power and the waist of the beam as given in figure B.1, depending on the specific situation. The remaining matrix elements can be directly calculated using the Wigner-Eckart theorem given on equation (B.19). Equation (B.31) is typically referred to as Kramers-Heisenberg Formula.

APPENDIX C

The Nine Distinct Atomic Hong-Ou-Mandel Events

In the following we will introduce the nine distinct events, which can occur in our atomic Hong-Ou-Mandel experiment. Dividing our 277 measured events into the different cases leads to the distribution, which is displayed in figure 5.5 in section 5.2.1. To allow for the chance of not correctly reconstructing the atoms' positions in the final fluorescence image, all lattices sites given in the following are always ± 1 lattice site. Furthermore, the lattice sites are defined as depicted in figure 5.4.

P_{2A} is a two-atom event, where one atom is found at lattice site 0 and the other at 1.

P_{1A} is a one-atom event, where the single atom is found at lattice site 0 or at 1.

P_{0A} is a zero-atom event, where no atoms are found at all key locations (-20,-10,0,10,20,30). In case we will find a single atom at a random position we will also count it as a zero atom event. During the pair production measurements discussed in section 3.3.4, we noticed that it is possible that some of the atoms, which are lost due to light assisted collisions, can get trapped again. However, this event only occurs in less than 5 % of all zero-atom events.

P_{1A}^{LA} is a one-atom event, where one atom is found at lattice site -20 site or at -10. This event is most likely caused by not spin-flipping the left atom, while the right one is independently lost.

P_{1A}^{RA} is a one-atom event, where one atom is found at lattice site 20 site or at 30. This event is most likely caused by accidentally spin-flipping the right atom, while the left one is independently lost.

P_{2A}^{LA} is a two-atom event, where one atom is found at lattice site -20 or -10 and the other at 0 or 10. This event is most likely caused by not spin-flipping the left atom, such that the atoms never meet at lattice site 0.

P_{2A}^{RA} is a two-atom event, where one atom is found at lattice site 0 or 10 and the other at 20 or 20. This event is most likely caused by accidentally spin-flipping the right atom, such that the atoms never meet at lattice site 0.

P_{2A}^{BA} is a two-atom event, where one atom is found at lattice site -20 or -10 and the other at 20 or 20. This event is most likely caused by not spin-flipping the left atom and simultaneously accidentally spin-flipping the right atom, such that the atoms never meet at lattice site 0.

P_{2A}^{T} is a two-atom event, where both atom is found at lattice site 0 or both at 10. Please not that this does not mean that the atoms are found in the exact same lattice site, instead it means that they are e.g. at -1 and 0, or 10 and 11, since we allow for ± 1 lattice site in our detection. This event is most likely caused by not correctly inferring the initial position of the two atoms, such that the atoms never meet at lattice site 0.

Acknowledgements

During my thesis I had the pleasure to work with a multitude of highly motivated and skilled colleagues, from whom I have received wonderful help and I will try my best to give thanks to everyone involved.

First of all I would like to thank Prof. Dr. Dieter Meschede for offering me such an exciting and stimulating research topic for my PhD thesis. Moreover, for his trust, his guidance, his warm words of motivation, and giving me the opportunity to start a scientific career. Furthermore I'm grateful to him for helping me gain a broad scientific perspective through numerous discussions and the scientific exchange with several other research groups.

Prof. Dr. Jean-Michel Raimond who spent his Humboldt Award in Prof. Dr. Dieter Meschede's research group during which I was fortunate to profit greatly from his experience and his short internship together with me in the lab will always remain a memorable time to me. I'm further glad that you have decided to become my second thesis advisor.

Prof. Dr. Reinhard F. Werner for a multitude of fruitful discussions during several joint meetings of his and Prof. Dr. Dieter Meschede's research group and for becoming the third member of my thesis committee.

Prof. Dr. Peter Koepke for taking on the duty of being the fourth member of my thesis committee.

I greatly acknowledge the ideational and financial support from the Studienstiftung des deutschen Volkes and the Bonn-Cologne Graduate School for Physics and Astronomy.

My gratitude especially goes to Dr. Andrea Alberti for his sheer endless knowledge of physics, theorems, and ways to write complicated Mathematica notebooks. I believe I will never meet a more motivated person, who at the same time possesses all skills to fulfill his dreams. Thank you for all your support, guidance, and friendship throughout my thesis. It was a pleasure working with you and I'm looking forward to do so in the future.

Stefan Brakhane who has been there from day one teaching me to do things efficiently and while doing so to of course always use the appropriate DIN norm. I'm especially grateful for the last months we spent together in our enclave, sharing every last bit of writing our thesis, including countless discussions, the joy of finishing a chapter, and the occasional frustrations.

Jonathan Zopes with whom I had the pleasure to share the most productive and joyful year in the lab. I believe utilizing MATLAB no one can stop the two of us from automizing the entire world.

Dr. Wolfgang Alt for not being an expert and yet always knowing more than the experts, while simultaneously increasing the entire group's happiness with his perpetual supply of sweets.

The office: Ricardo Gómez Escalante, Jose Gallego Fernández, Maximilian Genske, Tobias Macha, Dr. Geol Moon, Gautam Ramola, Dr. Andreas Steffen, and our honorable member Dr. Rene Reimann who during the last years have truly become like a second family. We have shared success and failure, while always making sure to motivate each other in some way or another.

Felix Kleißler who did not get tired of trying to adjust everything up to the last few nanometers when analyzing the high-NA objective lens.

Dr. Miguel Martinez-Dorantes in particular for his valuable suggestions during our first attempt of Raman sideband cooling.
Our new additions to the quantum walk team: Alexander Knieps, Manolo Rivera, Natalie Tau, Max Werninghaus, and Richard Winkelman with whom I had multiple stimulating discussions throughout writing my thesis. I'm convinced that you will bring the experiments to the next level.
My team of dauntless proofreaders: Dr. Jürgen Rohrwild who never ceases to amaze me with the diversity of his understanding of physics, Julia Bungenberg who meticulously analyzed all important sentences, and Dr. Ben O'Leary who put my Zealots into the correct build order and finally taught me that I'm not the queen of England.
Barbara Robens, my wife, who has endured every step of my thesis with me. Without you and your unshakable belief in myself, I could have never started my path of becoming a researcher. You have been an endless source of motivation, you always knew what to do and what to say, and you even taught me how to keep a healthy balance between the lab and our time together while simultaneously working on your own thesis.
My family: my parents, my sister as well as Barbaras parents and her sister for their never ending support and teaching me curiosity, tenacity, and that you are never too old to play.